ON MEASURING THE STOCHASTIC GRAVITATIONAL RADIATION BACKGROUND WITH LASER INTERFEROMETRIC ANTENNAS

by

NELSON LLOYD CHRISTENSEN, JR.

B.S., Stanford University

(1985)

SUBMITTED IN PARTIAL FULFILLMENT

OF THE REQUIREMENTS FOR THE

DEGREE OF

DOCTOR OF PHILOSOPHY

at the

MASSACHUSETTS INSTITUTE OF TECHNOLOGY

AUGUST, 1990

Signature of Author ______________________________

Department of Physics
August, 1990

Certified by ______________________________

Rainer Weiss
Thesis Supervisor

Accepted by ______________________________

George Koster
Chairman, Department Committee

ON MEASURING THE STOCHASTIC GRAVITATIONAL RADIATION BACKGROUND WITH LASER INTERFEROMETRIC ANTENNAS

by

NELSON LLOYD CHRISTENSEN, JR.

Submitted to the Department of Physics in August, 1990
in partial fulfillment of the requirements for
the degree of Doctor of Philosophy in Physics

ABSTRACT

A comprehensive study of the method of detecting a stochastic gravitation wave background (SGWB) with laser interferometric gravitational wave antennas is presented. The SGWB can be measured by correlating the output of two or more detectors. The results of this thesis can be applied to the planned new generation of kilometer length interferometers, such as the Laser Interferometer Gravitational-Wave Observatory (LIGO) in the United States, or similar systems in other countries. Advanced detectors will be able to limit the gravity wave background energy density per logarithmic interval at 100 Hz to 2×10^{-10} times the closure density of the universe. A survey of potential sources indicates that a pair of antennas will be able to confirm or deny the existence of cosmic strings, or may detect the background produced by extragalactic neutron star binaries.

Elements of the optimal interferometer design and orientation for detecting the SGWB, or any gravity wave, are given. In particular, the general transfer functions for various interferometers, the criteria for orienting a pair of antennas, the trade-off between sensitivity and bandwidth, and the effect of antenna separation on the correlation are presented.

A procedure for obtaining the correlated signal from two interferometers is given. The statistical basis of the correlation experiment is presented. The cause and effect of correlated noise is examined. Filtering and data analysis issues are also discussed. The thesis concludes with a presentation of some of my experimental work on interferometric antennas.

Thesis Supervisor: Dr. Rainer Weiss
Title: Professor of Physics

My interest in science, and especially physics, would not have developed without the encouragement of my mother and father. At an early age they fed my curiosity in many areas, from dinosaurs to microbiology, from perpetual motion machines to an infinite universe. More importantly, my parents taught me how to enjoy life. Mom and Dad, thanks for everything.

Karla Ballman has been a source of support, strength, and especially love. These years in Cambridge have been considerably more enjoyable because of her. Thanks Karla. Let's get out of here and have some fun.

Table of Contents

1. Introduction 7
   1.1 History. 7
   1.2 Gravity Waves in Linearized General Relativity 8
   1.3 Detection of Gravity Waves 11
   1.4 Sources 13
   1.5 Stochastic Gravitational Radiation 15
   1.6 Thesis Outline 18

2. Sources of a Stochastic Gravitational Radiation Background and Other Methods of Detection 20
   2.1 Introduction 20
   2.2 Phase Transitions in the Early Universe. 21
   2.3 Cosmic Strings 27
   2.4 Inflation 30
   2.5 Thermal Spectra 32
   2.6 Binary Systems 33
   2.7 Pulsar Timing Limits 35
   2.8 Doppler Tracking Limits 37
   2.9 Cosmic Background Radiation Anisotropy Limits 38
   2.10 Nucleosynthesis Limit 39
   2.11 Limits from the Earth's and Sun's Normal Modes. 39
   2.12 Limit from a Gravitational Lens 40
   2.13 Limits from Bar Antennas. 40
   2.14 Laser Interferometer in Space. 41

3. Interferometer Transfer Functions 42
   3.1 Introduction 42
   3.2 Michelson Delay Line Interferometer 44
   3.3 Fabry-Perot Interferometer 50
   3.4 Recycling Interferometer 54
   3.5 Dual Recycling Interferometer 60
   3.6 Resonant Recycling Interferometer. 65
   3.7 Common Feature of all Transfer Functions 68
   3.8 Finite Contrast and Modulation. 70

4. Interferometer Orientation. 72
4.1 Introduction 72
4.2 Coordinate System 72
4.3 Solving for an Optimum Orientation. 75
4.4 Physical Explanation for Orientation. 86
4.5 Single Interferometer Response. 90
4.6 Conclusion. 91

5. Two Detector Problem. 94
5.1 Introduction 94
5.2 Stochastic Gravitational Wave Background. 94
5.3 The Measurable Quantities 95
5.4 Practical Solution. 98
5.5 Noise. 99
5.6 Influence of Noise on Correlation. 101
5.7 Filtered Data. 102
5.8 Orientation and Location of the Antennas. 103
5.9 Dual Recycling Bandwidth Considerations 108
5.10 Sensitivity Limits 112

6. Multiple Detectors and Statistics 118
6.1 Introduction 118
6.2 Two Detector Statistics. 118
6.3 Multiple Detectors. 123
6.4 A System of One Half Length and Two Full Length Interferometers. 129
6.5 Correlated Noise at a Similar Site. 134
6.6 Other Coherence Statistics. 135
6.7 Non-Gaussian Data 137
6.8 Data Analysis 140

7. Coherent Noise in Different Interferometers. 142
7.1 Introduction 142
7.2 Seismic Noise 142
7.3 Fluctuations in the Residual Gas Column Density Inside the Common Vacuum System. 148
7.4 Magnetic Field Fluctuations 151
7.5 Acoustic Noise. 160

7.6 Cosmic Ray Showers. 161
7.7 Conclusion on Correlated Noise. 161
8. Experimental Projects. 164
8.1 Introduction 164
8.2 Fiber Optics 164
8.3 Low Noise High Voltage Amplifier for the Mass Suspension System. 178
9. Conclusion. 187

Appendices

A. Gravity Wave Fourier Transform. 190
B. Shot Noise Limit for an Interferometer 191
C. Some Exact Solutions 193
References 202

Chapter 1 Introduction

Section 1 History

General relativity is one of the greatest achievements of classical physics. It has withstood many stringent tests, and it appears that it is the correct theory of classical gravitation. A consequence of the theory, that was immediately noticed by Einstein (Einstein, 1916), was the presence of gravitational radiation. A perturbation of a massive system will produce a change in the gravitational field that will propagate at the speed of light. The waves that are generated by the gravitational disturbance will be ripples on the background metric which defines our space-time. Gravity waves are space-time ripples.

There are similarities between the electromagnetic theory of Maxwell and the theory of gravity. We are accustomed to electromagnetic radiation, and there is no trouble in accepting that accelerating charges will emit radiation. Analogously, we should not be surprised that accelerating masses will emit gravitational radiation. A travelling electromagnetic wave will have its fields transverse to its propagating direction, and so will a travelling gravity wave. There are two distinct polarizations for both electromagnetic and gravitational radiation. However, the electromagnetic force is much stronger than the gravitational force, and hence, the effects of gravitational radiation will be that much more difficult to observe. In fact, the gravitational force is so weak that no detectable gravity waves can feasibly be produced by humans. We must depend on extremely energetic and massive astronomical phenomena to produce observable events. Therefore, any detector of gravity waves will actually be an antenna looking at astronomical events. A new telescope.

An active experimental effort to detect gravitational radiation has been going on since the early 1960's. Weber's development of the resonant bar antennas initiated the research in this field. His unconfirmed detection of gravity waves (Weber, 1969) spawned the construction of other bar detectors around the world. These bars are generally cylindrical pieces of aluminum, which would have their fundamental mode excited by a passing gravity wave of sufficient amplitude. They tend to operate at about 1 KHz, with a bandwidth on the order of 10 Hz. Today these bars have advanced to impressive sensitivities, and they are likely to be the first devices to directly detect gravity waves.

The idea of a laser interferometric gravity wave antenna was conceived in the early 1970's (Moss, Miller and Forward, 1971; Weiss, 1972). This device measures the relative phase shift in the two arms of the interferometer which is produced by a passing gravity wave. The gravity wave would cause the two suspended mirrors in one arm to move away from each other, while the two mirrors in the other arm would move closer together. This detector would operate at a frequency around 1 KHz, with an equally large bandwidth. The first gravity wave interferometer was constructed at Hughes Research Laboratory by Forward (1978). Today there are numerous systems around the world. The construction of kilometer length interferometers in the 1990's will create a new astronomical observing system.

The existence of gravitation radiation has been verified via the observation of the binary pulsar system PSR 1913+16 (Taylor and Weisberg, 1982). The measured orbital period derivative of the two 1.4 $M_\odot$ neutron stars is in excellent agreement with what is predicted when the energy loss due to the emission of gravity waves is taken into account. Although this is not a direct detection of gravity waves, it is a piece of indirect evidence that is virtually irrefutable. The observations of PSR 1913+16 by Taylor and his collaborators throughout the 1980's have contributed more favorable evidence supporting the claim that gravity wave emission is the cause of the orbital decay

Section 2 Gravity Waves in Linearized General Relativity

In the weak field limit ($\Phi \ll c^2$, where Φ is the gravitational potential energy) the space-time metric can be approximated as

$$g_{\mu\nu} \approx \eta_{\mu\nu} + h_{\mu\nu} \quad ,$$

where $\eta_{\mu\nu}$ is the Minkowski metric, and it is assumed that $|h_{\mu\nu}| \ll 1$. See Misner, Thorne, and Wheeler (1973), Weinberg (1972), or Ohanian (1976), for a comprehensive treatment of gravity waves. The material of this section primarily comes from Ohanian (1976). The solution to the linearized field equations yields the wave equation for gravity waves propagating through the vacuum to infinity,

$$\left(\frac{-1}{c^2} \frac{\partial^2}{\partial t^2} + \nabla^2 \right) h_{\mu\nu} = 0 \quad .$$

If one expresses the metric perturbation in terms of a travelling wave,

$$h_{\mu\nu} = h_0\left(\epsilon_{\mu\nu}e^{ik_\mu x^\mu} + \epsilon^*_{\mu\nu}e^{-ik_\mu x^\mu}\right) \quad ,$$

where h_0 is the amplitude, and $\epsilon_{\mu\nu}$ is a constant unit polarization tensor, then the wave vector satisfies $k_\mu k^\mu = 0$. The freedom to make a gauge choice, $\partial^\mu h_{\mu\nu} = 0$, results in the transverse condition, $k^\mu \epsilon_{\mu\nu} = 0$. The are only two possible solutions for $\epsilon_{\mu\nu}$ that will satisfy the above equations, and carry energy to infinity. If the wave is travelling in the $\hat{z}$ direction, the two solutions are

$$\epsilon^{(+)}_{\mu\nu} = \begin{pmatrix} 0 & 0 & 0 & 0 \\ 0 & 1 & 0 & 0 \\ 0 & 0 & -1 & 0 \\ 0 & 0 & 0 & 0 \end{pmatrix} \quad , \ and, \quad \epsilon^{(\times)}_{\mu\nu} = \begin{pmatrix} 0 & 0 & 0 & 0 \\ 0 & 0 & 1 & 0 \\ 0 & 1 & 0 & 0 \\ 0 & 0 & 0 & 0 \end{pmatrix} \quad .$$

The solution $\epsilon^{(+)}_{\mu\nu}$ is called the "plus" polarization, while $\epsilon^{(\times)}_{\mu\nu}$ is the "cross" polarization.

The presence of a gravity wave will produce a gravitational tidal distortion. Figure 1.1 shows the influence a gravity wave has on a circular distribution of particles. The gravity wave is propagating into the page. If this circle of particles starts with a diameter of L, the wave will compress one axis to a distance of L_1, given by $L_1 = (1 - \frac{1}{2}h_0)L$. At the same time the other axis is expanded to a distance of L_2, given by $L_2 = (1 + \frac{1}{2}h_0)L$. The gravity wave behaves like a strain.

The emission of gravitational radiation is similar to the emission of electromagnetic radiation. However, the lowest allowed multipole moment of gravitational radiation is the quadrupole, whereas for electromagnetic radiation it is the dipole. If one could create a gravitational dipole (which is impossible), and express it as $\vec{d} = m\vec{r}$, then in analogy to the electromagnetic case, dipole radiation will only exist if the second derivative of the dipole is nonzero, or $d^2\vec{d}/dt^2 = d^2(m\vec{r})/dt^2 \neq 0$. However, this term is zero due to conservation of momentum. Hence, there can be no gravitational dipole radiation. A similar argument applies for the analog of magnetic dipole radiation. In this case conservation of angular momentum makes radiating impossible.

Gravity waves are generated by a mass quadrupole that has a nonzero third time derivative. For a quadrupole moment given by

$$Q^{kl} = \int \left(3x^k x^l - r^2\delta^l_k\right)\rho(\vec{x})d^3x \quad ,$$

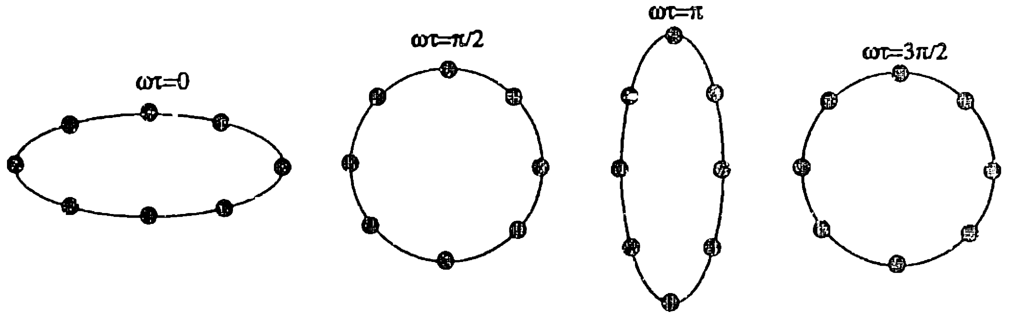

Plus Polarization

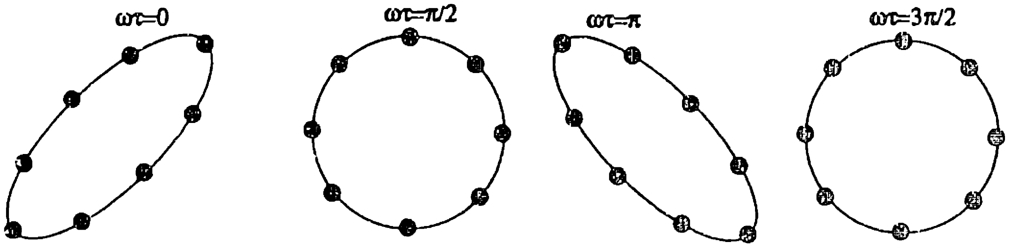

Cross Polarization

Figure 1.1 Response of a bead of particles to a gravity wave propagating into the page. The top row shows the influence of the plus polarization, the bottom row shows the cross polarization. The angular frequency of the wave is ω, the time is τ.

the total power of the emitted radiation is

$$P_{gw} = \frac{dE}{dt} = \frac{G}{45c^5}\left(\frac{d^3Q^{kl}}{dt^3}\right)\left(\frac{d^3Q^{kl}}{dt^3}\right) \quad ,$$

while the metric perturbation is

$$h^{kl}(t,\vec{x}) = \frac{2G}{3rc^4}\left(\frac{d^2Q^{kl}}{dt^2}\right)_{(t-r/c)} \quad .$$

The gravity wave is evaluated at retarded time $t - r/c$, where r is the distance from the quadrupole. It is convenient to make an order of magnitude estimation for a source. The amplitude of the wave will be close to

$$h \sim \frac{G(KE)_{ns}}{c^4 r} \quad ,$$

where $(KE)_{ns}$ is the total non-spherical kinetic energy of the source. Also, if one knows the radiated gravity wave power, P_{gw}, at frequency f, the strain at a distance r will be

$$h \sim \sqrt{\frac{GP_{gw}}{2\pi^2 f^2 c^3 r^2}} \quad .$$

Section 3 Detection of Gravity Waves

The goal of the research group is to build a laser interferometer that will detect the presence of a gravity wave. An outline of a simple delay line system is displayed in Figure 1.2. The four mirrors are the test masses. Each is suspended by a wire, like a pendulum, so they all are free to move in inertial space. A gravity wave of plus polarization travelling into the page will cause the two masses in one arm, say the arm labeled X, to separate, while the two masses of arm Y will come together. This is similar to the circular bead of particles above. Say the arms start with a length L before the gravity wave of amplitude h_0 arrives. The wave will cause the Y arm length to decrease in length to L_Y, given by $L_Y = (1 - \frac{1}{2}h_0)L$. At the same time, the X arm is expanded to a length of L_X, given by $L_X = (1 + \frac{1}{2}h_0)L$. This length change can be detected by a change in the interference fringe of the light hitting the photodetector at the output. Because the gravity wave produces a strain, the sensitivity of the detector can be increased by making the arms of the system longer. In the delay line system the light bounces back and forth a number of times to increase the effective length of the arms, and thereby increasing the sensitivity. In a variant of this system, some interferometric detectors use Fabry-Perot cavities in each arm. The light builds up and is stored in the cavities, thereby producing a similar increase in sensitivity.

Interferometers today have a displacement sensitivity of about $10^{-16} cm/\sqrt{Hz}$ at frequencies around 1 KHz. The Caltech Fabry-Perot system has an arm length of 40 meters, which would give it a strain sensitivity of $h(f) = 2.5 \times 10^{-20}/\sqrt{Hz}$, or a value of $h = 8 \times 10^{-19}$ for a 1KHz bandwidth. The M.I.T. group is working together with the Caltech group to design and build a pair of four kilometer arm length Fabry-Perot interferometers. This is the Laser Interferometer Gravitational-Wave Observatory (LIGO) project. The plan is to have these two interferometers located on opposite sides of the continental United States. One of these sites will have a two kilometer interferometer inside the same vacuum system as the four kilometer system. The goal is to have an initial system with a strain sensitivity of about $h(f) = 10^{-23}/\sqrt{Hz}$ at 100 Hz, yielding $h = 10^{-22}$ for a 100 Hz

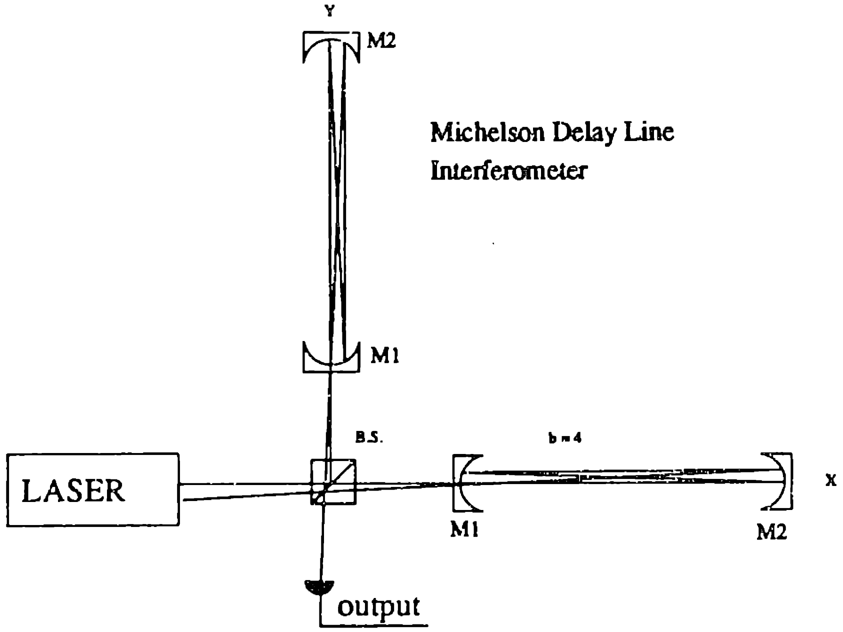

Figure 1.2 Example of a delay line system. Light enters a cavity through a hole in M1, traverses the cavity a total of b times, and exits through the same hole. The beams from the two cavities recombine at the beamsplitter.

bandwidth. The plan is to have these systems operating by the mid 1990's. Advanced interferometer designs that will be implemented in the late 1990's should increase the sensitivity by more than a factor of 10. These detectors will operate at frequencies from tens of Hz up to 10 KHz. The results of this thesis will be useful for the worldwide network of long baseline interferometers.

There are a number of laser interferometer gravity wave research groups around the world. A German–British research team is working on the development of another multiple kilometer length system. Their detector will be a delay line system, which will likely be located in the Federal Republic of Germany. A French-Italian team is also at work. They are planning to build an antenna in Italy. An Australian group intends to build their detector in western Australia. A Japanese group is considering an interferometer on the moon, and a group at the University of Colorado, Boulder, is researching a low frequency interferometer that would orbit in space in an orbit at 1 AU.

As mentioned above, groups using resonant bars are also trying to detect gravity waves. The technology associated with this area has evolved considerably since the field was conceived by Weber. The bars are now operated at 4°K. The transducers for sensing the bar motion have also improved. Piezoelectric crystal sensors have been replaced by inductive modulated resonant transducers that are monitored by a superconducting quantum interference device (SQUID). See Michelson, Price, and Taber (1987) for a current review of bar technology. These bars have a sensitivity of about $h \sim 10^{-18}$ at 1 KHz. There are operating bar antennas at Stanford, Louisiana State University, University of Maryland, and Rome University, and research groups working on bars at Rochester University, Western Australia and Moscow.

Section 4 Sources

The sources of gravity waves fall into three classes: bursts, periodic, and stochastic. The detection of burst events with laser interferometry was addressed by Dewey (1986). A burst event is a sharp, impulsive spike, with a low duty cycle. A likely burst source will be a type II supernova, where a massive star collapses to a compact object like a neutron star or a black hole. The collapse, and the bounce off the new neutron core will have a tremendous amount of kinetic energy. In order for there to be a nonzero quadrupole moment the collapse must be nonspherical. The dynamics of an actual collapse are not known, but if one assumes that $\varepsilon M_{\odot}c^2$ of energy goes into gravity waves, where ε is the efficiency factor, and that the energy is radiated in a time of $1/f$, then the strain at a distance r will be

$$h \sim 2 \times 10^{-17}(\varepsilon)^{1/2}\left(\frac{1KHz}{f}\right)^{1/2}\left(\frac{10Kpc}{r}\right) \quad .$$

A supernova with an efficiency of $\varepsilon \sim 10^{-4}$ at 1 KHz, in the center of our galaxy yields $h \sim 2 \times 10^{-19}$. For supernova 1987a at $r \sim 50Kpc$, and the other parameters the same, one would have $h \sim 4 \times 10^{-20}$. At a distance of 10 Mpc, which would be in the Virgo cluster, one would have $h \sim 2 \times 10^{-22}$, which should be just within the range of detectability for the LIGO system. The event rate for type II supernova in our galaxy is only about one per 50 years, while if we look all the way out to 10 Mpc there should be a few observable events per year. Other burst events could be a stellar or neutron star collapse to a black hole, collisions of collapsed objects, or objects plunging into a black hole and exciting the hole's normal modes.

The detection of periodic sources was investigated by Livas (1987). A periodic source emits continuous waves of gravitational radiation at a specific frequency. A sinusoidal signal wave will be produced. A likely source of periodic gravitational waves will be pulsars. These rotating neutron stars have been observed with periods as small as $1.6 \times 10^{-3} s$ (PSR 1937+214). In order for a pulsar to radiate gravity waves it must have a non-symmetric moment about its rotation axis. Say the pulsar rotates about the $\hat{z}$ axis, with a moment of inertia I_{zz}, and angular frequency ω. Also, call Q_{xx} and Q_{yy} the quadrupole moments, as defined above. Then if the ellipticity is defined to be

$$\epsilon = \frac{Q_{xx} - Q_{yy}}{I_{zz}} \quad ,$$

the emitted gravity wave power, at a frequency 2ω, is

$$P_{gw} = \frac{32G}{5c^5} I_{zz}^2 \omega^2 \epsilon^2$$

(Shapiro and Teukolsky, 1983). The gravity wave amplitude at a distance r for a $1.4 M_\odot$ pulsar with a radius of 10 km would be

$$h = 8 \times 10^{-20} \epsilon \left(\frac{f}{1KHz} \right)^2 \left(\frac{10Kpc}{r} \right)$$

(Thorne, 1987). The large uncertainty is the ellipticity. An advantage arises from the fact that the signal is periodic, so optimum filtering techniques, along with large integration times, may be used. A pulsar with a rotation frequency of 500 Hz, at a distance of 10 Kpc, and an ellipticity of $\epsilon = 10^{-6}$ will produce a strain amplitude of $h \sim 2 \times 10^{-26}$ and could be detectable by the initial LIGO system when one integrates for $10^7 s$.

A cross between the burst and the periodic signal is the chirp produced when two objects spiral into each other as their orbit decays. This will be the ultimate fate of the binary pulsar PSR 1913+16 mentioned above. This system of two neutron stars is losing energy via the emission of gravitational radiation, and the stars are moving closer together. When the stars finally collide a substantial amount of gravitational radiation will be produced. If one assumes that the orbit of the binary system is circular, which it will tend to as the orbit decays, then the radiated gravity wave power will be

$$P_{gw} = \frac{32G^{7/3}}{5c^5} M^{4/3} \mu^2 \omega^{10/3} \quad ,$$

where the total mass of the system is $M = m_1 + m_2$, the reduced mass is $\mu = m_1 m_2 / M$, and the angular frequency of the orbit is ω (Shapiro and Teukolsky, 1983). The gravity waves will have angular frequency 2ω. The average of the strain amplitude at a distance r will be

$$h = \frac{4G^2 m_1 m_2}{r c^4 \sqrt{5}} \left(\frac{\omega^2}{G(m_1 + m_2)} \right)^{1/3} \quad .$$

When two neutron stars are so close that they start experiencing tidal disruptions, the gravity wave frequency will be at about 1 KHz, and the gravity wave strain at a distance r from the system will be $h \sim 3 \times 10^{-18}(10Kpc/r)$. At a distance of 10 Mpc, in the Virgo cluster, the strain will be $h \sim 3 \times 10^{-21}$. The hope is that the event rate for neutron binary collapse will be large enough to produce a few events a year when one looks as far away as 100 Mpc, for which the signal strength would be $h \sim 3 \times 10^{-22}$. The periodic chirp produced when the binary system goes through its final orbits will also be an enlightening signal to observe. The chirp will go from 300 Hz to 1 KHz in 110 milliseconds (Dewey, 1986). The gravity wave signal will be even larger if two black holes spiral into each other as the mass will probably be larger, and they will get closer together before the collision takes place. Smith (1988) developed techniques for detecting a chirp event with a laser interferometer.

Section 5 Stochastic Gravitational Radiation

My thesis concerns the detection of stochastic gravitational radiation. Stochastic radiation is considerably different than burst or periodic radiation. It is a background fuzz, or a random noise of gravity waves. It will have no evidence of any sharp specific character in either the time or frequency domain. A burst event will be a definite signature in the time domain, while a periodic event will be a distinct signal in the frequency domain. Stochastic gravitational radiation will be neither. An example of electromagnetic stochastic radiation is the cosmic microwave background, or any other black body radiation. The stochastic gravitational radiation, should it exist, will probably be produced by some cosmological event, and would pervade the universe as a noise on the background metric.

Some specific statistical definitions are useful in describing this source of radiation. A stochastic process is defined in terms of an ensemble of functions, $\{{}^{k}x(t)\}$, where t represents time and k labels the particular member of the ensemble, such that one can describe the ensemble by statistical properties. A process is called a stationary random process when all the statistical properties are independent of time. A stationary random process is called ergodic if an average at a specific time of different ensemble members can be replaced by a time average of a single member of that ensemble (Bendat, 1958). The gravity waves that I am concerned with in this thesis are stochastic, stationary, and ergodic. They are assumed to be isotropic in that the statistical properties can be determined by looking at any section of the sky, just like the microwave background. These gravity waves are completely characterized by their power spectral density.

The stochastic gravitational wave background (SGWB) certainly exists at some level, and is probably produced by various cosmological events. These events could include phase transitions in the early universe, quantum fluctuations during inflation, the transition in the universe's expansion rate from the exponential inflation case to the slower radiation dominated case, the decay of cosmic stings, or a host of other events. The gravity wave sources are distributed throughout the universe, and as the waves interact only very weakly with matter, the background radiation will survive intact. The only change in the character of these cosmologically produced waves will be the redshift due to the expansion of the universe. The spectrum of the SGWB today will range from frequencies as low as $1/T_{Hubble}$, to as high as $10^{14} Hz$, if not higher. Just like the microwave background, the gravity wave background will be a randomly polarized relic of the early universe, and its observation will give clues about the history of our cosmos. This gravitational radiation is completely different in character than the burst from a supernova, or continuous periodic wave from a pulsar. This radiation is a constant noise, with its only characteristic change being its cosmological redshift. The SGWB's spectral density is its only defining quantity.

The task of detecting the SGWB will be different than for detecting a burst or periodic event. A single detector, be it a laser interferometer or a resonant bar, will be able to register and identify, but not confirm, a burst or a sine wave. This is not the case for the SGWB. The signal recorded by a detector from the SGWB will be indistinguishable from the detector's own intrinsic noise. With a single detector the only certain thing that can be said is that the level of the SGWB signal is less than or equal to the detector's noise level. Unfortunately, there is no way to turn the SGWB on and off to chop the signal. Therefore, in order to detect the SGWB one must use at least two detectors, and perform a correlation on the two signals, thereby extracting the common signal from the independent noise of each detector.

A simple version of the experiment is as follows. The time series for detectors one and two is given by

$$\begin{aligned} x_1 &= s(t) + n_1(t) \\ x_2 &= s(t) + n_2(t) \quad . \end{aligned}$$

The common signal is s, while the noise for detectors one and two is n_1 and n_2 respectively. When one assumes that s, n_1 and n_2 are all independent stationary random variables with zero mean, the correlation function $\psi(\tau)$ is found to be

$$\psi(\tau) = \lim_{T\to\infty} \frac{1}{T} \int_0^T x_1(t) x_2(t+\tau) dt = \lim_{T\to\infty} \frac{1}{T} \int_0^T s(t) s(t+\tau) dt \quad .$$

This gives the rms value of the signal. The spectral density of the signal, and its relation to the correlation function are given by the Wiener-Khinchin relations,

$$\begin{aligned} \psi(\tau) &= \int_0^\infty S(f) \cos[2\pi f \tau] df \\ S(f) &= 4 \int_0^\infty \psi(\tau) \cos[2\pi f \tau] d\tau \end{aligned}$$

(Rice, 1954). If s is unitless, then so is $\psi(\tau)$, while the spectral density $S(f)$ has units of $1/Hz$.

The gravity wave detectors measure the unitless strain, $h(t)$. The correlation measurement gives the rms value of the strain in the detectors bandwidth, h^2_{rms}, or its spectral density, $S_h(f)$. The gravity wave spectral density is related to the energy density of this radiation

$$\rho_{gw} = \int_{0}^{\infty} \rho_{gw}(f) df \quad ,$$

by

$$\rho_{gw}(f) = S_{h}(f) \frac{\pi c^2 f^2}{8G} \quad .$$

The energy density, ρ_{gw}, has units of erg/cm^3, while $\rho_{gw}(f)$, has units of $erg/(cm^3 - Hz)$. A useful quantity to express the amount of background gravitational waves is the ratio of the gravity wave energy density per logarithmic frequency interval to the closure density of the universe, ρ_c. This ratio, $\Omega_{gw}(f)$, is

$$\Omega_{gw}(f) = \frac{1}{\rho_c} \frac{d\rho_{gw}}{d \ln f} = \frac{f \rho_{gw}(f)}{\rho_c} \quad .$$

In this thesis I have used the value $\rho_c = 1.7 \times 10^{-8} erg/cm^3$. This assumes that the Hubble constant today is $100 km/s/Mpc$.

Section 6 Thesis Outline

The thesis addresses how one will measure and quantify the SGWB using laser interferometers. Chapter 2 contains a discussion of the sources of a SGWB. Also discussed are the methods, besides laser interferometry, that have been, or will be used to limit the strength of the SGWB. Chapter 3 presents my analysis of the general transfer functions of different interferometer designs. This is done for all the interferometer types that will likely be used in the LIGO system. The transfer functions are general solutions in that they are valid for gravity waves coming from any possible direction, with any polarization. Chapter 4 contains my work on how one can find the optimum orientation of two interferometers located anywhere on the surface of the earth. This solution optimizes the detector pair for a search of the SGWB, or for searching for randomly polarized gravity wave bursts. Chapter 5 contains the explicit analysis for the extraction of the gravity wave spectrum from the correlated output of two or more interferometers. Chapter 6 contains the statistical analysis of the correlation problem, and other statistical considerations. Chapter 7 addresses the problem of correlated noise, other than gravitational waves, in both of the interferometers being used for the observation. This is done for a detector pair at the same site, and for a pair separated by a continental distance. Chapter 8 presents some of the experimental work that I have done in connection with the development of laser interferometric gravity wave antennas. Chapter 9 is the conclusion.

Chapter 2 Sources of a Stochastic Gravitational Radiation Background and Other Methods of Detection

Section 1 Introduction

This chapter discusses the potential sources of a stochastic gravitational radiation background, and methods, besides ground based laser interferometry, to detect, or set limits on it. This will be done for wavelengths as large as the Hubble length, to as small as 1 mm. The potential sources range from binary star systems, to exotic sources such as cosmic strings. Needless to say, no gravity waves, stochastic or otherwise, have been directly detected. Of course, their existence is hardly doubted due to the observation of the binary pulsar system, PSR 1913+16 (Weisberg and Taylor, 1984). However, important constraints have been placed on the spectrum.

Some of the sources produce enough radiation, and at the right frequencies, for a system of four kilometer length interferometers to detect. The LIGO system (Vogt, 1989) has the potential to see the stochastic gravitational radiation from some important sources. If cosmic strings exist they will be seen. Various theorized phase transitions in the early universe may produce domain walls, or solitons, that will decay away via gravity wave emission, and also create binary systems, that may be seen. The initial creation of our universe definitely created gravity waves, and certain cosmological scenarios will leave that remnant in the LIGO's range of detectability. A more certain source, neutron star binary systems in other galaxies, will produce a background just at the level of sensitivity of the future advanced interferometers that will be used. The predicted spectra for different sources of a stochastic gravity wave background are displayed in Figure 2.1. Also shown are some of the limits that have, or will be placed on its intensity. The lines labeled LIGO 1 and LIGO 2 refer to the sensitivity that will be achieved with the first generation LIGO detectors, and the advanced LIGO detectors (see chapter 5). An integration time of 10^7 seconds was assumed.

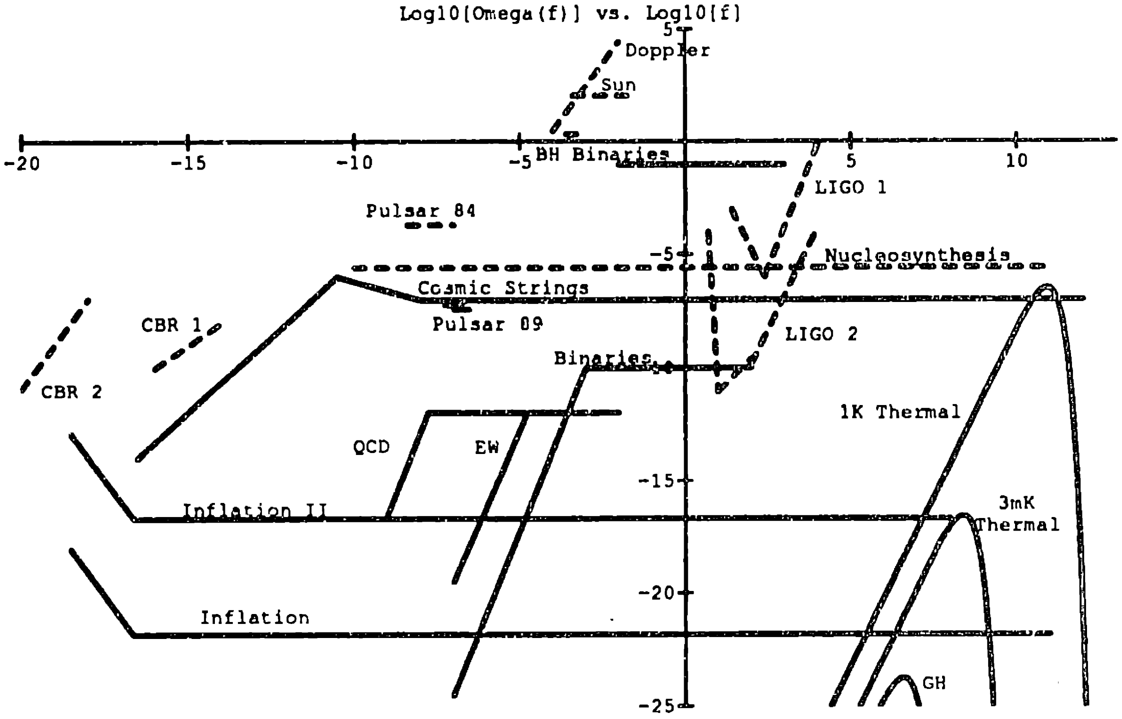

Figure 2.1 Plot of $\mathrm{Log}_{10}[\Omega_{gw}(f)]$ vs. $\mathrm{Log}_{10}[f]$. The solid lines show predicted spectra for the stochastic gravity wave background, while the dashed lines refer to limits placed, or to be placed on it. The lines labeled LIGO 1 and LIGO 2 refer to the sensitivity that will be achieved with the first generation LIGO detectors, and the advanced LIGO detectors (see chapter 5). An integration time of 10^7 seconds was assumed.

Section 2 Phase Transitions in the Early Universe

A first order phase transition may have occurred in the early universe. If this happened, gravitational radiation production would be a likely consequence. Witten (1984) and Hogan (1986) have investigated the scenario where the universe undergoes a phase transition due to QCD or electroweak interactions. The QCD transition is assumed to have occurred when quasifree light quarks begin to form mesons and Baryons at a temperature around 100 MeV. The electroweak phase transition would occur around 100 GeV when symmetry breaking occurs. Observation of these phenomena could yield information on these events.

The transition occurs when the cosmological expansion cools the universe to the critical temperature, T_c. Bubbles of the low temperature phase form and expand at speeds near that of light. This continues until the bubbles have compressed the remaining high temperature phase, and raised its temperature back up to T_c. Then the two phases can coexist in thermal equilibrium. As the universe continues to expand the temperature decreases and the bubbles of the high temperature phase shrink via evaporation, until they disappear.

During the bubble nucleation process, pressure fluctuation waves are generated, which in turn generate the gravity waves. Also, when the two phases are in equilibrium with one another, large scale density perturbations and hence gravity waves will be produced. These large scale waves are on the order of the Hubble length at that time. The analysis of Hogan (1986) displays that the peak in the spectra will correspond to wavelengths that were about the Hubble size during the transitions. When the waves were produced the ratio of energy density of gravity waves per logarithmic interval to the critical energy density was

$$\Omega_{gw}(f)/\Omega_{rad} = (\Delta T/T_c)^2 (R_n H)^3 v_s^6 \quad , for, \quad H < f < v_s/R_n \ ,$$

where ΔT is the temperature between the two phases at temperature T_c, v_s is the speed of sound (which will be about $c/3^{1/2}$ for a cosmic fluid), H is the Hubble constant at the time of the transition, R_n is the average distance between the bubbles when they come into equilibrium, and Ω_{rad} is the ratio of energy density of radiation to critical energy density ($\Omega_{rad} \sim 1$ then, $\Omega_{rad} \sim 2.4 \times 10^{-5}$ today). The spectrum of $\Omega_{gw}(f)$ is flat from wavelengths of the order of the Hubble distance down to c times the travel time for a sound wave from a bubble to another bubble. At frequencies $f \sim H$ there is production of gravity waves due to the universe expanding with different regions in different states, thereby producing large scale matter flow. This anisotropic expansion rate for the universe produces

$$\Omega_{gw}(f)/\Omega_{rad} \sim (R_n H)^3 v_s^6 \quad .$$

For frequencies $f < H$ the waves are produced when density perturbations enter the horizon, and have $\Omega_{gw}(f)/\Omega_{rad} \propto h_{enter}^2 \propto f^3$, where h_{enter} is the amplitude of the gravity wave then when it enters the horizon (Bardeen, 1980). For frequencies $f > v_s/R_n$ the gravity wave production depends on the details of the plasma motion on a scale less than the bubble separation, which can not be predicted with certainty, but an optimum scenario would have the spectrum decreasing at least as fast as $\Omega_{gw}(f)/\Omega_{rad} \propto f^{-1}$.

Because the energy densities ρ_{gw} and ρ_{rad} both decrease as a^{-4}, where a is the scale factor of the universe, $\Omega_{gw}(f)/\Omega_{rad}$ is constant as the universe expands.

Barring any out of equilibrium decays that would produce an entropy increase, the relationship between $\Omega_{gw}(f)$ and Ω_{rad} should be the same today as it was at this very early time.

Hogan (1986) assumed a strongly first order transition with $\Delta T/T \sim 1$, and he calculated that for QCD transitions that were nucleated by thermal fluctuations one would have $(R_n H/c) \sim 10^{-2}$ (Hogan, 1983). For the QCD transition at 100 MeV the peak value of $\Omega_{gw}(f) \sim 10^{-12}$ ranges from $2 \times 10^{-8} Hz < f < 10^{-6} Hz$ today, and goes down as f^{-1} after that. For an electroweak transition at 100 GeV, again with $\Delta T/T \sim 1$ and $(R_n H) \sim 10^{-2}$, the peak value of $\Omega_{gw}(f) \sim 10^{-12}$ would range from $2 \times 10^{-5} Hz < f < 10^{-3} Hz$ today, and then goes down as f^{-1} after that.

The QCD transition will be at the right frequency for pulsar timing to limit it (Stinebring, Ryba, Taylor, and Romani, 1990). As of today, the best limit is $\Omega_{gw}(f) \sim 10^{-7}$ at $2 \times 10^{-7} Hz$. This will be described in more detail in below. Achieving a limit of $\Omega_{gw}(f) \sim 10^{-12}$ with pulsar timing is quite a formidable task. The electroweak transition may actually be observed in the future. The predicted spectra fall within the detectability range of an interferometer in space (Faller, Bender, Hall, Hils, and Vincent, 1984, to be discussed below).

There are other phase transitions that may produce gravitational radiation. Stecker and Shafi (1983) considered the case where the dark matter in the universe is due to axions. Axions were used by Peccei and Quinn (1977) to explain why strong interactions do not violate CP invariance, which is consistent with the limit on the electric dipole of the neutron. The global symmetry was spontaneously broken at an energy scale that is thought to be around $10^{12}\ GeV$. A fluctuation on the order of the Hubble distance then would produce a gravity wave today with a frequency of about $2 \times 10^{5} Hz$. This phase transition would also produce domain walls that were bounded by cosmic strings. These topological monstrosities would begin to break up and decay via the emission of gravity waves at a temperature of about $100\ MeV$. The waves would have frequencies of $10^{4} Hz$ to $10^{5} Hz$ at the time of emission, and the decay would last for about $10^{4}\ to\ 10^{5}$ seconds. The domain walls and strings would have had a density comparable to that of the photon radiation. Such a background of gravity waves would exist today in the $10^{-4} Hz\ to\ 10^{-3} Hz$ band, with an energy density comparable to that of the photon background, namely $\Omega_{rad} \sim 2 \times 10^{-5}$, a level that may prove to be detectable in the future using Doppler tracking of spacecraft (Estabrook, 1987).

This technique will be discussed below.

Still another phase transition arises from the formation of solitons. Solitons are nonstable topological solutions of certain classical field theories. However, they can be stable for certain dynamical reasons (Kolb and Turner, 1990). Unlike the topological defects (topological defects such as magnetic monopoles, cosmic strings, and domain walls are produced as stable entities due to the spontaneous symmetry breaking of gauge and Higgs fields) that come from theories with nontrivial vacuum topology, the nontopological solitons are stable due a conserved charge in the theory. The domains with this charge are confined to specific regions of space (Frieman, Gelmini, Gleiser, and Kolb, 1988). These regions would have one phase of the field, a local minimum in its potential and hence a false vacuum, while the rest of the space would have the global minimum and would be the true vacuum. The soliton regions are held together by a self attracting interaction. The particle of the field considered by Frieman, et al. (1988) is massive in the vacuum, but massless inside the confined false vacuum region. When the number of particles in the region is large enough, the induced pressure prevents the collapse of the region and the soliton is stable.

Gleiser (1989) has calculated the stochastic background of gravity waves that would be produced due to soliton formation. He considered two types of solitons. Type I are described by a complex scaler field and are classically stable. However, the mass versus charge relationship for a type I soliton region is not linear. Type II soliton regions have their mass proportional to the total charge, just like ordinary matter. There are three ways that the gravity waves will be produced. The first way is through the vibration of nonspherical false vacuum bags. This would yield a value today of

$$\Omega_{gw}(f) \sim 10^{-9} n(N_{ev})(2\hbar c)^3/(m^2 M_{Pl}) \quad ,$$

where m is the energy scale of the phase transition (in eV), M_{Pl} is the Planck mass ($\sim 10^{19}$ GeV), and $n(N_{ev})$ is the number density of false vacuum bags at the time of the phase transition that were large enough so that they will not have evaporated away by now. The N_{ev} is the total charge in one of these large bubbles. Today, the spectrum of the gravity waves will be at frequencies around $f \sim 2.8 \times 10^{11}(N_{ev})^{-1/4}$. The characteristics of the spectrum are dependent on the specifics of the phase transition.

The second way that gravity waves will be produced is through bubble nucleation. This method is identical to that considered by Witten (1984) and

Hogan (1986) for the QCD and electroweak phase transitions. For the phase transition associated with the type II solitons today one would have

$$\Omega_{gw}(f) \sim 2 \times 10^{-41} N^{2/3} (m/1TeV)^2 \quad ,$$

at a frequency of $f \sim c/\left(8N^{1/3} cm\right)$. For type I solitons it would be

$$\Omega_{gw}(f) \sim 2 \times 10^{-41} N^{1/2} (m/1TeV)^2 \quad ,$$

at a frequency of $f \sim c/\left(8N^{1/4} cm\right)$. Once again the spectra is highly dependent on the characteristics of the phase transition. These spectra will not be accessible to the LIGO detectors. If the spectrum were peaked at 100 Hz and the energy of the transition were at 1 TeV, one would have $\Omega_{gw}(f) \sim 3 \times 10^{-26}$. A spectrum peaked at $10^{-4} Hz$ would have $\Omega_{gw}(f) \sim 3 \times 10^{-14}$ and could be detectable by an interferometer in space (Faller, et al. 1984).

The third way in which solitons would produce gravity waves would be from soliton star binary systems. For an energy scale of $m \sim 1GeV$, the remnants of the large false vacuum bags could remain today as solar mass objects, where they would be about the size of a neutron star. The hypothesis for this scenario is that the dark matter of the universe is comprised of these objects, which reside in the galactic halos with a significant percentage of them forming binary systems. The gravity wave energy density from this process would be

$$\Omega_{gw} \sim 10^{-10} \Omega_{ss} \left(\frac{1TeV}{m}\right)^{1/2} \quad ,$$

where Ω_{ss} is the ratio of the energy density of soliton star binary system, to the critical energy density. The frequency of the spectrum would be at $f \sim 10(m/1TeV)^{5/4} Hz$ today.

Minisoliton stars could also form. These are boson stars which are very small due to the condensation when all the bosons are in the ground state of the system. The uncertainty principle prevents these boson stars from becoming black holes because the bosons can not be confined to a region smaller than their Compton wavelength. The energy density of the gravity wave background from these binaries would be

$$\Omega_{gw} \sim 10^{-14} \Omega_{mss} \left(\frac{1TeV}{m}\right)^{1/4} \quad ,$$

where Ω_{mss} is the ratio of the energy density of minisoliton star binary system to the critical energy density. The frequency of the spectrum would be at $f \sim 4 \times 10^8 (m/1GeV)^{5/8} Hz$ today (Gleiser, 1990). If one had $m \sim 10^{-5} eV$, which is what one would expect for axions, then the gravity wave energy density today would be $\Omega_{gw} \sim 6 \times 10^{-10} \Omega_{mss}$ at a frequency of order of a few hertz.

One phase transition that may produce minisoliton stars in a regime that could be detectable by a LIGO type system (Gleiser, 1990) is that proposed by Hill, Schramm, and Fry (1989). According to this theory the universe undergoes a phase transition after photon decoupling, at a temperature of $T \sim 10^{-2} eV \sim 100°K$. The psuedo-Goldstone bosons of this theory generate a small ($m \sim 10^{-2} eV$) mass for the neutrino. A motivation for this concept is that it would solve the solar neutrino problem via neutrino mixing. The phase transition would produce a network of soft domain walls with thicknesses at that time ranging from 1pc to 1Mpc. Density perturbations of the order of $\delta\rho/\rho \sim 1$ would be produced, but since this is happening well after photon decoupling the resulting anisotropy in the CBR would be of order $\Delta T/T \sim 10^{-6}$. The domain walls, whose energy density could close the universe, would evolve into soliton star objects. The energy scale of this theory, $m \sim 10^{-2} eV$ would produce a gravity wave background of $\Omega_{gw}(f) \sim 3 \times 10^{-11} \Omega_{mss}$ at around 50 Hz, which may potentially be detectable with the advanced LIGO (Vogt, 1989) system of six advanced interferometers at one site, and three at the other (see chapter 5, section 10, for the derivation of this number).

Deryagin, Grigoriev, Rubakov and Sazhin (1987) have also investigated the generation of gravity waves in a phase transition. They considered a second order phase transition forming anisotropic W-boson condensation. Their derivation for the gravity wave spectrum is similar to that of Hogan (1986) and Witten (1984). The frequency of the gravity wave spectrum today would peak at $f \sim 4 \times 10^{-8} (T_g/1GeV) Hz$, where T_g is the temperature at which the W-boson condensation took place. The energy density of the gravity waves would be $\Omega_{gw}(f) \sim 4 \times 10^{-5} \Delta^2$, where Δ is the anisotropy in the energy density of the phases, which they estimate to be $\Delta \sim 2 \times 10^{-4}$. This would yield $\Omega_{gw}(f) \sim 2 \times 10^{-12}$.

Figure 2.1 shows the gravity wave spectra predicted by Hogan (1986) for the QCD and electroweak phase transitions.

Section 3 Cosmic Strings

A cosmic string is a one dimensional topological defect that is produced in certain field theories, such as an Abelian Higgs model, when the field undergoes spontaneous symmetry breaking (Kolb and Turner, 1990). Cosmic strings are predicted in many grand unified theories and would be produced when the universe went through this phase transition somewhere around $T \sim 10^{16} GeV$. They are either infinite in length or a closed loop. These strings could produce the density fluctuations that start galaxy formation (Vilenkin, 1981). Loops of strings would decay away via the emission of gravitational radiation. The radiation would form a stochastic background which may have sufficient strength to be observed by pulsar timing (Stinebring, Ryba, Taylor, and Romani, 1990), interferometers in space (Faller, Bender, Hall, Hils, and Vincent, 1985) and laser interferometers on the earth (Vogt, 1989).

Vachaspati and Vilenkin (1985) conducted a detailed analytic and numerical study on the radiating mechanism by the cosmic strings and predicted the spectra that would be observed today. The parameter that describes a string is its mass per unit length, μ. A loop of string will lose energy by radiating gravity waves at a rate of

$$\frac{dE}{dt} = \gamma G\mu \quad (in\ units\ where\ c = \hbar = 1),$$

where Vilenkin and Vachaspati found γ to have a value of order 100. The lifetime of a loop of length L_0 would be $\tau = L_0/(\gamma G\mu)$, giving the length as a function of time of $L(t) = L_0 - \gamma G\mu t$. The gravity waves would be emitted at specific frequencies of $f = 2n/L(t)$, where n is an integer. The factor γ for a string was determined analytically and numerically from the equation of motion, where modes up to $n = 100$ were considered. It was assumed that the loops of string were formed at time t (t is the time since the initial cosmic singularity) with an initial length of $L_0 \sim \alpha t$, and that the number of loops formed per unit volume per unit time is $dn/dt \sim \beta t^{-4}$. The quantities α and β are constants that are dependent on the specifics of the GUT phase transition. The resulting energy density of gravity waves today would be

$$\Omega_{gw}(f) = \frac{128\pi}{9}\alpha^{3/2}\beta\sqrt{\frac{G\mu}{\gamma}}\Omega_\gamma \quad ,$$

where Ω_γ is the ratio of the energy density of the cosmic background radiation to the critical energy density today. The spectrum is flat over the range

$$10^{-5}(\gamma G\mu)^{-1}\Omega h^2 yr^{-1} < f < \Omega_\gamma \left(t_{eq} t_f\right)^{-1/2} \quad ,$$

where Ω is the present ratio of the energy density of the universe to the critical energy density, h is the Hubble constant in units of $100 km/s/Mpc$, t_{eq} is the time when the radiation era ended ($t_{eq} = 4 \times 10^{10}(\Omega h^2)^{-2} s$), and t_f is the time when string-particle friction becomes unimportant ($t_f \sim 10^{-30} s$). For strings to be responsible for galaxy formation, one needs $G\mu \sim 10^{-6}$ (Vilenkin, 1981 b). With the prediction that $\alpha \sim \beta \sim 1$, the resulting spectrum today is then $\Omega_{gw}(f) \sim 10^{-7}$ from $8 \times 10^{-10} Hz$ to $10^5 Hz$. This limit is currently being constrained by timing measurements of the millisecond pulsar (Stinebring, Ryba, Taylor, and Romani, 1990). The LIGO system will ultimately have a sensitivity that will allow one to further constrain, or detect, cosmic strings, as it will have a sensitivity up to $\Omega_{gw}(f) \sim 10^{-10}$ (see chapter 5).

Calculation of the radiation by strings has been continued and expanded by many other investigators. Accetta and Krauss (1989) have taken a number of additional factors into account, and predict $\Omega_{gw}(f)$ to be two orders of magnitude smaller than previous estimates. Their numerical study indicates that the assumption of one string with length of order the horizon size at the time of formation is wrong, since the loops quickly break up into much smaller loops. There is still much uncertainty regarding the distribution of loops. This changes what Vachaspati and Vilenkin (1985) called α and β from order one, to a whole range of possibilities. In fact, they replace α by a probability distribution function. They also take into account that loops will appear to live longer when they are moving at relativistic velocities, and the additional effect of the universe being reheated as different species of particles are annihilated. Finally, they are very careful to account for the effect of the different universe expansion rates. For loops that form and decay during the radiation era, the spectrum is flat over the same frequency range as the spectra from Vachaspati and Vilenkin (1985). Loops that decay during the matter dominated era result in an amplification at low frequencies. The larger value results from the assumption that the energy was stored as matter throughout the era of radiation domination, and hence is redshifted less than radiation. So, the spectrum today is flat from $8 \times 10^{-10} Hz$ to $10^5 Hz$, and then increases by a factor 7 at $f \sim 3 \times 10^{-13} Hz$, and drops off. The overall level of $\Omega_{gw}(f)$ today ranges from 10^{-7} down to 10^{-9}.

Bouchet and Bennett (1990) have analyzed the string problem and also relaxed the limiting value of $\Omega_{gw}(f)$. Their numerical simulations reveal that the spectrum of loops is dominated by the smallest loops that they are able to resolve. They found that long strings have structure on scales much smaller than the horizon length. This tends to produce more kinks in the strings and more string-string interactions, which create smaller loops. Most of the energy density of all the strings will be in these small strings. This effect was missed in other simulations which employed numerical smoothing. The result of small loops is to decrease the amplitude of the gravity wave spectra. Their conclusion is that strings with $G\mu/c^2 < 4 \times 10^{-6}$ are consistent with the latest millisecond pulsar timing results. The cosmic strings would also be too small to have a significant influence on galaxy formation.

Yokoyama (1989) has also come up with a way to save cosmic strings from the limitations imposed by the millisecond pulsar observations. He generates the phase transition that creates the strings via a nonthermal scenario. The transition is triggered by curvature effects during inflation. The other string producing phase transitions occur thermally. Because the strings are produced during inflation the string density is diluted. String interaction occurs much latter, but would still start galaxy formation.

The amplitude of the gravity wave spectrum is further reduced (in all scenarios) if the strings are superconducting cosmic strings. In this case, the string can also lose energy through electromagnetic radiation. This dilutes the amount of energy going into gravity waves, reducing the amplitude of the gravity wave spectrum by an order of magnitude (Romani, 1988).

The cosmic string theory is constrained by observations of the microwave background and primeval nucleosynthesis arguments. A value of $\Delta T/T \sim 10^{-5}$ at an angular scale of $\theta \sim 1^\circ$ produces a limit of $G\mu/c^2 < 6\times 10^{-6}$ (Romani, 1988, Traschen, Turok, and Branndenberger, 1986). For cosmic strings to agree with the standard nucleosynthesis scenario, the energy density of the gravity waves must be less than 18% of the total energy density at that time. Albrecht and Turok (1989) claim that a value of $G\mu/c^2 \sim 10^{-6}$ is on the edge of acceptability, however, there is an uncertainty of at least three in this number.

Figure 2.1 shows the cosmic string spectra as predicted by Vachaspati and Vilenkin (1985). Note that it is right at the sensitivity of pulsar timing experiment (Stinebring, Ryba, Taylor, and Romani, 1990).

Section 4 Inflation

If the universe went through an initial period of exponential expansion, with Hubble constant H and energy density ρ related by

$$H = \sqrt{\frac{8\pi G\rho}{3c^2}} \quad ,$$

a definite spectrum of gravitational waves will result. Allen (1988) has undertaken a thorough investigation of the spectra that would exist today. The gravity waves produced would range in wavelength from as large as the current Hubble length, to as small as one millimeter. The source of the waves is the metric quantum fluctuations during the de Sitter phase. Some wavelengths even get amplified by the expansion of the universe.

The procedure for finding the present spectrum is to calculate the spectrum generated by quantum fluctuations during inflation and then follow it through the radiation and matter dominated eras. The modes of the gravity wave field must be connected by Bogoliubov coefficients (which relate the creation and annihilation operators in one curved space vacuum to those of another) as the vacuum changes from de Sitter space to radiation domination, and then again when it becomes matter dominated. Variations in the expansion rate are also expected to generate waves. The sudden change from the exponential expansion to the radiation era expansion is expected to produce a background of high frequency waves, with the highest frequencies corresponding to the time of the transition, yielding an upper limit of $\nu \sim 10^{11} Hz, \ or, \ \ \lambda \sim 3mm$ today. The spectrum increases at low frequencies because de Sitter space is globally unstable to perturbations. On a local level, observers see their Hubble volume smoothing out during expansion, but global perturbations do not die out in de Sitter space, instead they reenter the horizon sometime after the exponential expansion has ended. This causes the spectrum to increase at low frequencies. The matter domination era also suffers from this global instability and further amplifies waves with frequencies today below $10^{-15} Hz$.

Allen's (1988) prediction for $\Omega_{gw}(f)$, the ratio of the energy density of gravity waves today to the critical energy density is

$$\Omega_{gw}(f) = \frac{9\hbar H^4(t_p) H^2(t_1)}{\rho_c 64\pi^2 c^3 (2\pi f)^2} \quad , for, \ \ H(t_p)/2\pi < f < \frac{3H(t_p)}{8\pi}\sqrt{\frac{a(t_p)}{a(t_0)}},$$

$$\Omega_{gw}(f) = \frac{\hbar H^2(t_p) H^2(t_1)}{\rho_c 4\pi^2 c^3} \frac{a(t_0)}{a(t_p)} \quad , for, \quad \frac{3H(t_p)}{8\pi}\sqrt{\frac{a(t_p)}{a(t_0)}} < f < \frac{a(t_1)}{a(t_p)\Delta t},$$

$$\Omega_{gw}(f) = 0 \quad , for, \quad \frac{a(t_1)}{a(t_p)\Delta t} < f \ ,$$

where ρ_c is the critical energy density today, and $H(t_p)$, $H(t_0)$, $and\ H(t_1)$, and $a(t_p)$, $a(t_0)$, $and\ a(t_1)$ are the Hubble constants and scale factors at the present time, the beginning of the matter domination era, and the end of the inflationary epoch respectively.

The major uncertainty in the level of this spectrum is the value of the Hubble constant during inflation, or equivalently, the energy density then. They are related by

$$H = \sqrt{\frac{8\pi G\rho}{3c^2}} \quad .$$

Constraints can be placed on H and ρ via observations of the cosmic background radiation (CBR). The gravity waves from inflation will produce anisotropies in the CBR via the Sachs-Wolfe effect (Sachs and Wolfe, 1967). Rubakov, Sazhin, and Veryaskin (1982) have estimated the quadrupole component of the CBR anisotropy due to low frequency gravitational waves. They place a limit on the Hubble constant during inflation of $H < 8 \times 10^{39}/s$ from the observed upper limit of the quadrupole component

$$\left(\frac{\Delta T}{T}\right)^2_{quad} < 7 \times 10^{-8}$$

from Boughn, Cheng, and Wilkinson (1981). The limit has been improved in a recent measurement by Cottingham (1990) to

$$\left(\frac{\Delta T}{T}\right)^2_{quad} < 4 \times 10^{-10} \quad ,$$

at a 95% confidence level. With this new limit, the analysis of Rubakov, et al. (1982) gives $H < 6 \times 10^{38}/s$ for the Hubble constant during inflation.

Abbott and Wise (1984) also limited H by calculating the multipole moments of the CBR temperature produced by the energy density fluctuations from inflation.

From the observed dipole anisotropy of Fixen, Cheng, and Wilkenson (1983) they set $H < 3 \times 10^{37}/s$ during inflation.

The line in Figure 2.1 labeled "Inflation" shows the spectra predicted by Allen for a value of $H = 8 \times 10^{34}/s$, which corresponds to a mass scale of $M_x \sim 10^{15} GeV$ for the Coleman-Weinberg type of SU(5) GUT that may drive inflation. The spectra has the value of $\Omega_{gw}(f) \sim 10^{-22}$ over its higher frequency flat section. The limit imposed by Abbott and Wise (1984) is $\Omega_{gw}(f) \sim 2 \times 10^{-17}$. This is labeled "Inflation II" in Figure 2.1. This value is still out of range for all direct gravity wave detection methods. However, a CBR anisotropy produced by gravity waves with wavelengths around the horizon size may ultimately by observed.

Also given in Figure 2.1 is the thermal spectrum today for waves produced at the Gibbons-Hawking (Gibbons and Hawking, 1977) temperature $T_{GH} = \hbar H/(2\pi k_B)$. The value, H, is the Hubble constant during inflation. A freely falling detector in de Sitter space would see a thermal spectrum of gravity waves with temperature T_{GH} (Sciama, Candelas, and Deutch, 1981). Allen (1988) has pointed out that his spectrum, produced by the quantum fluctuations in de Sitter space, is different from the Gibbons-Hawking spectra because the de Sitter space is not globally stable to gravitational perturbations.

Section 5 Thermal Spectra

If the universe begins as a standard big bang, without inflation, then there will likely be a thermal spectrum of gravity waves, similar to the cosmic background radiation spectra. When one assumes that the expansion of the universe conserves entropy density, then the temperature of the gravity wave background today would be

$$T_{g0} = \left(\frac{2}{N}\right)^{1/3} T_{\gamma 0} \quad ,$$

where $T_{\gamma 0}$ is the CBR temperature today of 2.7°K, and N is the number of degrees of freedom at the Planck time (Weinberg, 1972). The temperature today would be $T_{g0} \sim 1°K$. This is displayed in Figure 2.1.

Another thermal spectrum shown in Figure 2.1 is the line labeled "3mK Thermal" which refers to a thermal spectra of 3×10^{-3}°K today that would result with an initially cold universe reheated by the decay of acoustic waves at about $10^{-28}s$ (Zel'dovich and Novikov, 1983).

There are a whole range of other near thermal spectra that would be produced in various cosmologies. For example, when the equation of state for the universe is allowed to change from the inflation era value of $p = -\rho$ to the radiation domination era value of $p = \rho/3$ various spectra are produced. For example, if the universe had the equation of state $p = -\rho/3$ from the Planck time until $10^{-27}s$, then a spectrum with a peak value of $\Omega_{gw}(f) \sim 10^{-4}$ at $10^{4}Hz$ would exist today (Grishchuk and Polnarev, 1980). See Zel'dovich and Novikov (1983) and Grishchuk (1988) for other examples.

Section 6 Binary Systems

An interesting astrophysical source of background gravitational radiation is produced by various binary star systems composed of main sequence stars, white dwarfs, neutron stars, or black holes. The emission of gravity waves from a binary system was calculated at least as early as 1938, by Robertson (1938). The observation of the binary pulsar PSR 1913+16 since 1974 has given evidence that the binary system's orbit is decaying exactly as one would predict through the loss of energy to gravitational radiation (Weisberg and Taylor, 1984). This is yet another piece of evidence in support of the general theory of relativity. It is through the coalescence of binary systems, in our galaxy and outside of it, that one expects a gravity wave background. The extragalactic component of this binary star radiation becomes significant because the amount of radiation produced in the final coalescence of two neutron stars is huge, about $10^{54} ergs/s$ when they finally collide into each other. The background radiation from main sequence stars in our galaxy alone will be large enough to partially obscure the sensitivity of an interferometer in space (Faller, Bender, Hall, Hils, and Vincent, 1984).

Many researchers have investigated the production of gravity waves by binaries. Rosi and Zimmerman (1976) made a comprehensive investigation. Their results predict an abundance of gravity wave energy density. They claim that at a minimum, galactic and extragalactic binary systems would produce a background of $\Omega_{gw}(f) > 5 \times 10^{-11}$ from $10^{-8}Hz$ to $10^{4}Hz$. Their more detailed calculation for the spectrum is quite optimistic. Dying binary systems of main sequence stars, white dwarfs, neutron stars, and black holes could produce a background of $\Omega_{gw}(f) \sim 2 \times 10^{-9}$ at $10^{-6}Hz$ to a value of $\Omega_{gw}(f) \sim 5 \times 10^{-3}$ at $10^{3}Hz$. The lack of knowledge of the precise number density of collapsed objects contributes to these large numbers, especially at high frequencies.

Hils, Bender, and Webbink (1990) have recently completed a comprehensive study of the background radiation from binary sources in the $10^{-6}Hz$ to $10^{-2}Hz$ frequency band. Because the planned interferometric gravity wave antenna in space (Falier, Bender, Hall, Hils, and Vincent, 1984) will operate in this frequency range, it is important to know whether individual sources will be able to be seen, or if they will be below the confusion limit of the binary background. The background they considered was made up of WUMa binaries (the system W Ursae Majoris consists of two stars of mass $.76M_{\odot}$ and $.57M_{\odot}$, with an orbital period of 8 hours; Ohanian, 1976), unevolved star binaries, cataclysmic binaries, neutron star binaries, and close white dwarf binaries. They found that the predictions by Rosi and Zimmerman (1976) were too optimistic. The rms gravity wave strain increased from $h \sim 3 \times 10^{-20}$ at $10^{-6}Hz$ to $h \sim 3 \times 10^{-19}$ at $10^{-4}Hz$, due to the unevolved binaries. The rms strain dropped roughly as $1/f$ after $10^{-2}Hz$ to $h \sim 3 \times 10^{-21}$, with the white dwarf binaries dominating in this frequency regime. The energy density is roughly $\Omega_{gw}(f) \sim 10^{-11}\ to\ 10^{-12}$ for $10^{-4}Hz < f < 10^{-2}$. Their composite spectrum stops at the frequency at which the number density of white dwarf binaries in our galaxy drops below one. They also found that 70% of the energy of the spectrum from these binaries came from sources in the galaxy, with the rest being extragalactic.

This problem has also been investigated by Lipunov, Postnov, and Prokhorov (1987, and, Lipunov and Postnov, 1987). Their results are much the same as those of Hils, Bender, and Webbink (1990), except they have extended the spectrum to higher frequencies. At frequencies higher than $10^{-2}Hz$, the binary gravity wave system is dominated by white dwarf systems in other galaxies. The predicted strain for the background radiation continues to decrease with frequency, but at a rate smaller than $1/f$, so the energy density increases. From the extragalactic white dwarf binaries they predict a value today of $h \sim 4 \times 10^{-22}$ or $\Omega_{gw}(f) \sim 5 \times 10^{-11}$ at $3 \times 10^{-2}Hz$, ending at about $1Hz$, with $h \sim 5 \times 10^{-23}$, or $\Omega_{gw}(f) \sim 8 \times 10^{-10}$. The extragalactic neutron star binaries pick up with, $h \sim 9 \times 10^{-24}$, or $\Omega_{gw}(f) \sim 2.5 \times 10^{-11}$. At $100Hz$ the background radiation is $h \sim 3 \times 10^{-25}$, or $\Omega_{gw}(f) \sim 3 \times 10^{-10}$. Lipunov, et el. (1987) considered the contribution of galaxies out to $z = 5$. The level of this spectrum at 100 Hz will be within the capabilities of the advanced LIGO system, and may potentially be an interesting astrophysical source to be observed. Figure 2.1 shows the upper limit for the predicted spectrum of the binaries.

Another species in the astrophysical zoo, should they exist, are binary black holes systems. Bond and Carr have studied the scenario where population III stars make up the missing matter in the galaxy. The stars with masses greater than 10^2 solar masses would collapse into black holes. They assume that a large percentage of these black holes will be in binaries. This assumption is based on observations of O stars, which have masses of about 25 to 65 solar masses. 53% of the observed O stars observed are in binary systems. The collapse of the objects from stars to black holes will also generate gravity waves. The range of possible values for the gravity wave background is extensive, as it is dependent on the mass spectrum for the holes, and their actual number density. It may be as large as $\Omega_{gw}(f) \sim 10^{-2}$ at 100 Hz if the universe is closed by 10^2 solar mass black holes. Carr (1980) has also investigated the production of gravity waves by the generation of primordial black holes. Again, there are a number of scenarios for the production of primordial holes, and a vast range for the possible spectra. Some scenarios will produce a background detectable by a LIGO system. Figure 2.1 shows the most optimistic spectrum from black hole binaries.

Section 7 Pulsar Timing Limits

In the sections above I have discussed some of the sources for a stochastic gravity wave background. In the following sections below I review the techniques (besides ground based laser interferometry) for measuring it, or at least constraining its amplitude. As of this time, no detection of the background has been made. However, limits have been placed, with serious cosmological implications.

The prospect for measuring a stochastic gravitational wave background by using the timing data from a millisecond pulsar is quite good. Cosmological theories are already being constrained via the application of this technique (Stinebring, Ryba, Taylor, and Romani, 1990). Sazhin (1978) and Detweiler (1979) were the first to propose the idea of using the highly stable pulse arrivals from a pulsar as a means of detecting gravity waves. The pulses are emitted in a very regular manner from the pulsar, and the uncertainty in the phase of the signals measured on the earth can be attributed to gravity waves traversing the signal's path. The signal from the pulsar PSR 1937+21 is so stable that it is rivaling man-made clocks (Rawley, Taylor, Davis, and Allan (1987).

The analysis for relating the gravity wave spectrum to the pulsar's phase residual is very similar to the analysis of relating the spectrum to a laser interferometer's signal. In fact, one can think of the pulsar and the earth as forming the two ends of a single arm interferometer. For a complete analysis of this problem see Detweiler (1979), Mashhoon (1982), Bertotti, Carr, and Rees (1983), and Blandford, Narayan, and Romani (1984). There are a number of ways to derive the result. One way is to apply the geodesic equation to the photon. If the photon is defined by its wave vector, k^μ, and the earth (at z_2) and the pulsar (at z_1) define the $\hat{z}$ direction, then

$$k^0(z_2) - k^0(z_1) \approx \frac{1}{2}k^3 \int_{z_1}^{z_2} \frac{dh_{33}}{dt} dz \quad ,$$

or in terms of the photon's redshift,

$$z = \frac{1}{2} \int_{z_1}^{z_2} \frac{dh_{33}}{dt} dz \quad .$$

The correlation of the redshift can be related to the gravity wave spectrum, $\Omega_{gw}(f) = \frac{f}{\rho_c}\frac{d\rho_{gw}}{df}$, by

$$\langle z(t) z(t+\tau) \rangle_{av} = 2 \int_0^\infty df \cos(2\pi f \tau) \frac{2\rho_c \Omega_{gw}(f) G}{3\pi c^2 f^3} B(2\pi f L/c) \quad ,$$

where

$$B(x) = 1 - \frac{3}{4}\left(\frac{2x - \sin 2x}{x^3}\right) \quad ,$$

and L is the earth-pulsar distance (Bertotti, Carr, Rees, 1983). The change in the wavelength of an electromagnetic signal will change the phase of the signal as it is measured on the earth.

Needless to say, the actual process for measuring the phase residual of a pulsar, such as pulsar PSR 1937+21, is complicated. Numerous effects other than gravitational radiation influence the phase of the signal. One must properly relate the pulsar's reference frame to that of the earth. The man-made atomic clocks must be stable enough so that they do not influence the phase uncertainty. One must account for dispersion of the signal by the interstellar medium, and also account for fluctuations in the dispersion. The period derivative of the pulsar, caused by its loss of rotational energy via the emission of radiation, must be included. Also, the exact location of the pulsar in the sky, along with its proper motion, must be known to a high degree of certainty (Rawley, et al. 1987). All of these effects have a different color in the spectral estimation. The frequencies of the gravity wave spectra that can be investigated are those above $1/T$, where T is the total period in which the pulsar and its signal have been observed.

The limits that have been achieved by the observations of PSR 1937+21 and PSR 1855+09 are beginning to have astrophysical consequences (Stinebring, et al. 1990). Observations were made at 1408 MHz and 2380 MHz at the Arecibo observatory. PSR 1937+21 has been observed over 7.1 years, and PSR 1855+09 has been observed over 3.9 years. The limit that has been placed on the gravity wave energy density around $4.5 \times 10^{-9} Hz$ is $\Omega_{gw}(f) < 9 \times 10^{-8}$ with a 68% confidence level, and $\Omega_{gw}(f) < 4 \times 10^{-7}$ with a 95% confidence level. This observation is beginning to place very serious constraints on the existence of cosmic strings. A residual was detected from PSR 1937+21. The measurement may be limited by the long term stability of the atomic clocks, uncorrected dispersion fluctuations, a slight error in the solar system model, or rotational instabilities in the pulsar. Further measurements of the system will improve the situation, as will observations of other pulsars. The correlation of signals from multiple pulsars will also help in beating the intrinsic noise of each individual pulsar measurement. Hellings and Downs (1983) cross-correlated the residuals of four pulsars, and made the limit of $\Omega_{gw}(f) < 1.4 \times 10^{-4}$ for $10^{-8} Hz < f < 10^{-7} Hz$. Figure 2.1 shows the pulsar timing limits as of 1990, and also the limits that were made in 1984. Note the significant improvement in sensitivity.

There is another way that pulsars can be used to help limit the gravity wave energy density. The binary pulsar (PSR 1913+16) system's orbit is so well understood that one can use it as a frequency reference (Mashhoon, Carr, and Hu, 1981, Taylor and Weisberg, 1982, Taylor, 1987). When one compares the signals from this system with atomic clocks on the earth, a limit can be placed for the energy density of gravity waves between there and the earth. At present the limit is $\Omega_{gw}(f) < .5$ for $10^{-13} Hz < f < 10^{-8} Hz$ (Thorne, 1987, Weisberg and Taylor, 1984).

Section 8 Doppler Tracking Limits

The same techniques that are applied to signals from pulsars can be applied to signals transmitted from spacecraft traveling through our solar system. In fact, the Doppler tracking of spacecraft was considered and analyzed (Estabrook and Wahlquist, 1975) before pulsar timing. Originally intended to look for pulses, the Doppler tracking technique is also applicable to a search for the SGWB. The earth and the spacecraft are considered free masses. A limit can be placed on their energy density in the frequency range $10^{-5}Hz < f < 10^{-2}Hz$ (Thorne, 1987). The space craft signals analyzed so far have been the Viking (Armstrong, Woo, Estabrook, 1979), Voyager (Hellings, Callahan, Anderson, and Moffet, 1981), Pioneer 10 (Anderson, Armstrong, Estabrook, Hellings, Law, Wahlquist, 1984), and Pioneer 11 (Armstrong, Estabrook, and Wahlquist 1987). The best limit so far is $\Omega_{gw}(f) < 10$. The sensitivity of future spaceship tracking experiments is expected to improve by a few orders of magnitude. This will be accomplished as new techniques are used to account for the noise due to index fluctuations in the solar plasma. Figure 2.1 shows the limits that have been achieved to date.

Section 9 Cosmic Background Radiation Anisotropy Limits

The isotropy of the cosmic microwave background radiation (CBR) can be used to constrain the energy density of a stochastic gravity wave background at very low frequencies. There are two ways in which gravity waves will disturb the CBR. Gravity waves today with wavelengths on the order of the horizon size will produce a quadrupole anisotropy, while waves at the time of recombination will cause fluctuations on smaller angular scales that can be observed today (Sachs and Wolfe, 1967). An order of magnitude analysis gives $h_{rms} \sim \Delta T/T$ for waves at around $f \sim 10^{-18}Hz$, which corresponds to the present Hubble radius. For waves around $f \sim 10^{-15}Hz\ to\ 10^{-16}Hz$, corresponding to horizon size wavelengths at recombination, the rms gravity wave strain today would be $h_{rms} \sim (\Delta T/T)/z_{rec}$ (Grishchuk, 1988). This would correspond to an anisotropy on an angular scale of around 4° today. Using a value of $\Delta T/T < 3 \times 10^{-5}$ yields $\Omega_{gw}(f) < 3 \times 10^{-9}$ at $f = 3 \times 10^{-18}Hz$, and $\Omega_{gw}(f) < 7 \times 10^{-11}$ at $f = 5 \times 10^{-16}Hz$. Other CBR limits of $h_{rms} < 10^{-6}$ for $10^{-16}Hz < f < 10^{-14}Hz$, and $h_{rms} < 3 \times 10^{-4}$ for $10^{-18}Hz < f < 10^{-16}Hz$ are given by Allen (1989) and Wilkinson (1987).

Linder (1988 a, 1988 b) has made an analysis of the CBR anisotropy as a function of gravity wave energy density for the fluctuations created at recombination. This analysis takes into account the dilution of the anisotropies due to the finite length of time over which recombination transpired. Using a value of

$\Delta T/T \sim 10^{-5}$ he limits the gravity wave energy density to $\Omega_{gw}(f) < 10^{-8}$ at $f = 10^{-14} Hz$ and $\Omega_{gw}(f) < 10^{-10}$ at $f = 10^{-16} Hz$.

Figure 2.1 shows the limits that have been placed on the stochastic gravity wave background energy density by the isotropy of the CBR.

Section 10 Nucleosynthesis Limit

The production of deuterium, helium, and lithium in the early universe can be used to constrain the energy density of the stochastic gravity wave background. If the energy density of the gravity waves is too large when these light nuclei are produced, the abundances today will be different from what is actually observed (Carr, 1980). Too much gravity wave energy will speed up the universe's expansion rate, and thereby reduce the amount of helium formed from deuterium, altering the observed ratios. The observed abundance is 29% helium, .001% deuterium. The observations of the mass ratio in primordial nucleosynthesis limits the energy density of gravity waves to $\Omega_{gw}(f) < 10^{-4}$ for $10^{-10} Hz < f < 10^{10} Hz$ (Carr, 1980, Thorne, 1987).

Bennett (1986a, 1986b) has extended this analysis in order to place constraints on cosmic strings. The result of the analysis is that $\Omega_{gw}(f) < .17$ at the time of nucleosynthesis, $T_{nuc} \sim 10^{9}$°K. The total energy density at this time ($t \sim 100s$ would be $\rho = 3c^2/(32\pi G t^2)$, giving an energy density of gravity waves today of

$$\Omega_{gw} = (.17)\frac{3c^2}{32\pi G t^2}\left(\frac{N_0}{N_{nuc}}\right)^{4/3}\left(\frac{T_0}{T_{nuc}}\right)^4 \quad ,$$

where N_0 and N_{nuc} are the number of degrees of freedom now and at nucleosynthesis, and T_0 and T_{nuc} are the temperatures now and then. This yields a limit of $\Omega_{gw} < 2.5 \times 10^{-6}$. Bennett's analysis also constrains the cosmic string linear mass density to $G\mu < 4 \times 10^{-6}$.

Figure 2.1 displays the limit of $\Omega_{gw} < 2.5 \times 10^{-6}$ (labeled "Nucleosynthesis") from this method.

Section 11 Limits from the Earth's and Sun's Normal Modes

The measurement of the excitations of the normal modes of the earth and the sun have been used to limit the energy density of the stochastic gravitational wave background. Boughn and Kuhn (1984) have analyzed the process by which a gravity wave background drives the normal modes of a spherical body. Using data of the observed line of sight velocity of the surface of the sun they are able to constrain $\Omega_{gw}(f)$ to be less than 100 at a frequency of $4 \times 10^{-4} Hz$. The earth's cross section to the background gravity waves is smaller than the sun's because the earth is much smaller. However the data on the seismic activity is much better for the earth. The limit achieved from the earth data was also $\Omega_{gw}(f) < 100$, at frequencies of $2 \times 10^{-3} Hz$ and $2 \times 10^{-2} Hz$. It is expected that improved seismic data will push the earth limit down to $\Omega_{gw}(f) < 1$. Figure 2.1 shows the limit from the sun, and the limit that scientists expect to achieve in the near future for the earth.

Section 12 Limit from a Gravitational Lens

A novel way to put a limit on the gravity wave energy density at very low frequencies is through the use of observed time delays in the images of a gravitational lens (Allen, 1989). The two images from a lens can be thought of as two extremely long interferometer arms. For wavelengths of gravity waves of order the horizon size, the limit on the rms size of the gravity wave strain, h_{rms}, in a bandwidth $\delta f = f$, is

$$h_{rms} \approx \left(\frac{\Delta T}{T}\right)_{rms} \frac{\pi f T}{\eta} \quad ,$$

where $T = L/c$ is the transit time for the light to travel from the source to earth, ΔT is the observed time delay for the two lensed images, and 2η is the observed angular separation between the two images.

There is a potential observation of a delay for the gravitational lens 0957+561 (Vanderriest, Schneider, Herpe, Chevreton, Moles, and Wlerick, 1989). They claim $\Delta T = 415 \pm 20\ days$, $T = 10^{10}\ years$, and $2\eta = 6.1\ arcsec$. Allen's analysis yields $h_{rms} < 2 \times 10^{-5}(f/3 \times 10^{-18} Hz)$. This constrains the energy density of gravity waves at $f = 3 \times 10^{-18} Hz$ to $\Omega_{gw} < 10^{-9}$. This also further constrains the inflationary universe model, requiring $M_x < 5 \times 10^{16} GeV$.

Section 13 Limits from Bar Antennas

Resonant bar detectors operate in the same frequency regime as laser interferometers, although interferometers will go to lower frequencies in the future. Bar antennas have been used to try and detect a stochastic gravity wave background. Hough, Pugh, Bland, and Drever (1975) correlated the output of two room temperature bars and limited the gravity wave energy density to $\Omega_{gw}(f) < 10^7$ at 985 Hz. Thorne (1987) and Michelson (1987) have discussed the application of the current bar antennas for detecting the gravity wave background. Good limits will be dependent on increasing the bandwidth of the bars, which is thought to be possible, so that frequencies as low as 200 Hz can be detected (Michelson, 1986, Michelson and Taber, 1984). Therefore, more improvements in the bar's isolation system must be made, along with improvements in the transducer and amplifier. Michelson (1987) has analyzed the situation for using bars (he has also looked at the laser interferometer situation) to detect the background, and predicts that two co-located bars with a length of 5 m, mass of $10^4 kg$, temperature of .1°K, mass Q of 5×10^7, suspension Q of 5×10^7, bar mode frequency of 800 Hz, suspension frequency .1 Hz, and total integration time of $10^6 s$, will be able to limit the energy density to $\Omega_{gw}(f) < 10^{-7}$ at 200 Hz.

Section 14 Laser Interferometer in Space

Laser interferometers can be used to detect a stochastic gravitational radiation background. The subject of this thesis is the use of a system of interferometers on the earth to achieve this goal. However, there are plans for creating an interferometer in space (Faller, Bender, Hall, Hils, and Vincent, 1985). The arm length for such a system would be about $10^{11} cm$. The system would operate in the $10^{-4} Hz$ to $10^{-1} Hz$ band. If built, this interferometer will likely observe numerous binary systems in, and outside of, our galaxy. It will also be sensitive to a stochastic gravity wave background. It's peak sensitivity, with $10^7 s$ of integration time, will be about $\Omega_{gw}(f) \sim 10^{-16}$ at $10^{-4} Hz$ (Thorne, 1987). It will be able to see the stochastic background produced by all the binary systems, the background from cosmic stings, and a background produced by an electroweak phase transition. There is an active research program for this project, but this interferometer will not be implemented for a number of years.

Chapter 3 Interferometer Transfer Functions

Section 1 Introduction

In this section the response of a real laser interferometer system to a gravitational wave is discussed. Several interferometer types are investigated. The transfer functions for all the systems are general solutions, taking into account the direction from which the wave came, as well as its polarization. The general transfer functions for a standard Fabry-Perot or a Michelson delay line have been given before (Weiss, Linsay, Saulson and Whitcomb, 1983, or Whitcomb, et al. 1983). The transfer function for more advanced systems, like recycling, dual recycling, or resonant recycling, have been given for gravity waves of normal incidence and optimum polarization (Meers, 1988, Vinet, 1986, Vinet, Meers, Man and Brillet, 1988). This chapter will present the extension of this work to the arbitrary gravity wave. This is necessary to estimate the detection of a stochastic background of gravity radiation because the interferometer will be responding to waves from all directions and polarizations.

One can express a gravitational wave as a Fourier series. If one demands that the perturbation to the background metric be real, then the gravity wave can be written as

$$h_{ij}(\vec{\mathbf{x}},t) = \int \frac{d^3\vec{\mathbf{k}}}{2\Omega}[e^{i(\vec{\mathbf{k}}\cdot\vec{x}-\Omega t)}(\widetilde{h_+}\left(\hat{\mathbf{k}}\right)\mathbf{e}^{+}_{\mathbf{ij}}\left(\hat{\mathbf{k}}\right)+$$

$$\widetilde{h_\times}\left(\hat{\mathbf{k}}\right)\mathbf{e}^{\times}_{\mathbf{ij}}\left(\hat{\mathbf{k}}\right)) \quad + \quad \mathrm{C.C.}] \quad .$$

The plus and the cross refer to the two polarizations of the gravity wave. The polarization tensors are given as

$$e^{+}_{ij}\left(\hat{\mathbf{k}}\right) \qquad , \; and, \qquad e^{\times}_{ij}\left(\hat{\mathbf{k}}\right) \quad .$$

They depend on the propagation direction, and the polarization angle of the wave.

The gravity wave is measured by a laser interferometer. What is detected is a change in the intensity of the light coming out the exit port of the interferometer. The signal is proportional to the difference in the phase of the two light beams that recombine at the beamsplitter. For a gravity wave with an angular frequency of Ω (complex time dependence of $e^{i\Omega t}$), one looks for the output laser light that has had its angular frequency changed from ω (complex time dependence of $e^{i\omega t}$) to ω+Ω (complex time dependence of $e^{i(\omega+\Omega)t}$). The output of the interferometer will be expressed in terms of the electric field of the laser light that has a angular frequency of ω+Ω. Note that the definitions have all been carried out with complex quantities and positive frequencies. In a real situation the gravity wave will have a time dependence of $\cos(\Omega t + \phi)$, and will produce sidebands on the laser light at the frequencies ω+Ω and ω–Ω. This is due to the $e^{i\Omega t}$ and $e^{-i\Omega t}$ components of the wave. The lower sideband transfer function can be found by just replacing Ω with –Ω. The output of the interferometer will be called z.

As an example, consider a traveling gravity wave coming from a particular part of the sky, with a frequency Ω, and a wave vector $\vec{k}$, $k = \Omega/c$. It has a component h_+ of one polarization, and $h_\times$ of the other. The gravity wave is given by

$$h_{ij} = \left(h_+ e^{+}_{ij}\left(\widehat{k}\right) + h_\times e^{\times}_{ij}\left(\widehat{k}\right)\right) e^{i\left(\vec{k}\cdot\vec{x} - \Omega t\right)} \quad .$$

The light from the laser that enters the interferometer can be expressed in terms of its electric field, $E_0 e^{-i\omega t}$. The output electric field is

$$\begin{aligned} E_{out} &= \left(h_+ S_+\left(\vec{k}, \Omega\right) + h_\times S_\times\left(\vec{k}, \Omega\right)\right) E_0 e^{-i(\omega+\Omega)t} \\ &\cong z E_0 e^{-i(\omega+\Omega)t} \quad . \end{aligned}$$

S_+ and S_x are the transfer functions for the plus and cross polarizations of the gravity wave with the interferometer. These transfer functions will be derived in this chapter. Different optical schemes will give different transfer functions. Some configurations will be better suited for a measurement of a stochastic background of gravitational radiation than others. The schemes range from broadband detectors, with a frequency range of kilohertz, to highly sensitive ones with an effective bandwidth of only tens of hertz. The transfer functions are general expressions that take into consideration the direction from which the wave is coming, and the polarization. These general expressions are needed because for a stochastic background one hopes to detect waves from all directions, with all polarizations. When an interferometer is responding to gravity waves from all directions, and of all frequencies, z can be expressed in terms of the waves' Fourier components, namely,

$$z(t) = \int \frac{d^3\vec{k}}{2\Omega}\Big\{ e^{i(\vec{k}\cdot\vec{x}-\Omega t)} \Big(\widetilde{h_+}\big(\hat{k},\Omega\big) S_+\big(\hat{k},\Omega\big) + \widetilde{h_\times}\big(\hat{k},\Omega\big) S_\times\big(\hat{k},\Omega\big) \Big) + C.C. \Big\} \quad .$$

Before starting, a remark should be made about notation. For a given mirror, or other optical device such as a beamsplitter, the reflection coefficient for the electric field is given by a lower case r, while the upper case R designates the reflection coefficient for power. Similarly, a lower case t is the electric field transmission coefficient, while the upper case T designates the power transmission coefficient. The electric field terms r and t are complex quantities, and their phase differs by $\pi/2$. One can relate the field and power coefficients, namely:

$$r = i\sqrt{R} \qquad , and, \qquad t = \sqrt{T} \quad .$$

The loss coefficient for the power is designated by the upper case P. Because of energy conservation, R + T + P = 1.

Section 2 Michelson Delay Line Interferometer

The first interferometer considered is the delay line Michelson interferometer. Figure 3.1 shows an example. The incoming light is split by the beamsplitter. The resulting two beams enter the two cavities of length l through holes in the end mirrors. The beams then bounce back and forth between the mirrors of their cavity a total of b times. Each beam travels a total distance of b*l, then exits through the same hole by which it entered. The beams then recombine at the beamsplitter. Some of the light, its intensity determined by the phase difference of the two interferometer beams, heads back in the direction of the laser. The light heading back towards the laser is said to come from the symmetric port of the beamsplitter, while the beam traveling toward the output photodetector is said to come from the antisymmetric port. The phase difference between the two light beams is measured at the photodetector. In Figure 3.1 the B.S. labels the beamsplitter, M1 identifies the front mirror of the cavity, and M2 refers to the rear mirror.

Described next is how a gravity wave will affect the phase of the light. Suppose that one arm of the interferometer defines the $\hat{x}$ axis of its coordinate

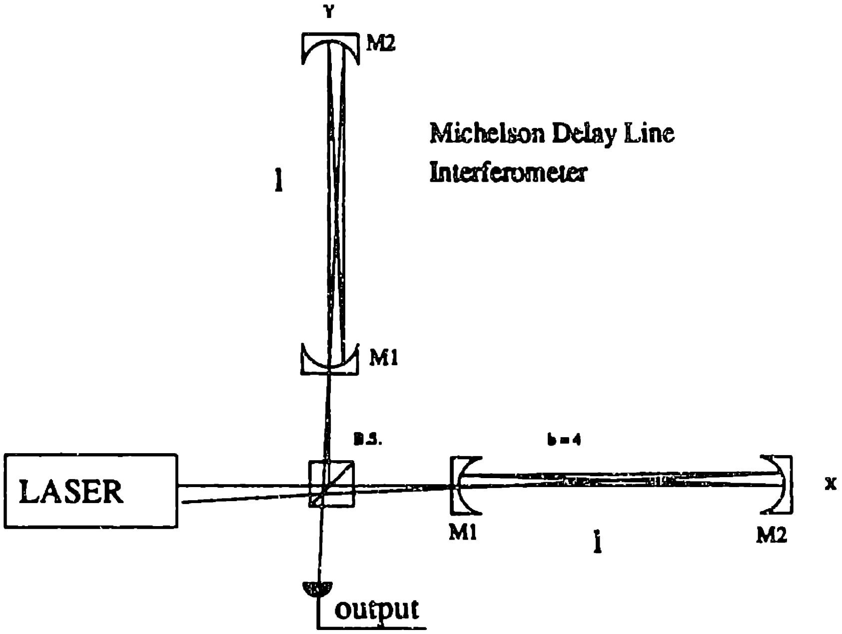

Figure 3.1 Example of a delay line system. Light enters a cavity through a hole in M1, traverses the cavity, of length l, a total of b times, and exits through the same hole. The beams from the two cavities recombine at the beamsplitter.

system, while the other arm defines the $\hat{y}$ axis. Consider the light traveling in the $\hat{x}$ arm. Light travels along a null geodesic, so in the linear approximation

$$ds^2 = 0 = -c^2dt^2 + (1+h_{11})dx^2$$
$$\Rightarrow (\pm)dx \;=\; (1+h_{11})^{-1/2}c\,dt \;\simeq\; \left(1-\frac{1}{2}h_{11}\right)c\,dt \quad ,since\ h_{11} \ll 1\ .$$

Now consider the incoming gravity wave that produces the metric perturbation h_{11}. In the gravity waves frame of reference one has

$$\begin{aligned} g_{\mu\nu} &= \eta_{\mu\nu} + h_{\mu\nu} \\ &= \eta_{\mu\nu} + h^{(+)}_{\mu\nu} + h^{(\times)}_{\mu\nu} \end{aligned}$$

where,

$$h^{(+)}_{\mu\nu} = h^{(+)}_0 e^{i(\vec{k}\cdot\vec{X}-\Omega t)} \begin{pmatrix} 0 & 0 & 0 & 0 \\ 0 & 1 & 0 & 0 \\ 0 & 0 & -1 & 0 \\ 0 & 0 & 0 & 0 \end{pmatrix} \quad ,and,$$

$$h_{\mu\nu}^{(\times)} = h_0^{(\times)} e^{i(\vec{k}\cdot\vec{X} - \Omega t)} \begin{pmatrix} 0 & 0 & 0 & 0 \\ 0 & 0 & 1 & 0 \\ 0 & 1 & 0 & 0 \\ 0 & 0 & 0 & 0 \end{pmatrix} \quad ,$$

and,

$$\vec{k} = \frac{\Omega}{c}(0,0,1) \quad .$$

If the gravity wave's coordinate system is represented as (X,Y,Z), and the detector's coordinate system is (x,y,z), then the metric in the detector's frame can be found via

$$g_{\mu\nu}^{(det)} = \frac{\partial X^\alpha}{\partial x^\mu} \frac{\partial X^\beta}{\partial x^\nu} g_{\alpha\beta}^{(g.w.)} \quad .$$

If the relationship between the two coordinate systems is defined in terms of Euler angle rotations, such as

$$\vec{X} = \widetilde{R_z}(-\psi)\widetilde{R_x}(\theta)\widetilde{R_z}(-\phi)\vec{x} \quad ,$$

where an example of one of these rotations is

$$\widetilde{R_x}(\theta) = \begin{pmatrix} 1 & 0 & 0 \\ 0 & \cos\theta & \sin\theta \\ 0 & -\sin\theta & \cos\theta \end{pmatrix} \quad ,$$

then the relevant components of the metric in the detector's frame are

$$\begin{aligned} h_{11} = {} & h_0^{(+)} e^{i(\vec{k}\cdot\vec{x} - \Omega t)} \left(\cos 2\psi\left(\cos^2\phi - \cos^2\theta \sin^2\phi\right) - \sin 2\psi \sin 2\phi \cos\theta\right) + \\ & h_0^{(\times)} e^{i(\vec{k}\cdot\vec{x} - \Omega t)} \left(\sin 2\psi\left(\cos^2\phi - \cos^2\theta \sin^2\phi\right) + \cos 2\psi \sin 2\phi \cos\theta\right) \\ & \equiv A(\theta,\phi,\psi) h_0^{(+)} + B(\theta,\phi,\psi) h_0^{(\times)} \quad . \end{aligned}$$

In terms of the interferometers coordinate system the angles θ, and ϕ describe the direction from which the wave came, while ψ defines the polarization. In terms of the Euler angles defined here, the wave vector in the detector's frame is

$$k_{det}^\mu = \frac{\partial x^\mu}{\partial X^\nu} k_{gw}^\nu = \frac{\Omega}{c}\{1, \sin\phi\sin\theta, -\cos\phi\sin\theta, \cos\theta\}$$

One can now integrate the null geodesic equation. First, integrate along the path from the front of mirror one to mirror two.

$$(\pm)\int_{x_0}^{x_0+l} dx = c\int_{t_0}^{t_1} dt\left[1-\frac{1}{2}\left(Ah_0^{(+)}+Bh_0^{(\times)}\right)e^{i(k_x x+k_y y+k_z z-\Omega t)}\right]$$

Two observations need to be made here, namely that one can make the substitution $x = x_0 + c(t - t_0)$, $y = y_0$, $z = z_0$, and also that the plus solution corresponds to having our clocks run forward. With this, the equation becomes

$$l = c(t_1-t_0) - \frac{c}{2}\left(Ah_0^{(+)}+Bh_0^{(\times)}\right)e^{i(\vec{k}\cdot\vec{x}_0-k_x ct_0)}\frac{\left(e^{i(k_x c-\Omega)t_1}-e^{i(k_x c-\Omega)t_0}\right)}{i(ck_x-\Omega)}.$$

The light beam bounces off mirror two, and travels back to mirror one.

$$(\pm)\int_{x_0+l}^{x_0} dx = c\int_{t_1}^{t_2} dt\left[1-\frac{1}{2}\left(Ah_0^{(+)}+Bh_0^{(\times)}\right)e^{i(k_x x+k_y y+k_z z-\Omega t)}\right]$$

One must now take the minus solution to insure that clocks move forward in time. The solution is

$$l = c(t_2-t_1) - \frac{c}{2}\left(Ah_0^{(+)}+Bh_0^{(\times)}\right)e^{i(\vec{k}\cdot\vec{x}_0+k_x ct_1)}\frac{\left(e^{-i(k_x c+\Omega)t_2}-e^{-i(k_x c+\Omega)t_1}\right)}{(-i)(ck_x+\Omega)}.$$

This process is repeated so that the beam traverses the cavity a total of b times. The time it takes the beam to travel the distance b*l in the $\hat{x}$ arm of the interferometer is

$$\Delta t_x = (t_f-t_0)_x = \frac{bl}{c}+\frac{l}{2c}\left(Ah_0^{(+)}+Bh_0^{(\times)}\right)[e^{\frac{il}{2c}(ck_x+\Omega)}sinc\left(\frac{l}{2c}\{ck_x-\Omega\}\right)$$
$$+e^{\frac{il}{2c}(ck_x-\Omega)}sinc\left(\frac{l}{2c}\{ck_x+\Omega\}\right)]e^{i(\vec{k}\cdot\vec{x}_0-\Omega t_0)}\frac{\sin\left(\frac{\Omega lb}{2c}\right)}{\sin\left(\frac{\Omega l}{c}\right)}e^{\frac{-i\Omega lb}{2c}} .$$

Next, one calculates the time for a beam of light to traverse the $\hat{y}$ arm. The metric component that affects this is

$$h_{22} = h_0^{(+)}e^{i(\vec{k}\cdot\vec{x}-\Omega t)}(\cos 2\psi(\sin^2\phi-\cos^2\theta\cos^2\phi)+\sin 2\psi\sin 2\phi\cos\theta)-$$
$$h_0^{(\times)}e^{i(\vec{k}\cdot\vec{x}-\Omega t)}(\sin 2\psi(\cos^2\phi\cos^2\theta-\sin^2\phi)+\cos 2\psi\sin 2\phi\cos\theta)$$
$$\equiv C(\theta,\phi,\psi)h_0^{(+)}+D(\theta,\phi,\psi)h_0^{(\times)} .$$

For the $\widehat{y}$ arm one has

$$\Delta t_y = (t_f - t_0)_y = \frac{bl}{c} + \frac{l}{2c}\left(Ch_0^{(+)} \; + Dh_0^{(\times)}\right)[e^{\frac{il}{2c}(ck_y+\Omega)} sinc\left(\frac{l}{2c}\{ck_y - \Omega\}\right)$$

$$+e^{\frac{il}{2c}(ck_y-\Omega)} sinc\left(\frac{l}{2c}\{ck_y + \Omega\}\right)]e^{i(\vec{k}\cdot\vec{x}_0-\Omega t_0)}\frac{\sin\left(\frac{\Omega l b}{2c}\right)}{\sin\left(\frac{\Omega l}{c}\right)}e^{\frac{-i\Omega l b}{2c}} \qquad .$$

The phase difference for the two beams can now be calculated. It is

$$\Delta\Phi = \frac{2\pi c}{\lambda}(\Delta t_x - \Delta t_y)$$

$$= \frac{\pi l}{\lambda}[\left(Ah_0^{(+)} \; + Bh_0^{(\times)}\right)[e^{\frac{il}{2c}(ck_x+\Omega)} sinc\left(\frac{l}{2c}\{ck_x - \Omega\}\right)$$

$$+e^{\frac{il}{2c}(ck_x-\Omega)} sinc\left(\frac{l}{2c}\{ck_x + \Omega\}\right)]-$$

$$\left(Ch_0^{(+)} \; + Dh_0^{(\times)}\right)[e^{\frac{il}{2c}(ck_y+\Omega)} sinc\left(\frac{l}{2c}\{ck_y - \Omega\}\right)$$

$$+e^{\frac{il}{2c}(ck_y-\Omega)} sinc\left(\frac{l}{2c}\{ck_y + \Omega\}\right)]]e^{i(\vec{k}\cdot\vec{x}_0-\Omega t_0)}\frac{\sin\left(\frac{\Omega l b}{2c}\right)}{\sin\left(\frac{\Omega l}{c}\right)}e^{\frac{-i\Omega l b}{2c}}$$

$$= \frac{\pi l}{\lambda}\sin\left(\frac{\Omega l b}{2c}\right)e^{\frac{-i\Omega l b}{2c}}e^{i(\vec{k}\cdot\vec{x}_0-\Omega t_0)}[h_0^{(+)}(AR_x - CR_y)+$$

$$h_0^{(\times)}(BR_x - DR_y)] \qquad ,$$

where λ is the wavelength of the light in the interferometer, and R_x and R_y are defined as

$$R_x = [e^{\frac{il}{2c}(ck_x+\Omega)} sinc\left(\frac{l}{2c}\{ck_x - \Omega\}\right)+$$

$$e^{\frac{il}{2c}(ck_x-\Omega)} sinc\left(\frac{l}{2c}\{ck_x + \Omega\}\right)]\frac{1}{\sin\left(\frac{\Omega l}{c}\right)}$$

and,

$$R_y = [e^{\frac{il}{2c}(ck_y+\Omega)} sinc\left(\frac{l}{2c}\{ck_y - \Omega\}\right)+$$

$$e^{\frac{il}{2c}(ck_y-\Omega)} sinc\left(\frac{l}{2c}\{ck_y + \Omega\}\right)]\frac{1}{\sin\left(\frac{\Omega l}{c}\right)}.$$

Note that $\Delta\Phi$ is proportional to $e^{-i\Omega t_0}$. The time here is t_0, the time when the light entered the arm of the interferometer. However, one measures the light coming out at a time bl/c later. So, in terms of the final time, $t_f = t_0 + bl/c$ one measures a phase difference of

$$\Delta\Phi = \frac{\pi l}{\lambda} \sin\left(\frac{\Omega l b}{2c}\right) e^{\frac{i\Omega l b}{2c}} e^{i\left(\vec{k}\cdot\vec{x}_0 - \Omega t_f\right)} \times$$
$$\left[h_0^{(+)}(AR_x - CR_y) + h_0^{(\times)}(BR_x - DR_y)\right] \quad .$$

One now has the tools needed to express the transfer function. As stated above, the transfer function relates the output electric field that has been frequency shifted to $\omega+\Omega$ to the incident electric field. Let's call the input beam E_0. The beam exiting from the $\hat{x}$ arm will have an electric field given by

$$E_{xout} = t_s r_m^{b-2} E_0 e^{\frac{i\Omega b l_x}{c}} e^{i\delta\phi_x} \quad ,$$

where the subscript m refers to the four mirrors whose reflectivity coefficient is assumed to be the same, and the subscript s refers to the beamsplitter. The beam exiting the $\hat{y}$ arm is given by

$$E_{yout} = r_s r_m^{b-2} E_0 e^{\frac{i\Omega b l_y}{c}} e^{i\delta\phi_y} \quad .$$

The lengths of the two arms are adjusted such that

$$e^{2ikl_x} = e^{2ikl_y} \quad .$$

In the absence of a gravity wave the intensity of this beam would be zero. This is called the dark fringe condition. The electric field heading towards the photodetector is given by

$$\begin{aligned} E_{out} &= t_s r_s r_m^{b-2} E_0 \left(e^{i\delta\phi_x} - e^{i\delta\phi_y}\right) e^{\frac{i\Omega l b}{c}} \\ &= t_s r_s r_m^{b-2} E_0 e^{i\delta\phi_x} \left(1 - e^{-i(\delta\phi_x - \delta\phi_y)}\right) e^{\frac{i\Omega l b}{c}} \\ &= \frac{i^{b-1}}{2}(1 - P_s) R_m^{\frac{b-2}{2}} E_0 \left(1 - e^{-i\Delta\Phi}\right) e^{\frac{i\Omega l b}{c}} e^{i\delta\phi_x} \\ &\simeq \frac{e^{i\gamma}}{2}(1 - P_s) R_m^{\frac{b-2}{2}} E_0 \, \Delta\Phi \, e^{\frac{i\Omega l b}{c}} \quad , for \;\; \Delta\Phi << 1 \quad . \end{aligned}$$

All the nonessential phases have been lumped into γ.

One can now read off the transfer functions for the two polarizations. Namely,

$$S_{+mc} = \frac{\pi l}{2\lambda}(1 - P_s)R^{\frac{b-2}{2}} \sin\left(\frac{\Omega l b}{2c}\right) e^{\frac{ilb(2\omega+\Omega)}{2c}} (AR_x - CR_y)$$

and,

$$S_{\times mc} = \frac{\pi l}{2\lambda}(1 - P_s)R^{\frac{b-2}{2}} \sin\left(\frac{\Omega l b}{2c}\right) e^{\frac{ilb(2\omega+\Omega)}{2c}} (BR_x - DR_y) \quad .$$

The term in the transfer function that depends on the incoming direction and polarization for the wave is $AR_x - CR_y$ for the plus polarization, and $BR_x - DR_y$ for the cross polarization. These angular and polarization dependent terms appear in the transfer functions for all the interferometer schemes considered in this chapter. Their effect is to diminish the transfer function from the ideal case when $\theta=\phi=\psi=0$. When this is the case, these terms reduce to A=1; C=-1; B=D=0; $R_x = R_y = 2c/\Omega l$. It should be noted that R_x and R_y differ very little from the ideal value of $2c/\Omega l$ over the entire range of the angles θ and ϕ, and over the proposed frequency range of the detectors, from 0 to about 10000 Hz. For instance, at 1000 Hz, the extreme value of R_x occurs at $\theta=\phi=\pi/2$. The difference between the product $R_x * \Omega l/2c$ and one is $3*10^{-4}$ for a four kilometer arm length. Also, the difference between one and $R_x * \Omega l/2c$ at its extreme value at 10KHz. is only .025. To summarize, R_x and R_y differ very little from $2c/\Omega l$ over all angles, and over the intended frequency range of the interferometer. The angular dependent terms only enter the problem to a appreciable degree through the terms A, B, C, and D. These are the angular dependent terms that relate the metric components h_{11} and h_{22} of the detectors frame to the metric in the frame of the gravity wave. They were defined above. However, to keep the transfer functions as general as possible, all these terms have been kept in the expressions.

Section 3 Fabry-Perot Interferometer

The next system considered is the Fabry-Perot interferometer. Here the light beams enter each cavity through the front mirrors, labeled M1. A standing wave develops inside each cavity. The light that exits the cavities is a sum of beams that have traveled a distance of 2l, 4l, 6l, ... Figure 3.2 illustrates such a system.

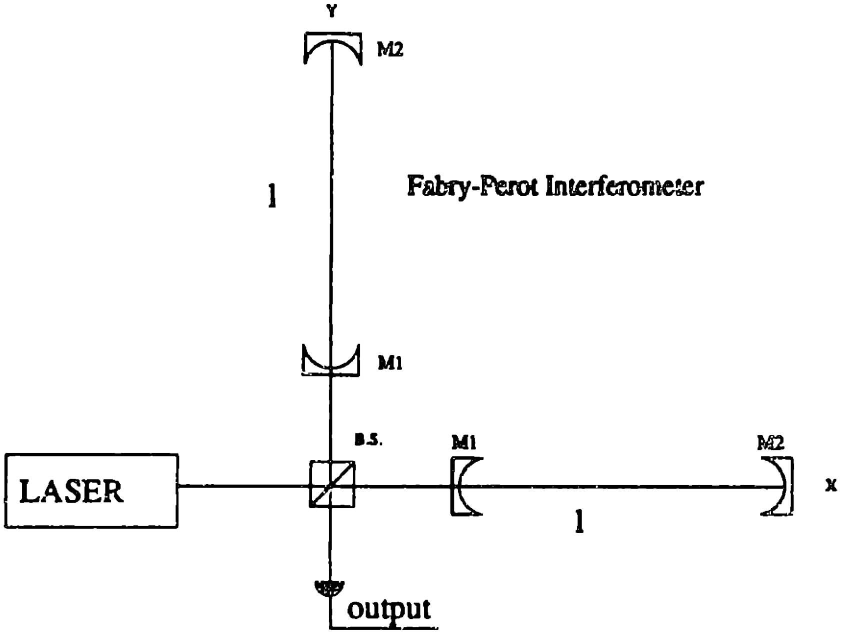

Figure 3.2 Example of a Fabry-Perot Interferometer. The length of the cavity is l.

Consider the $\hat{x}$ arm. The light exiting M1 at time t is

$$E^{(x)}_{exit}(t) = r_1 E^{(x)}_{in} e^{-i\omega t} + \sum_{n=1}^{\infty} \frac{t_1^2}{r_1}(r_1 r_2)^n E^{(x)}_{in} e^{i\left(-\omega t + \frac{2\omega l n}{c} + \delta\phi_x(n)\right)} \quad .$$

The subscript 1 refers to the front mirror M1, while the subscript 2 labels the rear mirror. It is an infinite series of Michelson interferometer type terms. Note that n=1 corresponds with b=2, n=2 corresponds with b=4, n=3 with b=6, and so on. The $\delta\phi_x(n)$ term is the phase shift a beam will accrue from the gravity wave after traversing the cavity a total of b=2n times. This term is $\delta\phi_x(n) = \frac{2\pi c}{\lambda}(\Delta t_x(b = 2n) - \frac{l2n}{c})$ where $\Delta t_x(b)$ is defined above for the Michelson interferometer. Also, one has to express $\Delta t_x(b)$ in terms of the time t, not when the individual beam entered the cavity, namely,

$$t = t_0(b) + \frac{bl}{c} \quad .$$

The calculation can be simplified by noting that since $\Delta t_x(b)$ is proportional to the gravity wave, h_{11}, and one can say

$$e^{i\delta\phi_x(n)} \simeq 1 + i\delta\phi_x(n) \quad ,$$

because $h_{11} << 1$. In this case the electric field can be expanded into the form

$$E^{(x)}_{exit}(t) = r_1 E^{(x)}_{in} e^{-i\omega t} + \sum_{n=1}^{\infty} \frac{t_1^2}{r_1} (r_1 r_2)^n E^{(x)}_{in} e^{i\left(-\omega t + \frac{2\omega l n}{c}\right)}$$
$$\left(1 + \frac{i\omega l}{2c} R_x e^{i(\vec{k}\cdot\vec{x}_0 - \Omega t)} \left(A h_0^{(+)} + B h_0^{(\times)}\right) \sin\left(\frac{\Omega l 2n}{2c}\right) e^{\frac{i\Omega 2nl}{2c}}\right) \quad .$$

This equation can be successfully summed. The result is

$$E^{(x)}_{exit}(t) = E^{(x)}_{in} e^{-i\omega t} \quad \left[\frac{r_1 + r_2\left(t_1^2 - r_1^2\right) e^{\frac{2i\omega l}{c}}}{1 - r_1 r_2 e^{\frac{2i\omega l}{c}}}\right] +$$
$$E^{(x)}_{in} e^{i\left(\vec{k}\cdot\vec{x}_0 - (\omega+\Omega)t\right)} \frac{i t_1^2 r_2 \omega l R_x \left(A h_0^{(+)} + B h_0^{(\times)}\right) \sin\left(\frac{\Omega l}{c}\right) e^{\frac{il(2\omega+\Omega)}{c}}}{2c\left(1 - r_1 r_2 e^{\frac{2il(\omega+\Omega)}{c}}\right)\left(1 - r_1 r_2 e^{\frac{2i\omega l}{c}}\right)}$$
$$= E^{(x)}_{in} e^{-i\omega t} i \left[\frac{\sqrt{R_1} + \sqrt{R_2}(T_1 + R_1) e^{\frac{2i\omega l}{c}}}{1 + \sqrt{R_1 R_2} e^{\frac{2i\omega l}{c}}}\right] -$$
$$E^{(x)}_{in} e^{i\left(\vec{k}\cdot\vec{x}_0 - (\omega+\Omega)t\right)} \frac{T_1 \sqrt{R_2} \omega l R_x \left(A h_0^{(+)} + B h_0^{(\times)}\right) \sin\left(\frac{\Omega l}{c}\right) e^{\frac{il(2\omega+\Omega)}{c}}}{2c\left(1 + \sqrt{R_1 R_2} e^{\frac{2il(\omega+\Omega)}{c}}\right)\left(1 + \sqrt{R_1 R_2} e^{\frac{2i\omega l}{c}}\right)} \quad .$$

This derivation can be found in Whitcomb, et al. , (1983). Similarly, for the $\hat{y}$ cavity one has

$$E^{(y)}_{exit}(t) = E^{(y)}_{in} e^{-i\omega t} i \left[\frac{\sqrt{R_1} + \sqrt{R_2}(T_1 + R_1) e^{\frac{2i\omega l}{c}}}{1 + \sqrt{R_1 R_2} e^{\frac{2i\omega l}{c}}}\right] -$$
$$E^{(y)}_{in} e^{i\left(\vec{k}\cdot\vec{x}_0 - (\omega+\Omega)t\right)} \frac{T_1 \sqrt{R_2} \omega l R_y \left(C h_0^{(+)} + D h_0^{(\times)}\right) \sin\left(\frac{\Omega l}{c}\right) e^{\frac{il(2\omega+\Omega)}{c}}}{2c\left(1 + \sqrt{R_1 R_2} e^{\frac{2il(\omega+\Omega)}{c}}\right)\left(1 + \sqrt{R_1 R_2} e^{\frac{2i\omega l}{c}}\right)} \quad .$$

Call the electric field from the input laser light E_0 . Then,

$$E^{(x)}_{in} = t_s E_0 = \sqrt{T_s} E_0 \quad , \; and, \quad E^{(y)}_{in} = r_s E_0 = i\sqrt{R_s} E_0 \quad .$$

Finally, assuming that the interferometer operates at a dark fringe, the electric field for the light at the photodetector is

$$E_{out}(t) = E_0 e^{i(\vec{k}\cdot\vec{x}_0-(\omega+\Omega)t)} \frac{(-i)(1-P_s)T_1\sqrt{R_2}\omega l \sin\left(\frac{\Omega l}{c}\right) e^{\frac{il(2\omega+\Omega)}{c}}}{4c\left(1+\sqrt{R_1R_2}e^{\frac{2il(\omega+\Omega)}{c}}\right)\left(1+\sqrt{R_1R_2}e^{\frac{2i\omega l}{c}}\right)} \times\left((AR_x - CR_y)h_0^{(+)} + (BR_x - DR_y)h_0^{(\times)}\right) \quad .$$

One can now read off the transfer functions

$$S_{+fp} = \frac{(-i)(1-P_s)T_1\sqrt{R_2}\omega l \sin\left(\frac{\Omega l}{c}\right) e^{\frac{il(2\omega+\Omega)}{c}}}{4c\left(1+\sqrt{R_1R_2}e^{\frac{2il(\omega+\Omega)}{c}}\right)\left(1+\sqrt{R_1R_2}e^{\frac{2i\omega l}{c}}\right)}(AR_x - CR_y) \quad , \textit{and},$$

$$S_{\times fp} = \frac{(-i)(1-P_s)T_1\sqrt{R_2}\omega l \sin\left(\frac{\Omega l}{c}\right) e^{\frac{il(2\omega+\Omega)}{c}}}{4c\left(1+\sqrt{R_1R_2}e^{\frac{2il(\omega+\Omega)}{c}}\right)\left(1+\sqrt{R_1R_2}e^{\frac{2i\omega l}{c}}\right)}(BR_x - DR_y) \quad .$$

Note that the transfer functions above are the general solutions for a Fabry-Perot cavity. It has not been demanded that the cavities necessarily be on resonance. The cavity resonance condition is achieved by the condition

$$e^{\frac{2i\omega l}{c}} = -1 \quad .$$

The transfer functions for the delay line can be optimized for detection at a specific frequency, f_g. For the delay line, one demands that $sinc(\pi f_g bl/c) = 1/\sqrt{2}$. The optimum frequency is $f_g = 1.39/(\pi\tau_s)$. The storage time for a delay line cavity is $\tau_s = bl/c$. The storage time of a Fabry-Perot cavity is

$$\tau_s = \frac{2l}{c(1-\sqrt{R_1R_2})} \quad .$$

For a standard, unrecycled Fabry-Perot interferometer there is no clear optimum choice for τ_s.

Figure 3.3 compares the delay line and Fabry-Perot transfer functions, S_{+mc} and S_{+fp}, for the case when $\theta=\phi=\psi=0$. The length of the interferometer arms is 4 kilometers. For the Michelson delay line system the values used are: 50 for b, number of times the beam traverses the cavity; .9999 for R_m, the reflectivity of the cavity mirrors; $5.83 * 10^{14}$ Hz, the frequency of the laser light, which corresponds to a wavelength of .5145 microns. The storage time for this cavity is $\tau_s = 6.67 * 10^{-4} s$, with an optimum frequency of 665 Hz. The parameters for the

Fabry-Perot cavity were chosen so that the sensitivity of the two systems would be the same at 665 Hz. The parameters for the Fabry-Perot are: .9253 for R_1, the reflectivity of the front mirror of the cavity; .0746 for T_1, the transmission of the front mirror; .9999 for R_2, the reflectivity of the rear mirror. The storage time for this cavity is $\tau_s = 6.99 * 10^{-4} s$. It is assumed that the loss coefficient of all the mirrors, P, is 10^{-4}.

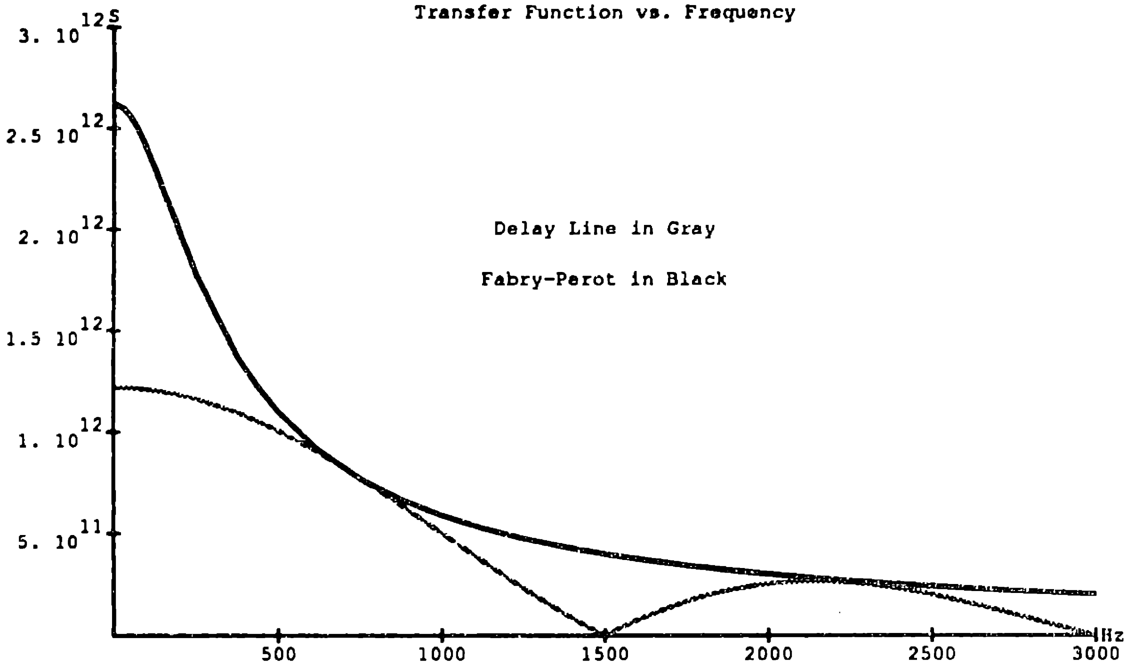

Figure 3.3 Transfer functions for a delay line and a Fabry-Perot. The optimum frequency for the delay line is 665 Hz. The delay line and Fabry-Perot systems here have equal sensitivities at 665 Hz.

Section 4 Recycling Interferometer

A broadband recycling interferometer is the next scheme to be considered. This technique was invented by Drever (1982). In this scheme the light that would normally leave the interferometer, and head back towards the laser, is reflected back into the system by a mirror. This system is illustrated in Figure 3.4. The recycling mirror is labeled as M0.

In Figure 3.4 the cavities have been left undefined. One could have either a delay line, or a Fabry-Perot system. Once one knows how the light exiting the

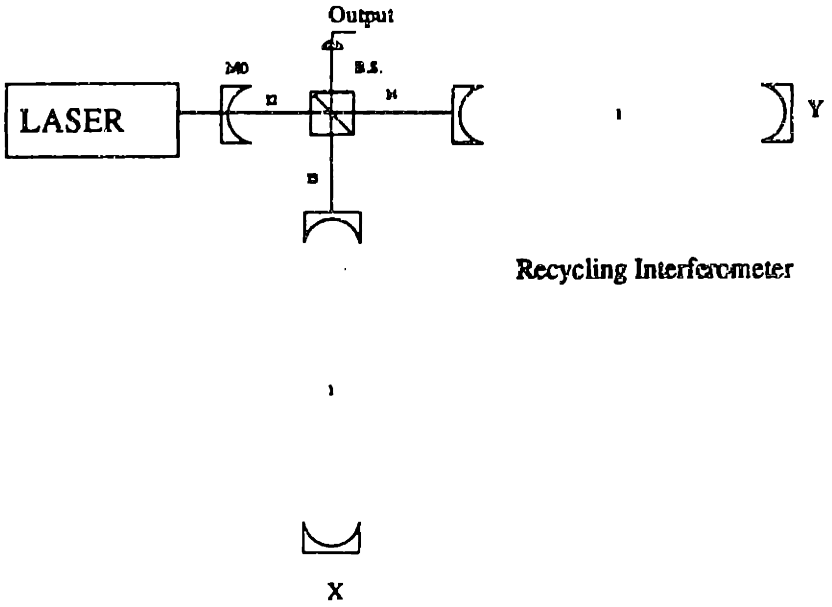

Figure 3.4 A standard recycling interferometer. The light that would normally exit the system towards the laser is reflected with mirror M0 back into the interferometer. The cavities are undefined, they can be either a delay line or a Fabry-Perot

cavities is related to the entering light, it is a straight forward algebraic procedure to find the output signal. The distances between some of the objects have been labeled in the figure. The length of each cavity is l, the distance from the recycling mirror to the beamsplitter is l_2, the distance from the beam splitter to the front of the $\hat{x}$ cavity is l_3, and l_4 is the distance from the beam splitter to the front of the $\hat{y}$ cavity.

For the case where one has Fabry-Perot cavities and a dark fringe condition, the electric field at the output is:

$$E_{out}(t) = \frac{E_0 e^{i\left(\vec{k}\cdot\vec{x}_0-(\omega+\Omega)t\right)} i\omega l(1-P_s)\sqrt{T_0R_2}T_1}{\left(1+\sqrt{R_1R_2}e^{\frac{2i\omega l}{c}}\right)\left(1+\sqrt{R_1R_2}e^{\frac{2i(\omega+\Omega)l}{c}}\right)4c} \times$$

$$\frac{\sin\left(\frac{\Omega l}{c}\right)e^{\frac{il(2\omega+\Omega)}{2c}}e^{\frac{i\omega}{c}(2l_4+l_2)}}{\left(1+\sqrt{R_0}F_{fp}(1-P_s)e^{\frac{2i\omega}{c}(l_4+l_2)}\right)}\left[(AR_x-CR_y)h_0^{(+)}+(BR_x-DR_y)h_0^{(\times)}\right]$$

where,

$$F_{jp} = \frac{\sqrt{R_1} + \sqrt{R_2} e^{\frac{2i\omega l}{c}} (1 - P_1)}{1 + \sqrt{R_1 R_2} e^{\frac{2i\omega l}{c}}} \quad .$$

The quantity F relates the electric field exiting a cavity in terms of the field entering it in the absence of a gravity wave, namely,

$$E_{out} = iFE_{in} \quad .$$

The dark fringe condition is satisfied by demanding

$$e^{2ikl_3} = e^{2ikl_4} \quad .$$

The transfer functions can be read off from the electric field:

$$S_{+fprec} = \frac{i\omega l (1 - P_s) \sqrt{T_0 R_2 T_1}}{\left(1 + \sqrt{R_1 R_2} e^{\frac{2i\omega l}{c}}\right)\left(1 + \sqrt{R_1 R_2} e^{\frac{2i(\omega+\Omega)l}{c}}\right) 4c} \times \frac{\sin\left(\frac{\Omega l}{c}\right) e^{\frac{il(2\omega+\Omega)}{2c}} e^{\frac{i\omega}{c}(2l_4+l_2)} (AR_x - CR_y)}{\left(1 + \sqrt{R_0} F (1 - P_s) e^{\frac{2i\omega}{c}(l_4+l_2)}\right)}$$

$$S_{\times fprec} = \frac{i\omega l (1 - P_s) \sqrt{T_0 R_2 T_1}}{\left(1 + \sqrt{R_1 R_2} e^{\frac{2i\omega l}{c}}\right)\left(1 + \sqrt{R_1 R_2} e^{\frac{2i(\omega+\Omega)l}{c}}\right) 4c} \times \frac{\sin\left(\frac{\Omega l}{c}\right) e^{\frac{il(2\omega+\Omega)}{2c}} e^{\frac{i\omega}{c}(2l_4+l_2)} (BR_x - DR_y)}{\left(1 + \sqrt{R_0} F (1 - P_s) e^{\frac{2i\omega}{c}(l_4+l_2)}\right)} .$$

A resonance condition for the recycled light develops when

$$Arg(F) + 2k(l_2 + l_4) = (2n - 1)\pi \quad ,$$

and n is some integer. The transfer functions can be maximized with respect to the variable R_0. One must remember to express T_0 in terms of R_0 before one maximizes. In general, given the characteristics of the cavities, it is easier to find the value of R_0 numerically. Maximizing S_+ for the case where $\Omega \to 0$ one has an optimum value of

$$\sqrt{R_0} = (1 - P_s)(1 - P_1)|F| \quad .$$

(Note: The loss of a cavity, L_c, is given by $L_c = 1 - |F|^2$, yielding a value for the optimum recycling mirror transmission of $T_0 \simeq L_c$.) The cavity reflectivity for the Fabry-Perot, F_{fp}, was defined above, while the Michelson delay line value, F_{mc}, is defined below. The optimum frequency for the broadband recycled delay line is $f_g = 1.39/(\pi\tau_s)$. The storage time for a delay line cavity is $\tau_s = bl/c$. The optimum frequency for the broadband recycled Fabry-Perot system is $f_g = 1/(2\pi\tau_s)$, where

$$\tau_s = \frac{2l}{c(1-\sqrt{R_1 R_2})} \quad .$$

Figure 3.5 shows the transfer functions for broadband recycled Fabry-Perot and delay systems, both optimized for 240 Hz. It is for the case where the gravity wave is coming from the optimum direction, with the optimum polarization. The parameters for the Fabry–Perot system are; .9212 for R_1, the reflectivity of the front mirror of the cavity; .0787 for T_1, the transmission of the front mirror; .9999 for R_2, the reflectivity of the rear mirror; .990 for R_0, the optimum recycling mirror reflectivity;10^{-4} for P, the loss coefficient of the mirrors. For the Michelson delay line system the values used are: 138 for b, number of times the beam traverses the cavity; .9999 for R_m, the reflectivity of the cavity mirrors, .986 for R_0, the optimum recycling mirror reflectivity;10^{-4} for P, the loss coefficient of the mirrors. The frequency of the laser light is $5.83 * 10^{14}$ Hz, which corresponds to a wavelength of .5145 microns.

Another plot of the transfer function of the broadband recycled Fabry-Perot system is given in Figure 3.6. The system is optimized for 240 Hz. It is for the case where the gravity wave is coming from the optimum direction, with the optimum polarization. The standard Fabry-Perot transfer function optimized is shown for comparison. The parameters of the Fabry-Perot cavities are; .9221 for R_1, the reflectivity of the front mirror of the cavity; .0778 for T_1, the transmission of the front mirror; .9995 for R_2, the reflectivity of the rear mirror; 10^{-4} for P, the loss coefficient of the mirrors. A value of .9705 for the recycling mirror, R_0, maximizes the transfer function. This produces a factor of 5.8 improvement for the transfer function in this example.

The next system considered is recycling for a Michelson interferometer. The output electric field for the dark fringe condition is

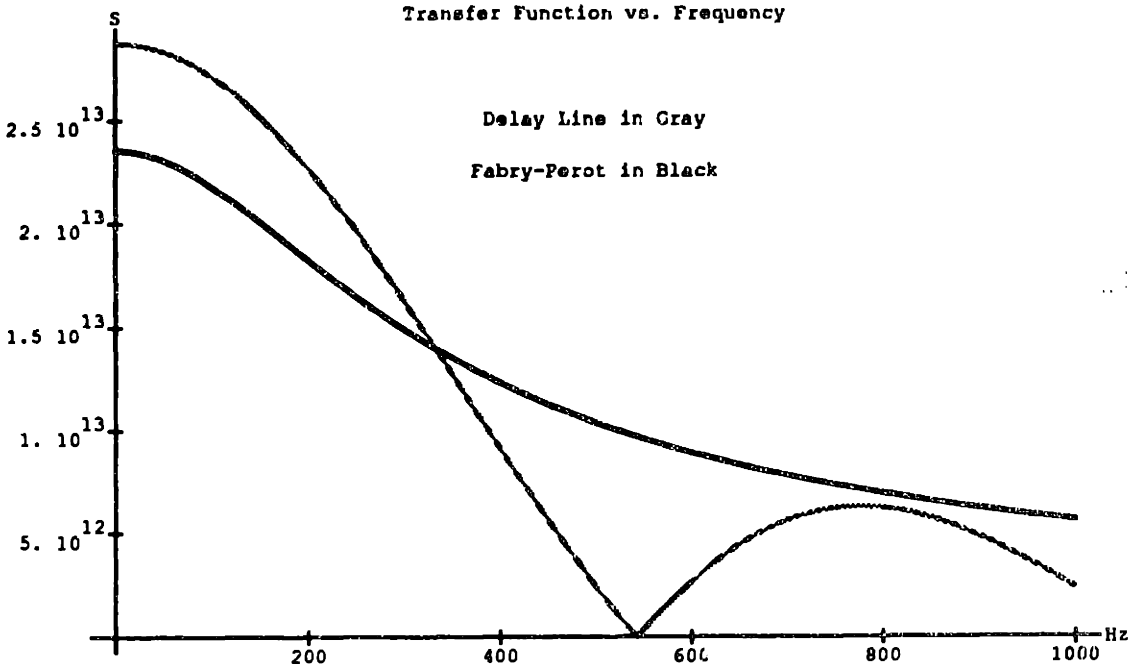

Figure 3.5 Comparison of the transfer functions for a broadband recycled Fabry-Perot and a broadband recycled delay line. Both systems are optimized for 240 Hz.

$$E_{out}(t) = \frac{E_0\left(i\sqrt{R_{mc}}\right)^{b-2} e^{i\left(\vec{k}\cdot\vec{x}_0-(\omega+\Omega)t\right)} i\omega l(1-P_s)\sqrt{T_0}}{4c\left(1+\sqrt{R_0}F_{mc}(1-p_s)e^{\frac{2i\omega}{c}(l_1+l_2)}\right)} \times$$
$$\sin\left(\frac{\Omega l b}{2c}\right) e^{\frac{ibl(2\omega+\Omega)}{2c}} e^{\frac{i\omega}{c}(2l_1+l_2)} \left[(AR_x - CR_y)h_0^{(+)} + (BR_x - DR_y)h_0^{(\times)}\right]$$

The quantity F_{dl} relates the exiting electric field to the incident electric field for the delay line cavity, and is given by

$$F_{mc} := i^{b-3} R_{mc}^{\frac{b-2}{2}} e^{\frac{i\omega l b}{c}} \quad .$$

The transfer functions are

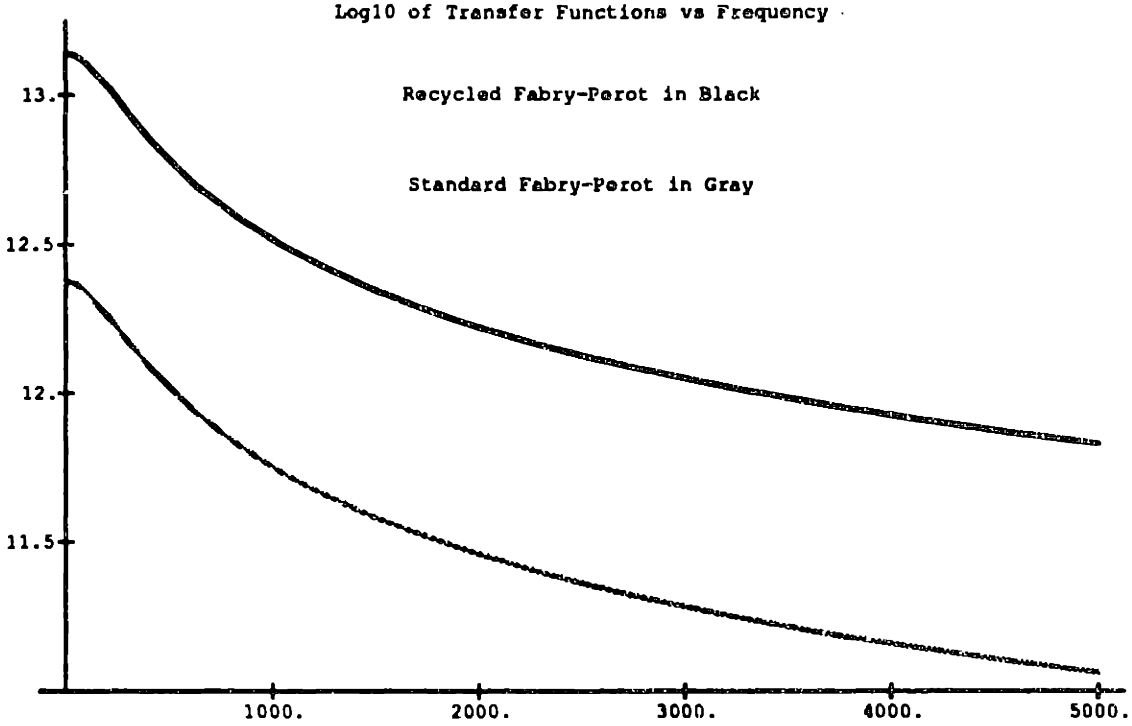

Figure 3.6 Comparison of the transfer functions for a broadband recycled Fabry-Perot and a standard Fabry-Perot. For the numbers used in the example a gain of 5.8 was achieved.

$$S_{+mcres} = \frac{\left(i\sqrt{R_{mc}}\right)^{b-2} i\omega l(1-P_s)\sqrt{T_0}}{4c\left(1+\sqrt{R_0}F_{mc}(1-P_s)e^{\frac{2i\omega}{c}(l_4+l_2)}\right)} \times$$

$$\sin\left(\frac{\Omega l b}{2c}\right) e^{\frac{ibl(2\omega+\Omega)}{2c}} e^{\frac{i\omega}{c}(2l_4+l_2)} (AR_x - CR_y)$$

$$and,$$

$$S_{\times mcres} = \frac{\left(i\sqrt{R_{mc}}\right)^{b-2} i\omega l(1-P_s)\sqrt{T_0}}{4c\left(1+\sqrt{R_0}F_{mc}(1-P_s)e^{\frac{2i\omega}{c}(l_4+l_2)}\right)} \times$$

$$\sin\left(\frac{\Omega l b}{2c}\right) e^{\frac{ibl(2\omega+\Omega)}{2c}} e^{\frac{i\omega}{c}(2l_4+l_3)} (BR_x - DR_y) \quad .$$

A resonance condition for the recycled light develops when

$$Arg(F_{mc}) + 2k(l_2 + l_4) = (2n-1)\pi \quad ,$$

and n is some integer.

Figure 3.7 is a plot of the broadband recycled delay line system's transfer function for a gravity wave with $\theta=\phi=\psi=0$. The transfer function of the standard delay line interferometer is given for comparison. The parameters for the delay line system, optimized at 665 Hz, are; 50 for b, number of times the beam traverses the cavity; .9995 for R_m, the reflectivity of the cavity mirrors; 10^{-4} for P, the loss coefficient of the mirrors. One finds that a reflectivity of .9761 for the recycling mirror, R_0, maximizes the transfer function. The recycled system here is a factor of 6.48 times better in sensitivity than the standard interferometer.

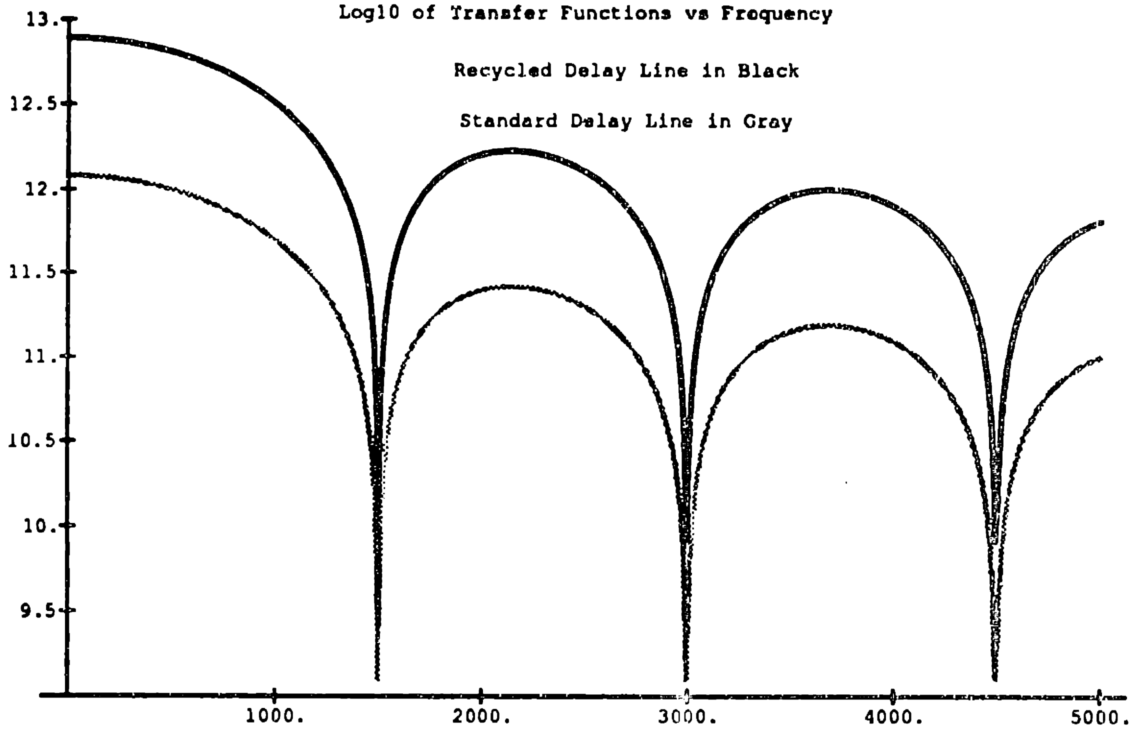

Figure 3.7 Comparison of the transfer functions for a recycled delay line and a standard delay line. For the numbers used in the example a gain of 6.48 was achieved.

Section 5 Dual Recycling Interferometer

The next system takes the recycling strategy a step further. This system is called dual recycling and is due to Meers (1988). Another mirror is added to the system. This mirror creates a resonance condition for the output signal at a certain frequency. The sensitivity of the interferometer can be greatly improved, but only in a narrow frequency range. A drawing of the interferometer is given in Figure 3.8.

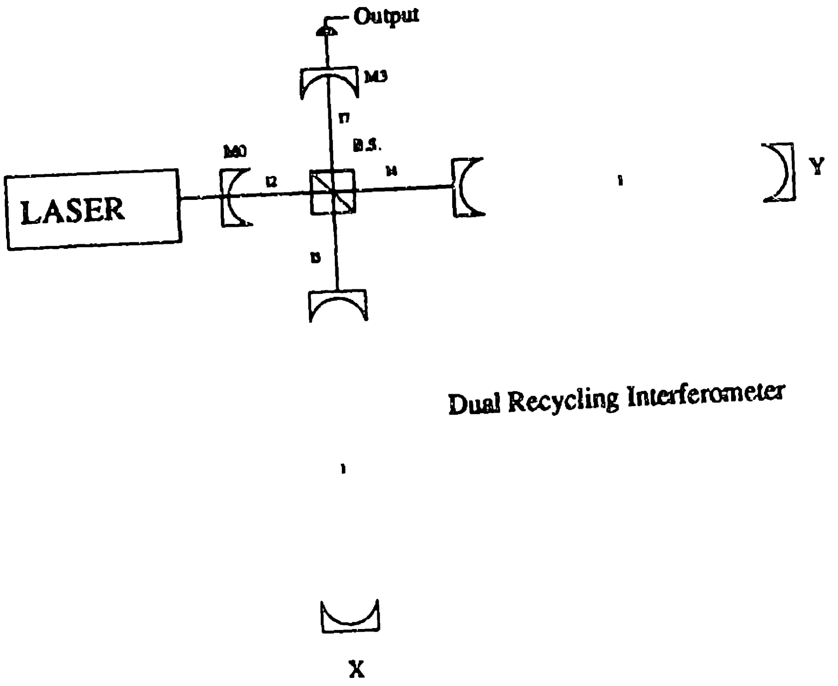

Figure 3.8 A dual recycling interferometer. The light that would normally exit the system towards the laser is reflected with mirror M0 back into the interferometer, and the light that would exit towards the photodetector is reflected back so that the signal will build up and have a resonance at a certain frequency.

The second recycling mirror is M3. The cavities have been left undefined. They can be either delay line or Fabry-Perot. The distance from the beam splitter to mirror M3 is l_7. Consider the case for Fabry-Perot cavities first. The output electric field under the dark fringe condition is

$$E_{out}(t) = \frac{E_0 e^{i(\vec{k}\cdot\vec{x}_0-(\omega+\Omega)t)} i\omega l(1-P_s)\sqrt{T_0 T_3 R_2 T_1}}{\left(1+\sqrt{R_1 R_2}e^{\frac{2i\omega l}{c}}\right)\left(1+\sqrt{R_1 R_2}e^{\frac{2i(\omega+\Omega)l}{c}}\right)4c} \times$$

$$\frac{\sin\left(\frac{\Omega l}{c}\right)e^{\frac{il(2\omega+\Omega)}{2c}} e^{\frac{i\omega}{c}(2l_4+l_2+l_7)}\left[(AR_x - CR_y)h_0^{(+)} + (BR_x - DR_y)h_0^{(\times)}\right]}{\left(1+\sqrt{R_0}F_{fp}(1-P_s)e^{\frac{2i\omega}{c}(l_4+l_2)}\right)\left(1-\sqrt{R_3}F_{fp+}(1-P_s)e^{\frac{2i\omega}{c}(l_4+l_7)}\right)} .$$

The quantity F_{fp+}, when multiplied by i, is the reflection coefficient of the cavity for the electric field of the laser light that has been shifted up in frequency by the gravity wave. It is expressed as

$$F_{+fp} = \frac{\sqrt{R_1} + \sqrt{R_2}e^{\frac{2il(\omega+\Omega)}{c}}(1-P_1)}{1+\sqrt{R_1R_2}e^{\frac{2il(\omega+\Omega)}{c}}} \quad .$$

The transfer functions are

$$S_{+fpdual} = \frac{E_0 i\omega l(1-P_s)\sqrt{T_0T_3R_2}T_1}{\left(1+\sqrt{R_1R_2}e^{\frac{2i\omega l}{c}}\right)\left(1+\sqrt{R_1R_2}e^{\frac{2i(\omega+\Omega)l}{c}}\right)4c} \times$$
$$\frac{\sin\left(\frac{\Omega l}{c}\right)e^{\frac{il(2\omega+\Omega)}{2c}}e^{\frac{i\omega}{c}(2l_4+l_2+l_7)}(AR_x - CR_y)}{\left(1+\sqrt{R_0}F_{fp}(1-P_s)e^{\frac{2i\omega}{c}(l_4+l_2)}\right)\left(1-\sqrt{R_3}F_{fp+}(1-P_s)e^{\frac{2i\omega}{c}(l_4+l_2)}\right)}$$

$$S_{\times fpdual} = \frac{E_0 i\omega l(1-P_s)\sqrt{T_0R_2}T_1}{\left(1+\sqrt{R_1R_2}e^{\frac{2i\omega l}{c}}\right)\left(1+\sqrt{R_1R_2}e^{\frac{2i(\omega+\Omega)l}{c}}\right)4c} \times$$
$$\frac{\sin\left(\frac{\Omega l}{c}\right)e^{\frac{il(2\omega+\Omega)}{2c}}e^{\frac{i\omega}{c}(2l_4+l_2+l_7)}(BR_x - DR_y)}{\left(1+\sqrt{R_0}F_{fp}(1-P_s)e^{\frac{2i\omega}{c}(l_4+l_2)}\right)\left(1-\sqrt{R_3}F_{fp+}(1-P_s)e^{\frac{2i\omega}{c}(l_4+l_2)}\right)} .$$

The laser light resonance condition is achieved when

$$Arg(F_{fp}) + 2k(l_2 + l_4) = (2n-1)\pi \quad ,$$

where n is any integer, and the signal resonance condition is reached when

$$Arg(F_{+fp}) + 2k(l_7 + l_4) = 2m\pi \quad ,$$

where m is any integer. The transfer functions can be maximized by choosing optimum values for the reflectivities of mirrors M0 and M3. If the dual recycling mirror's reflectivity is chosen to be something other than the one that maximizes the peak height of the resonance, the maximum sensitivity of the detector decreases, but the effective bandwidth increases. The trade-off between maximum sensitivity and bandwidth is one of the topics that is explored later when the subject of designing the best interferometer for detecting a stochastic background of gravitational radiation is addressed.

A plot of the transfer function of the dual recycling Fabry-Perot system is shown in Figure 3.9. The parameters for the Fabry-Perot cavities are that of the 240 Hz optimized broadband recycled system illustrated above. The optimum value for the recycling mirror's reflectivity is R_0=.9705, while the optimum value for the dual recycling mirror's reflectivity is frequency dependent. The resonance frequency was chosen to be 250 Hertz, and at this frequency the optimum value for this example system is R_3 = .9855. Also, the transfer function of the recycled Fabry-Perot system is shown for comparison. The gain in the sensitivity at the resonance is 8.33 for this example. The full width at half maximum is 12.8 Hertz.

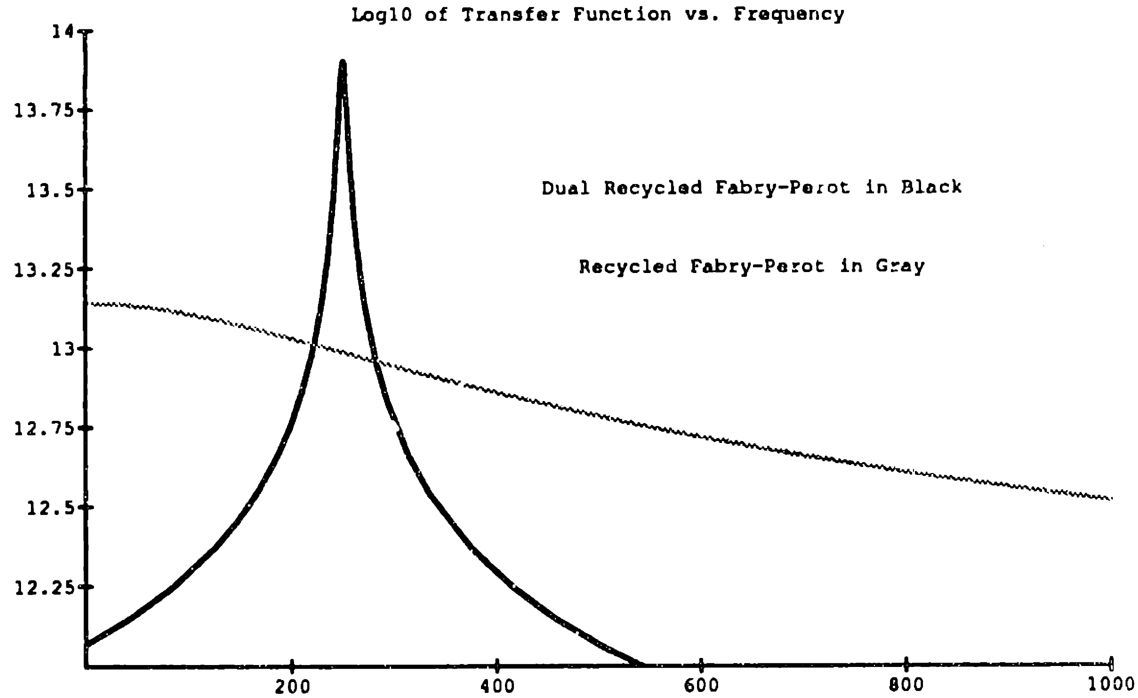

Figure 3.9 A comparison of the dual recycling Fabry-Perot transfer function and the broadband recycled Fabry-Perot transfer function. The resonant frequency here is 250 Hertz, with the dual recycling having a better sensitivity by a factor of 8.33 here, and a FWHM of 12.8 Hertz.

It should be noted that for a dual recycling Fabry-Perot system the storage time of the cavity formed by the dual recycling mirror, M3, and the mirror at the front of the interferometer arm cavity, M1, determines the resonance frequency. Therefore, the optimum value of the dual recycling mirror changes with frequency.

R3	.975	.9823	.988	.992	.994	.9956	.9966	.9972	.9977	.9981
f	100	200	300	400	500	600	700	800	900	1000

Figure 3.10 The optimum dual recycling mirror reflectivity, R_3, for different frequencies. These values were computed for the Fabry-Perot example used above.

Figure 3.10 is a table displaying the optimum value of R_3 for different frequencies of the Fabry-Perot interferometer example used above.

When delay line cavities are used, the output electric field for the dark fringe condition is

$$E_{out}(t) = \frac{E_0\left(i\sqrt{R_{mc}}\right)^{b-2} e^{i\left(\vec{k}\cdot\vec{x}_0-(\omega+\Omega)t\right)} i\omega l(1-P_s)\sqrt{T_0T_3}}{4c\left(1+\sqrt{R_0}F_{mc}(1-P_s)e^{\frac{2i\omega}{c}(l_4+l_2)}\right)} \times$$

$$\frac{\sin\left(\frac{\Omega lb}{2c}\right)e^{\frac{ibl(2\omega+\Omega)}{2c}} e^{\frac{i\omega}{c}(2l_4+l_2+l_7)}\left[(AR_x-CR_y)h_0^{(+)}+(BR_x-DR_y)h_0^{(\times)}\right]}{\left(1-\sqrt{R_3}F_{mc+}(1-P_s)e^{\frac{2i\omega}{c}(l_4+l_7)}\right)} .$$

The function F_{mc+} is given by

$$F_{mc+} = i^{b-3} R_{mc}^{\frac{b-2}{2}} e^{\frac{ilb(\omega+\Omega)}{c}} \quad .$$

The transfer functions are

$$S_{+mcres} = \frac{\left(i\sqrt{R_{mc}}\right)^{b-2} i\omega l(1-P_s)\sqrt{T_0T_3}}{4c\left(1+\sqrt{R_0}F_{mc}(1-P_s)e^{\frac{2i\omega}{c}(l_4+l_2)}\right)} \times$$

$$\frac{\sin\left(\frac{\Omega lb}{2c}\right)e^{\frac{ibl(2\omega+\Omega)}{2c}} e^{\frac{i\omega}{c}(2l_4+l_2+l_7)}(AR_x-CR_y)}{\left(1-\sqrt{R_3}F_{mc+}(1-P_s)e^{\frac{2i\omega}{c}(l_4+l_7)}\right)}$$

and,

$$S_{\times mcres} = \frac{\left(i\sqrt{R_{mc}}\right)^{b-2} i\omega l(1-P_s)\sqrt{T_0T_3}}{4c\left(1+\sqrt{R_0}F_{mc}(1-P_s)e^{\frac{2i\omega}{c}(l_4+l_2)}\right)} \times$$

$$\frac{\sin\left(\frac{\Omega lb}{2c}\right)e^{\frac{ibl(2\omega+\Omega)}{2c}} e^{\frac{i\omega}{c}(2l_4+l_2+l_7)}(BR_x-DR_y)}{\left(1-\sqrt{R_3}F_{mc+}(1-P_s)e^{\frac{2i\omega}{c}(l_4+l_7)}\right)} .$$

The laser light resonance condition is achieved when

$$Arg(F_{mc}) + 2k(l_2+l_4) = (2n-1)\pi \quad ,$$

where n is any integer, and the signal resonance condition is reached when

$$Arg(F_{mc+}) + 2k(l_7 + l_4) = 2m\pi \quad ,$$

where m is any integer. And just as in the case with the Fabry-Perot cavities, these transfer functions can be maximized with respect to the reflectivities of mirrors M0 and M3. It turns out that the values of R_0 and R_3 needed to optimize the system are equal. This is due to the fact that the magnitude of the reflectivity factor for light off of the delay line cavities is independent of light frequency. It is the same for the laser light with angular frequency ω, and for the light that has been shifted up in frequency to $\omega+\Omega$. Also, this means that the optimum value of R_3 is the same for all frequencies at which one may want to operate the dual recycling interferometer. This is not the case for Fabry-Perot cavities.

One wants the light whose frequency has been shifted upwards to $\omega+\Omega$, to be resonant. An example of a transfer function for a dual recycled delay line system is shown in Figure 3.11. The parameters for the delay line cavities are the same as those used in the broadband recycled delay line example above. The value of the recycling mirrors is $R_0=R_3 = .976$. The resonance was chosen to be at 250Hz, and the gain in sensitivity for the dual recycling system over the standard recycled delay line is a factor of 6.5, while the full width at half maximum is 20Hz.

Section 6 Resonant Recycling Interferometer

The final interferometer system to be considered is one called resonant recycling, which is due to Drever (1982). Its affect is almost identical to that of dual recycling. However, it is a more complicated system, and the simple geometry of dual recycling will have an advantage in operation. A drawing of the scheme is presented in Figure 3.12.

The idea underlying this interferometer is that light will be stored in each cavity for half of the gravity wave period, and then it will be switched into the other cavity for the other half period, and then back to the first cavity for the next half period, and so on. The affect of the gravity wave will build up until losses in the system limit it. Note that there are two optical paths to the cavity. Light travels in both directions along each of these paths. Let's say a beam of light enters the X cavity along the path labeled l4. It would exit the cavity along the path l6. Similarly, light entering the X cavity along the l6 path will exit along the l4 path. In a delay line system this is easy to visualize as the light beam

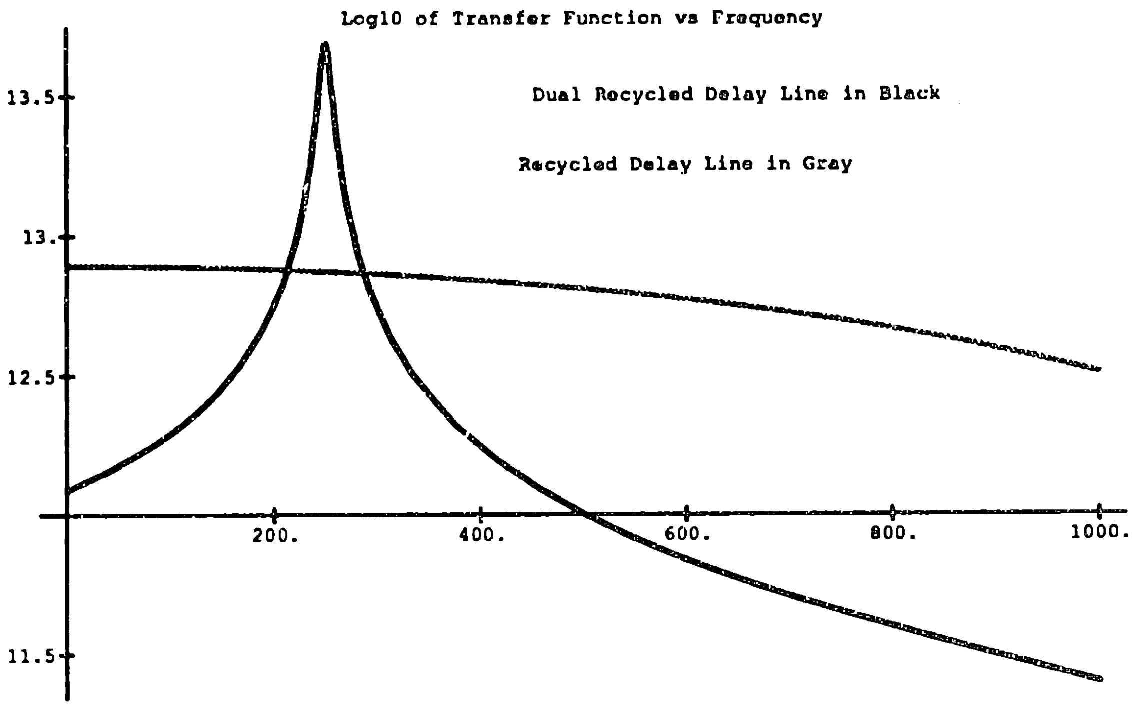

Figure 3.11 A comparison of the dual recycling delay line transfer function and the recycled delay line transfer function.

exiting the system does not overlap the light beam entering. In a Fabry-Perot system it is more complicated. The light exiting the cavity is retracing the path of the entering light. For one to separate this light into two paths, one must place a polarizing beamsplitter and a quarter wave plate in the light path before each cavity (Drever, 1982). Another point that should be made is that this system is really only useful for a Fabry-Perot system. One wants to have the ability to change the frequency of the resonance. This is equivalent to changing the storage time of each cavity. For a delay line, there is only one possible storage time, namely $\tau_s = bl/c$. For a Fabry-Perot cavity, one can change the storage time by changing the parameters of the cavity.

Only resonant recycling for Fabry-Perot cavities will be considered because of the severe frequency range limitations for the delay line case. For the dark

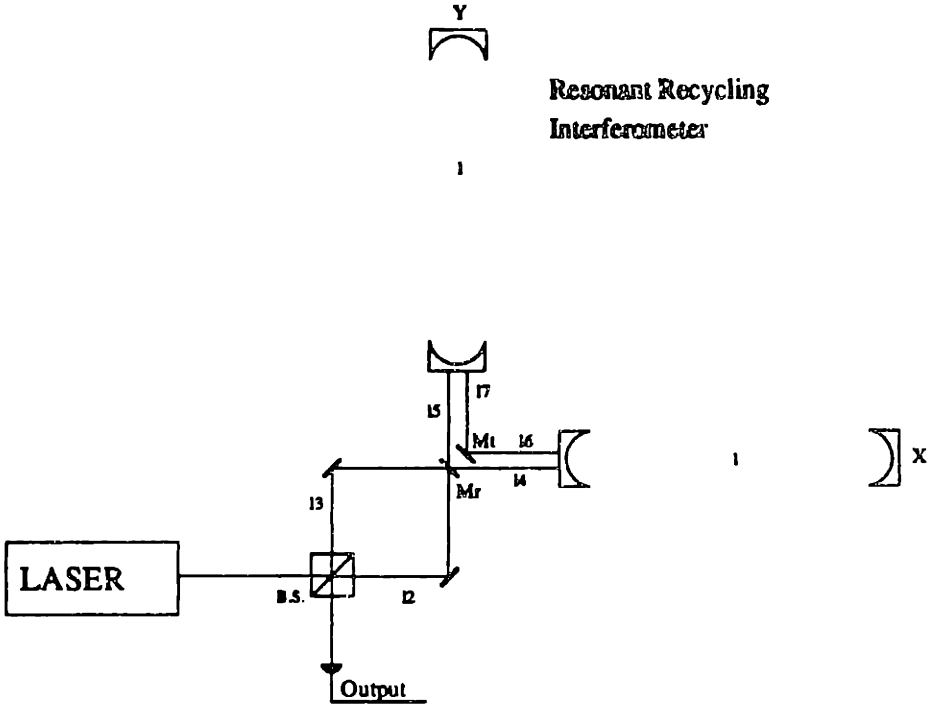

Figure 3.12 The resonant recycling Fabry-Perot system. The light's phase change due to the gravity wave builds up in a cavity for half the period of the wave, and the switches over to the other cavity for the second half of the period. The affect of the gravity wave builds up until losses in the system limit it.

fringe condition, the output electric field is

$$E_{out}(t) = \frac{E_0 e^{i\left(\vec{k}\cdot\vec{x}_0-(\omega+\Omega)t\right)}(\quad)\omega l(1-P_s)T_r T_1^2 R_2\sqrt{R_t}}{\left(1+\sqrt{R_1R_2}e^{\frac{2i\omega l}{c}}\right)^2\left(1+\sqrt{R_1R_2}e^{\frac{2i(\omega+\Omega)l}{c}}\right)^2 2c}\times$$

$$\frac{\sin^2\left(\frac{\Omega l}{c}\right)e^{\frac{2il(2\omega+\Omega)}{c}}e^{\frac{i\omega}{c}(l_2+l_3)}e^{iz}\left[(AR_x-CR_y)h_0^{(+)}+(BR_x-DR_y)h_0^{(\times)}\right]}{\left(1-\sqrt{R_tR_r}F_{fp}^2e^{iz}\right)\left(1-\sqrt{R_tR_r}F_{fp+}^2e^{iz}\right)} \quad .$$

In the equation above z is given by

$$z = \frac{\omega}{c}(l_4+l_5+l_6+l_7) \quad .$$

The quantities F_{fp} and F_{fp+} are the same as those defined above for the Fabry-Perot cavities. The transfer functions can be read off directly

$$S_{+resrec} = \frac{(-1)\omega l(1-P_s)T_rT_1^2R_2\sqrt{R_t}(AR_x-CR_y)}{\left(1+\sqrt{R_1R_2}e^{\frac{2i\omega l}{c}}\right)^2\left(1+\sqrt{R_1R_2}e^{\frac{2i(\omega+\Omega)l}{c}}\right)^2 2c}\times$$

$$\frac{\sin^2\left(\frac{\Omega l}{c}\right)e^{\frac{2il(2\omega+\Omega)}{c}}e^{\frac{i\omega}{c}(l_2+l_3)}e^{iz}}{\left(1-\sqrt{R_tR_r}F_{fp}^2e^{iz}\right)\left(1-\sqrt{R_tR_r}F_{fp+}^2e^{iz}\right)}\ ,\quad and,$$

$$S_{\times resrec} = \frac{(-1)\omega l(1-P_s)T_rT_1^2R_2\sqrt{R_t}(BR_x-DR_y)}{\left(1+\sqrt{R_1R_2}e^{\frac{2i\omega l}{c}}\right)^2\left(1+\sqrt{R_1R_2}e^{\frac{2i(\omega+\Omega)l}{c}}\right)^2 2c}\times$$

$$\frac{\sin^2\left(\frac{\Omega l}{c}\right)e^{\frac{2il(2\omega+\Omega)}{c}}e^{\frac{i\omega}{c}(l_2+l_3)}e^{iz}}{\left(1-\sqrt{R_tR_r}F_{fp}^2e^{iz}\right)\left(1-\sqrt{R_tR_r}F_{fp+}^2e^{iz}\right)}\ .$$

Figure 3.13 shows a plot of the transfer function for resonant recycling at 483 Hz. Again, this is for the plus polarization with $\theta=\phi=\psi=0$. The optimum value for the recycling mirror, when the parameters for the 240 Hz optimized Fabry-Perot cavities are the same as defined above, is $R_r=.97$. The folding mirror Mt was assigned a reflectivity of $R_t=.999$. A plot of the dual recycling transfer function with a resonance at 483 Hz is also given. The dual recycling mirror for this frequency is $R_3=.994$. The two transfer functions are virtually identical, and no difference can be seen in Figure 3.13. The full width at half maximum for the two systems is 13 Hz.

Section 7 Common Feature of all Transfer Functions

A property of all the transfer functions that will prove to be useful in the investigation of a SGWB is that all transfer functions can be written in the form

$$\begin{aligned} S_+\left(\hat{k},\Omega\right) &= B(\Omega)[AR_x-CR_y]\frac{\Omega l}{2c} \\ S_\times\left(\hat{k},\Omega\right) &= B(\Omega)[BR_x-DR_y]\frac{\Omega l}{2c}\ . \end{aligned}$$

The term $B(\Omega)$ is one half the transfer function for a normally incident, and optimally polarized gravity wave. This is because for $\theta=\phi=\psi=0$ one has

$$S_+ = 2B(\Omega)\ ,\quad and,\qquad S_\times = 0\ .$$

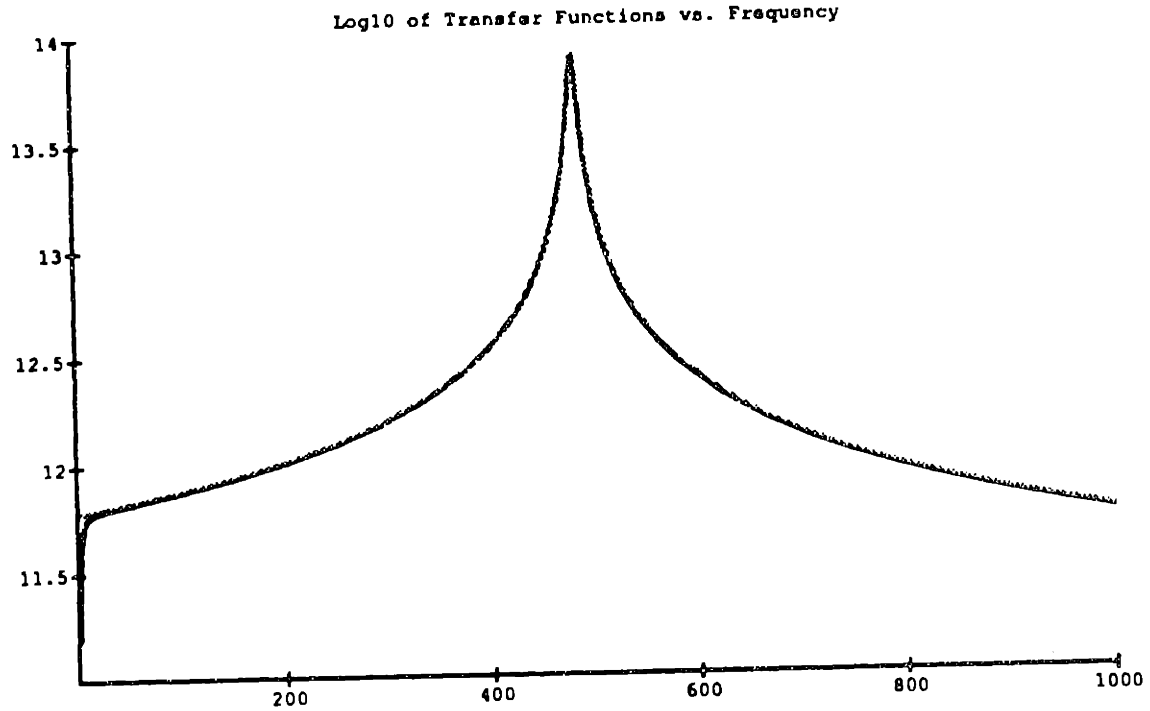

Figure 3.13 A comparison of the dual recycling Fabry-Perot transfer function and the resonant recycled Fabry-Perot transfer function. They overlap one another.

B(Ω) is only dependent on the frequency of the wave, and the characteristics of the interferometer. All the angular and polarization terms enter through $[AR_x - CR_y]$ and $[BR_x - DR_y]$. R_x and R_y have a frequency dependence, but the quantities $R_x\frac{\Omega l}{2c}$ or $R_y\frac{\Omega l}{2c}$ are virtually constant at one for a four kilometer system between 0 and 10KHz, especially below 1KHz, where the search for the SGWB will predominantly take place. Therefore, for the purposes of a SGWB detection one can make the approximation

$$S_+\left(\hat{k},\Omega\right) = B(\Omega)[A - C]$$
$$S_\times\left(\hat{k},\Omega\right) = B(\Omega)[B - D] \quad ,$$

where all the frequency and interferometer dependent terms appear in B(Ω), while the angular dependent terms are found in A,B,C, and D.

Section 8 Finite Contrast and Modulation

The interferometer schemes that have been presented in this chapter are all ideal systems. The actual systems will be much more complicated in order to accommodate real world problems. The laser light used in gravity wave interferometers is modulated at a frequency at which the laser is shot noise limited, usually in the few megahertz regime. This is accomplished with Pockel cells. An RF drive is applied to these crystals, and the phase of the light traveling through them is changed by an amount Γ, which is proportional to the applied voltage. The light then consists of the carrier, with an angular frequency ω, and sidebands with angular frequencies $\omega \pm n\omega_m$, where ω_m is the modulation angular frequency, and n is an integer. The amount of power in each sideband depends on the modulation index Γ. The interferometer output intensity is then swept about its minimum dark fringe value at the modulation frequency.

The optical scheme is further complicated by the fact that the beams returning to the beamsplitter do not perfectly recombine. The beams from the two cavities may have distortions in their phase fronts, they may be misaligned, or have other modes present. The light power at the photodetector of the antisymmetric port is given by

$$P = P_0(1 - C\cos\phi) \quad ,$$

where P_0 is the total power exiting the system, the phase difference between the light from the two arms is ϕ, and the contrast, C, is defined to be

$$C = \frac{P_{max} - P_{min}}{P_{max} + Pmin} \quad .$$

The modulation and the contrast will affect the sensitivity of the interferometer. There are different types of interferometer modulation techniques. The inline scheme is illustrated in Figure 3.14. The Pockel cells are between each cavity and the beamsplitter. The RF drive applied to the Pockel cells is the same, except that they are 180° out of phase. The M.I.T. 1.5 meter delay line interferometer used inline modulation (Dewey, 1986, and Livas, 1987). A .5 meter recombined Fabry-Perot interferometer, with stationary mirrors and inline modulation has been developed and tested at M.I.T. (Shoemaker, Fritschel, Giaime, Christensen, and Weiss, 1990). Inline modulation with a recycled interferometer has been investigated by Weiss (1990).

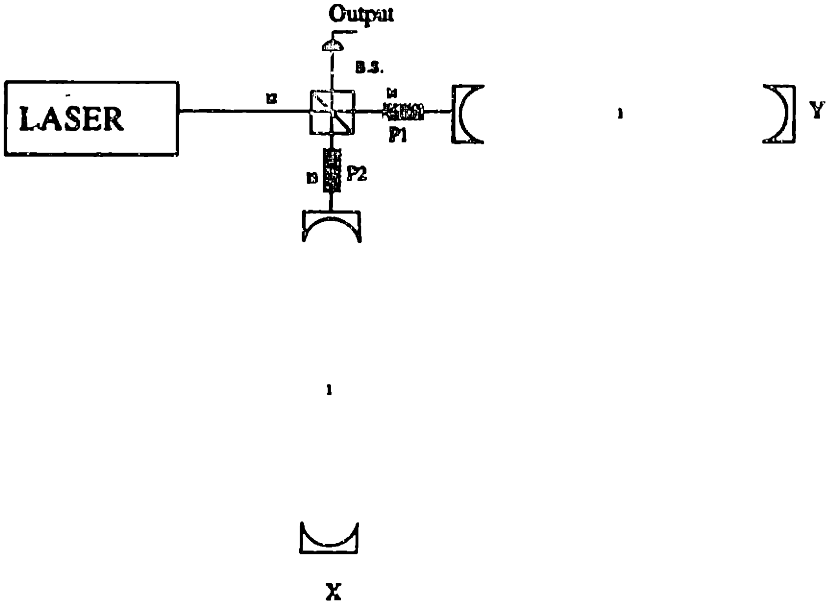

Figure 3.14 An interferometer with inline modulation. The Pockel cells are labeled P1 and P2. The RF drive applied to P1 is the same as that on P2, except that it is 180° out of phase.

Another modulation technique is called external modulation. The optical set up for this will be quite complicated. The Pockel cells are removed from the arms of the interferometer. The light will be modulated before, or after the interferometer, and will be interfered with a modulated reference beam that has not entered the interferometer. Weiss (1990) has analyzed one such recycled system. One may possibly achieve a sensitivity that is $\sqrt{2}$ better than the inline case. A recycled one bounce delay line interferometer with external modulation has been constructed and tested by Man, Shoemaker, Pham Tu, and Dewey (1990). The analysis for a modulated dual recycling has not been done at present.

Chapter 4 INTERFEROMETER ORIENTATION

Section 1 Introduction

In the following I discuss how one determines the optimum orientation of two laser interferometric gravitational wave antennas. These antennas are situated at different locations on the surface of the earth. In all the work that follows I assume that the two arms of an interferometer are perpendicular to each other. The orientation is optimized for a search for a stochastic background of gravitational radiation. This orientation is equivalent to maximizing the response of two detectors to a burst of randomly polarized waves, where one assumes that the bursts can occur in any part of the sky with equal probability. Throughout, the transfer functions of the interferometers are neglected.

Section 2 Coordinate System

The coordinate systems that I use to describe the response of a detector to an incoming wave are described first. The coordinates (X,Y,Z) will be associated with the incoming gravity wave. The coordinates (x,y,z) will be fixed with respect to the earth. If one were at the north pole, the $\widehat{x}$ direction would point along the Greenwich mean line, 0° longitude. The $\widehat{y}$ direction points along the 90°E longitude line. The $\widehat{z}$ direction is perpendicular to the surface of the earth at the north pole. Finally, (x_1,y_1,z_1) and (x_2,y_2,z_2) refer to the local coordinate systems of our two detectors.

The coordinate systems are related to each other by series of Euler rotations. I have defined my rotations, and coordinate systems such that

$$\vec{X} = \widetilde{R_z}(-\psi)\widetilde{R_x}(\theta)\widetilde{R_z}(-\phi)\vec{x} \qquad ,$$

and,

$$\vec{x_1} = \widetilde{R_z}(g_1)\widetilde{R_x}(b_1)\widetilde{R_z}(a_1)\vec{x} \qquad .$$

An example of one of these rotation matrices would be :

$$\widetilde{R_x}(\theta) = \begin{pmatrix} 1 & 0 & 0 \\ 0 & \cos\theta & \sin\theta \\ 0 & -\sin\theta & \cos\theta \end{pmatrix} \qquad .$$

The angles θ and ϕ define the direction from which the gravity wave is coming. The angle ψ defines the polarization of the wave. The angles a_1 and b_1 define the location of detector one on the earth. Specifically,

$$a_1 = \gamma_E - \frac{3\pi}{2} \quad ,and, \quad b_1 = \frac{\pi}{2} - \beta_N \quad ,$$

where γ_E is east longitude value, and β_N is the north latitude value. The variable g_1 represents the angle between the local east–west line and the interferometer arm that defines its $\hat{x}$ axis. The $\hat{x}$ arm is uniquely defined if one demands that the $\hat{z}$ points radially out from the earth at the detector, and that one has a right hand coordinate system. See Figure 4.1.

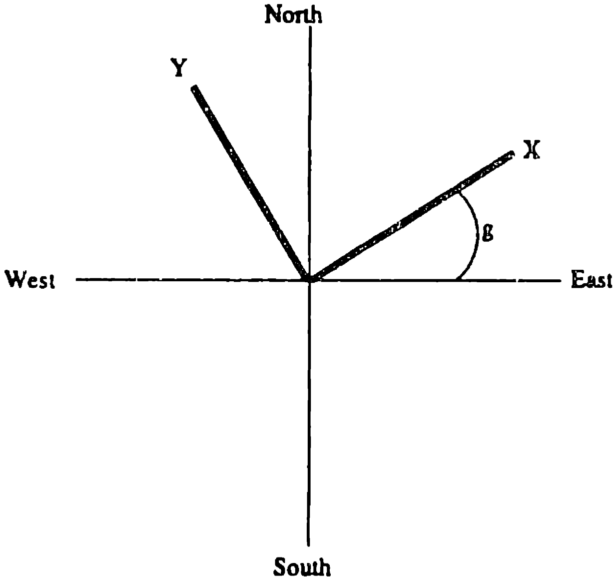

Figure 4.1 This displays the interferometer, in bold, in relation to its local longitude and latitude lines. The angle g represents the angle between the local east–west line and the interferometer arm that defines its $\hat{x}$ axis.

In the gravity wave frame the metric tensor is given by

$$\begin{aligned} g_{\mu\nu} &= \eta_{\mu\nu} + h_{\mu\nu} \\ &= \eta_{\mu\nu} + h^{(+)}_{\mu\nu} + h^{(\times)}_{\mu\nu} \quad . \end{aligned}$$

where,

$$h^{(+)}_{\mu\nu} = h^{(+)}_0 \begin{pmatrix} 0 & 0 & 0 & 0 \\ 0 & 1 & 0 & 0 \\ 0 & 0 & -1 & 0 \\ 0 & 0 & 0 & 0 \end{pmatrix} \quad ,and, \quad h^{(\times)}_{\mu\nu} = h^{(\times)}_0 \begin{pmatrix} 0 & 0 & 0 & 0 \\ 0 & 0 & 1 & 0 \\ 0 & 1 & 0 & 0 \\ 0 & 0 & 0 & 0 \end{pmatrix} \; .$$

Let us assume that a gravity wave interferometer has its arms along the $\hat{x}$ and the $\hat{y}$ axes of the earth centered coordinate system. The metric in this coordinate system can be related to the metric in the gravity wave's coordinate system, namely,

$$g_{\mu\nu}^{(earth)} = \frac{\partial X^\alpha}{\partial x^\mu}\frac{\partial X^\beta}{\partial x^\nu} g_{\alpha\beta}^{(g.w.)} \quad .$$

The gravity wave interferometer would measure a signal with an amplitude of

$$h = \left(\frac{1}{2}\right)(h_{11} - h_{22}) \quad ,$$

where

$$\begin{aligned} h_{11} &= A(\theta,\phi,\psi)h_0^{(+)} + B(\theta,\phi,\psi)h_0^{(\times)} \quad , and, \\ h_{22} &= C(\theta,\phi,\psi)h_0^{(+)} + D(\theta,\phi,\psi)h_0^{(\times)} \quad , \end{aligned}$$

and so,

$$\begin{aligned} h &= \frac{1}{2}\left[h_0^{(+)}(A-B) + h_0^{(\times)}(C-D)\right] \\ &= h_0^{(+)}F_+ + h_0^{(\times)}F_\times \quad , \end{aligned}$$

where,

$$\begin{aligned} F_+ &= \frac{1}{2}(1+\cos^2\theta)\cos 2\phi\cos 2\psi - \cos\theta\sin 2\phi\sin 2\psi \quad ,and, \\ F_\times &= \frac{1}{2}(1+\cos^2\theta)\cos 2\phi\sin 2\psi + \cos\theta\sin 2\phi\cos 2\psi \quad . \end{aligned}$$

When a detector is located at some general location on the earth F_+ and F_x become very long and cumbersome. They are a function of the six variables, θ, ϕ, ψ, a, b, and g. However, using the software Mathematica on a Sun4 system one may calculate and manipulate these functions. For example, detector one would measure a strain

$$\begin{aligned} h &= \left(\frac{1}{2}\right)(h_{11} - h_{22}) \\ &= h_0^{(+)}F_+ + h_0^{(\times)}F_\times \quad , \end{aligned}$$

where h_{11} and h_{22} can be found in a straight forward manner from

$$g_{\mu\nu}^{(det\#1)} = \frac{\partial X^{\alpha}}{\partial x_1^{\mu}} \frac{\partial X^{\beta}}{\partial x_1^{\nu}} g_{\alpha\beta}^{(g.w.)} \qquad ,$$

while the relationship between the two coordinate systems is given by,

$$\vec{X} = \widetilde{R_z}(-\psi)\widetilde{R_x}(\theta)\widetilde{R_z}(-\phi)\widetilde{R_z^T}(a)\widetilde{R_x^T}(b)\widetilde{R_z^T}(g)\vec{x_1} \quad .$$

The exact expressions for F_+ and F_x are given in appendix C.

Section 3 Solving for an Optimum Orientation

As described in chapter 5, the optimum orientation of two detectors is found by locating extrema in the correlated output of these two antennas in an isotropic, stochastic background of gravitational radiation. In other words, given the location of the two detectors, specified by (a_1 , b_1), and (a_2 , b_2), one must find the values of g_1 and g_2 that correspond with the extrema of

$$\int_0^{2\pi} d\phi \int_0^{\pi} \sin\theta d\theta (F_{1+}F_{2+} + F_{1\times}F_{2\times}) \quad . \tag{A}$$

This will then yield the best correlation measurement. There is no F_+F_x cross term because the correlation between the two polarizations of a stochastic, and randomly polarized background, is zero. In fact, the correlation of the output of the two detectors is independent of the polarization angle ψ for a stochastic, and randomly polarized background. This simplifies the calculation, for one may now set ψ equal to zero. This is equivalent to averaging over the angle ψ. Also, because F_+ and F_x range between +1 and –1 it is the extrema of equation (A) that signifies the ideal orientation, not just the maxima. It should be noted that there are four ideal orientations for these interferometers. A rotation of 90° about the detectors $\hat{z}$ axis does not change the amplitude of the response of a interferometric gravity wave antenna. Sometimes the extrema of equation (A) are found for the situation where the orientation of one of the detectors is fixed. It may happen that certain detector sites only allow a particular orientation. In this case the optimum orientation for the other detector must be found in accordance with this constraint.

Schutz and Tinto (1987) have calculated the optimum orientation of two detectors by a similar method. They search for the maxima in the function

$$\int_0^{2\pi} d\phi \int_0^{\pi} \sin\theta d\theta \int_0^{2\pi} d\psi\, F_{1+}^2 F_{2+}^2 \quad . \tag{B}$$

They claim that because F_+ and F_x can take on negative values the average represented by equation (A) is too seriously reduced. According to their reasoning, one should average the product of the squared output of the detectors. Also, they average over the polarization angle ψ, and therefore do not include the F_x terms. Their method is intended to maximize the common response of two detectors to bursts of randomly polarized gravity waves. When one averages over all incident directions it is equivalent to an average of a stochastic process. Schutz and Tinto (1987) also showed that the maximum of equation (B) can be related to the probability of a coincidence detection, where one averages over all detection thresholds for the two detectors.

I have carried out the computation represented by equations (A) and (B). I claim that they give identical results. An extrema for equation (A) corresponds to a maxima for equation (B). This is true for the case when both g_1 and g_2 need to be found, or when one of them is fixed and the other is unknown. This simplifies the calculation since equation (A) is easier to compute than equation (B). It is shown below that the two methods are equivalent.

The published paper, Schutz and Tinto (1987), does not give the optimum orientation of two detectors that are free to rotate when they are responding to an isotropic source of gravity waves. They do give values for the case where the coincidence detection probability is maximized for detecting gravity waves from a source in the Virgo cluster. The optimum solution to methods A and B are given in Figure 4.2 for the antenna location examples of the given in Schutz and Tinto (1987). Tinto and Gursel (1990) have also calculated the optimum orientation angles via method B. Their orientations agree with mine. This has confirmed the computer intensive solutions to equation (B).

Figure 4.2 gives the optimum values of g_1 and g_2 that I have found by searching for the extrema of equation (A), or the maximum of equation (B). The detector coordinates are the same as those used by Schutz and Tinto. The column marked longitude difference represents the value of detector 2's longitude (East) minus detector 1's longitude (East). It is only the difference in the longitudes, not the individual values, that effect the result. Schutz and Tinto express their result in terms of the angle α, which is the angle between the bisector of the interferometer, and the local east-west line. The angle α is related to my angle g by $\alpha = g + \pi/4$. Figure 4.2 also gives the normalized value of method A and B. What I call the normalized value of equations (A) and (B) is the value calculated for the coordinates given, divided by the maximum value that one gets when both detectors are perfectly aligned with one another, i.e., $a_1 = a_2$, $b_1 = b_2$, and $g_1 = g_2$.

Det. 1 latitude, degrees north.	Det. 2 latitude, degrees north.	Longitude differ-ence in degrees.	g1, in degrees.	g2, in degrees.	Eqn. (A) normal-ized.	Eqn. (B) normal-ized.
30	55	120	59.8	49.4	.513	.509
30	45	135	59.9	37.9	.503	.502
45	45	90	35.3	54.7	.625	.594
45	30	- 45	7.4	35.9	.809	.770

Figure 4.2 The optimum orientations for various interferometer pairs. The normalized solutions for equations (A) and (B) are also given for these calculated values of g_1 and g_2. The first pair of coordinates is supposed to approximate the Las Vegas, Nevada-Glasgow, Scotland detector pair, the second refers to Las Vegas-southern Germany, the third refers to Maine-southern Germany, while the fourth refers to Las Vegas-Maine.

Another way of examining the optimum orientation problem is through the use of contour plots. Schutz and Tinto (1987) presented a series of plots displaying their optimal solutions for a series of interferometer pairs. They did this for a fixed source location in the sky, the Virgo cluster, and for the case where one averages over all source directions. Figures 12(a) through 12(e) of Schutz and Tinto (1987) are the examples where they have integrated over all source directions. This would be their solution to equation (B). They have expressed their solution in terms of the angles, α_1 and α_2, which refer to the angle between a line that bisects the two arms of the interferometer, and the local east-west line. The angle α is related to my angle g by $\alpha = g + \pi/4$.

Figures 4.3 through 4.6 show my contour plots for the absolute value of the solution of equation (A). It is expressed in terms of the angles g1, and g2, that were defined above. Figure 4.3 corresponds with Figure 12(a) of Schutz and Tinto (1987). It considers an interferometer in Maine (45°N latitude) and Las Vegas

(30°N), where the longitudinal displacement is 45°. My optimal orientation occurs at g1=1.6998 + nπ/2, g2=2.19791 + nπ/2, where n is any integer.

Figure 4.4 corresponds with Figure 12(b) of Schutz and Tinto (1987). It considers an interferometer in Las Vegas (30°N latitude) and Glasgow, Scotland (65°N), where the longitudinal displacement is 120°. My optimal orientation occurs at g1=2.61416 + nπ/2, g2=2.4304 + nπ/2, where n is any integer.

Figure 4.5 corresponds with Figure 12(c) of Schutz and Tinto (1987). It considers an interferometer in Las Vegas (30°N latitude) and Bavaria, in Southern Germany (45°N), where the longitudinal displacement is 135°. My optimal orientation occurs at g_1=2.61616 + nπ/2, g2=2.2323 + nπ/2, where n is any integer.

Figure 4.6 corresponds with Figure 12(e) of Schutz and Tinto (1987). It considers an interferometer in Maine (45°N latitude) and Bavaria, in Southern Germany (45°N), where the longitudinal displacement is 90°. My optimal orientation occurs at g1=2.1863 + nπ/2, g2=.95532 + nπ/2, where n is any integer.

It should be noted that the general appearance of the contour plots is pretty much the same as for the plots displayed in Schutz and Tinto (1987). They used the equation (B), while I used equation (A). The location of extrema on the contour plots are the same.

It is also interesting to look at the case where the orientation of one of the detectors is fixed. A possible detector site may have local geographical constraints that only allow a certain orientation. This is the case for the possible detector site near Columbia, Maine. For this site the detector is required to have g_1 = 27°. I have calculated the optimum orientation for detectors in Southern California, Munich Germany, Glasgow Scotland, and Western Australia, if they are to have the maximum overlap with the antenna in Maine. The location and the coordinates are; Maine, with 45°N latitude, 67.5°W longitude; Southern California, with 36°N latitude, 115°W longitude; Glasgow , Scotland, with 56°N latitude, 5°W longitude; Munich , Germany, with 48°N latitude, 11.5°E longitude; and Western Australia, with 32°S latitude, 117°E longitude. The optimum orientations are given in Figure 4.7. The normalized solutions for equations (A) and (B) are also given.

Another interesting example to consider is the sensitivity of a system of three particular interferometers. These three locations are under serious consideration for the U.S. and the German sites (As of this time the decision on the location of

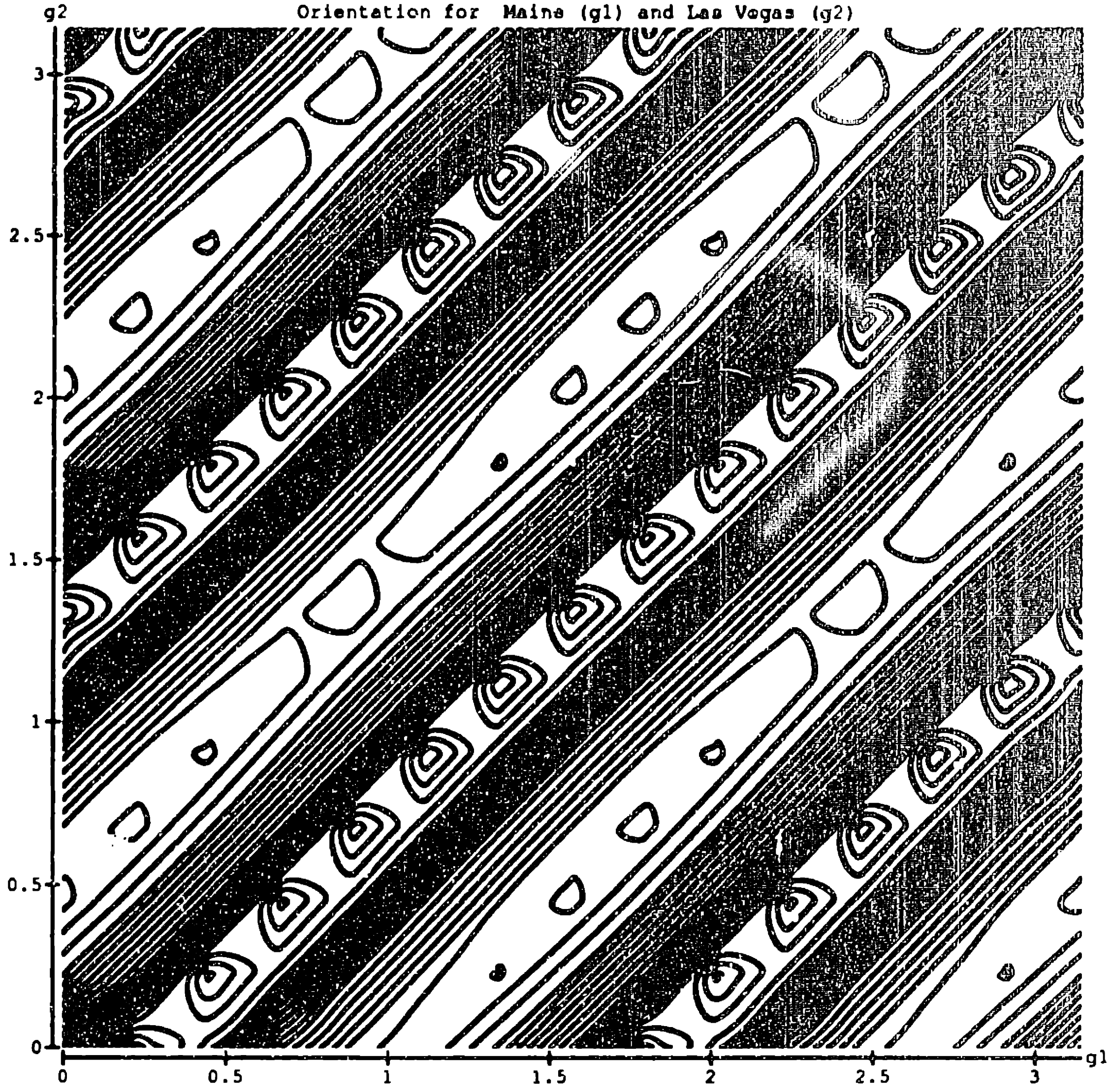

Figure 4.3 Contour plot of the absolute value of the solution of equation (A) for Maine (g1), and Las Vegas (g2). The angles, g1 and g2, are the number of radians between the interferometer's X axis and the local east-west meridian. The maxima of this plot occurs for g1=1.6998 + nπ/2, g2=2.19791 + nπ/2, where n is any integer. The maxima has a value of 4.07, and the difference in value between two neighboring contours is .163.

the actual sites have not been made). All three of these sites have geographical constraints that will limit the possible allowed orientations. The first interferometer is near Hanover, F.R.G. Its latitude is 52.50° N, longitude 9.75°E. The bisector of this interferometer, α_1, makes a 45° angle with the local east-west line, with the east direction defining the local X direction from which the angle

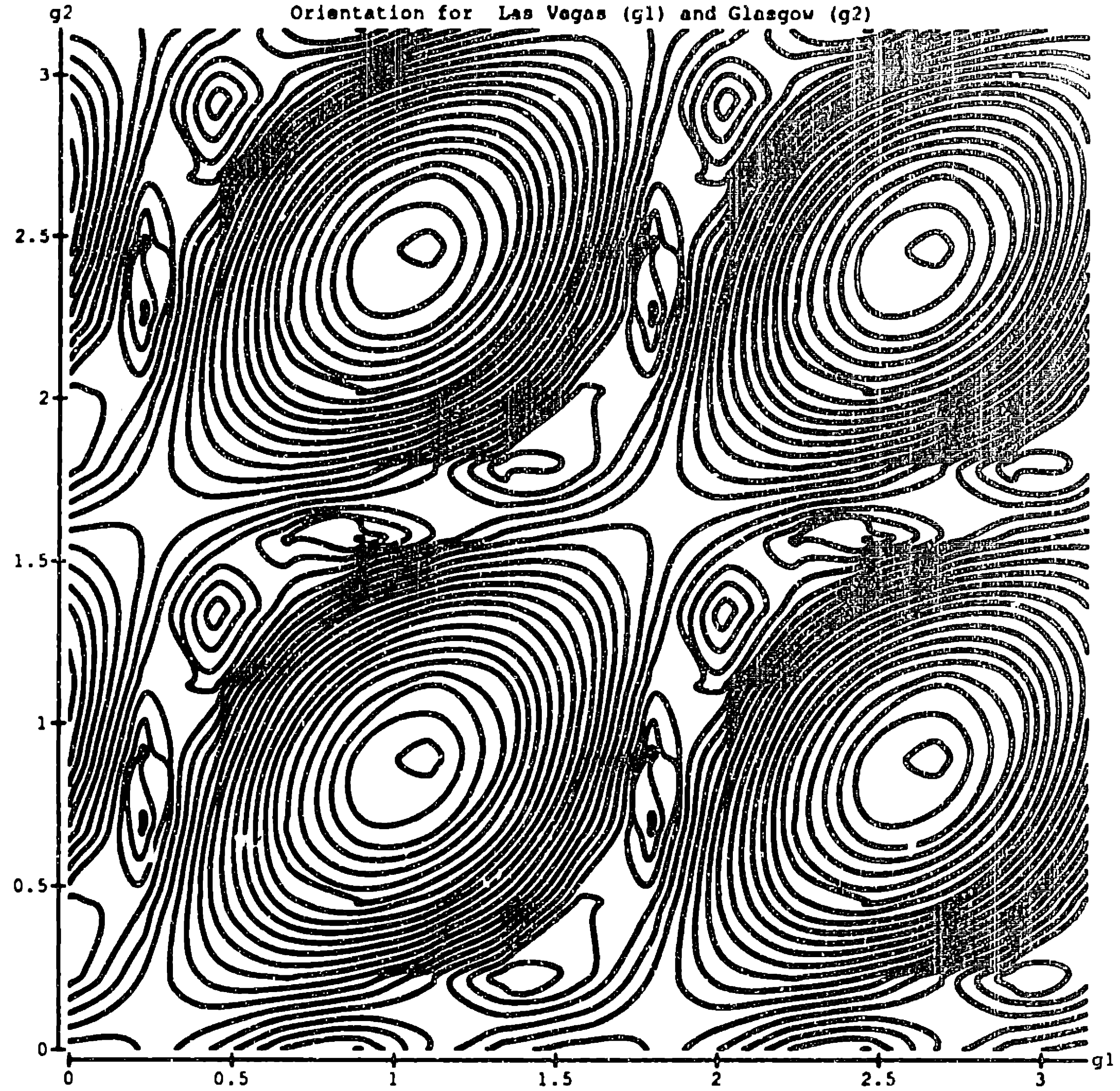

Figure 4.4 Contour plot of the absolute value of the solution of equation (A) for Las Vegas (g1), and Glasgow, Scotland (g2). The angles, g1 and g2, are the number of radians between the interferometer's X axis and the local east-west meridian. The maxima of this plot occurs for g1=2.61416 + $n\pi/2$, g2=2.4304 + $n\pi/2$, where n is any integer. The maxima has a value of 2.43, and the difference in value between two neighboring contours is .00972.

is measured. All bisector angles will be defined in this manner. The location of the Maine detector is 44.66°N, 67.85°W, with its bisector being constrained to an angle of 70.52° from the local east-west line. Owens Valley has latitude = 37°, 14', 28" N, longitude = 118°, 15', 53" W, with its bisector being constrained to an angle of 200° from the local east-west line.

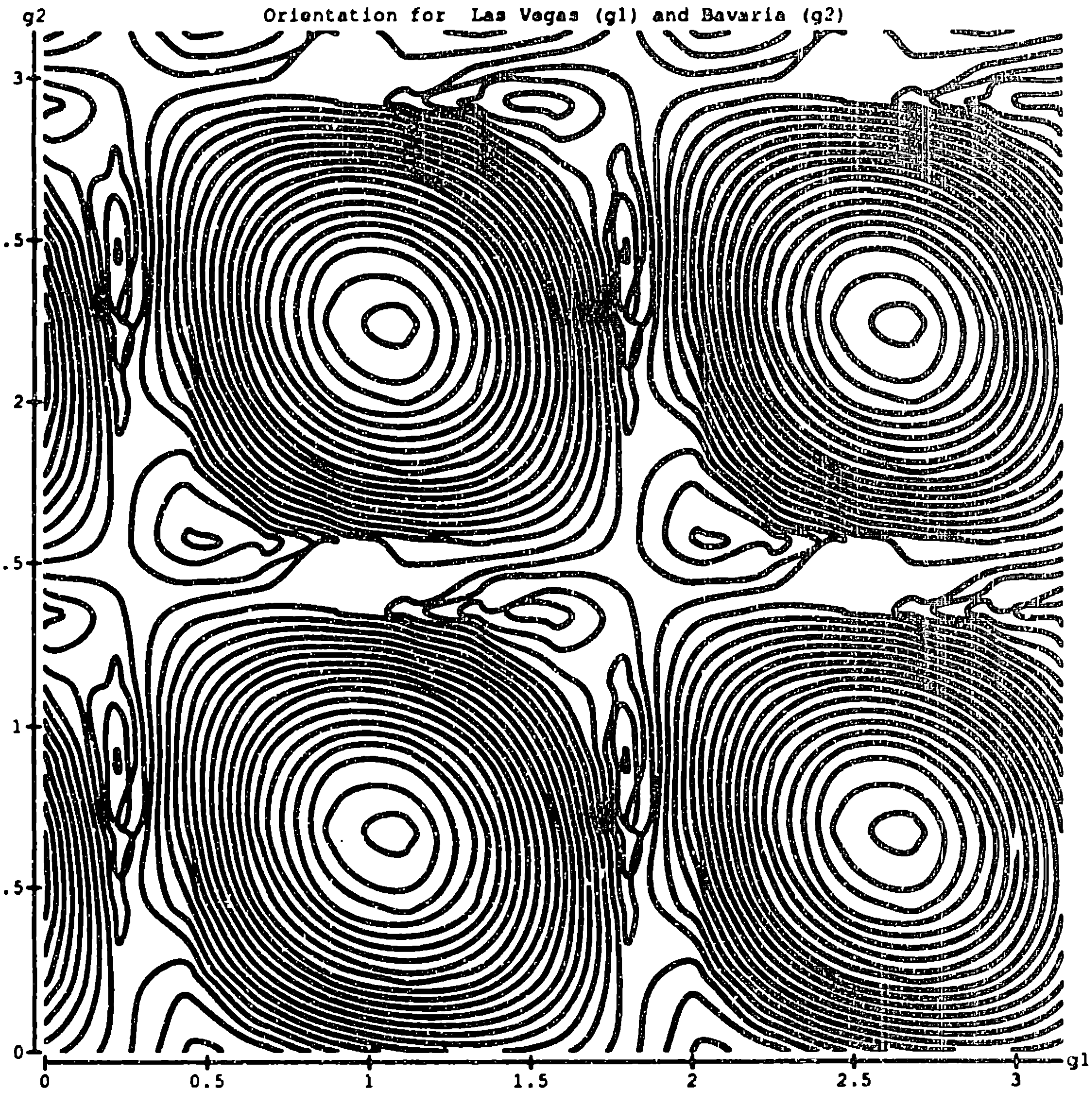

Figure 4.5 Contour plot of the absolute value of the solution of equation (A) for Las Vegas (g1), and Bavaria, Germany (g2). The angles, g1 and g2, are the number of radians between the interferometer's X axis and the local east-west meridian. The maxima of this plot occurs for $g1=2.61616 + n\pi/2$, $g2=2.2323 + n\pi/2$, where n is any integer. The maxima has a value of 2.53, and the difference in value between two neighboring contours is .101.

The first plot, Figure 4.8, considers the interferometer of fixed orientation in Hanover, and a detector in Maine. The best orientation for the Maine detector would be a bisector angle of .279 radians, or 16° from the local east axis. This would give a normalized solution for method A of .679, and a normalized solution for method B of .641.

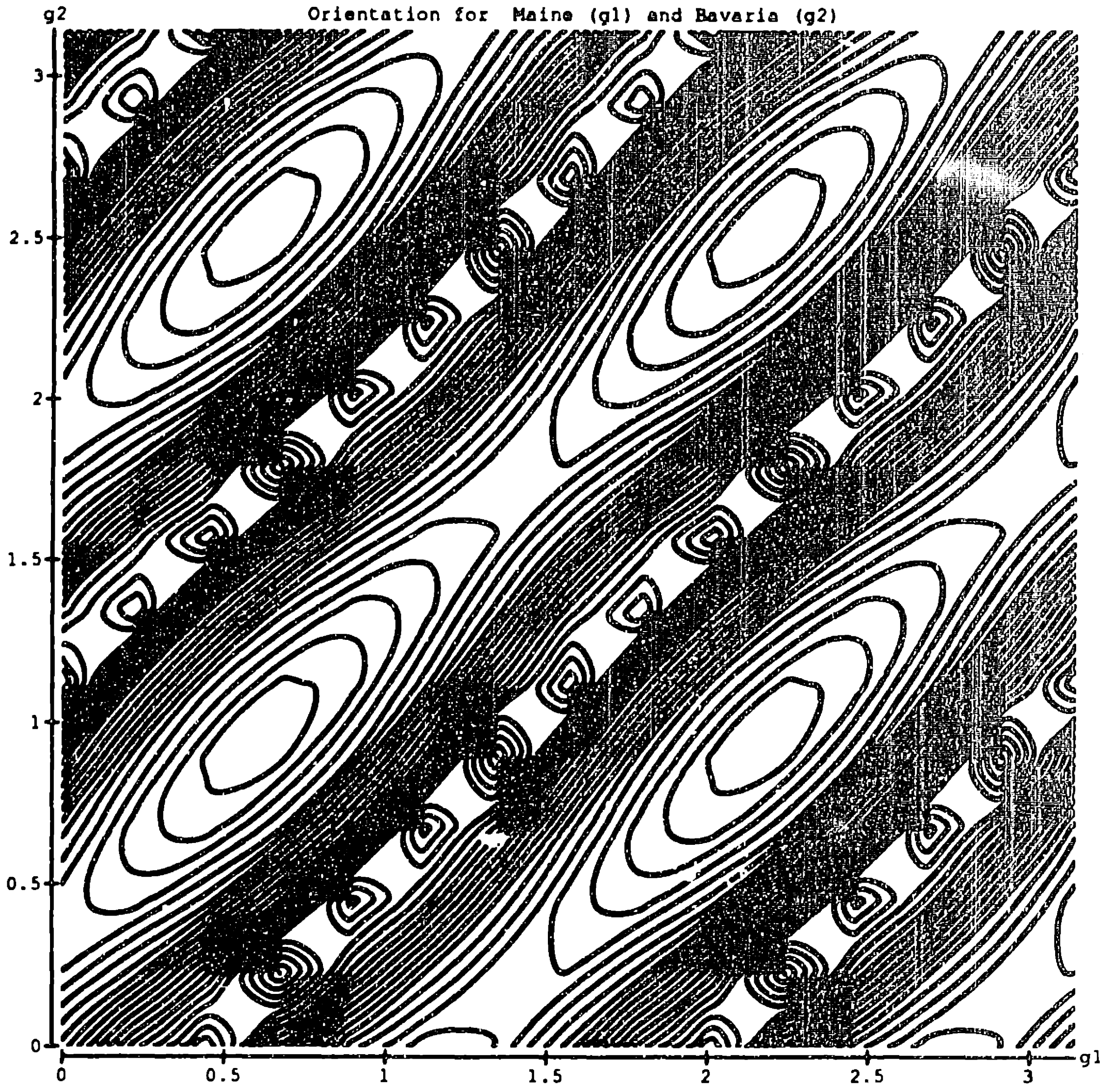

Figure 4.6 Contour plot of the absolute value of the solution of equation (A) for Maine (g1), and Bavaria, Germany (g2). The angles, g1 and g2, are the number of radians between the interferometer's X axis and the local east-west meridian. The maxima of this plot occurs for g1=2.1863 + nπ/2, g2=.95532 + nπ/2, where n is any integer. The maxima has a value of 3.14, and the difference in value between two neighboring contours is .126.

Figure 4.9 has the Maine interferometer fixed at an orientation of 70.52° for the angle between the bisector and the east-west line. The angle of the Hanover bisector is allowed to vary. The best orientation for the Hanover detector would be a bisector angle of 9.2° from the local east axis. This would give a normalized solution for method A of .700, and a normalized solution for method B of .660.

Site	g2 in degrees	Eqn. (A), value, normalized	Eqn. (B), value, normalized
Southern California	58.7	.807	.768
Munich, Germany	55.9	.686	.647
Glasgow, Scotland	67.0	.791	.751
Western, Australia	65.8	.973	.964

Figure 4.7 Optimum orientations for when the Maine interferometer is fixed at $g_1 = 27°$. The normalized values for equations (A) and (B) are also presented.

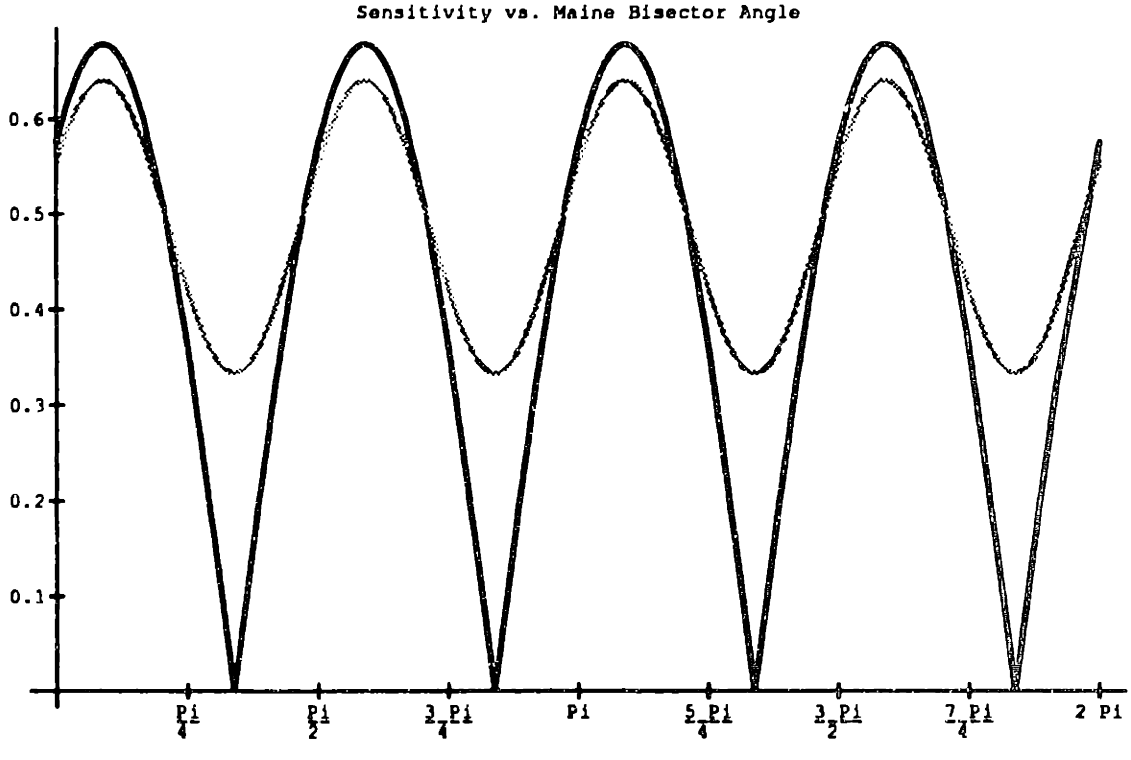

Figure 4.8 Normalized solution of method A (in black) and method B (in gray) versus bisector angle for Maine detector (in radians). The Hanover detector's orientation is fixed.

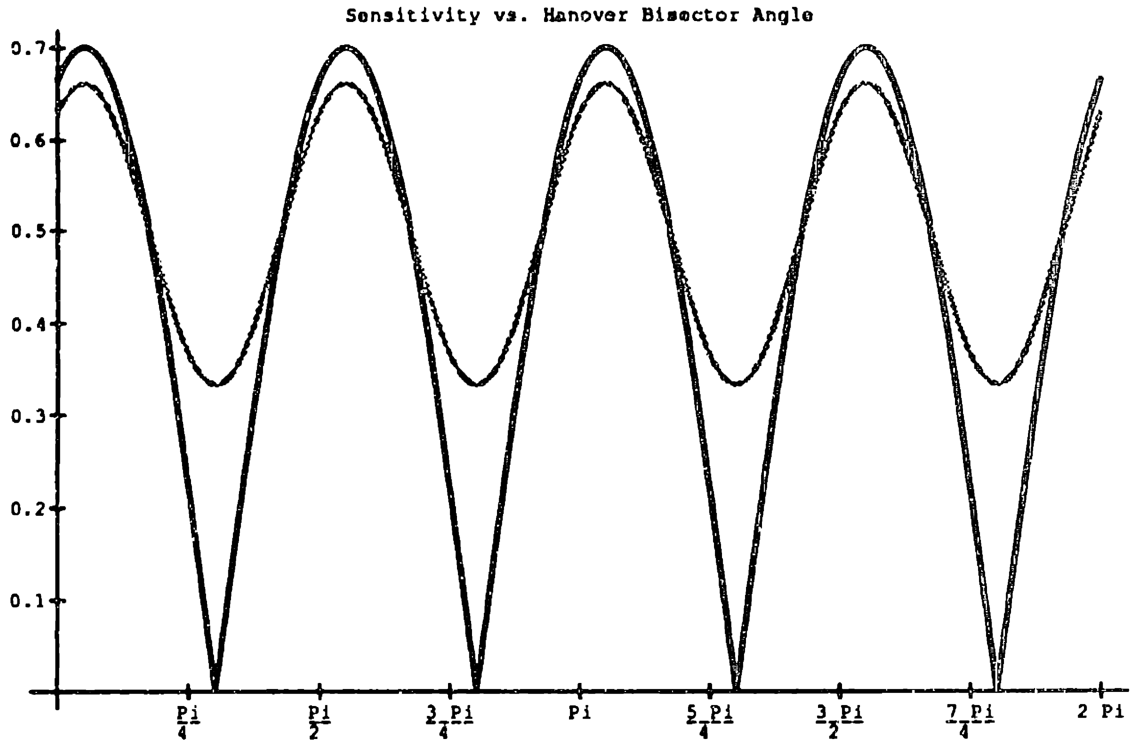

Figure 4.9 Normalized solution of method A (in black) and method B (in gray) versus bisector angle for the Hanover detector (in radians). The Maine detector's orientation is fixed.

The ultimate optimal orientation for the Maine-Hanover locations is: 83.47° for the Maine bisector; 21.18° for Hanover. This gives a normalized solution for method (A) of .712, and .671 for method (B). If the Maine interferometer had an orientation of 70.52° for its bisector angle, and Hanover had 45°, then the value given by method (A) would be only .221, while method (B) would have .366.

The Hanover, Owens Valley pair is considered next. Figure 4.10 has the Hanover detector fixed at an orientation of 45° for the angle between the bisector and the east-west line. The angle of the Owens Valley bisector is allowed to vary. The best orientation for the Owens Valley detector would be a bisector angle of 74.97°. This gives a normalized solution for method (A) of .203, and .342 for method (B).

Figure 4.11 has the Owens Valley interferometer fixed at an orientation of 200° for the angle between the bisector and the east-west line. The angle of the Hanover bisector is allowed to vary. The best orientation for the Hanover detector would be a bisector angle of 86.12° from the local east axis. This would

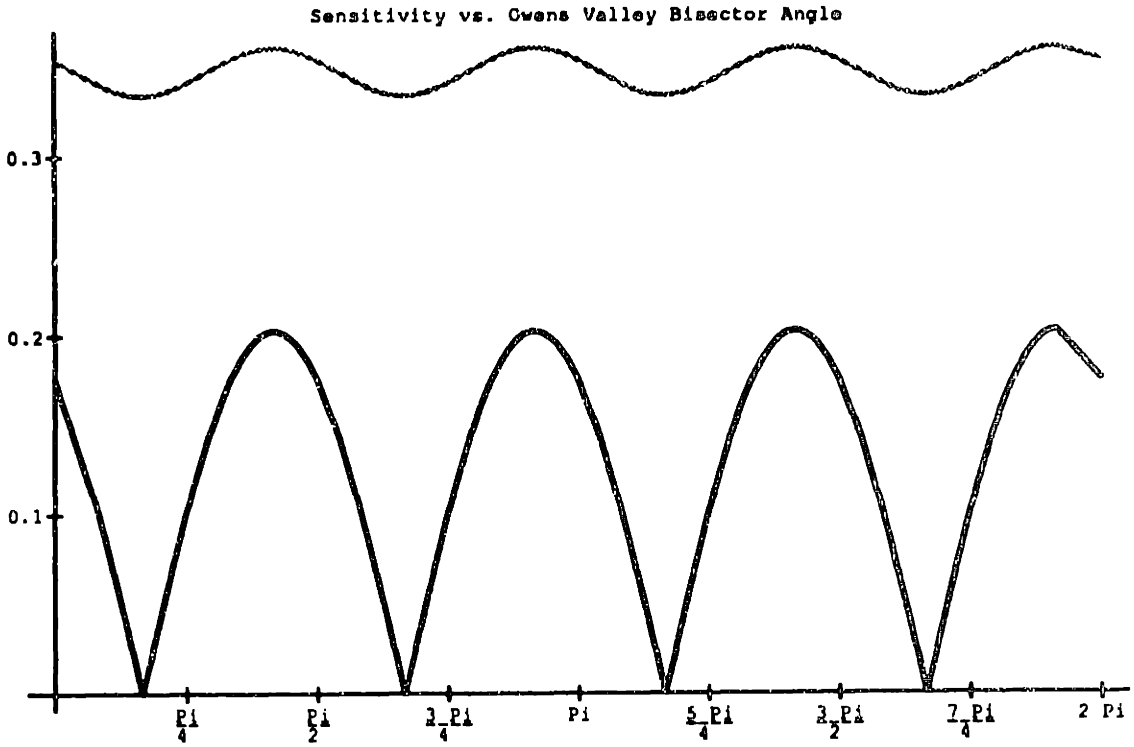

Figure 4.10 Normalized solution of method A (in black) and method B (in gray) versus bisector angle for the Owens Valley detector (in radians). The Hanover detector's orientation is fixed.

give a normalized solution for method (A) of .512, and a normalized solution for method (B) of .508.

The ultimate optimal orientation for the Owens Valley-Hanover locations is: 84.63° for the Owens Valley bisector; 15.81° for Hanover. This gives a normalized solution for method (A) of .517, and .511 for method (B). If the Owens interferometer had an orientation of 200° for its bisector angle, and Hanover had 45°, then the value given by method (A) would be only .069, while method (B) would give .337.

The Maine, Owens Valley pair is considered next. Figure 4.12 has the Maine detector fixed at an orientation of 70.52° for the angle between the bisector and the east-west line. The angle of the Owens Valley bisector is allowed to vary. The best orientation for the Owens Valley detector would be a bisector angle of 194.56°. This gives a normalized solution for method (A) of .790, and .750 for method (B). Note that the Hanover orientation severely limits its overlap between it and Owens Valley.

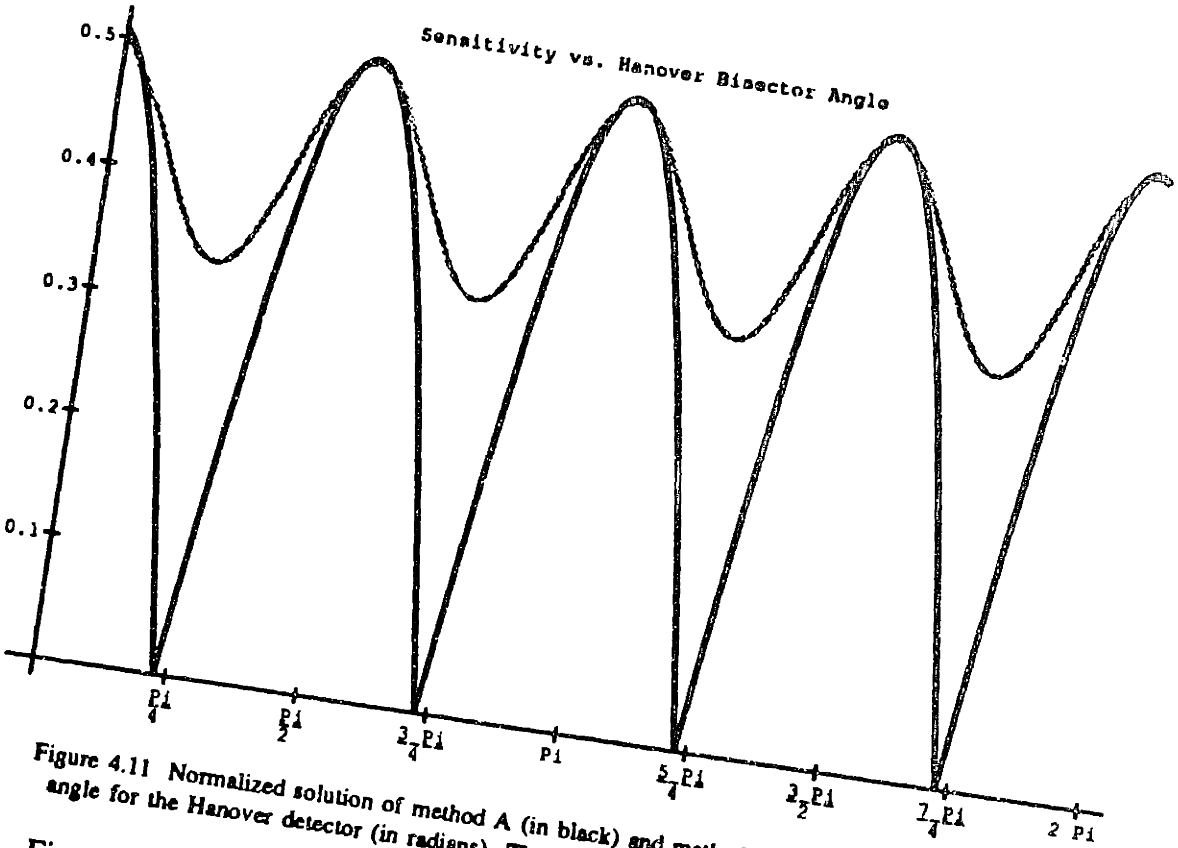

Figure 4.11 Normalized solution of method A (in black) and method B (in gray) versus bisector angle for the Hanover detector (in radians). The Owens Valley detector's orientation is fixed.

Figure 4.13 has the Owens Valley interferometer fixed at an orientation of 200° for the angle between the bisector and the east-west line. The angle of the Maine bisector is allowed to vary. The best orientation for the Maine detector would be a bisector angle of 75.4° from the local east axis. This would give a normalized solution for method (A) of .788, and a normalized solution for method (B) of .747.

The ultimate optimal orientation for the Owens Valley-Maine locations is: 72.49° for the Owens Valley bisector; 38.14° for Maine. This gives a normalized solution for method A of .809, and .770 for method B. If the Owens interferometer had an orientation of 200° for its bisector angle, and Maine had 70.52°, then the value given by method A would be only .776, while method B would have .735.

Section 4 Physical Explanation for Orientation

Finally, there is a nice physical picture for the optimum orientation of two

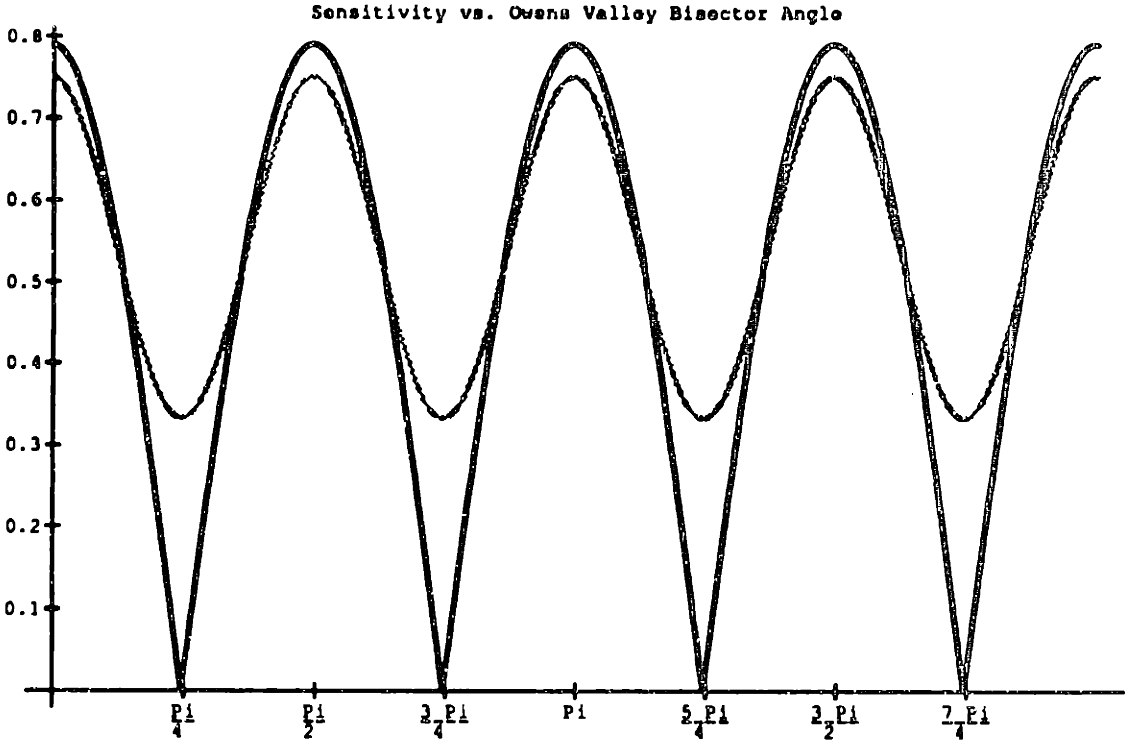

Figure 4.12 Normalized solution of method A (in black) and method B (in gray) versus bisector angle for the Owens Valley detector (in radians). The Maine detector's orientation is fixed.

interferometric detectors. When one finds values of g_1 and g_2 that correspond with an extrema for equation (A), or the maximum of equation (B), then one has the physical situation where one arm of each interferometer points along the great circle that connects the centers of the each interferometer, while the other arms are parallel to each other. Using this method one can easily find the optimum orientation of two detectors located at different points on the earth. In the earth centered coordinate system, the unit vector that defines the detector's $\hat{x}$ direction is

$$\widehat{e^{(x)}} = \{\cos a \cos g - \cos b \sin a \sin g, \sin a \cos g + \cos a \cos b \sin g, \sin b \sin g\} .$$

Therefore, the optimum orientation is that in which the $\hat{x}$ direction for detector one is parallel to the $\hat{x}$ for detector two. Mathematically, this is the same as

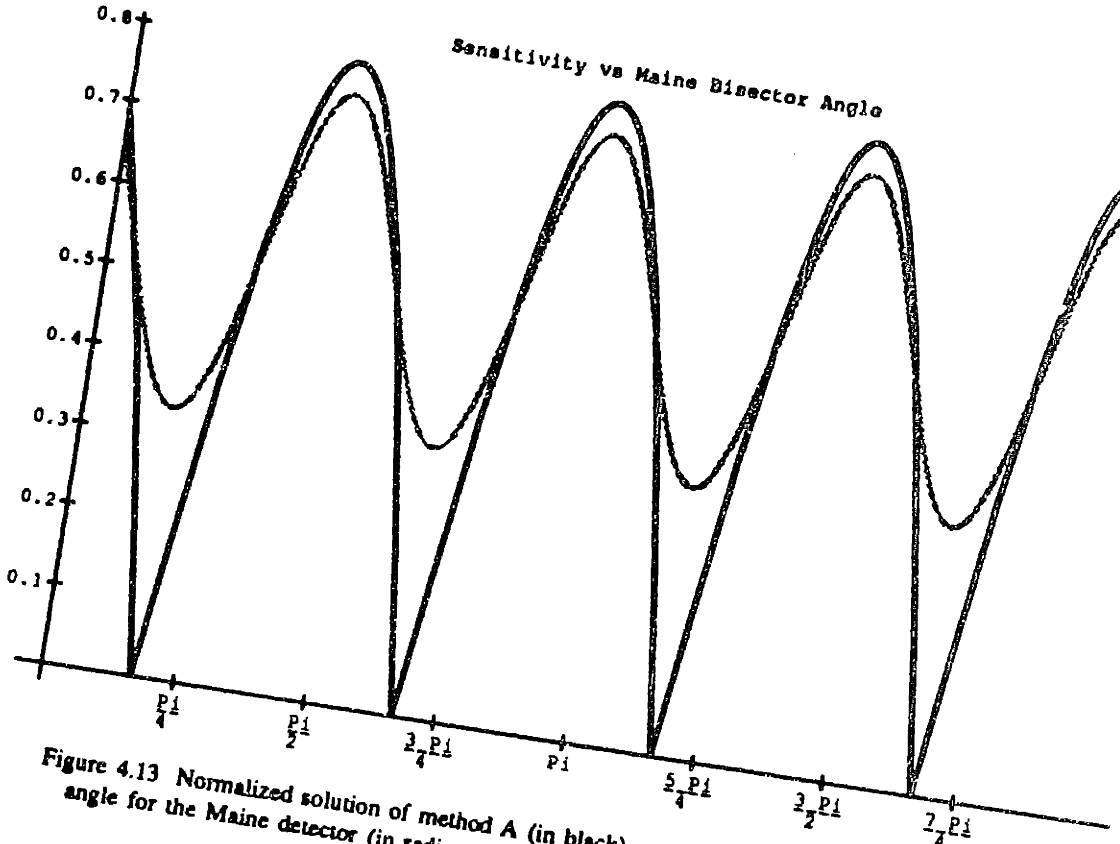

Figure 4.13 Normalized solution of method A (in black) and method B (in gray) versus bisector angle for the Maine detector (in radians). The Owens Valley detector's orientation is fixed.

demanding that

$$\begin{aligned}(\cos a_1 \cos g_1 - \cos b_1 \sin a_1 \sin g_1)(\cos a_2 \cos g_2 - \cos b_2 \sin a_2 \sin g_2)+\\ (\sin a_1 \cos g_1 + \cos a_1 \cos b_1 \sin g_1)(\sin a_2 \cos g_2 + \cos a_2 \cos b_2 \sin g_2)+\\ \sin g_1 \sin b_1 \sin g_2 \sin b_2 \quad = \quad 1 \end{aligned} \qquad (C)$$

This method only works for the case when g_1 and g_2 are free to change. If one of the orientations is fixed, then maximizing equation (C), as opposed to equating it with one, does not give the same value for the orientation of the other detector as would the methods associated with equations (A) and (B).

In fact, the great circle connecting the two sites defines a nice coordinate system that makes the solutions to equations (A) and (B) trivial. Consider the scenario where

$$a_1 = b_1 = g_1 = 0 \quad , and, \quad a_2 = a, \quad b_2 = b, \quad g_2 = g \quad .$$

The solution to equation (A), normalized to the case where the two interferometers are aligned at the same location, is

$$S_A = \frac{1}{2}\left(1+\cos^2 b\right)\cos 2a \cos 2g - \cos b \sin 2a \sin 2g \quad .$$

The normalized solution to method (B) is

$$S_B = \frac{1}{3}\left[1 + 2\left\{\frac{1}{2}\left(1+\cos^2 b\right)\cos 2a \cos 2g - \cos b \sin 2a \sin 2g\right\}^2\right]$$
$$= \frac{1}{3}\left[1 + 2S_A^2\right] \quad .$$

The local direction of the geodesic can be found by the method described above. That solution yielded the angles g_1 and g_2 when the $\hat{x}$ arms of the two detectors are parallel. Therefore, $g_1 + \pi/2$ and $g_2 + \pi/2$ are the angles between the great circle and the local east-west line. The now defined great circle direction will define the new coordinate system. Call the angle between the $\hat{x}$ arm of detector #1 and the great circle η_1, and the angle between the $\hat{x}$ arm of detector #2 and the great circle η_2. Also, call the angle between the interferometer bisector of detector #1 and the great circle ψ_1, and the angle between the interferometer bisector of detector #2 and the great circle ψ_2. See Figure 4.14.

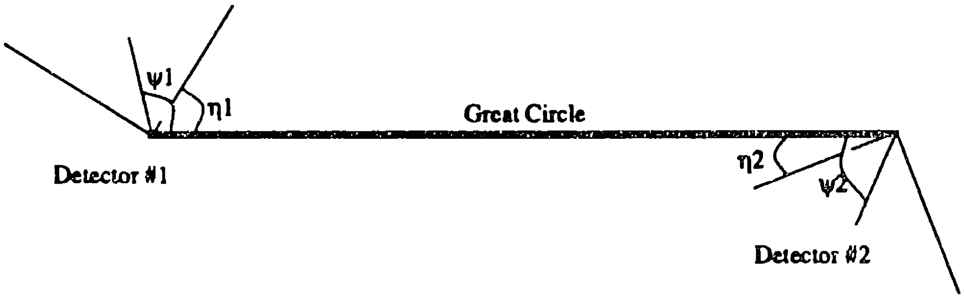

Figure 4.14 Definition of the angles for the two detectors with respect to the great circle. The angle η is between the great circle and the $\hat{x}$ arm of the detector, while ψ is the angle between the great circle and the interferometer's bisector.

The solution, S_A, given above can be expressed in terms of these angles. One needs to make the substitutions

$$\eta_1 = a, \quad \psi_1 = a + \pi/4, \quad \eta_2 = g - \pi/2, \quad \psi_2 = g - \pi/4 \quad .$$

The result is

$$\begin{aligned} S_A &= -\frac{1}{2}(1+\cos^2 b)\cos 2\eta_1 \cos 2\eta_2 + \cos b \sin 2\eta_1 \sin 2\eta_2 \\ &= -\frac{1}{2}(1+\cos^2 b)\sin 2\psi_1 \sin 2\psi_2 + \cos b \cos 2\psi_1 \cos 2\psi_2 \quad . \end{aligned}$$

The solution for method B, S_B, is found from S_A by

$$S_B = \frac{1}{3}(1 + 2S_A^2) \quad .$$

From this one can see why methods A and B give the same results.

When both interferometers have the optimum alignment, with each having one arm point along the great circle connecting the two locations, then normalized solutions for methods A and B only depend on the azimuthal angle between them. This angle, which I'll call β, is given by

$$\beta = \arccos\left[\cos b_1 \cos b_2 + \sin b_1 \sin b_2 \cos(a_1 - a_2)\right] \quad .$$

The normalized general solution for method A is

$$\frac{1}{2}(1 + \cos^2 \beta) \quad .$$

The normalized general solution for method B is

$$\frac{1}{3}\left[1 + \frac{\left(1+\cos^2\beta\right)^2}{2}\right] \quad .$$

A plot of these two solutions are given in Figure 4.17. Method A in black, method B in gray.

Section 5 Single Interferometer Response

The measured rms response of a single interferometer to a randomly polarized gravity wave is

$$y = h_0\sqrt{F_+^2 + F_\times^2} \quad ,$$

where h_0 is the amplitude of the wave, and F_+ and $F_\times$ are defined above. This response is a function of the incident direction of the gravity wave, which is

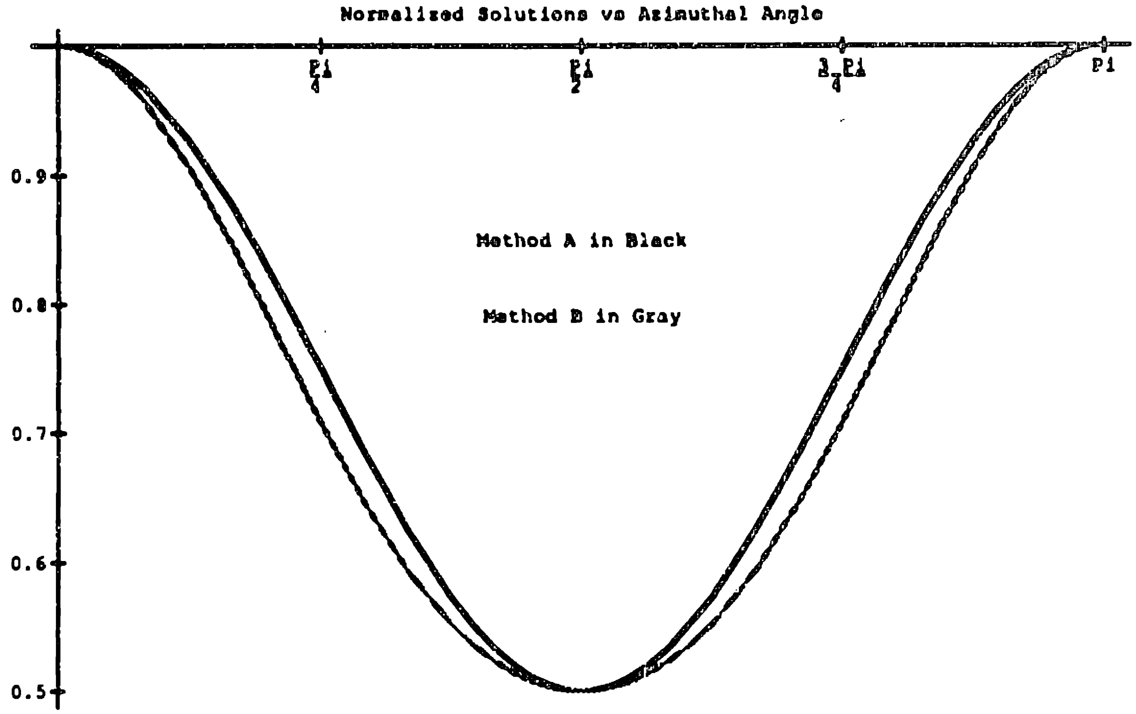

Figure 4.15 Normalized solution of method A (in black) and method B (in gray) versus azimuthal angle (in radians). Both methods give a value of 1 at β=0, or π, and a value of .5 at b=π/2.

defined by the two angles θ and ϕ. Figure 4.17 displays the response of the interferometer to waves from all directions. If the arms of the interferometer lie along the square drawn in the figure, then the response is given by the distance between the center of the drawing and the surface. Note that the response is zero for $\theta = \pi/2$ and $\phi = \pi/4$. This will be a blind spot for the detector. Otherwise, the antenna has virtual isotropic coverage of the sky.

Section 6 Conclusion

This chapter has considered three methods for finding the optimum orientation of two interferometers. Method A was developed because it directly relates to the correlated output of two detectors that are both responding to a stochastic gravity wave background. This is also equivalent to optimizing the mutual response of the two detectors to a randomly polarized burst of gravity waves, where one assumes that the bursts are isotropically distributed on the sky. Schutz and Tinto (1987)

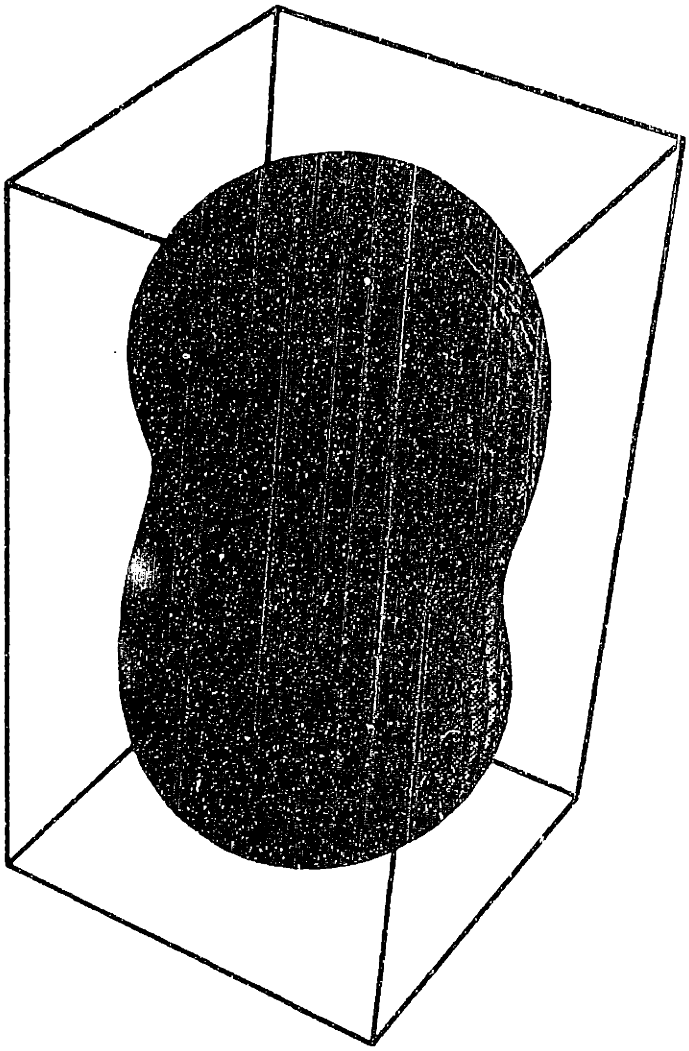

Figure 4.16 Response of an interferometer to randomly polarized gravity waves from all directions. The arms of the antenna are assumed to be parallel to two of the sides of the square drawn. The response is given by the distance between the center of the drawing and the surface. A single detector has little directional capability, as can be seen in this figure.

have shown that the maximum of equation (B) can be related to the probability of a coincidence detection, where one averages over all detection thresholds for the two detectors. I have shown how these two methods give the same results. See appendix C for the exact solutions of these functions.

Method C offers the most intuitive solution for detector alignment. Given two locations anywhere on the surface of the earth it is possible to align the two interferometers such that each one has one arm parallel to an arm in the other. When this is the case the other arms point along the great circle defined by the two locations.

Chapter 5 Two Detector Problem

Section 1 Introduction

This chapter presents the general solution for the correlation of the output of two arbitrary interferometric gravitational radiation antennas, and how it is to be related to a stochastic gravity wave background. The solution is general in that the individual interferometers can have any transfer function, they can be located at any site on the surface of the earth, they can have any orientation at these sites, and their intrinsic noise spectral density may take any shape.

Section 2 Stochastic Gravitational Wave Background

The first question to be addressed is, what is a stochastic gravitational wave background (SGWB)? That can only be answered if one knows what a stochastic process is. From the definition of Bendat (1958), a stochastic process is an ensemble of functions, $\{{}^{k}x(t)\}$, where t ranges over all time, and k labels the particular member of the ensemble, such that the ensemble can be described by statistical properties. It is a random process. A random process is called a stationary random process when all the statistical properties of the process are independent of time. A stationary random process can be called ergodic if an average at a specific time of the different ensemble members can be replaced by a time average of a single member of that ensemble.

The gravitational radiation background that is examined in this thesis is assumed to be stochastic, stationary, and ergodic. It can be expressed as a Fourier transform, namely,

$$h_{ij}(\vec{\mathrm{x}},\mathrm{t}) = \int \frac{d^3\vec{\mathbf{k}}}{2\eta}[e^{i(\vec{\mathbf{k}}\cdot\vec{\mathrm{x}}-\eta \mathrm{t})}\{\widetilde{h_+}\left(\hat{\mathbf{k}},\eta\right)\mathrm{e}^{+}_{\mathrm{ij}}\left(\hat{\mathbf{k}},\eta\right)$$
$$+\widetilde{h_\times}\left(\hat{\mathbf{k}},\eta\right)\mathrm{e}^{\times}_{\mathrm{ij}}\left(\hat{\mathbf{k}},\eta\right)\} + \mathrm{C.C.}] \quad .$$

The form of this expression is explained in appendix A. The angular frequency of the wave is η (Note the difference in this chapter). The $\tilde{h}$ terms are the Fourier transforms of $h_{ij}(\vec{\mathrm{x}},\mathrm{t})$ for each polarization. They are assumed to be stochastic random variables. Also, it is assumed that the component $\widetilde{h_+}\left(\hat{\mathbf{k}},\eta\right)$

is uncorrelated with any other $\widetilde{h_+}\left(\hat{\mathbf{k}}',\eta'\right)$, unless $\vec{\mathbf{k}} = \vec{\mathbf{k}}'$. We can express this formally as

$$< \widetilde{h_+}\left(\hat{\mathbf{k}},\eta\right)\widetilde{h_+}\left(\hat{\mathbf{k}}',\eta'\right) \underset{av}{>}= \left|\widetilde{h_0}(\eta)\right|^2 \delta^{(3)}\left(\vec{\mathbf{k}}-\vec{\mathbf{k}}'\right)$$

$$and,$$

$$< \widetilde{h_\times}\left(\hat{\mathbf{k}},\eta\right)\widetilde{h_\times}\left(\hat{\mathbf{k}}',\eta'\right) \underset{av}{>}= \left|\widetilde{h_0}(\eta)\right|^2 \delta^{(3)}\left(\vec{\mathbf{k}}-\vec{\mathbf{k}}'\right) \quad .$$

The magnitude of the two polarization terms are the same. Also, it was assumed here that the background is isotropic. The terms

$$e^+_{ij}\left(\hat{k}\right) \quad , \; and, \; e^\times_{ij}\left(\hat{k}\right)$$

are the polarization tensors for a wave coming from the $\hat{k}$ direction. It is assumed that for a given $\hat{k}$, the two polarization states are uncorrelated. The background is randomly polarized. This can be expressed as

$$< \widetilde{h_+}\left(\hat{\mathbf{k}},\eta\right)\widetilde{h_\times}\left(\hat{\mathbf{k}},\eta\right) \underset{av}{>}= 0 \quad .$$

Also, for the way the angles have been defined in chapter 4, the wave vector of the gravitational wave is

$$\vec{k} = \frac{\eta}{c}(\sin\phi\sin\theta, -\cos\phi\sin\theta, \cos\theta) \quad .$$

Section 3 The Measurable Quantities

The first measurable quantity to consider is the output of the interferometric gravity wave antenna. What is detected is the change in the intensity of the output laser light due to a phase difference of the light in each arm of the interferometer. The interferometer is typically operating on a dark fringe, so in the absence of a gravity wave, the output light intensity is zero. When a traveling gravity wave of angular frequency η passes through the interferometer a beam of laser light with components of angular frequency $\eta+\omega$ and $\eta-\omega$, where ω is the angular frequency of the input laser light, will be produced. The measurable will be the output electric field of the exiting laser beam. This exiting electric field will be defined as $z^* E_0$, where E_0 is the electric field of the laser light that enters the interferometer. The explicit expressions for the electric fields for different interferometer schemes are given in chapter 3. Then the output of interferometer one, at time t and location $\vec{x}_1$, due to the gravity wave $h_{ij}(\vec{x},t)$, is

$$z_1(t) = \int \frac{d^3\vec{k}}{2\eta}[e^{i(\vec{k}\cdot\vec{x}_1-\eta t)}\{\tilde{h}_+(\hat{k},\eta)\, S_+(\hat{k},\eta) \\ + \tilde{h}_\times(\hat{k},\eta)\, S_\times(\hat{k},\eta)\} \ + \ C.C.] \quad .$$

This quantity is real. The terms S_+ and S_x are the transfer functions for the interferometer to the two polarizations of gravity waves of angular frequency Ω and coming from direction $\hat{k}$. These terms are derived for specific interferometer schemes in chapter 3.

As described in chapter 3, every plus and cross polarization transfer function can be written in the form

$$S_+\left(\hat{k},\eta\right) = B(\eta)[AR_x - CR_y]\frac{\eta l}{2c}$$
$$S_\times\left(\hat{k},\eta\right) = B(\eta)[BR_x - DR_y]\frac{\eta l}{2c} \quad .$$

The term $B(\eta)$ is one half the transfer function for a gravity wave approaching the interferometer at normal incidence, when the polarization is optimal. As noted in chapter 3, the terms R_x and R_y depend on the frequency and the direction of the gravity wave. However, the terms $R_x\frac{\eta l}{2c}$ and $R_y\frac{\eta l}{2c}$ are virtually constant at a value of one for the frequency range at which the interferometers will be operating.

In terms of all these quantities, it is possible to express the correlation of the output of two gravity wave interferometers located at $\vec{x}_1$ and $\vec{x}_2$, with a time delay τ, as

$$\langle z_1(t)z_2(t+\tau)\rangle_{av} = \left\langle\left(\left(\int \frac{d^3\vec{k}}{2\eta}\{e^{i(\vec{k}\cdot\vec{x}_1-\eta t)}B_1(\eta)\frac{\eta l_1}{2c}\right.\right.\right. \\ \left.\times\left(\{A_1R_{z1} - C_1R_{y1}\}\hat{h}_+\left(\vec{k}\right) + \{B_1R_{x1} - D_1R_{y1}\}\hat{h}_\times\left(\vec{k}\right)\right)\right) \\ \times\left(\int \frac{d^3\vec{k}'}{2\eta'}\{e^{i(\vec{k}'\cdot\vec{x}_2-\eta'\{t+\tau\})}B_2(\eta')\frac{\eta' l_2}{2c}\right. \\ \left.\left.\times\left(\{A_2R_{x2} - C_1R_{y2}\}\hat{h}_+\left(\vec{k}'\right) + \{B_2R_{x2} - D_2R_{y2}\}\hat{h}_\times\left(\vec{k}'\right)\right)\right)\right\rangle_{av}$$

This is quite a cumbersome equation. It can be reduced to a single $d^3\vec{k}$ integral by using the fact that

$$< \widetilde{h_+}\left(\hat{\mathbf{k}},\eta\right)\widetilde{h_+}\left(\hat{\mathbf{k}}',\eta'\right) \underset{av}{>}= \left|\tilde{h}_0(\eta)\right|^2 \delta^{(3)}\left(\vec{\mathbf{k}}-\vec{\mathbf{k}}'\right)$$

and,

$$< \widetilde{h_\times}\left(\hat{\mathbf{k}},\eta\right)\widetilde{h_\times}\left(\hat{\mathbf{k}}',\eta'\right) \underset{av}{>}= \left|\tilde{h}_0(\eta)\right|^2 \delta^{(3)}\left(\vec{\mathbf{k}}-\vec{\mathbf{k}}'\right) \ .$$

When this is done one is still left with an equation that lacks physical terms that are easy to comprehend. The correlation of the output of two interferometers should be related to the physical characteristics of the gravity waves. One particularly important property is the energy density of this background. It is given by

$$T_{00} = \int_0^\infty \rho_g(\eta)d\eta = \int_0^\infty \rho_g(f)df = \frac{c^2}{32\pi G} < \sum_{i,j} \frac{\partial h_{ij}}{\partial t}\frac{\partial h_{ij}}{\partial t} \underset{av}{>}$$

(Misner, Thorne, and Wheeler, 1973). A related useful quantity is the ratio of the energy density per unit logarithmic interval of frequency to the critical energy density of the universe,

$$\Omega_{gw}(f) = \frac{1}{\rho_c}\frac{dT_{00}}{d\,ln(f)} = \frac{f\rho_g(f)}{\rho_c} \ .$$

(The ratio of the energy density of the gravity wave background per unit logarithmic interval of frequency to the critical energy density of the universe will be expressed as $\Omega_{gw}(f)$, while the angular frequency of the wave is η.) Finally, the variance of the gravity waves is defined to be

$$h^2_{rms} =< \sum_{i,j} h_{ij}h_{ij} \underset{av}{>}= \int_0^\infty df S_h(f) \quad ,$$

where $S_h(f)$ is the spectral density of the waves. Using the statistical averages, the correlation is simplified to

$$\langle z_1(t)z_2(t+\tau)\rangle_{av} = \int_0^\infty \frac{d\eta G\rho_g(\eta)}{c^2\eta^2} \int_0^{2\pi} d\phi \int_0^\pi \sin\theta d\theta \Big[e^{i\left(\vec{k}\cdot(\vec{x}_1-\vec{x}_2)+\eta\tau\right)}$$
$$\times\left(\frac{\eta}{2c}\right)^2 l_1 l_2 \Big\{ (A_1R_{x1} - C_1R_{y1})(A_2R^*_{x2} - C_2R^*_{y2})B_1(\eta)B^*_2(\eta) +$$
$$(B_1R_{x1} - D_1R_{y1})(B_2R^*_{x2} - D_2R^*_{y2})B_1(\eta)B^*_2(\eta)\Big\} + \ C.C.\Big].$$

The energy density can be related to the spectral density of the wave by

$$\rho_g(f) = \frac{\pi c^2 f^2}{8G} S_h(f) \quad .$$

This is the general expression relating the correlation of the output of any two interferometric antennas to the energy density of the SGWB, or to its variance. All of the quantities in the expression for $\langle z_1 z_2 \rangle_{av}$ are known, except for the size and spectrum of the SGWB.

Section 4 Practical Solution

The expression for $\langle z_1 z_2 \rangle_{av}$ can be simplified by noting that for the range of frequencies in which the LIGO system will be operating, from about 50 Hz to 10,000 Hz, the terms $R_x \frac{\eta l}{2c}$ and $R_y \frac{\eta l'}{2c}$ are virtually constant at one. The most extreme variation is at 10 KHz, where at certain angles, θ and ϕ, these terms can decrease to about .97. On top of this, the search for the SGWB will likely concentrate on frequencies below 1 KHz, where the variation of these terms is far less. Knowing this, the correlation can be simplified to

$$\langle z_1(t) z_2(t+\tau) \rangle_{av} = \int_0^\infty \frac{d\eta G \rho_g(\eta)}{c^2 \eta^2} \int_0^{2\pi} d\phi \int_0^\pi \sin\theta d\theta \Big[\Big\{ (A_1 - C_1)(A_2 - C_2) +$$
$$(B_1 - D_1)(B_2 - D_2) \Big\} \Big(e^{i(\vec{k}\cdot(\vec{x}_1 - \vec{x}_2) + \eta\tau)} B_1(\eta) B_2^*(\eta) +$$
$$e^{-i(\vec{k}\cdot(\vec{x}_1 - \vec{x}_2) + \eta\tau)} B_1^*(\eta) B_2(\eta) \Big) \quad .$$

The LIGO system is to be built with identical interferometers at each antenna location. The transfer functions of the two systems will be identical. In this case, the correlation reduces to

$$\langle z_1(t) z_2(t+\tau) \rangle_{av} = \int_0^\infty \frac{d\eta 2G \rho_g(\eta) |B(\eta)|^2}{c^2 \eta^2} \int_0^{2\pi} d\phi \int_0^\pi d\theta \sin\theta \times$$
$$\Big[\Big\{ (A_1 - C_1)(A_2 - C_2) + (B_1 - D_1)(B_2 - D_2) \Big\} \cos\Big[\Big(\vec{k}\cdot(\vec{x}_1 - \vec{x}_2) + \eta\tau \Big) \Big]$$
$$= \int_0^\infty \frac{d\eta 8G \rho_g(\eta) |B(\eta)|^2}{c^2 \eta^2} \int_0^{2\pi} d\phi \int_0^\pi \sin\theta d\theta \Big[(F_{1+} F_{2+} + F_{1\times} F_{2\times}) \times$$

$$\cos\left[\left(\vec{k}\cdot(\vec{x}_1-\vec{x}_2)+\eta\tau\right)\right]\Bigg]$$

$$= \int_0^\infty \frac{d\eta 8G\rho_g(\eta))|B(\eta)|^2}{c^2\eta^2}\gamma(\vec{x}_1,\vec{x}_2,\eta,\tau) \quad , \qquad where$$

$$\gamma(\vec{x}_1,\vec{x}_2,\eta,\tau) = \int_0^{2\pi} d\phi \int_0^{\pi} \sin\theta d\theta\Big[(F_{1+}F_{2+} + F_{1\times}F_{2\times})\times$$

$$\cos\left[\left(\vec{k}\cdot(\vec{x}_1-\vec{x}_2)+\eta\tau\right)\right].$$

Notice that all the angular dependent terms are within γ, as it contains all the information about the relative separation and orientation of the two antennas. The F terms are defined and explained in chapter 4. The value of $|\gamma|$ will range from an ideal value of $(8\pi/5)$, to the worst case, zero.

Section 5 Noise

The correlation measurement for the interferometers will be complicated by the intrinsic noise of each antenna. There are a number of factors that will contribute. A quick summary of the more dominant terms is presented here. A more detailed description of the noise sources of an interferometric antenna can be found in Dewey (1986), Livas (1987), Weiss (1979), or the LIGO proposal (Vogt, 1989). The noise numbers given below are the estimates for the LIGO system.

At low frequencies the interferometer will be limited by seismic noise that passes, albeit filtered, through the masses' isolation system. The ground motion at the detector site will be around

$$x(f) = 10^{-5}\left(\frac{1Hz}{f}\right)^2 cm/\sqrt{Hz} \ , \ for \ \ f > 10Hz \ .$$

The proposed isolation system will consist of a five layer stack of springs and masses, followed by a wire suspension supporting the mass. The gravity wave sensitivity for the proposed four kilometer antenna would then be

$$h(f) = 5\times 10^{-11}\left(\frac{1Hz}{f}\right)^4\left(\frac{7Hz}{f}\right)^{10}/\sqrt{Hz} \ .$$

Another important noise source will be the thermal noise caused by the mechanical losses of the pendular component of the suspension. For frequencies above the resonance of the pendulum, f_0, the noise will be

$$h(f) = \frac{1}{l}\sqrt{\frac{kTf_0}{mQ\pi^3 f^4}} \quad ,$$

where k is Boltzmann's constant, T is the temperature, m is the mode's effective mass, and Q is the quality factor. The LIGO system hopes to have $f_0 = 1Hz$, $m = 10kg$, and $Q = 10^7$.

At frequencies above 100 Hz it is hoped that the noise limitation will be due to the photon shot noise. See appendix B for a more detailed description. In terms of the interferometer transfer function component $B(\eta)$, the shot noise limit is

$$h(f) = \frac{1}{4|B(\eta)|}\sqrt{\frac{\hbar\omega}{P}} \quad ,$$

where P is the laser light power and ω is the angular frequency of the light.

The total noise from these three terms is given in Figure 5.1. The interferometer is assumed to be a recycled Fabry-Perot with five watts of laser light of wavelength $.5145\text{x}10^{-4}$ cm.

The electric field of the laser light that exits the interferometer is proportional to the phase difference of the light beams of each arm. If the output of antenna one is given by

$$x_1(t) = z_1(t) + n_1(t) \quad ,$$

where z_1 is defined above in terms of the gravity wave and the antennas' transfer function. The spectral density of the photon shot noise would be given by

$$N_1(f) = \frac{\hbar\omega}{4P} \quad ,$$

where

$$\lim_{T\to\infty} \frac{1}{T}\int_0^T n_1^2(t)dt = \int_0^\infty N_1(f)df \quad .$$

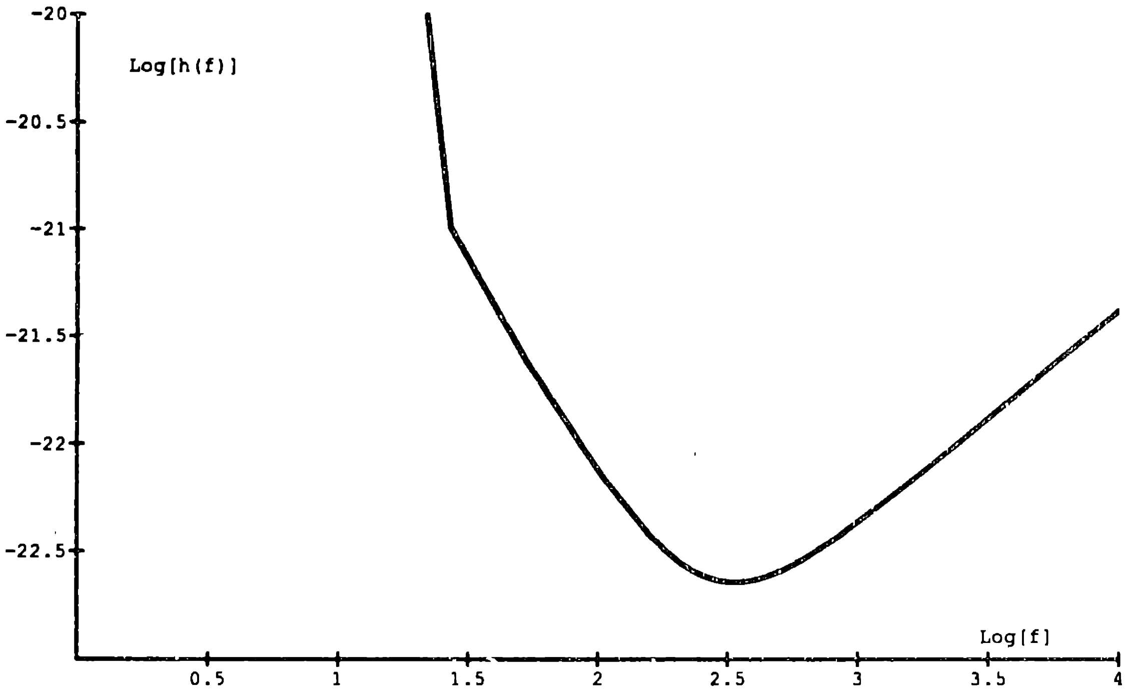

Figure 5.1 Log of the Interferometer noise, h(f), vs. log of frequency.

Section 6 Influence of Noise on Correlation

The presence of noise in each interferometer will affect the measured correlation. The larger the noise, the greater the uncertainty in the result. The two output signals will be expressed as

$$x_1(t) = z_1(t) + n_1(t)$$
$$x_2(t) = z_2(t) + n_2(t) \ .$$

The noise terms, n_1 and n_2, are assumed to be stochastic and stationary with a Gaussian distribution of zero mean. The gravity wave background is assumed to be a stochastic and stationary process with a Gaussian distribution. The signal to noise ratio after a length of time T will be expressed as

$$\frac{S}{N} = \frac{\langle z_1 z_2 \rangle_{av}}{\sqrt{\frac{1}{2T}\int\limits_0^\infty N_1(f)\,N_2(f)df}}$$

(Bendat, 1958). The denominator can be thought of as the variance of the correlation. The 95% confidence interval for the correlation is

$$\langle z_1 z_2 \rangle_{av} \leq 1.645 \sqrt{\frac{1}{2T} \int_0^\infty N_1(f)\, N_2(f) df}$$

(Morrison, 1976). The statistics of the correlation are explained in chapter 6.

Section 7 Filtered Data

The influence of the noise can be reduced by filtering the data. This will have the affect of increasing the signal to noise ratio. Call the filter h. The data from the interferometer, x(t), is passed through h to yield the time series w(t), given as

$$w(t) = \int_0^\infty h(\tau) x(t-\tau) d\tau \ .$$

A physically realizable filter can not predict the signal, hence the condition

$$h(\tau) = 0 \ , \ for \quad \tau < 0 \ .$$

The Fourier transform of h is given by

$$H(f) = \int_0^\infty h(\tau) e^{-2\pi i f \tau} d\tau \ .$$

When two interferometers have the same transfer functions, and the filters applied to each data stream are the same, the correlation will be

$$\langle z_1(t) z_2(t+\tau) \rangle_{av} = \int_0^\infty \frac{d\eta 8 G \rho_g(\eta) |B(\eta)|^2 |H(\eta)|^2}{c^2 \eta^2} \gamma(\vec{x}_1, \vec{x}_2, \eta, \tau) \ ,$$

while the variance of this will be

$$\sigma^2 = \sqrt{\frac{1}{2T} \int_0^\infty N_1(f)\, N_2(f) |H(f)|^4 df} \ .$$

The signal to noise ratio can be maximized with the choice of the proper filter (Fante, 1988). When one assumes that the signal is much smaller than the noise, the ideal filter will be one such that

$$|H(f)|^2 = k\frac{\rho_g(f)|B(f)|^2\gamma(\vec{x}_1,\vec{x}_2,f)}{N_1(f)N_2(f)f^2} \quad ,$$

where k is a constant. In this case, the power signal to noise ratio after a time T will be

$$\frac{S}{N} = \frac{2G}{\pi^2c^2}\sqrt{2T\int_0^\infty\left(\frac{\rho_g(f)|B(f)|^2\gamma(\vec{x}_1,\vec{x}_2,f)}{f^2}\right)^2\frac{df}{N_1(f)N_2(f)}} \quad .$$

The limits on the energy density background of the gravity waves, or the rms value of the strain can be derived from this equation. For some small frequency band spanning Δf around a frequency f, the 95% confidence limit on the gravity wave energy density would be

$$\begin{aligned}\Omega_{gw}(f) &= \frac{5\pi c^2f^3}{8\rho_cG}\sqrt{\frac{2}{\Delta f\ T}}\left(\frac{8\pi/5}{|\gamma(\vec{x}_1,\vec{x}_2,f)|}\right)(1.645)h_n^2(f)\\ &= \frac{\pi c^2f^3}{\rho_cG|\gamma(\vec{x}_1,\vec{x}_2,f)|}\sqrt{\frac{2}{\Delta f\ T}}(1.645)h_n^2(f).\end{aligned}$$

This is expressed in terms of the noise spectral density of the interferometer, $h_n(f)$. The limiting rms value of the strain detectable against the interferometer noise would be

$$h_{rms} = \sqrt{5}\left(\frac{2\Delta f}{T}\right)^{1/4}\sqrt{\frac{8\pi/5}{|\gamma(\vec{x}_1,\vec{x}_2,f)|}}h_n(f)\sqrt{1.645} \quad .$$

Section 8 Orientation and Location of the Antennas

The limit that one can place on the SGWB is affected by the fact that the antennas are at different locations, and have orientations that are not mutually parallel. This effect enters the correlation through the term $\gamma(\vec{x}_1,\vec{x}_2,\eta)$. It is defined to be

$$\begin{aligned}\gamma(\vec{x}_1,\vec{x}_2,\eta,\tau) = \int_0^{2\pi}d\phi\int_0^{\pi}\sin\theta d\theta\Big[(F_{1+}F_{2+} + F_{1\times}F_{2\times})\times\\ \cos\left[\left(\vec{k}\cdot(\vec{x}_1-\vec{x}_2)+\eta\tau\right)\right].\end{aligned}$$

In chapter 4 the F factors are explained. They are functions of: the angles θ and ϕ, which define the direction of the wave in some earth centered coordinate system; the angle ψ which defines the polarization angle of the wave; the location of the detector, given by the angles a and b which are related to the longitude and the latitude; and the orientation of the detector, given by the angle g. As explained in chapter 4, since the SGWB is assumed to be unpolarized, one need not average over ψ, but can give it some value for all θ and ϕ, namely ψ=0. The expressions for F_+ and F_x are given in appendix C.

For the ideal case where the two detectors are aligned and at the same location, one has $\gamma = 8\pi/5$. $\gamma(\vec{x}_1, \vec{x}_2, \eta)$ may take negative values depending on the orientation of the detectors. A rotation of one of the detectors by 90° will switch the sign of γ, but leave its amplitude the same. The first interferometer pair to be considered is the Maine — Southern California detector locations. This is one of the location pairs considered for the LIGO antennas. The explanation of the optimum orientation is given in chapter 4. The angles used are: Maine, a=22.2°, b=45.3°, g=27°; Southern California, a=332.2°, b=55.1°, g=59.9°. A plot of γ vs. f for this geometry is given in Figure 5.2. The function γ can not be solved in closed form for this geometry so a numerical integration was performed.

It should be noted that there are certain frequencies for which γ is zero. It is impossible to perform a correlation measurement at these frequencies. The zeros fall at about 37 and 75 Hz, and repeat about every 70.6 Hz after these values. The frequency 70.6 Hz corresponds to the distance between the two sites, $4.25 \times 10^8 cm$, divided by c. At low frequencies γ takes on its maximum amplitude of 3.92. The next extrema occurs at 52 Hz with a value of .89, followed by a value of $-.41$ at 90 Hz. Extrema then occur near $52 + 70.6 * n \;\; Hz$ and $90 + 70.6 * n \;\; Hz$, where n is some integer. It was stated in the LIGO proposal (Vogt, 1989) that the rms value of the strain h that two detectors can detect is proportional to $\sqrt{1 + fD/c}$ which would imply that γ should be proportional to $(1 + fD/c)^{-1}$. D is the distance between the antennas. Aside from the fact that this neglects the oscillatory nature of γ, this is not a fast enough decrease. It turns out that for the Maine-Southern California geometry the amplitudes at the extrema fall more like $(1 + fD/c)^{-2}$, implying that the rms value of the detectable strain should go as $(1 + fD/c)$. This can be seen in Figure 5.3. Envelope #1 is made up of the curves $\pm 3.92/(1 + fD/c)$, while envelope #2 is made up of the curves $\pm 3.92/(1 + fD/c)^2$. Both curves have the low frequency value of 3.92, and the distance used is $4.25 \times 10^8 cm$.

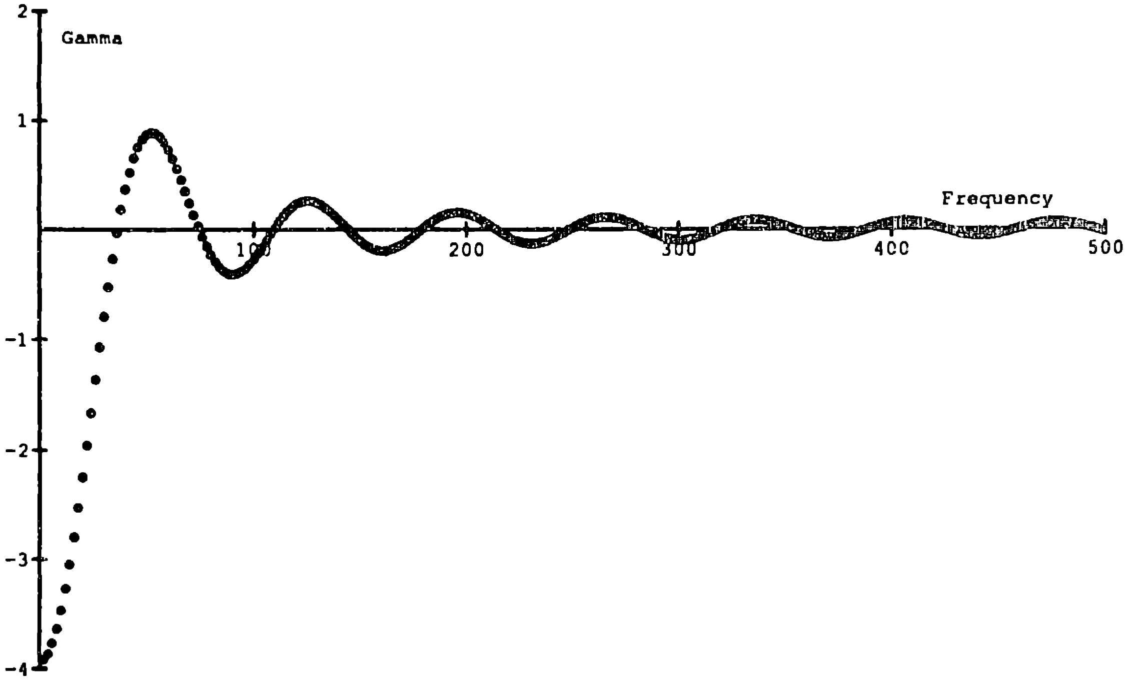

Figure 5.2 Plot of γ vs. frequency (in Hz) for the Maine — Southern California LIGO geometry.

In the case when the two detectors are located on different sides of the earth, it is possible to solve for the γ term exactly. This is actually an interesting case, because Australian scientists have proposed constructing an interferometer in Western Australia. This location is almost exactly on the opposite side of the earth from the possible American site in Maine. Some insight is gained to the character of this function. For detectors that are aligned and separated by 2R, where R is the earth's radius, one has

$$\gamma = \cos\left[4\pi fR/c\right]\left\{\frac{c^2}{2\pi f^2R^2} - \frac{3c^4}{64\pi^3 f^4R^4}\right\} + \\ \sin\left[4\pi fR/c\right]\left\{\frac{c}{fR} - \frac{3c^3}{16\pi^2 f^3R^3} + \frac{3c^5}{256\pi^4 f^5R^5}\right\}.$$

For frequencies of hundreds of Hertz, the envelope appears to go as $(1 + fD/c)^{-1.5}$. From the above expression one can see that the envelope will eventually go as $(1 + fD/c)^{-1}$ at high frequencies. The character of γ is much

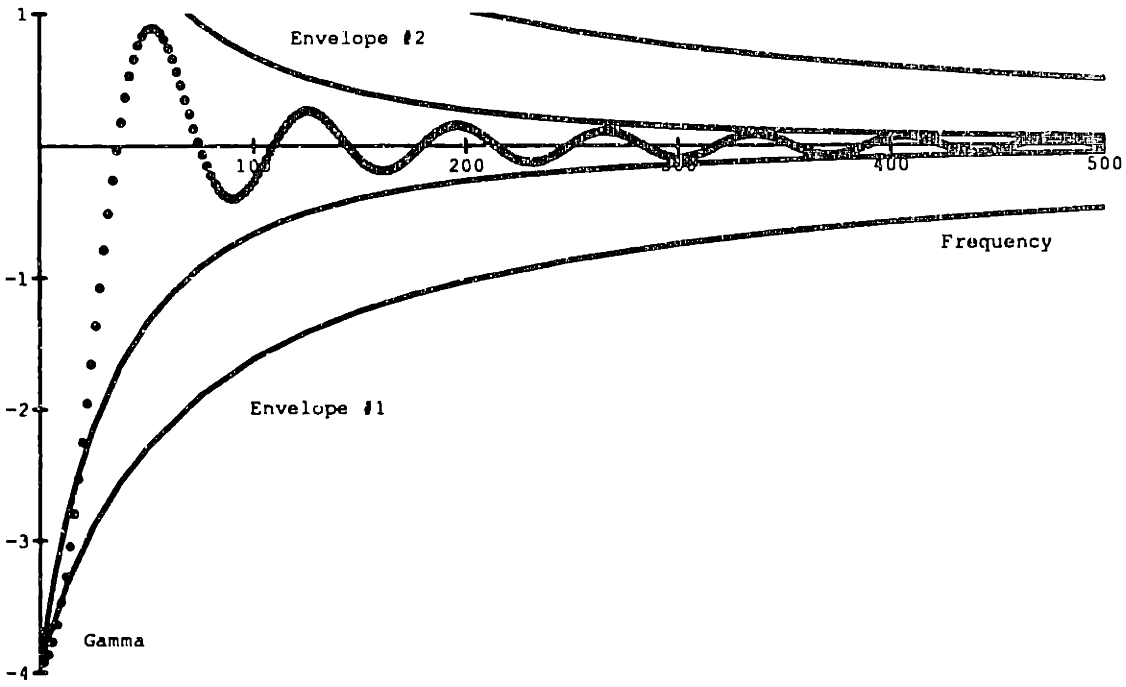

Figure 5.3 Plot of γ vs. frequency (in Hz) for the Maine — Southern California LIGO geometry along with envelopes #1 and #2.

more complicated than what was previously assumed. The exact solution for two detectors on opposite sides of the earth, but with an arbitrary orientation, is given in appendix C.

There are other groups around the world that are planning to build interferometric gravity wave antennas. The antenna that will probably be closest in distance to the detectors in the United States will be constructed by a German-British collaboration (German-British Proposal: Hough, J. et al. 1989). There are many potential locations for this detector: Bavaria; Northern Germany; Scotland. For the purpose of an example, the gamma coefficient is calculated for a correlation between the example American antennas in Maine and Southern California, and a detector located near Munich. The orientation of the Munich detector is chosen so that it is optimally aligned with the Maine antenna. The angles for Munich are; a=101.5° or 11.5°E longitude; b=42° or 48°N latitude; g=55.9°. The γ for the two correlations are illustrated in Figure 5.4 and 5.5.

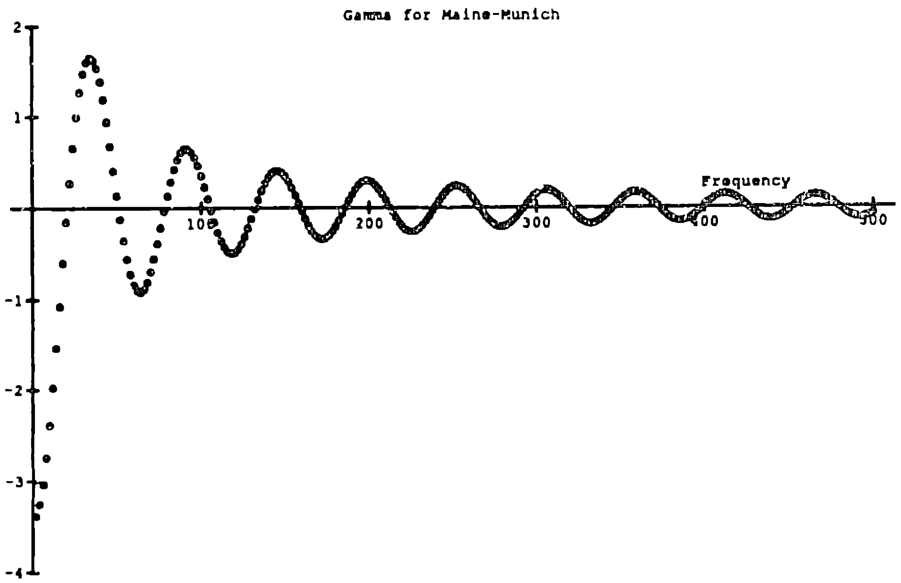

Figure 5.4 Plot of γ vs. frequency (in Hz) for the Maine — Munich LIGO geometry.

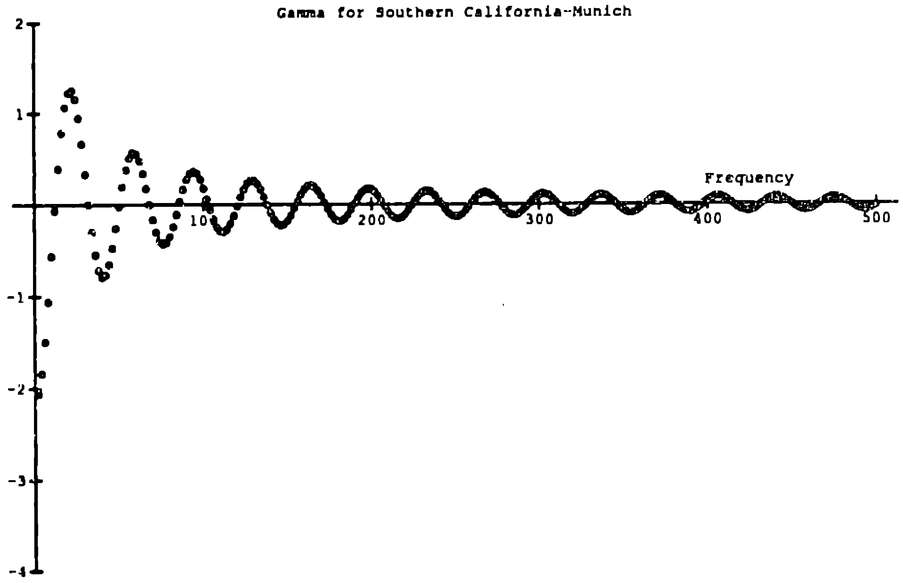

Figure 5.5 Plot of γ vs. frequency (in Hz) for the Munich— Southern California LIGO geometry.

The low frequency value for the Maine-Munich γ is –3.43, while for Southern California-Munich it is –2.14.

It should be noted that the extrema for the three γ's calculated in this section are located at different places. This will help in extracting a SGWB limit at certain frequencies. When the extrema for the three γ's coincide at some frequency a three way correlation can be utilized, and the limit on $\Omega_{gw}(f)$ at that frequency will be reduced by $\sqrt{3}$. This would be the case at f=92, and 198 Hz in the current example. However, an extrema for one pair may result in a null value for the others. This is the case for the extrema at 172 Hz for the Maine-Munich correlation. The other two γ's are near zero there. However, there are cases where two extrema occur near each other, as happens at f= 126, 146, and one gains by a factor of $\sqrt{2}$ in the limit of $\Omega_{gw}(f)$. In summary, adding a third detector increases the accessible frequency regime, more extrema are provided, and the null areas begin to get covered. In some cases the three extrema overlap and a nontrivial increase in sensitivity is achieved.

If a detector has its orientation changed the zeros for the correlation fall at slightly different places. For example, consider the Maine–Southern California example above. When the California detector has its orientation changed by 17° the first zero of the correlation moves from 37 Hz to 42 Hz, while the second zero goes from 75 Hz to 78 Hz. The difference in the frequency values decreases with increasing frequency. It becomes insignificant above 150 Hz. Also, the location of the zeros can not be moved by introducing a delay in the correlation.

For any pair of detectors that are displaced from one another there will be certain frequencies where $\gamma = 0$. Consider a stochastic background of waves at one of these frequencies. The waves from one spot on the sky will give a positive value for the correlated output of the pair of detectors. However, waves from another spot on the sky will give a negative value for the correlation, but of equal amplitude as that from the first spot. This is due to a phase change in the wave as it travels from one detector to the other, thereby changing the sign of the response in the later detector. The effect of the two spots on the sky is to cancel each other out. When one averages over a uniformly distributed gravity wave background on the sky a value of $\gamma = 0$ will result for these specific gravity wave frequencies.

Section 9 Dual Recycling Bandwidth Considerations

Dual, or resonant recycling are techniques that will be applied to the LIGO interferometers to enhance the sensitivity at a certain frequency, while decreasing the effective bandwidth of the system. It has been assumed that the best sensitivity for a shot noise limited interferometer to the SGWB will be when the dual, or resonant recycling systems have their sensitivity maximized. This is not necessarily the case, and will be explained below.

There is no doubt that the data from the interferometers will be filtered. One will obviously try to have the filter as similar as possible with the ideal case. Therefore, the integral

$$\int_0^\infty \left(\frac{\rho_g(f)|B(f)|^2 \gamma(\vec{x}_1, \vec{x}_2, f)}{f^2} \right)^2 \frac{df}{N_1(f) N_2(f)}$$

from section 7 must be maximized. Note, in order to maximize this quantity by adjusting the transfer function term B(f) one must know the spectral density of the noise, the location-orientation factor γ, and the spectrum of the SGWB. The unknown parameter is ρ_g(f), the energy density spectrum. One has to make a hypothesis about its character. In estimating the system performance it is useful to look at two plausible cases for ρ_g(f). The first is that it is flat: the energy density per unit logarithmic interval is constant. The other is that $\rho_g(f) \propto f^2$, which implies that the spectral density of the gravity wave amplitude, h_{rms}, is constant. The optimization will also be dependent on the specific noise spectrum of each detector, namely $N_1(f)$ and $N_2(f)$. The noise spectra will have to be measured.

As an example, consider two detectors at the same location. This makes γ flat. Also, it is assumed that the interferometers are *shot noise* limited down to 100 Hz. The dual recycling Fabry-Perot system will be identical to the example of chapter 3. The losses for all the optical components will be 10^{-4}, while the storage time for the cavities will be the same as that of a 50 bounce delay line. The reflectivities for the mirrors are R_1=.9221, R_2=.9995, while the optimum recycling mirror value for this system would be R_0=.9705. The reflectivity for the dual recycling mirror that would maximize the sensitivity at a frequency of 250 Hz would be R_3=.988. However, .988 may not be the ideal value when one looks for the SGWB.

Consider this system along with the assumption that $\rho_g(f)$ is flat. For a shot noise limited system, the integral

$$\int \frac{|B(f)|^4 df}{f^4}$$

must be maximized with respect to R_3. A plot of

$$\frac{1}{(2\pi)^3 10^{46}} \int \frac{|B(f)|^4 df}{f^4}$$

vs. mirror reflectivity is given in Figure 5.6.

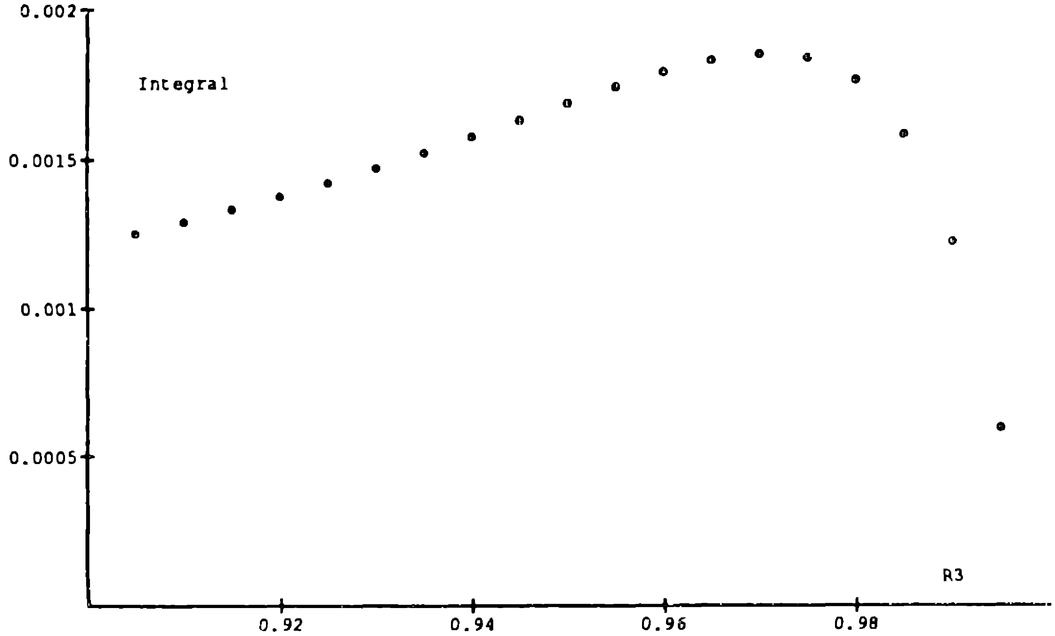

Figure 5.6 Plot of Integral value vs. Dual Recycling Mirror Reflectivity, R_3.

The optimum reflectivity for the dual recycling mirror turns out to be $R_3 = .97$ instead of the .99. The increase in the signal to noise ratio turns out to be 1.23, a slight increase, but an increase nonetheless. When one assumes that the SGWB energy density term $\rho_g(f)$ is proportional to f^2 then the integral

$$\int |B(f)|^4 df$$

must be maximized. For the same interferometer scenario the optimum dual recycling mirror reflectivity again is again .97 instead of .99. The increase in the signal to noise ratio is 1.23.

It happens that the two cases for $\rho_g(f)$ produce the same values for the reflectivity R_3 at other frequencies. Because the effective bandwidth is still small, the difference in the scenarios does not arise. A table listing the optimum reflectivity for a SGWB search along with the maximum sensitivity value and the signal to noise ratio gain is given in Figure 5.7. These values were computed for the same interferometer example.

Frequency (Hertz)	SGWB R3	Max Sensitivity R3	Signal to Noise Gain
100	.95	.975	1.10
175	.96	.98	1.09
250	.97	.99	1.23
290	.975	.99	1.16
325	.9775	.99	1.11
500	.988	.994	1.08

Figure 5.7 Table of Different Optimum Dual Recycling Mirror Reflectivities.

The 250 Hz case has the largest difference, although the affect is not too extreme. For the case when the detectors are located on different sides of the country the optimum reflectivity approaches the optimum sensitivity case. This is due to the fact that the SGWB signal is effectively confined to narrowband regions, so it requires a more narrowband measurement. For the 250 Hz example above the full width at half maximum for the antennas transfer function changes from 10.6 Hz to 19.5, while the maximum value at the resonance decreases by only 4.8%. The effective bandwidth almost doubles while the sensitivity barely changes. The two transfer functions are shown in Figure 5.8.

The example above displayed the results for a particular interferometer design that was *shot noise* limited. (In general, one must actually measure the noise of the detectors, and optimize accordingly.) The solution is intended to display that for a shot noise limited system one must find the optimum dual recycling mirror reflectivity, R_3, by maximizing the integral

$$\int \frac{|B(f)|^4 \rho_g^2(f) df}{f^4} \quad .$$

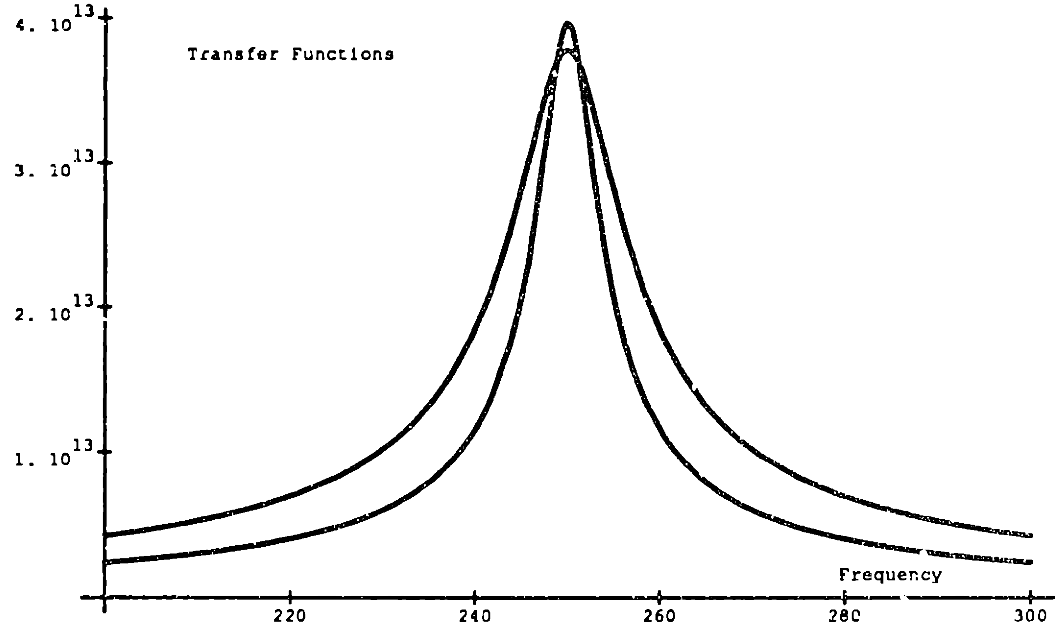

Figure 5.8 Transfer Functions for the Two Optimum Dual Recycling Systems.

In order to maximize the integral one must make an assumption about the spectrum of the gravity wave background, $\rho_g(f)$. When the prediction of the character of $\rho_g(f)$ has been made then there is one unique value of R_3 that will maximize the signal to noise ratio of the filtered correlation. This will then be the optimum dual recycling system for detecting the SGWB. In practice this must be done numerically. A closed form solution of the maximum of the integral would be quite complicated. The case where one has the optimum sensitivity and minimum bandwidth does not guarantee the best design for detecting the SGWB.

Section 10 Sensitivity Limits

The sensitivity for interferometer pairs will now be presented. The initial interferometer should be shot noise limited above about 200 Hz with 5 watts of .5145 nm laser light in a recycled Fabry-Perot system. Figure 5.1 shows the interferometer noise predicted for this system. The LIGO system hopes to employ more advanced techniques as the technology is developed. It is hoped that a recycled Fabry-Perot with 60 watts of .5145 nm light will be shot noise limited above 100 Hz. In addition a narrow-band dual recycling system is intended to be used with 60 watts of light.

The 95% confidence limit achieved by the correlation between the full and half length system at a particular site is illustrated in Figure 5.9. This plot shows the sensitivity of the three interferometer systems, the initial recycled Fabry-Perot (#1), the advanced recycled Fabry-Perot (#2), and the envelope for the advanced dual recycling Fabry-Perot (#3). The rms value of the strain sensitivity is given by

$$h_{rms} = \sqrt{5}\left(\frac{2\Delta f}{T}\right)^{1/4} h_n(f)\sqrt{2 * 1.645} \quad ,$$

where it is assumed that the bandwidth Δf of the measurement is equal to the frequency f, and it has been assumed that $T = 10^7$. Also shown is the sensitivity in terms of the energy density of the SGWB, $\Omega_{gw}(f)$.

Figure 5.10 illustrates the sensitivity for the three interferometer designs, but where the full length antennas are located in Southern California and Maine. The rms value of the strain sensitivity is given by

$$h_{rms} = \sqrt{5}\left(\frac{2\Delta f}{T}\right)^{1/4} \sqrt{\frac{8\pi/5}{|\gamma(\vec{x}_1, \vec{x}_2, f)|}} h_n(f)\sqrt{1.645} \quad ,$$

where the γ for the detector geometry is exhibited in section 8 and Figure 5.3.

There is another point that should be raised about the limit that one places on h$_{\rm rms}$ or $\Omega_{gw}(f)$. The standard practice is to read the values from the expression

$$h_{rms} = \sqrt{5}\left(\frac{2\Delta f}{T}\right)^{1/4} \sqrt{\frac{8\pi/5}{|\gamma(\vec{x}_1, \vec{x}_2, f)|}} h_n(f)\sqrt{1.645} \quad ,$$

or,

$$\Omega_{gw}(f) = \frac{5\pi c^2 f^3}{8\rho_c G} \sqrt{\frac{2}{\Delta f\, T}} \left(\frac{8\pi/5}{|\gamma(\vec{x}_1, \vec{x}_2, f)|}\right)(1.645) h_n^2(f) \quad ,$$

and assume that the bandwidth of the measurement Δf is about the same as the frequency at which the measurement is concentrating. This is an approximation that works well for broadband detection, but is not correct for a narrowband measurement, like dual recycling. Remember, when optimum filter techniques are applied to the outputs of each antenna, then the 95% confidence limit is given

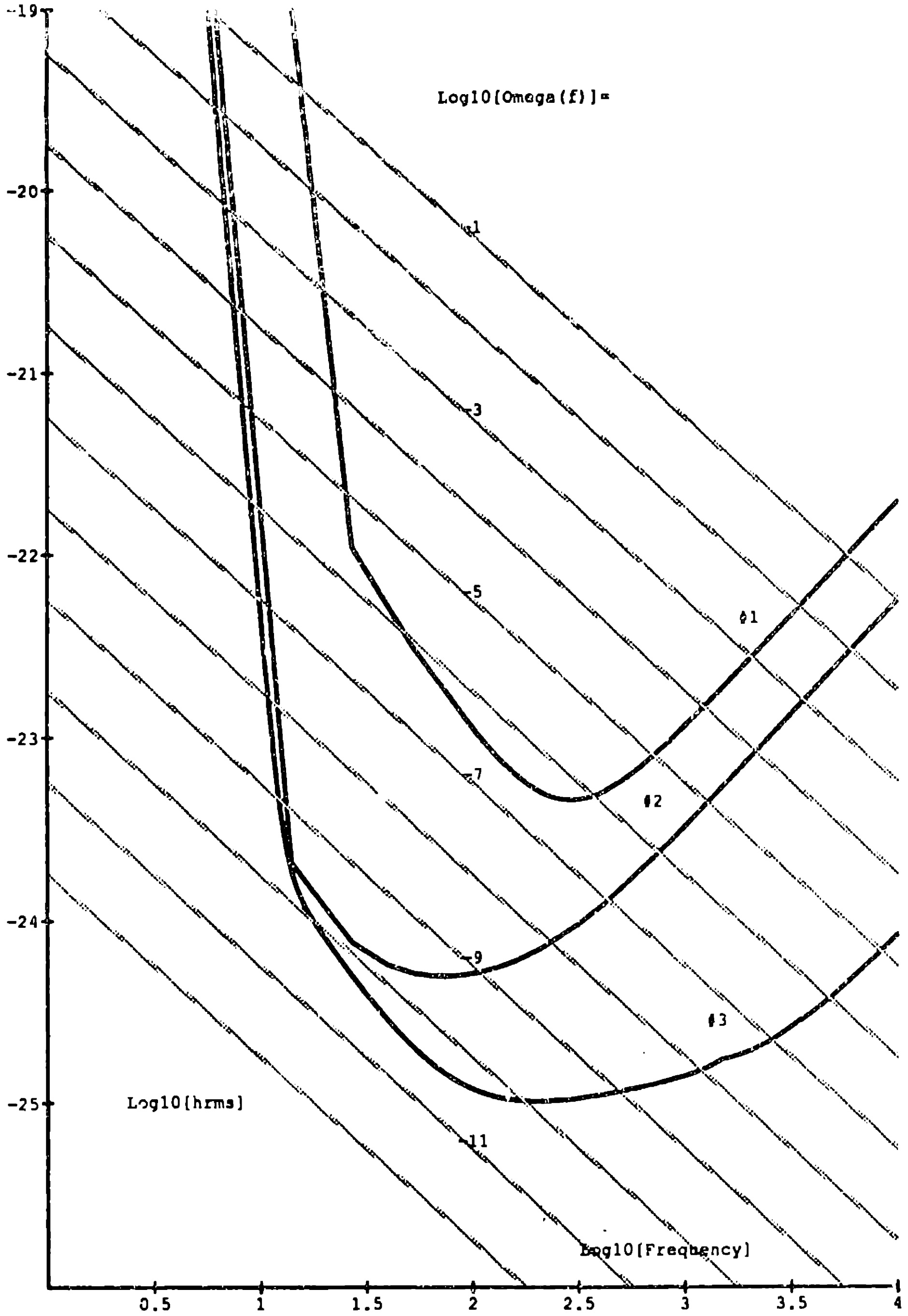

Figure 5.9 Plot of sensitivity to h_{rms} and $\Omega_{gw}(f)$ (diagonal gray lines) vs. frequency for the initial recycled Fabry-Perot (#1), the advanced recycled Fabry-Perot (#2), and the envelope for the advanced dual recycling Fabry-Perot (#3). This assumes a 4 km and a 2 km interferometer at the same site.

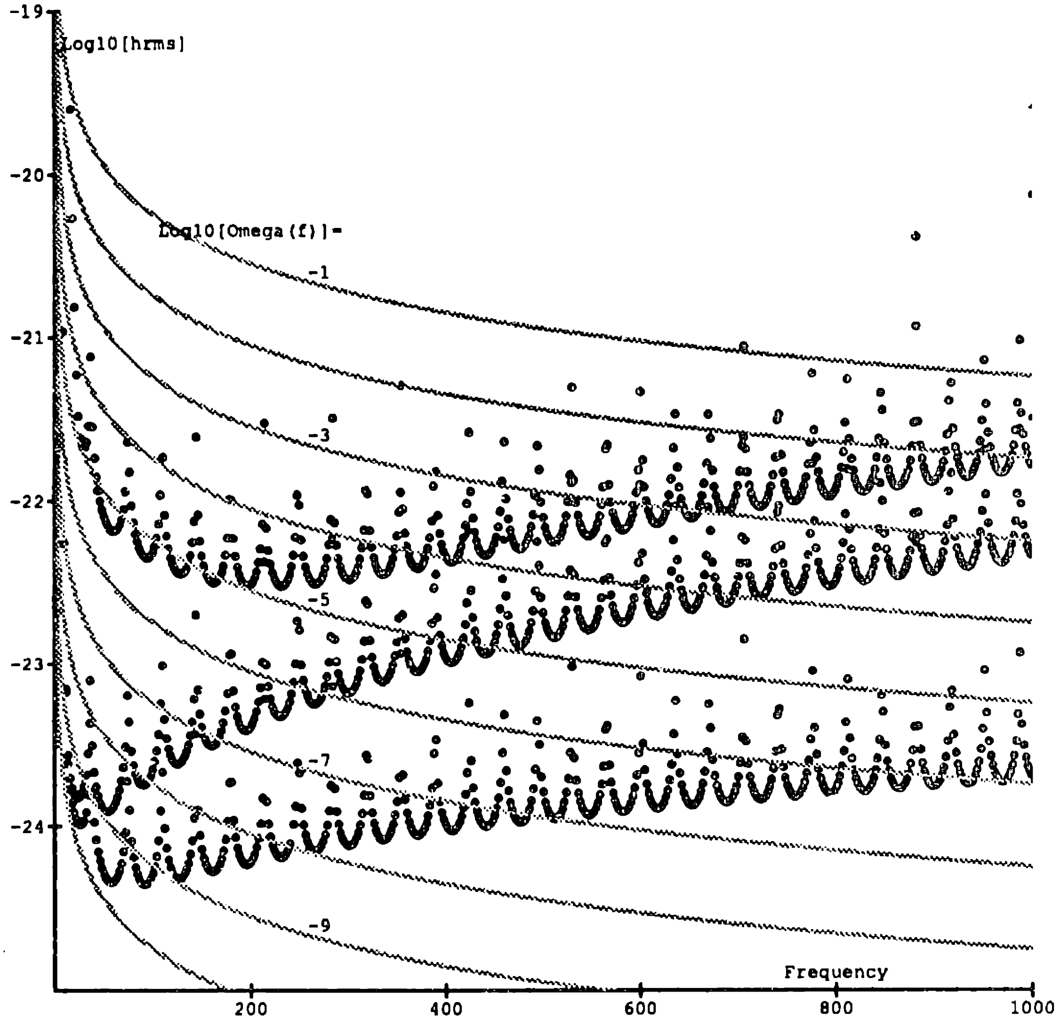

Figure 5.10 Plot of sensitivity to h_{rms} and $\Omega_{gw}(f)$ (gray lines) vs. frequency for the initial recycled Fabry-Perot (#1), the advanced recycled Fabry-Perot (#2), and the envelope for the advanced dual recycling Fabry-Perot (#3) located in Southern California and Maine.

by

$$\frac{S}{N} = 1.645 = \frac{2G}{\pi^2 c^2}\sqrt{2T\int_0^\infty \left(\frac{\rho_g(f)|B(f)|^2\gamma(\vec{x}_1,\vec{x}_2,f)}{f^2}\right)^2 \frac{df}{N_1(f)N_2(f)}}\,.$$

The bottom line is that for dual recycling the effective bandwidth is much smaller than the frequency where the measurement is taking place. One can not approximate the integral by assuming a $\Delta f \approx f$. Figure 5.11 shows the result of this. The sensitivity of the advanced recycling Fabry-Perot (#2) and the advanced dual recycling Fabry-Perot (#3) systems according to the approximation $\Delta f=f$ are plotted against $\Omega_{gw}(f)$. The dots show the result when the optimum filter output is properly integrated over frequency. Therefore, the actual dual recycling limit is not quite as good as what one would normally expect.

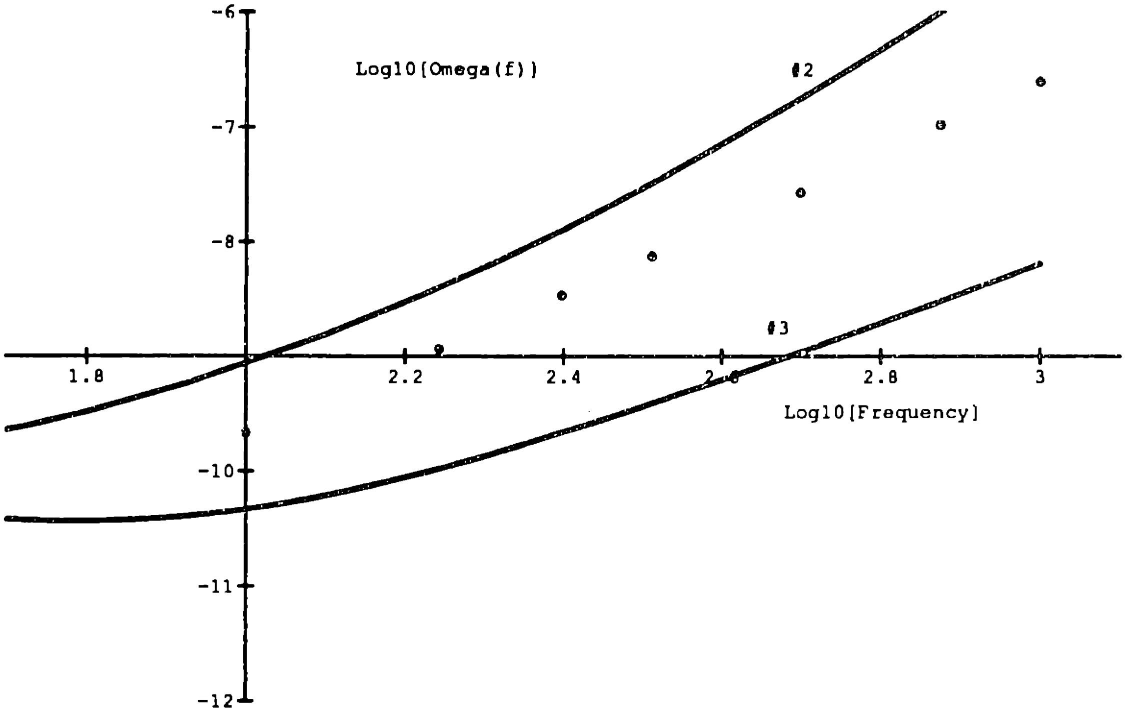

Figure 5.11 The solid lines show the sensitivity to $\Omega_{gw}(f)$ for the advanced recycling Fabry-Perot (#2) and the advanced dual recycling Fabry-Perot (#3) according to the approximate solution where $\Delta f=f$. The dots show the result when the optimum filter output is properly integrated over frequency.

The LIGO system plans to expand the number of interferometers at each site as a latter development (LIGO Proposal: Vogt, 1989). The plan is to have three full length and three half length interferometers at one location, and three full length interferometers at the other site. This will result in 36 correlations. Chapter 6 explains the statistics of a multiple correlation with the use of the multivariate normal distribution. Out of the 36 correlations, 18 will be from two detectors at a similar site, called near correlations, while the other 18 will be from having the detectors at different sites, called far correlations.

For the near correlations, six will be from full length-full length pairs, nine from full length-half length pairs, and three from half length-half length pairs. This will result in a decrease in the limit for $\Omega_{gw}(f)$ of 5.8 over the single full length-half length correlation. As an example, consider the advanced dual recycling system with the bandwidth properly accounted for. At 100 Hz the single full length-half length correlation of 10^7 seconds limits the SGWB energy density to $\Omega_{gw}(f) = 2.14 \times 10^{-10}$, while all 18 near correlations the limit would be $\Omega_{gw}(f) = 3.7 \times 10^{-11}$.

For the far correlation there will nine full length-full length pairs, and nine full length-half length pairs. This will result in a decrease in the limit for $\Omega_{gw}(f)$ of 3.67 over the single full length-full length correlation. As an example, consider the advanced dual recycling system limits illustrated in Figure 5.10. At 126 Hz, where there is an extrema in γ, the single full length-full length correlation of 10^7 seconds limits the SGWB energy density to $\Omega_{gw}(f) = 5.5 \times 10^{-9}$, while all 18 near correlations the limit would be $\Omega_{gw}(f) = 1.5 \times 10^{-9}$.

Chapter 6 Multiple Detectors and Statistics

Section 1 Introduction

The statistics for the correlation function are presented in this chapter. The application of more than two interferometric detectors to a correlation that will detect or limit the stochastic gravitational radiation background (SGRB) is examined. The statistical improvement of having multiple detectors will be presented. This will be done via the Neyman-Pearson criteria. Also, the gain that one may achieve be adding a second interferometer of half the length at one site will be presented.

Section 2 Two Detector Statistics

To begin, consider two time series. Each series is composed of the signal, s, and its noise, n. The ith component of the time series for detectors one and two is given by

$$\begin{aligned} x_{1i} &= s_i + n_{1i} \\ x_{2i} &= s_i + n_{2i} \quad . \end{aligned}$$

It is assumed that the terms s, n_1, and n_2, are all independent stationary Gaussian random processes with zero mean. A correlation will be calculated to determine the variance of s, σ_s^2. The variance σ_s^2 is assumed to be much smaller than the variance for either noise term, σ_{n1}^2, or σ_{n2}^2. The correlation will be determined from a string of N data points from the bivariate normal distribution via

$$r = \frac{\sum_{i=1}^{N} x_{1i}x_{2i}}{\sqrt{\left(\sum_{i=1}^{N} x_{1i}^2\right)\left(\sum_{i=1}^{N} x_{2i}^2\right)}} \simeq \frac{\sigma_s^2}{\sigma_{n1}\sigma_{n2}} \quad .$$

Before it is possible to make a definite detection of σ_s^2, one will want to place a limit on its size. To do this in a statistically proper way one should use the Neyman-Pearson lemma. The application of the Neyman-Pearson criteria to the correlation test in this chapter is due to Morrison (1976).

The Neyman-Pearson approach compares two hypotheses, one which will be called H_0, the null hypothesis, and the other H_1, the alternative hypothesis. From the data set one would like to determine which hypothesis can be supported. If the true state is either H_0, or H_1, then one can make two types of errors. A type I error is when H_0 is actually the correct state, but the data leads one to declare that H_1 is the true state. A type II error is when H_1 is the correct state, but one declares H_0 to be true. The probability for a type I error is α, while the probability for a type II error is β. The probability α is called the *size* or the *level of significance* of the test. The term $1-\beta$ is called the *power* of the test. One chooses between the hypotheses via a likelihood ratio test. Call $L(H_0)$ the likelihood that H_0 describes the data, while $L(H_1)$ is the likelihood that H_1 describes the data. The Neyman-Pearson lemma declares that for a given α, the most powerful test will have a critical region given by the decision rule: accept H_0 if

$$\lambda = \frac{L(H_0)}{L(H_1)} > k \ ,$$

or accept H_1 if $\lambda < k$, where k is defined to be the probability $P(\lambda < k | H_0\, true) = \alpha$. When the hypothesis H_0 is true the variate

$$\chi^2 = -2\, ln(\lambda)$$

approximates a chi-squared distribution with the number of degrees of freedom equal to the number of free parameters determined by H_0.

The Neyman-Pearson test can be used to put a limit on the size of the correlation between two detector signals. The data will be used to test the null hypothesis

$$H_0: \ \ r = 0$$

against the alternative hypothesis

$$H_1: \ \ r \neq 0 \ .$$

Under the assumption that $r = 0$, and with N data points per detector, the variable

$$t = r\sqrt{\frac{N-2}{1-r^2}}$$

has a Student-Fisher t distribution with N-2 degrees of freedom. If one knows that the correlation must be positive, which is the case for this example, then one will accept the null hypothesis, H_0, with a probability α of type I error if

$$t_{\alpha,N-2} \geq r\sqrt{\frac{N-2}{1-r^2}} \quad ,$$

or reject it in favor of the alternative hypothesis, H_1, if

$$t_{\alpha,N-2} < r\sqrt{\frac{N-2}{1-r^2}} \quad .$$

The term $t_{\alpha,N-2}$ represents the value for the upper α percentage point of the Student-Fisher t distribution with N-2 degrees of freedom. When one demands a probability of .05 for a type I error, and the number of points N is large, then the limit on r and σ_s will be

$$r \leq \frac{1.645}{\sqrt{N}} \quad , \quad \Rightarrow \sigma_s^2 \leq \frac{1.645\sigma_{n1}\sigma_{n2}}{\sqrt{N}} \quad .$$

If the correlation produced a value of r such that $r > 1.645/\sqrt{N}$ then there would be less than a 5% chance that one actually has r=0. The correlation that is being tested for in this example is either zero, or positive. The probability of rejecting the hypothesis

$$H_1' : \ r \neq r_0 \ , \ and, \ r > 0$$

when it is actually true and one has chosen $\alpha = .05$ is β, and it can be expressed as

$$\beta = \frac{1}{\sqrt{2\pi}} \int_{-\infty}^{1.645} e^{-(y-r\sqrt{N})^2/2} dy \quad .$$

Therefore, the power for the hypothesis r>0 would be

$$1 - \beta = \frac{1}{2}\left(1 + erf\left[\frac{1}{\sqrt{2}}\left\{1.645 - r\sqrt{N}\right\}\right]\right) \quad .$$

In the test described above one tried to verify, or deny that no correlation existed. If it suspected that there is some positive correlation r_0, one can apply the Neyman-Pearson lemma to test this hypothesis. The null hypothesis is

$$H_0 : \ r = r_0 \quad ,$$

while the alternative hypothesis is

$$H_1 : \ r \neq r_0 \ .$$

The alternative hypothesis can be expanded to two alternative hypothesis, namely,

$$H_1' : \ r > r_0 \quad , \ or, \ \ H_1'' : \ r < r_0 \quad .$$

For large N, the variable z, given by

$$z = tanh^{-1} r$$

tends to a normal distribution with mean

$$\zeta_0 = tanh^{-1} r_0$$

and variance

$$var(z) = \sigma_z^2 = \frac{1}{N-3} \quad .$$

The null hypothesis, H_0 should be accepted with a probability of type I error α if

$$|z - \zeta_0| \leq \frac{z_{\alpha/2}}{\sqrt{N-3}} \quad ,$$

and the alternative hypothesis, H_1, should be accepted if

$$|z - \zeta_0| > \frac{z_{\alpha/2}}{\sqrt{N-3}} \quad .$$

The power for the hypothesis H_1', where $r>r_0$, is

$$1 - \beta = \frac{1}{2}\left(1 - erf\left[\frac{1}{\sqrt{2}}\left\{z_\alpha + (\zeta_0 - z)\sqrt{N-3}\right\}\right]\right) \quad ,$$

while the power for the hypothesis H_1'', where $r<r_0$, is

$$1 - \beta = \frac{1}{2}\left(1 + erf\left[\frac{1}{\sqrt{2}}\left\{-z_\alpha + (\zeta_0 - z)\sqrt{N-3}\right\}\right]\right) \quad .$$

The term z_α represents the upper α percentage point of the normal distribution.

A simulation was performed for two cases, $r_0 = 0$ and $r_0 = 1.48 \times 10^{-2}$, with N=4096, and was repeated 500 times with random Gaussian data. Independent Gaussian noise with variance $\sigma_n^2 = 1$ and zero mean was present in each of the two data streams. For the correlation test with a signal present, each data stream contained the common Gaussian distributed signal with variance $\sigma_s^2 = 1.48 \times 10^{-2}$ and mean zero. For the other test no common signal was present. The statistics from the simulation matched what was predicted. When no signal was present, 94.8% of the correlations had a value of $r < .0269$. The theoretical prediction is that 95% of the correlations should have $r < .0257$. When the signal was present, 5% of the correlations had $r > .045$, while 5% had $r < -.016$, which matches the theoretical prediction.

When N data points from two detectors are correlated the result will be one number, r. The first task to take is to see if this number is consistent with zero. For a level of significance of .05, any value of r such that $r < 1.645/\sqrt{N}$ is consistent with the actual correlation, r_0 being zero. However, for the same level of significance, there is a spread of values for r_0 that can be acceptable. In fact, for a measured value r, there will be a probability of .95 that r_0 is in the interval

$$\frac{-1.96}{\sqrt{N-3}} + r < r_0 < r + \frac{1.96}{\sqrt{N-3}} \quad .$$

The ideal scenarios presented above will be replaced by the actual case when one has data from two interferometric gravity wave antennas. The correlated output of two detectors in some bandwidth Δf will be

$$\frac{1}{N}\sum_{i=1}^{N} x_{1i}x_{2i} = \frac{8G}{c^2}\int^{\Delta f} df \frac{\rho_g(f)}{(2\pi f)^2}[B_1B_2^* + B_1^*B_2] \times$$

$$\int_0^{2\pi} d\phi \int_0^{\pi} \sin\theta d\theta (F_{1+}F_{2+} + F_{1\times}F_{2\times}) \cos \vec{k}\cdot(\vec{x}_1 - \vec{x}_2)$$

$$= \frac{8G}{c^2}\int^{\Delta f} df \frac{\rho_g(f)}{(2\pi f)^2}[B_1B_2^* + B_1^*B_2]\,\gamma(f)$$

This expression is from chapter 5. The equivalent 95% confidence limit will be

$$\frac{8G}{c^2}\int^{\Delta f} df \frac{\rho_g(f)}{(2\pi f)^2}[B_1B_2^* + B_1^*B_2]\,\gamma(f) \le 1.645\sqrt{\frac{1}{2T}\int^{\Delta f} N_1(f)N_2(f)df} \quad .$$

As explained in chapter three, N_1 and N_2 are the spectral density for each interferometer's phase noise, the B terms are one half times the transfer function's for interferometers responding to gravity wave of normal incidence and of optimum polarization.

Figure 6.1 displays the relationship between the level of significance, α, and the signal to noise ratio. Namely, it is a plot of α versus $r\sqrt{N} = (\sigma_s/\sigma_n)^2\sqrt{N}$. This is for the two detector correlation. The level of significance rapidly goes to zero as the correlation and the number of points increases.

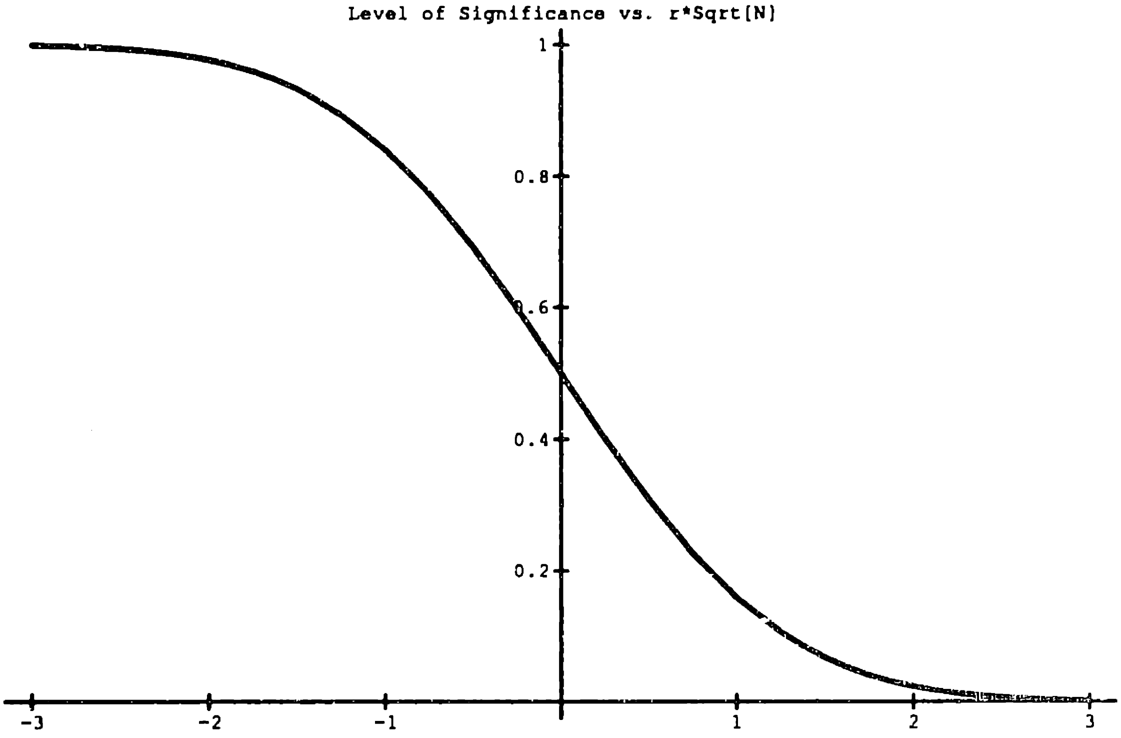

Figure 6.1 Plot of the level of significance, α, versus $r\sqrt{N} = (\sigma_s/\sigma_n)^2\sqrt{N}$.

Section 3 Multiple Detectors

The process of finding a correlated signal in multiple detectors can be accomplished by using the multivariate normal distribution. Consider M detectors, with N data points from each detector, and each signal is the sum of the signal and the detector's intrinsic noise. The i^{th} data point of the j^{th} detector is

$$x_{ji} = s_i + n_{ji} \quad .$$

There will be $\frac{M}{2}(M-2)$ correlations. The correlation between the i$^{\text{th}}$ and the j$^{\text{th}}$ detector's data is given by r_{ij}. For simplicity in this example, the size of the signal is the same in all detectors, and the variance of the independent Gaussian noise in each detector is the same. This will make the expected correlation for all the $\frac{M}{2}(M-2)$ pairs the same. This value will be called r. The null hypothesis for the Neyman-Pearson test will be

$$H_0 : \ r_{ij} = r = 0 \ \ , \ \ for\ all \ \ i\ and\ j,$$

while the alternative hypothesis is

$$H_1 : \ r_{ij} = r \neq 0 \ \ , \ \ for\ all \ \ i\ and\ j.$$

An approximate test statistic can be given by

$$\chi^2 = \left(N - 1 - \frac{2M+5}{6}\right) \sum_{i<j}\sum r_{ij}^2 \quad .$$

This is a chi squared distribution with one degree of freedom, since the size of the correlation is the same for all the detector pairs. Also, it is known that the correlation will be positive. This allows one to attribute the 2α value of the χ^2 to this variate for a α level test. For a probability of .05 for a type I error, and the number of points N is large, the limit on r, and σ_s^2, will be given by

$$r \leq 1.645\sqrt{\frac{2}{NM(M-1)}} \quad , \quad \Rightarrow \sigma_s^2 \leq 1.645\sigma_n^2\sqrt{\frac{2}{NM(M-1)}} \quad .$$

A measured value of σ_s^2 that falls below the above limit will lead to the acceptance of the null hypothesis. The power for the hypothesis r>0 would be

$$1 - \beta = \frac{1}{2}\left(1 - erf\left[\frac{1}{\sqrt{2}}\left\{1.645 - r\sqrt{\frac{2N}{M(M-1)}}\right\}\right]\right) \quad .$$

The Neyman-Pearson test can be applied to the multiple detector scenario, where the existence of a positive correlation is to be tested. Again, the null and alternative hypotheses will be

$$H_0 : \ r = r_0 \ \ , \ \ and, \quad H_1 : \ r \neq r_0 \ \ ,$$

and the alternative hypothesis can be expanded to two alternative hypothesis, namely,

$$H_1' : \ r > r_0 \quad , \ or, \quad H_1'' : \ r < r_0 \quad .$$

The null hypothesis is then accepted with a probability of .05 for a type I error when

$$|r - r_0| \leq 1.96\sqrt{\frac{2}{NM(M-1)}} \quad ,$$

and the alternative hypothesis, H_1, should be accepted if

$$|r - r_0| \geq 1.96\sqrt{\frac{2}{NM(M-1)}} \quad .$$

The power for the hypothesis H_1', where $r>r_0$, is

$$1 - \beta = \frac{1}{2}\left(1 - erf\left[\frac{1}{\sqrt{2}}\left\{1.645 + (r_0 - r)\sqrt{\frac{NM(M-1)}{2}}\right\}\right]\right) \quad ,$$

while the power for the hypothesis H_1'', where $r<r_0$, is

$$1 - \beta = \frac{1}{2}\left(1 + erf\left[\frac{1}{\sqrt{2}}\left\{-1.645 + (r_0 - r)\sqrt{\frac{NM(M-1)}{2}}\right\}\right]\right) \quad .$$

The limit that one can place on σ_s^2 improves as the number of detectors is increased. If one assumes that the noise variance is the same in all detectors the limit that one can place on σ_s^2 will be:

$$\sigma_s^2 \leq \frac{1.645\sigma_n^2}{\sqrt{N}} \quad , \ for \ \ M = 2,$$
$$\sigma_s^2 \leq \frac{.950\sigma_n^2}{\sqrt{N}}, \ for \ \ M = 3,$$
$$\sigma_s^2 \leq \frac{.672\sigma_n^2}{\sqrt{N}}, \ for \ \ M = 4.$$

These statistical limits have been confirmed with a simulation involving three and four detectors. The number of points per detector was, N=4096. The simulation had $\sigma_s^2 = 0$ and $\sigma_n^2 = 1$ to test for the level of significance, α. The simulation with a signal used $\sigma_s^2 = 1.48 \times 10^{-2}$ to test the power, $1-\beta$. The Gaussian random data was generated 500 times, and the distribution of the correlations yielded results for α and $1-\beta$ that confirmed the prediction of the multivariate normal distribution. Figure 6.2 displays the result of the simulation for the case where there are three detectors. The plot shows the level of significance, α, versus the correlation, r. When no signal is present the mean is $r = 0$, and 5.8% of the correlations fall in the range $r > .0149$. The theory predicts that 5% of the correlations will have $r > 1.645/\sqrt{3 * 4096} = .0148$. When the signal is present the mean is at $r = .0148$, as expected. The simulation has 5% of the correlations in the range $r > .0299$. The theory predicts that 5% of the correlations will have $r > .0148 + 1.645/\sqrt{3 * 4096} = .0296$.

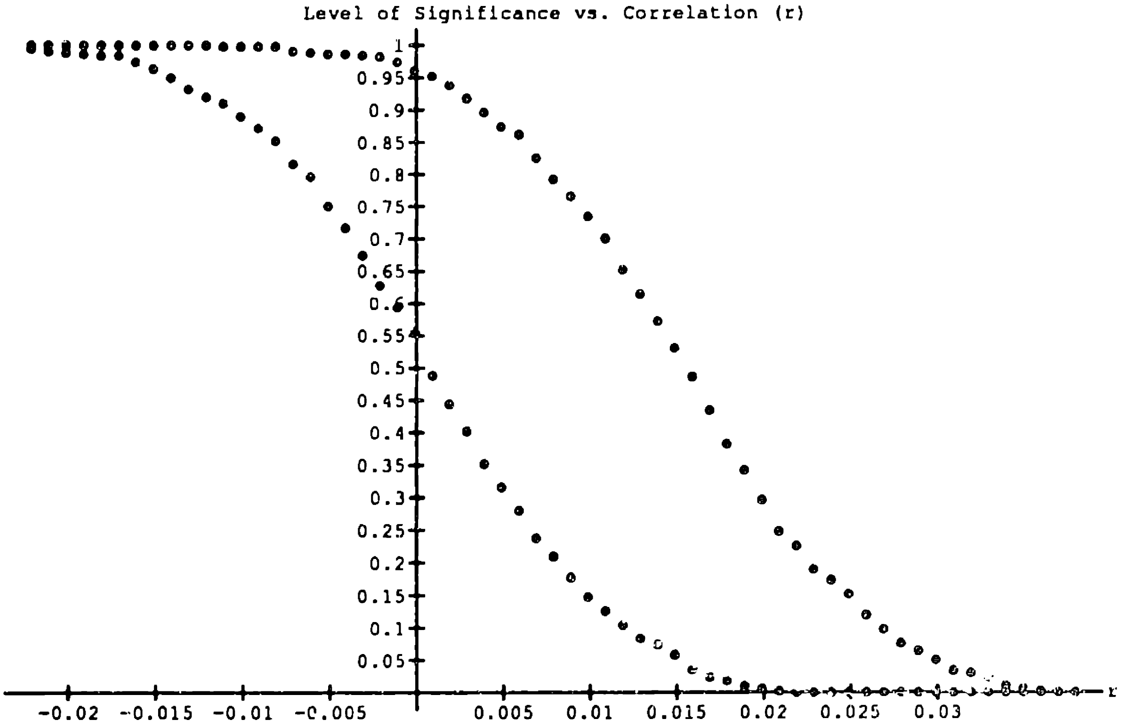

Figure 6.2 The result of 500 correlations, each with 4096 data points. The level of significance is plotted against the correlation. A three detector correlation was simulated. The first curve on the left had three detectors with no signal, but each having a noise value of $\sigma_n^2 = 1$. The other curve had a signal in each detector of $\sigma_s^2 = 1.48 \times 10^{-2}$ and noise $\sigma_n^2 = 1$. The results closely match the predictions.

In general, the strength of the correlation will not be the same for all pairs of detectors. In the multiple gravity wave antenna problem, the correlations will be different for different detector pairs, but the ratios of the correlations will be calculable. It is the relative orientation of the detectors, their displacement from one another, their individual transfer functions, and their intrinsic noise that will change the correlation strength. These affects can all be calculated or measured. However, all the detectors are responding to the same stochastic gravitational wave background. It is the magnitude of this background which is the uncertainty.

The correlation between the signal from detectors i and j will be given by

$$r_{ij} = \frac{\sum_{k=1}^{N} x_{ik}x_{jk}}{\sqrt{\left(\sum_{k=1}^{N} x_{ik}^2\right)\left(\sum_{k=1}^{N} x_{jk}^2\right)}} = \frac{a_{i,j}\sigma_s^2}{\sigma_{ni}\sigma_{nj}} = \alpha_{i,j}\sigma_s^2 \quad .$$

The term $a_{i,j}$ takes into account the difference in response of each interferometer pair, while the $\alpha_{i,j}$ term is $a_{i,j}$ divided by the square root of the variance of the noise for the two detectors that make up the pair. We can use the same null hypothesis of $r = 0$ to be tested against the alternative hypothesis of $r \neq 0$. Again the test statistic is the chi squared with one degree of freedom. Because the sign of all the $a_{i,j}$ are known, one can attribute the 2α value of this variate for a α level test (one can change the sign of any non-positive $a_{i,j}$ term by a global -1 multiplication to the series). Namely,

$$\chi^2 = \left(N - 1 - \frac{2M+5}{6}\right) \sum_{i<j}\sum r_{ij}^2 \quad .$$

For a type I error level of .05, and where the number of points N is large, a limit on σ_s^2 will be given by

$$\sigma_s^2 \leq \sigma_n^2(1.645)\sqrt{\frac{1}{N\left(\alpha_{1,2}^2 + \cdots + \alpha_{M-1,M}^2\right)}} \quad .$$

There are $\frac{M}{2}(M-1)$ correlation terms in the denominator inside the radical. A measured value of σ_s^2 that falls below the above limit will lead to the acceptance of the null hypothesis. The power of this test for a $\sigma_s^2 > 0$ hypothesis is

$$1 - \beta = \frac{1}{2}(1 - erf[\frac{1}{\sqrt{2}}\{1.645 - \sigma_s^2$$
$$\times\sqrt{N\left(\alpha_{1,2}^2 + ... + \alpha_{M-1,M}^2\right)}\}]) \quad .$$

If there were a correlated signal, of a level Σ_s^2, and the measured value was σ_s^2, then the hypothesis $\Sigma_s^2 = \sigma_s^2$ can accepted if

$$|\sigma_s^2 - \Sigma_s^2| \le 1.96\sqrt{\frac{1}{N\left(\alpha_{1,2}^2 + \ldots + \alpha_{M-1,M}^2\right)}} \quad .$$

The power of the hypothesis $\sigma_s^2 < \Sigma_s^2$ would be

$$\begin{aligned} 1-\beta = \frac{1}{2}(1 + erf[\frac{1}{\sqrt{2}}\{-1.645 + (\Sigma_s^2 - \sigma_s^2) \\ \times\sqrt{N\left(\alpha_{1,2}^2 + \ldots + \alpha_{M-1,M}^2\right)}\}]) \quad , \end{aligned}$$

while the power for the hypothesis $\sigma_s^2 > \Sigma_s^2$ would be

$$\begin{aligned} 1-\beta = \frac{1}{2}(1 - erf[\frac{1}{\sqrt{2}}\{1.645 + (\Sigma_s^2 - \sigma_s^2) \\ \times\sqrt{N\left(\alpha_{1,2}^2 + \ldots + \alpha_{M-1,M}^2\right)}\}]) \quad . \end{aligned}$$

In the case of actual gravity wave antenna data being correlated, the σ_s^2 will correspond with the energy density of the gravity wave background, while the $\alpha_{i,j}$ term will contain all the information about the interferometers and their respective orientations and relative separations. For some bandwidth Δf around the frequency f, the energy density of gravitational radiation would be $\sigma_s^2 = \rho_g(f)\ \Delta f$ and

$$\frac{8G}{c^2}\int^{\Delta f} df\,\frac{\rho_g(f)}{(2\pi f)^2}[B_1B_2^* + B_1^*B_2]\,\gamma(f) \le 1.645\sqrt{\frac{1}{2T}\int^{\Delta f} N_1(f)N_2(f)df} \quad ,$$

where T is the total integration time. The $\alpha_{i,j}$ term is given by

$$\alpha_{i,j} = \frac{8G}{c^2}\frac{\left[B_iB_j^* + B_i^*B_j\right]\gamma(f)}{(2\pi f)^2\sqrt{N_1(f)N_2(f)}(\Delta f)} \quad ,$$

and the number of data points, N, can be expressed as $N = 2T\Delta f$.

As an example, consider two identical detectors at the same location. This will make $\gamma = 8\pi/5$. The antennas will be the broadband recycling Fabry-Perot interferometers with 60 watts of laser light power, and arm length of four kilometers, as proposed for the advanced LIGO system (LIGO Proposal: Vogt, 1989). Say the total integration time is 10^7 seconds, and that $f = \Delta f = 150$ *Hertz*. Assuming that the energy density of the gravity waves is very small, and that a level of significance of α=.05 for the hypothesis $\sigma_s^2 = 0$ is desired, this system will be able to limit the ratio of gravity wave energy density per unit logarithmic interval of frequency to critical energy density to

$$\Omega(f) \leq 1.8 \times 10^{-9} \quad .$$

On the other hand, say a value of $\Omega(f) = 10^{-7}$ is derived from the measured correlation. This is about the value that one would expect from a background of cosmic strings that were responsible for galaxy formation. The power for the hypothesis that $\sigma_s^2 > 0$ and $\Omega(f) > 0$ would be effectively one. There would be no doubt about accepting the alternative hypothesis. The range of possible values for the true energy density background that would be allowed by this measurement at a level of significance of .05 would be

$$9.6 \times 10^{-8} < \Omega(f) < 1.04 \times 10^{-7} \quad .$$

Section 4 A System of One Half Length and Two Full Length Interferometers

The initial LIGO system will consist of two four kilometer arm length interferometers located on opposite sides of the country. There will also be a half length interferometer at one of the sites. The consequences of a half length interferometer will be examined here.

The signal of the gravitational wave in a interferometer scales with the length of the arms at frequencies below $1/\tau_s$, where τ_s is the storage time of the interferometer, as described in chapter four. The expected signal strength for the half length system will be half that of the full system. The question then is, how can this information about the scaling of the signal be put to its full use in identifying or limiting the signal.

All of this can be handled under the multivariate normal distribution. First consider the output of three detectors, where one of them is half the length of the other two. To keep this example as simple as possible, the variance of the noise for all three detectors will be σ_n^2. The i$^{\text{th}}$ data point of the detectors is

$$\begin{aligned} x_{1i} &= s_i + n_{1i} \\ x_{2i} &= s_i + n_{2i} \\ x_{3i} &= \frac{1}{2}s_i + n_{3i} \ . \end{aligned}$$

The limit that one can place on the variance σ_s^2 is

$$\sigma_s^2 \leq 1.645\sigma_n^2\sqrt{\frac{2}{3N}} \quad ,$$

which should be compared with the limit that one would get from two or three full length systems

$$\sigma_s^2 \leq \frac{1.645\sigma_n^2}{\sqrt{N}} \quad for \ \ M = 2, \ \ and, \quad \sigma_s^2 \leq \frac{1.645\sigma_n^2}{\sqrt{3N}} \quad for \ \ M = 3.$$

One does not directly measure σ_s^2, but instead measures the three correlations r_{12}, r_{13}, and r_{23}. The measured value of the signal's variance is found via the weighted average

$$\sigma_s^2 = \frac{1}{(1 + \frac{1}{2} + \frac{1}{2})}(r_{12} + r_{13} + r_{23}) = \frac{1}{2}(r_{12} + r_{13} + r_{23}) \quad .$$

When an actual signal is present, with a variance Σ_s^2, a straightforward application of the multivariate normal shows that there is a probability of .95 that one will extract from the three correlations a measured value of the variance of the signal, σ_s^2, that lies in the range

$$\Sigma_s^2 - 1.96\sigma_n^2\sqrt{\frac{2}{3N}} < \sigma_s^2 < \Sigma_s^2 + 1.96\sigma_n^2\sqrt{\frac{2}{3N}} \quad .$$

This is the most sensible way to use the three correlations, just combine them all under the auspices of the multivariate normal. This gives the minimum uncertainty in discerning Σ_s^2.

However, one may want to know the probability that the correlations r_{13} and r_{23} will turn out to be half the size of r_{12} when Σ_s^2 is zero, and when it is not? When there is an actual nonzero Σ_s^2 giving an expected value for the correlation

$r_{12}=r_0$ and $r_{13}=r_{23}=(1/2)r_0$, then there is a probability of .95 that r_{12} falls in the range

$$r_0-\frac{1.96}{\sqrt{N}}<r_{12}<r_0+\frac{1.96}{\sqrt{N}} \quad ,$$

and a .95 probability that r_{13} and r_{23} fall within

$$\frac{r_0}{2}-\frac{1.96}{\sqrt{N}}<r_{13}<\frac{r_0}{2}+\frac{1.96}{\sqrt{N}} \quad ,$$
$$\frac{r_0}{2}-\frac{1.96}{\sqrt{N}}<r_{23}<\frac{r_0}{2}+\frac{1.96}{\sqrt{N}} \quad .$$

However, if Σ_g^2 is in fact zero, the probability that the same ranges contain r_{12}, r_{23}, and r_{13} would be

$$P_{r_{12}}=\frac{1}{2}\left\{erf\left(r_0\sqrt{\frac{N}{2}}+\frac{1.96}{\sqrt{2}}\right)-erf\left(r_0\sqrt{\frac{N}{2}}-\frac{1.96}{\sqrt{2}}\right)\right\},$$
$$P_{r_{13}}=\frac{1}{2}\left\{erf\left(\frac{r_0}{2}\sqrt{\frac{N}{2}}+\frac{1.96}{\sqrt{2}}\right)-erf\left(\frac{r_0}{2}\sqrt{\frac{N}{2}}-\frac{1.96}{\sqrt{2}}\right)\right\},$$
$$P_{r_{23}}=\frac{1}{2}\left\{erf\left(\frac{r_0}{2}\sqrt{\frac{N}{2}}+\frac{1.96}{\sqrt{2}}\right)-erf\left(\frac{r_0}{2}\sqrt{\frac{N}{2}}-\frac{1.96}{\sqrt{2}}\right)\right\}.$$

The plots of $P(r_{12})$ and $P(r_{13})$ are given in Figure 6.3.

The probability that both r_{12} and r_{13} are contained in this range is given by $P2=P_{r_{12}}*P_{r_{13}}$, while the probability for all three correlations to be contained in the appropriate range is $P3=P_{r_{12}}*P_{r_{13}}*P_{r_{23}}$. The plots of P2 and P3 are given in Figure 6.4.

Initially, the actual LIGO three detector system will be considerably different than the simple model above. While one of the full length interferometers will be at the same location and at the same orientation as the half length antenna, the second full length detector will be located on the other side of the country. Not only will the orientation of the detectors be different, but the correlation function will have a frequency dependence to it.

As an example, the discussion here will concentrate on the case where a full and half length system are located in Southern California, while a single full length antenna is in Maine. The orientation of the detectors is chosen according to the method discussed in chapter five. The frequency dependence of

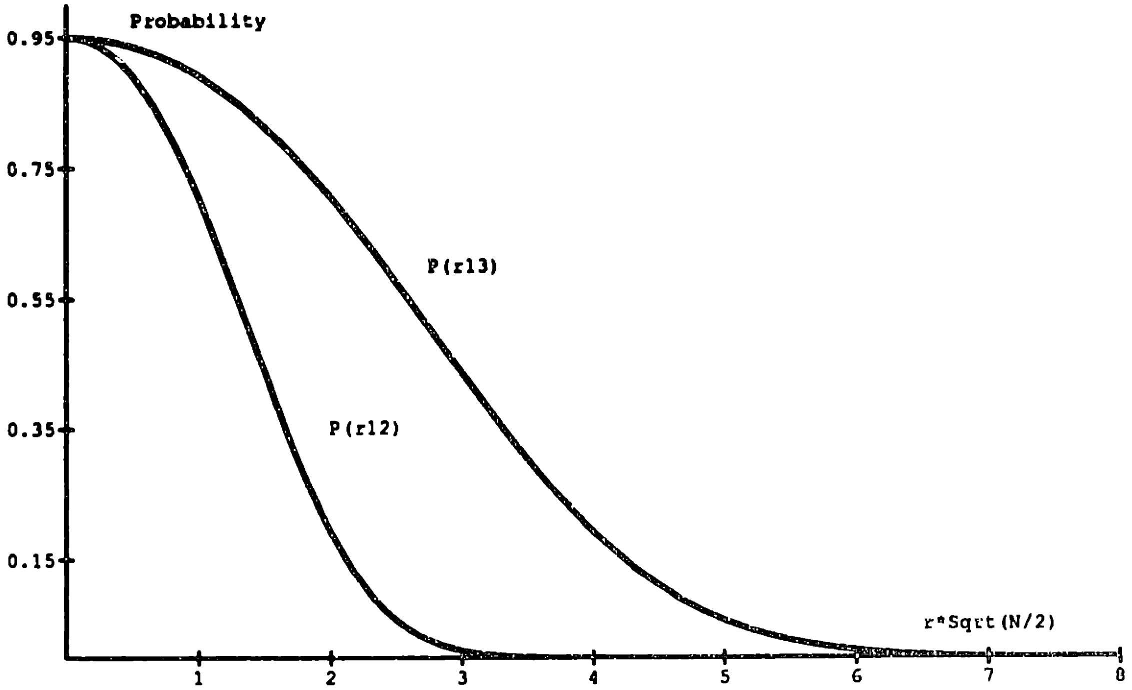

Figure 6.3 Probability curves for the correlations r12 and r13.

the correlation is found via the method developed in chapter three. The antennas will be the broadband recycling Fabry-Perot interferometers with 60 watts of laser light power, and arm length of four and two kilometers. At 126 Hertz there is a local maximum in the frequency dependence of the correlation function. This is where this example will be carried out. The other two local maximum below this one are too low in frequency, and the detectors' noise will be too great. For this example it will be assumed that the noise spectrum will be the same for all three detectors.

Call the full length antenna in Maine #1, the full length one in California #2, and the half length one there #3. The three expected correlations, up to a common constant, are

$$r_{12} = .104 r_0 \ , \quad r_{13} = 5.2 \times 10^{-2} r_0 \ , \quad r_{23} = r_0 \quad .$$

These values considered the lengths of the interferometers, the relative orientations, and the distance separations. The limit of the size of r_0 via the three channel

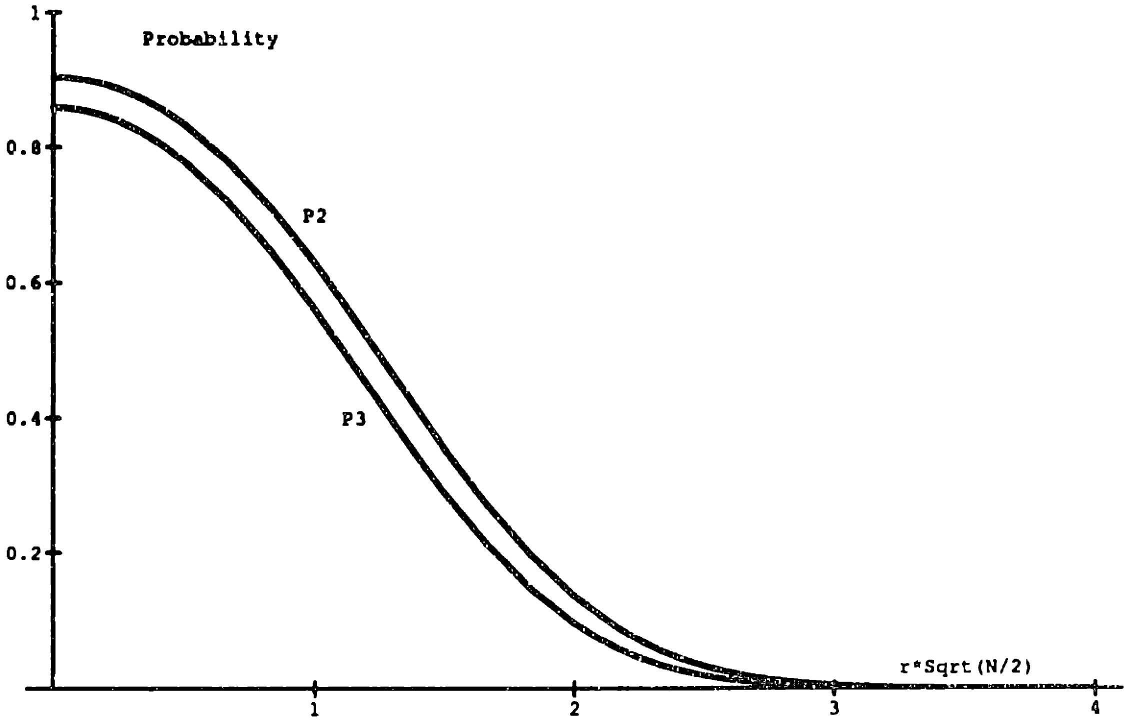

Figure 6.4 Probability curve for r12 and r13 to fall in the same range, P2 and the probability for r12, r13, and r23 to all fall in the same range.

multivariate normal method to a level of significance .05 would be

$$r_0 \leq \frac{1.634}{\sqrt{N}} ,$$

while if one used only the one correlation from the full and half length system at the same location the limit would be

$$r_0 \leq \frac{1.645}{\sqrt{N}} .$$

One hardly gains anything over the two detectors at the same location scenario. The ideal case of a correlation from two interferometers at the same location is much better than the correlation from two antennas separated by a continental displacement. Of course, correlated noise at this common location has been ignored for this example.

It should be noted that since the correlation r_{12} is ten times smaller than the correlation r_{23} it will take one hundred times longer to place the same limit on the energy density with r_{12} than by using r_{23}. The limit goes as

$$\frac{1}{\sqrt{N}} = \frac{1}{\sqrt{2T\Delta f}} \quad .$$

Section 5 Correlated Noise at a Similar Site

The full and half length combination at one site appears to be a very convenient arrangement. However, there will almost certainly be some common, correlated noise. This will be from such things as seismic noise, electrical power fluctuations, or residual gas pressure since the two interferometers will be in the same vacuum system. This will hinder the task of extracting the signal. Whatever the cause of the correlated noise, it will place a limit on the measurement.

Consider the two data streams,

$$\begin{aligned} x_{1i} &= s_i + n_{1i} \\ x_{2i} &= \frac{1}{2} s_i + n_{2i} \quad . \end{aligned}$$

Next, call

$$\langle n_1 n_2 \rangle_{av} = \frac{1}{N} \sum_{i=1}^{N} x_{1i} x_{2i} = \rho \sigma_{n1} \sigma_{n2} \quad .$$

So, the correlation between channels one and two will be

$$r_{12} = \frac{\frac{1}{2}\sigma_s^2 + \rho \sigma_{n1} \sigma_{n1}}{\sqrt{\left(\sigma_s^2 + \sigma_{n1}^2\right)\left(\frac{1}{4}\sigma_s^2 + \sigma_{n2}^2\right)}} \simeq \frac{\frac{1}{2}\sigma_s^2 + \rho \sigma_{n1} \sigma_{n1}}{\sigma_{n1} \sigma_{n1}} \quad .$$

It was assumed that the noise variance is much bigger than the signal's variance. So, the correlated noise will contribute as much to the correlation as the signal when

$$\rho = \frac{\sigma_s^2}{2 \sigma_{n1} \sigma_{n1}} \quad .$$

For a numerical example, say there is a background energy density of gravity waves that has $\Omega(f) = 10^{-7}$, about that which would be produced from cosmic strings. The detectors will be the broadband recycling Fabry-Perot interferometers with 60 watts of laser light power, and arm lengths of four and two kilometers.

At 150 Hertz the signal variance to noise variance would be 1.66x10^{-3}, so a correlation between the two noise terms of $\rho = 8.3 \times 10^{-4}$ would mask the signal.

If a correlation is measured between the full and half length detectors at one site, say in Southern California, after a time T, then it will take 100*T before the correlation between two full length detectors, one in Southern California, and one in Maine, can be confirmed at 126 Hertz.

Section 6 Other Coherence Statistics

The standard correlation function that has been developed in this chapter is not the only measure that could be used to extract the variance of a common stationary Gaussian signal from the outputs of two detectors. Two other statistics, the F-statistic and the semblance were examined to determine if their use would increase the probability of detecting a stochastic gravitational radiation background. The F-statistic and the semblance have been employed in geophysical experiments. Their use has improved coherence signals in seismic activity determination (Blandford, 1974), and in borehole acoustic wave reception (Kimball and Marzetta, 1984). The semblance statistic has also been shown to improve the chance of possibly detecting a periodic gravitational wave (Joo, 1989).

Assume that there are M data streams from the M detectors , x_1 through x_M. The i^{th} data point is represented by

$$x_{1i} = s_i + n_{1i}$$

$$\dots$$

$$x_{Mi} = s_i + n_{Mi} \quad .$$

There is a total of N points per detector. Again, it is assumed that the terms s, and n_1 through n_M, are all independent stationary Gaussian random processes with zero mean. For now it has been assumed that the variance of the noise terms in all M detectors is the same, σ_n^2. All three methods are intended to determine the variance of s, σ_s^2. The standard coherence measure, the correlation, would be expressed here as

$$r_{kl} = \frac{\sum_{i=1}^{N} x_{ki} x_{li}}{\sqrt{\left(\sum_{i=1}^{N} x_{ki}^2\right)\left(\sum_{i=1}^{N} x_{li}^2\right)}} \quad .$$

The distribution of the correlation is described by the multivariate distribution (Morrison, 1976). The F-statistic would be given by

$$F(N_1, N_2, \lambda) = \frac{(M-1)\sum_{i=1}^{N}\left[\sum_{j=1}^{M} x_{ji}\right]^2}{M\sum_{i=1}^{N}\sum_{j=1}^{M} x_{ji}^2 - \sum_{i=1}^{N}\left[\sum_{j=1}^{M} x_{ji}\right]^2} ,$$

where x_{ji} refers to the i^{th} data point of detector j, N_1=N, N_2=(M-1)N, and $\lambda = MN_1\sigma_s^2/\sigma_n^2$ (Douze and Laster, 1979). The F-statistic is a well understood and often used statistical distribution (DeGroot, 1986). The semblance is given by

$$S = \frac{\sum_{i=1}^{N}\left[\sum_{j=1}^{M} x_{ji}\right]^2}{M\sum_{i=1}^{N}\sum_{j=1}^{M} x_{ji}^2} ,$$

and its characteristics are described in Neidell and Taner (1971).

It turns out that for the problem of extracting the variance of the stationary Gaussian signal from each detector, where each detector has its own independent, stationary Gaussian noise, all three methods are equivalent in the regime where N is large. It can be shown theoretically that the statistics for limiting or measuring σ_s^2 via the correlation-multivariate normal method are identical to the F-statistic method. To prove this, one must use the fact that for large N, the F-statistic can be approximated by a normal random variable, x_1, of zero mean and unit variance, given by

$$x_1 = \frac{F - \frac{N_2(N_1+\lambda)}{N_1(N_2-2)}}{\frac{N_2}{N_1}\sqrt{\frac{2}{(N_2-2)(N_2-4)}\left\{\frac{(N_1+\lambda)^2}{(N_2-2)} + N_1 + 2\lambda\right\}}} ,$$

(Abramowitz and Stegun, 1972).

The examination of the three coherence measures described above had the size of the signal being the same in all the channels. It also had the variance of each noise term being the same. The limitations that one can place on the strength of σ_s^2, via the different methods, change as the variance of the noise is changed. For instance, consider two detectors with differing variance in their noise. The limit on σ_s^2 from the correlation technique, to a level of significance of .05 is

$$\sigma_s^2 \leq \frac{1.645\sigma_{n1}\sigma_{n2}}{\sqrt{N}} \quad ,$$

while the limit via the semblance technique is

$$\sigma_s^2 \leq \frac{1.645(\sigma_{n1}^2 + \sigma_{n2}^2)}{2\sqrt{N}} \quad .$$

The limit via the correlation method is always better.

In fact, for the problem that has been defined, where the signal and noise are all independent stochastic Gaussian processes, the correlation-multivariate normal method is the optimum technique (Segal, 1990). Also, the optimum way to process the N data points from each of the M detectors is to not split up the data stream, but instead process all of it together.

The semblance and F-statistic yield no advantage when one looks for a stochastic gravitational wave background. However, they may prove to be very advantageous in the identification of burst sources of gravity waves. Blandford (1974) has shown that the semblance was very useful in identifying seismic events from a network of seismometers. The application of semblance techniques to a network of interferometric antennas warrants further investigation.

Section 7 Non-Gaussian Data

The applicability of the statistical examination above rests on the premise that the signal and all of the noise terms are stationary Gaussian processes. Considering that the signal, a background of gravitational radiation, is of cosmological origin, and that the central limit theorem (Bendat, 1958, or Rice 1954) will certainly apply to this situation, the stationary normal character of the signal will be virtually guaranteed.

The actual detector noise will likely diverge from a normal distribution at some level. The data from the M.I.T. 1.5 meter Michelson interferometer was analyzed by Dan Dewey (1986) and found to be Gaussian up to 5.5σ. This data spanned about 165 minutes at a sampling of 20,000 points per second, for a total of about $2\text{x}10^8$ points. The multiple template detection of events had been removed. The fact that the data from this prototype antenna is Gaussian out to 5.5σ is very encouraging. The rate of occurrence of large events in the non-Gaussian tail dropped by a factor of ten between 5.5σ and 15σ, much less than what would have happened if the data stayed Gaussian. There is no way of knowing how Gaussian the data from the LIGO interferometers will be, but at some level it must certainly diverge from this ideal situation. However, if one can extrapolate from the prototypes, the prospects are good that the non-Gaussian tail will not start until at least 5.5σ.

The statistics of the actual data stream will have to be developed after the data has been taken. A statistic that is commonly used with data that contains heavy tails is the multivariate t distribution (Lange, Little and Taylor, 1989). This statistic has three parameters; the normal distribution has two, the mean and the variance. The third parameter allows for larger than normal tails of the distribution. However, if the actual LIGO data is as good as the prototype's data, then the t-statistic will not be an appropriate statistic for describing the data.

There are a number of ways to model heavy tails. This field of study is called robust statistics. One method that can be used is the contamination distribution (Segal, 1990). Here one assumes that the detector's noise is caused by two separate normally distributed processes that have occurrence probabilities of $(1-\epsilon)$ and ϵ. The probability distribution of the noise would then be

$$\begin{aligned} f_t(x) &= (1-\varepsilon) f_1(x) + \varepsilon f_2(x) \\ &= \frac{(1-\varepsilon)}{\sqrt{2\pi}\sigma_1} e^{\frac{-x^2}{2\sigma_1^2}} + \frac{\varepsilon}{\sqrt{2\pi}\sigma_2} e^{\frac{-x^2}{2\sigma_2^2}} \quad . \end{aligned}$$

The first term models the bulk of the noise. If one had $\varepsilon = 0$ there would be no excessive number of tail events, and the data would be totally Gaussian. The tail events are caused be the second term. The variance of this distribution is assumed to be very large, while its probability of occurrence is very low.

Figure 6.5 shows the probability distributions for f_1 and f_t. The parameters used were; $\sigma_1 = 1$; $\sigma_2 = 6.5$; $\varepsilon = 2.5 \times 10^{-6}$. These numbers correspond to the scenario where the non-Gaussian tail appears at 5.5σ, and the tail's probability value drops by 10 between 5.5σ and 15σ. This plot is very similar to the probability distribution measured by Dewey (1986).

A non-Gaussian tail that is similar to the shown in Figure 6.5 will hardly affect the measurement, or limiting of the stochastic gravity wave background (SGWB).

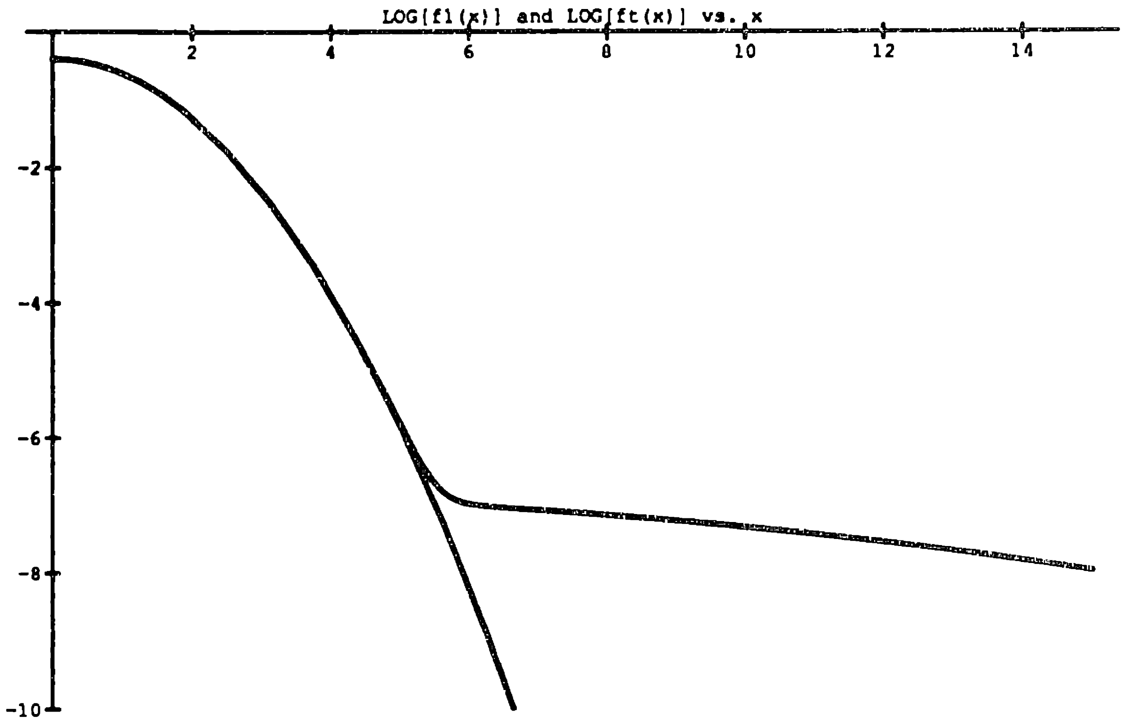

Figure 6.5 Probability Distributions for f1 and ft. f1 is truly Gaussian, while ft has a non-Gaussian tail that appears at 5.5 .

The added power to the noise due to this tail is virtually nil. The variances for the two curves in Figure 6.5 are $\sigma_1^2 = 1$, and $\sigma_t^2 = 1.000103$.

As discussed previously, the full and half length interferometer pair at one location will be very useful for measuring or limiting the SGWB if the amount of correlated noise is low. It may turn out that common noise of the two detectors will be due to these large events that make up the non-Gaussian tail. These large mutual events will likely be caused by such thing as spikes on the power lines, or ground motion due to seismic events or man made phenomena. If it is assumed that the non-Gaussian tail is fully correlated between the two systems, and the output of the two detectors is given as

$$x_{1i} = s_i + n_{1i}$$
$$x_{2i} = \frac{1}{2} s_i + n_{2i} \, ,$$

and the noise spectra for each detector are given by the contamination distribution, with parameters σ_1^2 for the Gaussian noise and σ_c^2 for the variance of the common tail, then the minimum signal variance that can be measured would

$$\sigma_s^2 = \frac{2\sigma_c^2}{1 + \frac{\sigma_1}{\sigma_c} e^{\frac{y^2}{2}\left(1 - \frac{\sigma_1^2}{\sigma_c^2}\right)}} \quad ,$$

where y is the number of σ_1 for which the noise remains Gaussian. Taking the numbers from the M.I.T. 1.5 meter prototype data, y=5.5 and $\sigma_2/\sigma_1 = 6.5$, the limit on the signal variance would be $\sigma_s^2/\sigma_1^2 = 2.1 \times 10^{-4}$. If this is applied to LIGO type interferometers, where the antennas will be the broadband recycling Fabry-Perot interferometers with 60 watts of laser light power, and arm lengths of two and four kilometers, and $f = \Delta f = 150 \ Hertz$, then the energy density of the SGWB could be constrained to a level of

$$\Omega(f) = 1.3 \times 10^{-8} \quad .$$

A way to reduce this level even more would be to apply an amplitude filter to the data. Since the variance of the signal is much smaller than the variance of the noise we could choose to remove all the events in the non-Gaussian tail and not affect the normal correlation limits. It would likely reject much common noise though. The prospects for successfully using the full and half length interferometers at the same site to constrain the SGWB are encouraging.

Section 8 Data Analysis

The data handling and data analysis of a correlation experiment can both be done with present technology. The output data from an interferometer will be sampled at about 2×10^4 per second, giving a Nyquist frequency of 20 KHz. Various housekeeping signals and monitor signals will also be recorded. These will include data from seismic monitors, magnetic field monitors, servo data from the various interferometer components, etc. The interferometer will produce 5×10^9 bytes per day, which will fill a high density 8 mm video tape cassette once every two days (LIGO Proposal: Vogt, 1989).

A correlation involving as many as 10^{12} data points is also achievable. Correlation experiments with this much data, from two or more separated antennas, have been successful in Very Long Baseline Interferometry (VLBI). There one may record up to 10^{12} data points from antennas displaced by thousands of kilometers. A useful trick that the VLBI people use to decrease the size of the stored data is to quantize it. Instead of storing each output data point as a 12 or 16 bit integer, one can quantize it and reduce the size to one or two bits. A two level state would have the data take on the values of 1 or –1 depending on the sign of the data. A three level system would take on the values 1, 0, or –1, with the cutoff parameters for each state being determined by optimal means. The same would go for a four level state. This quantized data can be correlated. One has a small, but acceptable loss in the signal to noise ratio of the correlation. A two state system sampled at the Nyquist frequency, f_{Ny}, will have a relative sensitivity of .64 with respect to the unquantized case. When the data is sampled at $2f_{Ny}$ the relative sensitivity is .74. When the optimal cutoff criteria is applied to a three state system the relative sensitivity is .81 for data sampled at f_{Ny}, and .89 for $2f_{Ny}$. The optimal four state system's relative sensitivities are .88 for f_{Ny}, and .94 for $2f_{Ny}$. See Thompson, Moran, and Swenson (1986) for details of the VLBI correlation techniques.

The quantized data will also allow digital techniques to be applied to the correlation. A system where a number of correlations at different delay times are analyzed has been used by VLBI scientists. When one has the correlation as a function of delay one can Fourier transform it and get the spectral density.

Chapter 7 Coherent Noise in Different Interferometers

Section 1 Introduction

The extraction of the stochastic gravity wave background signature from the correlated output of two interferometers can be limited by the presence of a noise source common to each interferometer. The common noise will contribute to the correlation. This problem will obviously be more severe for the case where one full length and one half length interferometer are at the same site, and in the same vacuum system. This is also the case where one has the most potential sensitivity, so it is important to see how bad the limitations will be. The existence of a problematic coherent noise source for two detectors separated by thousands of kilometers seems unlikely, but is not completely excluded. This will also be investigated in this chapter.

Section 2 Seismic Noise

Seismic noise will contribute to the noise spectrum of the interferometric antenna. The ground motion will cause the mirror masses to move as the vibration propagates through the isolation and suspension system. This motion of the mirrors induced by the seismic wave will mimic the effect of a gravity wave. Two interferometers at the same site will each respond to the same seismic wave. This will certainly be a problem at some level. The influence of seismic waves on a correlation decreases as the interferometers are displaced from one another. All this will be quantified below.

Consider a full length and a half length interferometer at a certain site. Also, consider a stochastic background of surface seismic waves, that propagate at velocity v_s. Most seismic waves are surface waves (Frantti, 1963). This stochastic background of surface seismic waves is assumed to follow the same stationary and ergodic assumptions that were applied to the gravity waves. For simplicity both the longitudinal and transverse components of the seismic displacement will be lumped together. The ground displacement, $s(\vec{x}, t)$, has units of cm. It can be expressed as a two dimensional Fourier transform, namely

$$s(\vec{x},t) = \int d^2\vec{k}\left[\tilde{S}\left(\vec{k}\right)e^{i(\vec{k}\cdot\vec{x}-\omega t)} + C.C.\right] \quad ,$$

where $\vec{k} = \frac{2\pi f}{v_s}(\cos\phi, \sin\phi)$, and $\omega = 2\pi f$. The angle ϕ defines the direction of the wave. The spectral density of the motion is defined by

$$\langle s^2(x,t)\rangle_{av} = \int_0^\infty S_s(f)df \quad ,$$

so $S_s(f)$ has units of cm^2/Hz. The spectral density is related to the Fourier components by

$$S_s(f) = \lim_{A\to\infty} \frac{16\pi^2}{Av_s} k \left|\tilde{S}\left(\vec{k}\right)\right|^2 \quad ,$$

where A is the area over which the average is taken. The transfer function for the mirror displacement from a seismic displacement is defined to be T(f). It has been assumed that a seismic wave from a certain direction will move a mirror in both of the directions in the horizontal plane by similar amount. This is a worst case assumption. The four mirrors of the interferometer are assumed to have identical suspension and isolation systems.

The difference in the length of one of the interferometer's arms, say the X one, with the central mass at $\vec{x}_0$ and the end mass at $\vec{x}_0 + (L,0)$, due to the seismic waves is given by

$$\Delta x = \int d^2\vec{k}\left[\tilde{S}\left(\vec{k}\right)T(f)e^{i\left(\vec{k}\cdot\vec{x}_0-\omega t\right)}e^{ik_xL} + C.C.\right] - \int d^2\vec{k}\left[\tilde{S}\left(\vec{k}\right)T(f)e^{i\left(\vec{k}\cdot\vec{x}_0-\omega t\right)} + C.C.\right] \quad .$$

The change in the length of the Y arm is similarly defined. If one defines the difference in the length of the two arms of an interferometer as $z = \Delta x - \Delta y$ then the correlated difference for interferometer #1, of length L, and interferometer #2 of length L/2 would be given by

$$\langle z_1 z_2\rangle_{av} = \int_0^{2\pi} d\phi \int_0^\infty \frac{df S_s(f)|T(f)|^2}{2\pi}\left\{\cos\left(\frac{2\pi f}{v_s}\frac{L}{2}\cos\phi\right) + \cos\left(\frac{2\pi f}{v_s}\frac{L}{2}\sin\phi\right) - \cos\left(\frac{2\pi f}{v_s}L\left(\cos\phi - \frac{1}{2}\sin\phi\right)\right) - \cos\left(\frac{2\pi f}{v_s}L\left(\sin\phi - \frac{1}{2}\cos\phi\right)\right)\right\} \quad .$$

This equation assumes a constant seismic wave propagation velocity v_s. It takes into account the surface waves from all directions. This is exhibited in the ϕ terms inside the cosines. The resulting delay for a given wavefront striking the four different end masses is the cause of these cosine terms. The ϕ integration can be carried out to give

$$\langle z_1 z_2 \rangle_{av} = \int_0^\infty df S_s(f) |T(f)|^2 2 \left[J_0\left(\frac{\pi f L}{v_s}\right) - J_0\left(\frac{2\pi f L}{v_s}\sqrt{\frac{5}{4}}\right) \right] \quad .$$

The derivation above is a bit incomplete. A given seismic wave that moves a mass in the X arm in the positive $\hat{x}$ direction is assumed to move a mass in the Y arm in the positive $\hat{y}$ direction. In actuality, there is no way of knowing if the Y mass will move in the positive or negative $\hat{y}$ direction. The suspension systems for the two masses considered here are at 90° with respect to each other, and there is no way of knowing at this time how the suspension and isolation system will deal with longitudinal and transverse surface seismic waves. So, another worst case assumption for the total mass motion will be made. Call $w = \Delta x + \Delta y$. Following the same procedure as that for z will produce

$$\langle w_1 w_2 \rangle_{av} = \int_0^\infty df S_s(f) |T(f)|^2 2 \left[J_0\left(\frac{2\pi f L}{v_s}\sqrt{\frac{5}{4}}\right) - J_0\left(\frac{\pi f L}{v_s}\right) - 2 J_0\left(\frac{2\pi f L}{v_s}\right) + 2 \right] \quad .$$

Because of the uncertainty in the direction of the motion of the masses the two terms are added in quadrature. The correlated noise in the mass motion, which will be called q, is then

$$\langle q_1 q_2 \rangle_{av} = \int_0^\infty df S_s(f) |T(f)|^2 2 \left(\left[J_0\left(\frac{2\pi f L}{v_s}\sqrt{\frac{5}{4}}\right) - J_0\left(\frac{\pi f L}{v_s}\right) - 2 J_0\left(\frac{2\pi f L}{v_s}\right) + 2 \right]^2 + \left[J_0\left(\frac{\pi f L}{v_s}\right) + J_0\left(\frac{2\pi f L}{v_s}\sqrt{\frac{5}{4}}\right) \right]^2 \right)^{1/2} .$$

The limit on the energy density of the stochastic gravity wave background that can be detected by the full length—half length system at the same site that is also contaminated by seismic noise is given by

$$\Omega(f) = \frac{5\pi c^2 f^3}{2G\rho_c L^2} S_s(f)|T(f)|^2 \left(\left[J_0\left(\frac{2\pi f L}{v_s}\sqrt{\frac{5}{4}}\right) - J_0\left(\frac{\pi f L}{v_s}\right) - 2J_0\left(\frac{2\pi f L}{v_s}\right) + 2 \right]^2 + \left[J_0\left(\frac{\pi f L}{v_s}\right) + J_0\left(\frac{2\pi f L}{v_s}\sqrt{\frac{5}{4}}\right)\right]^2 \right)^{1/2}.$$

This limit is independent of the length of integration time, and the type of interferometer used.

As an example, consider the system proposed for the LIGO system (LIGO Proposal: Vogt, 1989). It is a five layer stack of elastomer springs and masses, with a pendular suspension that holds the mirror. The proposed system will have a transfer function of

$$T(f) = \left(\frac{1Hz.}{f}\right)^2 \left(\frac{7Hz.}{f}\right)^{10}$$

for horizontal isolation and for frequencies above tens of Hertz. The proposed transfer function for vertical isolation is

$$T(f) = \left(\frac{6Hz.}{f}\right)^2 \left(\frac{15Hz.}{f}\right)^{10}$$

for frequencies above about 10 Hertz. The spectral density for the seismic noise is expected to be on the order of

$$S_s(f) = 10^{-10} cm^2/Hz. \left(\frac{1Hz.}{f}\right)^4$$

for frequencies above 10 Hertz. Figure 7.1 shows the limit for Ω_{gw} that one can achieve with the proposed transfer function and the surmised spectral density for the seismic waves. It was assumed that the interferometers' lengths were four and two kilometers, and the sound velocity for the seismic waves was 5 kilometers per second. However, the limit changes very little over the range of $1km/s < v_s < 10km/s$.

Figure 7.1 shows that the limit that can be achieved on Ω_{gw} at about 100 Hertz is interesting. Large seismic events, such as earthquakes, will be identified

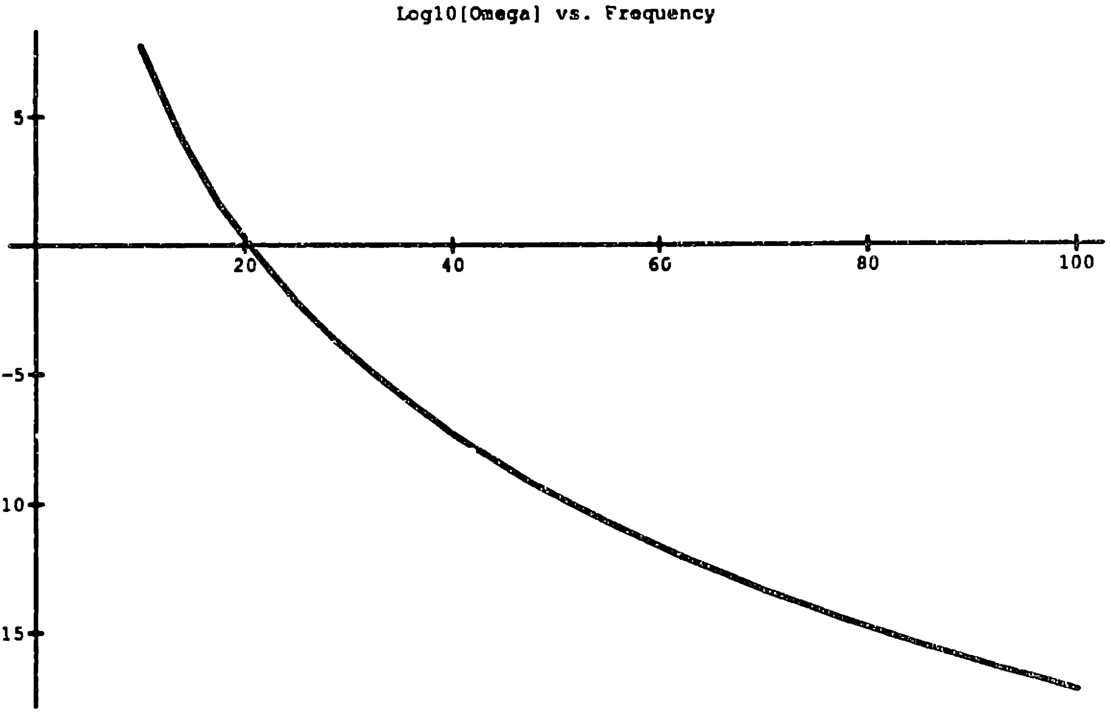

Figure 7.1 Log$_{10}$[Ω_{gw}] that can be detected vs. frequency.

at the interferometer sites by seismometers and accelerometers. This will allow large, identifiable events to be removed from the correlation.

Another interesting limit that can be examined is the relationship between the value placed on Ω_{gw} by two full length parallel interferometers separated by the distance, D, between their central masses, at some specific frequency. For the example, consider two kilometers located on the surface of a plane, with their arms pointing in the $\widehat{x}$ and $\widehat{y}$ directions, and the central masses displaced a distance D along the $\widehat{x}$ axis. Following the same procedure as was given for the last seismic example, the ultimate limit that can be placed on Ω_{gw} is

$$\Omega_{gw}(f) = \frac{5\pi c^2 f^3}{2G\rho_c} S_s(f)|T(f)|^2 \Bigg(\Bigg[3J_0\left(\frac{2\pi f D}{v_s}\sqrt{2}\right) + \frac{1}{2}J_0\left(\frac{2\pi f(L+D)\sqrt{2}}{v_s}\right)$$

$$\frac{1}{2}J_0\left(\frac{2\pi f(L-D)\sqrt{2}}{v_s}\right) - 2J_0\left(\frac{2\pi f D}{v_s}\sqrt{\left(1-\frac{L}{D}\right)^2+1}\right) -$$

$$2J_0\left(\frac{2\pi fD}{v_s}\sqrt{\left(1+\frac{L}{D}\right)^2+1}\right)\Bigg]^2 + \Bigg[J_0\left(\frac{2\pi fD}{v_s}\sqrt{2}\right) -$$

$$\frac{1}{2}J_0\left(\frac{2\pi f(L+D)\sqrt{2}}{v_s}\right) - \frac{1}{2}J_0\left(\frac{2\pi f(L+D)\sqrt{2}}{v_s}\right)\Bigg]^2\Bigg)^{1/2}$$

Figure 7.2 shows the limiting value of Ω_{gw} at 100 Hertz that can be detected by two full length interferometers that are displaced from one another by the distance D. The spectral density for the seismic waves and the isolation system's transfer function are the same as for the last example. As can be seen from this figure, the sensitivity limit for even small distances is quite good. The seismic noise will not restrict a correlation experiment. The oscillatory components of this graph are due to the fact that the speed of sound for the ground was assumed to be a constant value of 5 km/s. An actual spectrum will lose this feature due to a range of velocities. However, the envelope shape will not change much.

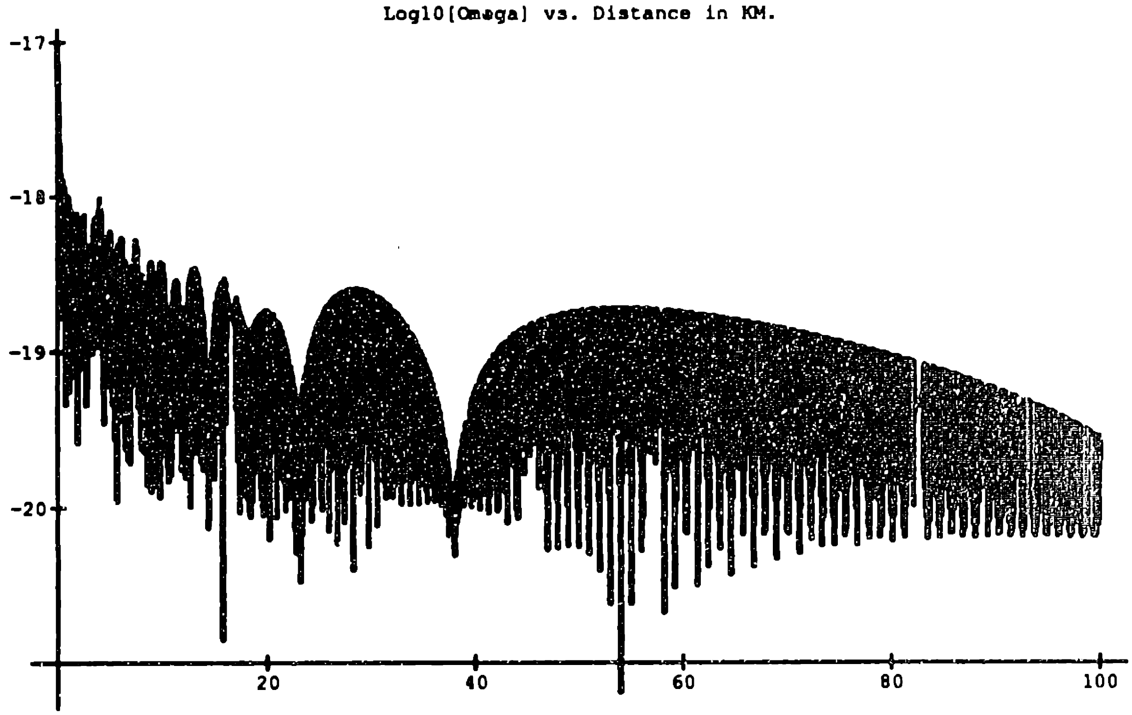

Figure 7.2 $\text{Log}_{10}[\Omega_{gw}]$ at 100 Hertz that can be detected with two four kilometer interferometers displaced versus the distance (in kilometers) between them. This assumes that the experiment is limited by seismic noise only.

Section 3 Fluctuations in the Residual Gas Column Density Inside the Common Vacuum System

The next noise source to consider is from the column density fluctuations of the residual gas in the vacuum system. A column density fluctuation will change the number of molecules in the laser light beam, and this in turn will change the index of refraction, and thereby the phase of the light. This phase change will mask the phase change produced by a gravity wave. This effect will produce coherent noise in two interferometers only when they are both in the same vacuum system. The primary cause of these fluctuations will be from bursts of gas from the walls of the system. These bursts will have a unique signature and may be identifiable in the output data, or from monitoring devices such as UV absorption spectroscopy (LIGO Proposal: Vogt, 1989). If the gas burst can be identified, then the data from the time of the burst can be removed. Otherwise it will add to the value of the correlation. The work below shows how the presence of this common noise will affect the limit on $\Omega_{gw}(f)$ that one can make using the proposed full and half length interferometers in the same vacuum system.

The column density fluctuation, $\delta\sigma$, is the change in the number of molecules per cm^2. If there is a gas burst containing N molecules, then one has $\delta\sigma = N/A$, where A is the cross sectional area of the beam tubes. The noise induced in an interferometer due to these fluctuations is given by $h_n(f) = 2\pi\alpha\ \delta\sigma(f)/L$, where α is the polarizability of the molecule. The gas bursts, if they occur at all, would be expected to consist of N_2, H_2O, or H_2 molecules.

Since the beams for each interferometer are within the same walls, the noise induced from a fluctuation is assumed to affect each beam by the same amount. This is a worst case scenario, but it is not likely to be much different in practice. In order for the column density fluctuations to contribute as much to the correlation of the output data as the stochastic gravity wave background, one must have

$$\Omega_{gw}(f) = \frac{5c^2\pi^3 f^3\alpha^2\ \delta\sigma^2(f)}{L^2\rho_c G} \quad ,$$

where $\delta\sigma(f)$ is the spectral density of the fluctuation, in molecules per cm^2 per $\sqrt{Hz}$, and L is the full length interferometer's arm length. Figure 7.3 shows the relationship between Ω_{gw} and $\delta\sigma(f)$ for a four kilometer interferometer system, and with a molecular polarizability $\alpha = 1.6 \times 10^{-24} cm^3$, which is the value for N_2. For one to limit Ω_{gw} to smaller than $2*10^{-9}$, the column density fluctuation spectral density must be smaller than 10^3 molecules per cm^2 per $\sqrt{Hz}$.

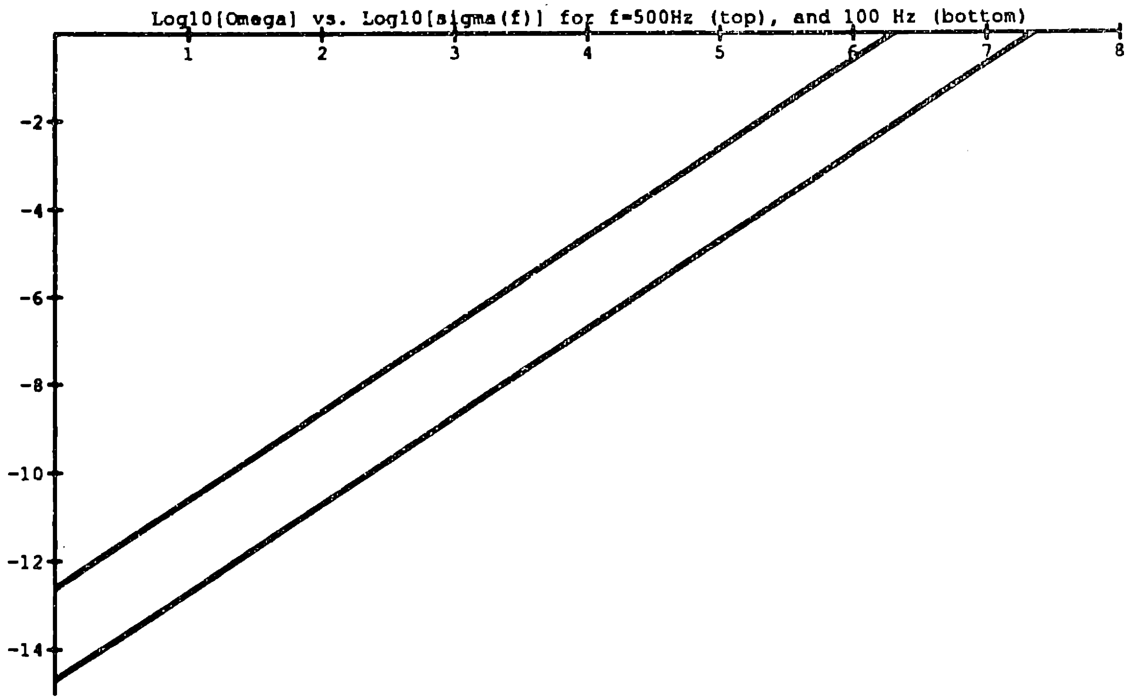

Figure 7.3 Log$_{10}$[Ω_{gw}] that can be detected vs. the log of spectral density of residual gas fluctuations, Log$_{10}$[$\delta\sigma(f)$]. This is done for f=500 Hertz, the top line, and 100 Hertz, the bottom line.

The signature of an individual gas burst that the laser beam sees is expected to be quite unique. (Weiss, 1989). The fluctuation will rise from zero to $\delta\sigma(0)$ in a time $t0$ given by $t0 = 2w/v_{th}$, where w is the 1/e radius of the beam, and v_{th} is the thermal velocity of the gas. The decay time for the burst is given by $T = V/F$, where F is pumping speed for the vacuum system, and V is the volume. Figure 7.4 illustrates the expected evolution of a burst $\delta\sigma$ as a function of time. For the LIGO system the expected values are $t0 \approx 1.2 \times 10^{-4}s$, and $T = 100s$.

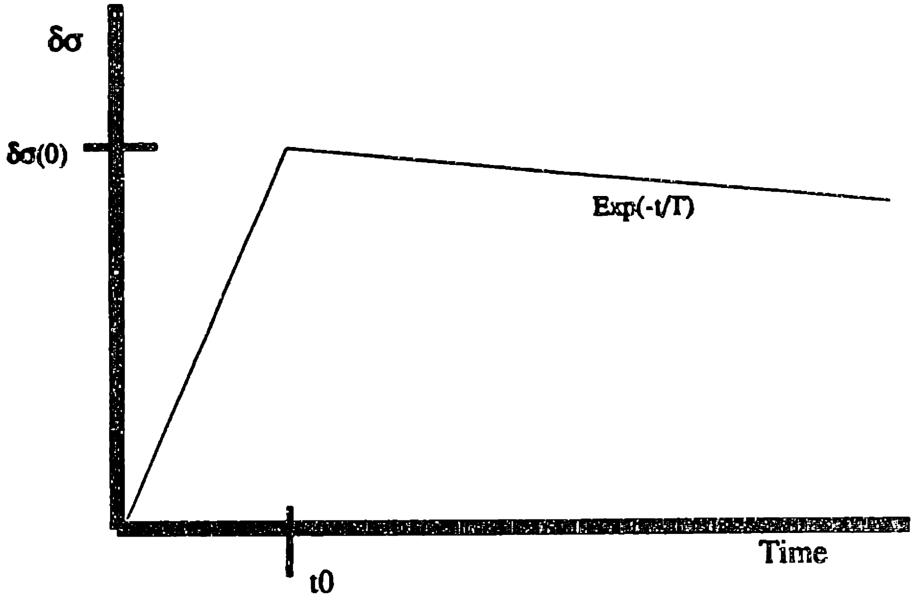

Figure 7.4 A column density fluctuation from a gas burst, $\delta\sigma$, as a function of time. The burst starts at t=0, and rises to a value of $\delta\sigma(0)$ at time t0, then decays away with time constant T.

The column density fluctuation signal, $\delta\sigma$(t), from Weiss' burst model can be Fourier transformed to yield the spectral density. If there is a burst with peak magnitude $\delta\sigma(0)$ every τ seconds, then the spectral density is

$$\delta\sigma(f) = \frac{\delta\sigma(0)}{\sqrt{\tau}}|\Sigma(f)| \quad ,$$

where the where Σ(f) is Fourier transform of the unit amplitude signal, $\delta\sigma$(t), given by

$$\Sigma(f) = \frac{-1}{4\pi^2 f^2 t_0} + e^{-2\pi i f t_0}\left(\frac{1}{4\pi^2 f^2 t_0} + \frac{i}{2\pi f}\right) + \frac{e^{-2\pi i f t_0}}{(2\pi i f + \frac{1}{T})} \quad .$$

Figure 7.5 shows the limit on Ω_{gw} that can be achieved versus $\delta\sigma(0)/\tau^{1/2}$ using the above gas burst model and the same numbers as the previous example. For f=100 Hertz, a limit of $\Omega gw = 2\times10^{-9}$ can be achieved if $\delta\sigma(0)/\tau^{1/2} < 6.25\times10^{5}$. For this limit on Ω_{gw} one could tolerate a burst producing a column density change of 6.25*10^5 N_2 molecules per cm^2 every second.

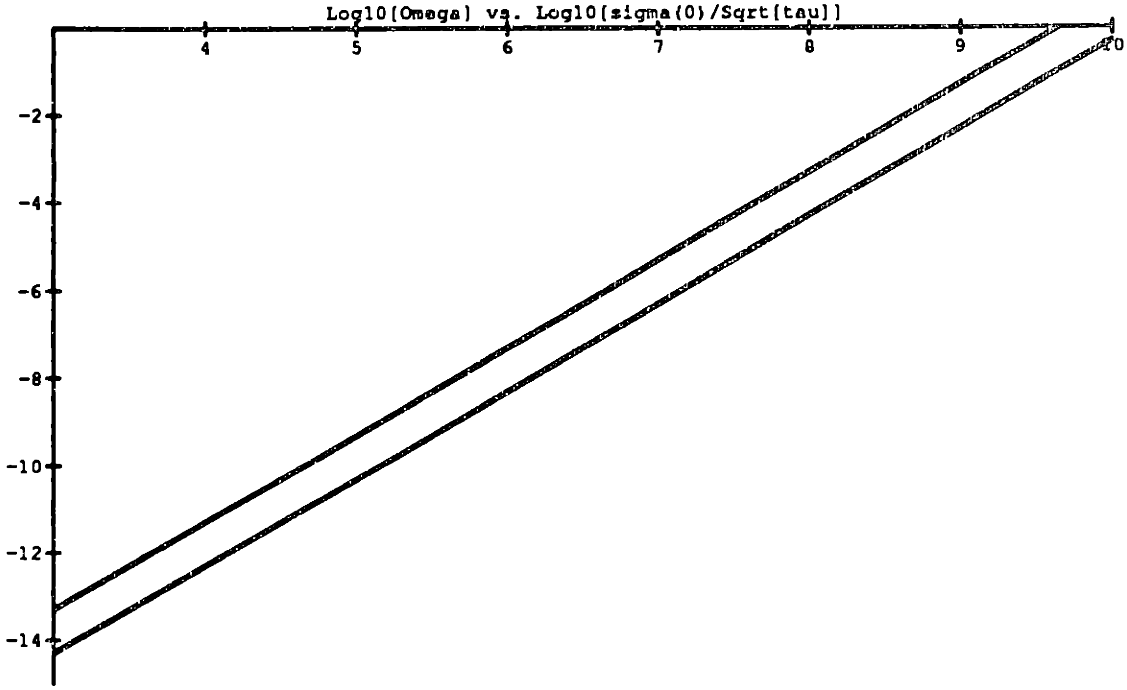

Figure 7.5 $\mathrm{Log}_{10}[\Omega_{gw}]$ that can be detected vs. $\mathrm{Log}_{10}[\delta\sigma(0)/\tau^{1/2}]$. This is done for f=1000 Hertz, the top line, and 100 Hertz, the bottom line.

Section 4 Magnetic Field Fluctuations

The next type of noise to be considered is that due to fluctuating magnetic fields. This could be the major source of correlated noise for a full length-half length system at one site. It may even be a problem for two detectors that are separated by thousands of kilometers. There are a number of sources of magnetic field fluctuations in the regime around 100 Hertz. Power lines will carry and propagate disturbances. Lightning will create impulsive events that can be detected thousands of miles away. The earth and the ionosphere form a resonant cavity that allow magnetic disturbances to propagate and resonate at certain frequencies. Ionospheric currents cause magnetic noise that propagate down to the earth along field lines, and can be detected simultaneously at the North and South poles, and at mid-latitudes.

The force on a magnetic dipole, $\vec{\mu}$, by a external magnetic field $\vec{B}$, is

$$\vec{F} = \nabla\left(\vec{\mu} \cdot \vec{B}\right) \quad .$$

The dipole moment for a mirror mass will be caused by magnets attached to it. These magnets are to be used as magnetic pushers for the isolation system. If the magnetic pushers are not used, the major source of a dipole moment will be due to iron impurities. The amount of iron in premium quality fused silica from Corning can be as high as 5 parts per million (Corning, 1989). In order for a force to be experienced it is necessary for there to be a spatial dependence in $\vec{B}$. The gradient in the magnetic field will be caused by the presence of ferromagnetic materials (steel materials, etc.) that are near the mass, and thereby distort the background field.

If the position displacement of the mass, m, and dipole moment μ, is x(f), in $cm/\sqrt{Hz}$, and the spectral density of the force is F(f), in $dynes/\sqrt{Hz}$, then they are related by

$$x^2(f) = \frac{F^2(f)}{m^2(2\pi f)^4} \quad .$$

The divergence of the magnetic field spectral density, B(f) $gauss/\sqrt{Hz}$, is approximated by

$$\nabla B(f) \sim B(f)/l \quad ,$$

where l is the characteristic distance to the ferromagnetic objects that will disrupt the field. The noise limit in the gravity wave strain, h(f), for the interferometer of length L with four masses is

$$h(f) \approx \frac{F(f)}{2Lm(\pi f)^2} \approx \frac{\mu B(f)}{2Lm(\pi f)^2 l} \quad .$$

The LIGO system will have a full length-half length at one site, and the central masses will be only about 15 meters from each other. The dominant source of correlated noise will likely be due to these two central masses responding to the same magnetic field fluctuation. In this case the best limit that can be placed on the energy density of the gravity wave background is

$$\Omega_{gw}(f) = \frac{5c^2\mu^2B^2(f)}{16\pi^3L^2m^2l^2G\rho_c f} \quad .$$

Figure 7.6 shows the relationship between Ω_{gw} and B(f) for $f = 100Hz$ and $f = 1000Hz$, $m = 10kg$, $l = 5m$, and $L = 4km$. The dipole moment, μ, for the mass is defined by the characteristics of the magnets used. If one has a total of two magnets per mass, each of which has $B_0 = 500\ gauss$, and a volume of $V = .1cc$, then

$$\mu = N\frac{B_0 V}{4\pi} \approx 8\ gauss - cm^3 \quad .$$

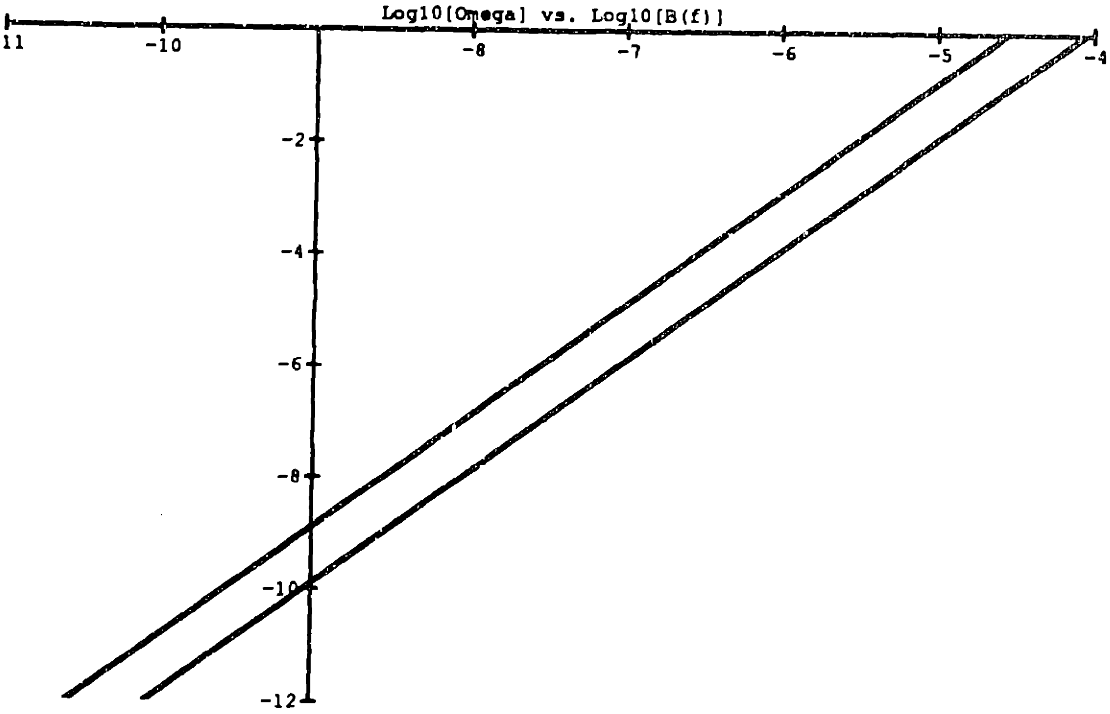

Figure 7.6 Plot of $\mathrm{Log}_{10}[\Omega_{gw}]$ versus $\mathrm{Log}_{10}[B(f)]$. Bottom is line is for f=1000Hz, while the top one is for f=100Hz.

As Figure 7.6 displays, if one wants to limit Ω_{gw} to a value of 10^{-10} at 1000 Hz, or 10^{-9} at 100 Hz, then the magnetic field spectral density should be less than $10^{-9} gauss/\sqrt{Hz}$ at these frequencies.

It is possible that magnetic pushers will not be used in the isolation and suspension system for the mass. In this case the dipole moment will most likely result from iron impurities in the mass. Using the worst case estimate (Corning, 1989) for iron in fused silica of five parts per million, one would have about 50 milligrams of iron in a 10 kg mass. The magnetic moment for this amount of iron in the earth's .5 gauss field would be about $8 \times 10^{-2} gauss - cm^3$. This is a factor of 100 less than that for the magnets on the mass. Since the limit on Ω_{gw} goes as μ^2, the bounds given in Figure 7.6 will be reduced by 10^{-4}.

There is a logical question to ask here: what is the magnetic field spectral density that one can expect at a given site? This subject has been investigated by numerous geophysicists studying geomagnetic fluctuations, and electrical engineers concerned with extremely low frequency (ELF) propagation of electromagnetic waves to communicate with submarines. In the frequency regime from the tens of hertz up to a few kilohertz one sees a somewhat Gaussian background of magnetic field fluctuations, with a non-Gaussian distribution of burst events superimposed on this. This makes the total probability distribution for the field fluctuations non-Gaussian. The background is predominantly caused by world wide lightning events and ionospheric activity, while the bursts are usually due to lightning events within hundreds of kilometers. The background has resonances at certain frequencies, called Schumann resonances (Polk, 1982), which are caused by the cavity formed by the earth and the ionosphere. The lightning burst events will be discussed in more detail below, after some measurements of the background are presented.

Many scientists have measured magnetic field fluctuations, and a few have expressed it in terms of a spectral density. Figure 7.7 shows the results from two experimental programs. Evans and Griffiths (1974) recorded ELF noise at Malta and Saipan. The curves labeled a and b are a rough reproduction of the measured values for the spectral density B(f) (in units of $gauss/\sqrt{Hz}$). Curve a is the spectrum measured in Saipan during a period when there were many thunderstorms in the area. Note that B(f) goes roughly as $1/f^{.95}$ between 2 and 20 Hertz, and then falls at about $1/f^{.44}$ from 20 to 100 Hz. Curve b is the measured spectrum in Malta during a period of moderate weather. B(f) goes as $1/f^{.45}$ between 2 and 15 Hz, and $1/f^{.22}$ from 15 to 45 Hz. The Schumann resonances have been omitted from curve b. They are visible in the data, and the spectral density takes the values of $9.4 \times 10^{-10} gauss/\sqrt{Hz}$ at 7 Hz, $6.3 \times 10^{-10} gauss/\sqrt{Hz}$ at 14 Hz, $5.3 \times 10^{-10} gauss/\sqrt{Hz}$ at 20 Hz, and $3.5 \times 10^{-10} gauss/\sqrt{Hz}$ at 27 Hz. Curves c and d in Figure 7.7 are from ELF studies by Ginsberg (1974) at Malta and Guam, respectively. The measurements on the magnetic field were made during a ten month study from July 1, 1969 to April 30, 1970. Curve c is the spectral density B(f) at Malta, measured throughout the fall of 1969. The fall season had the

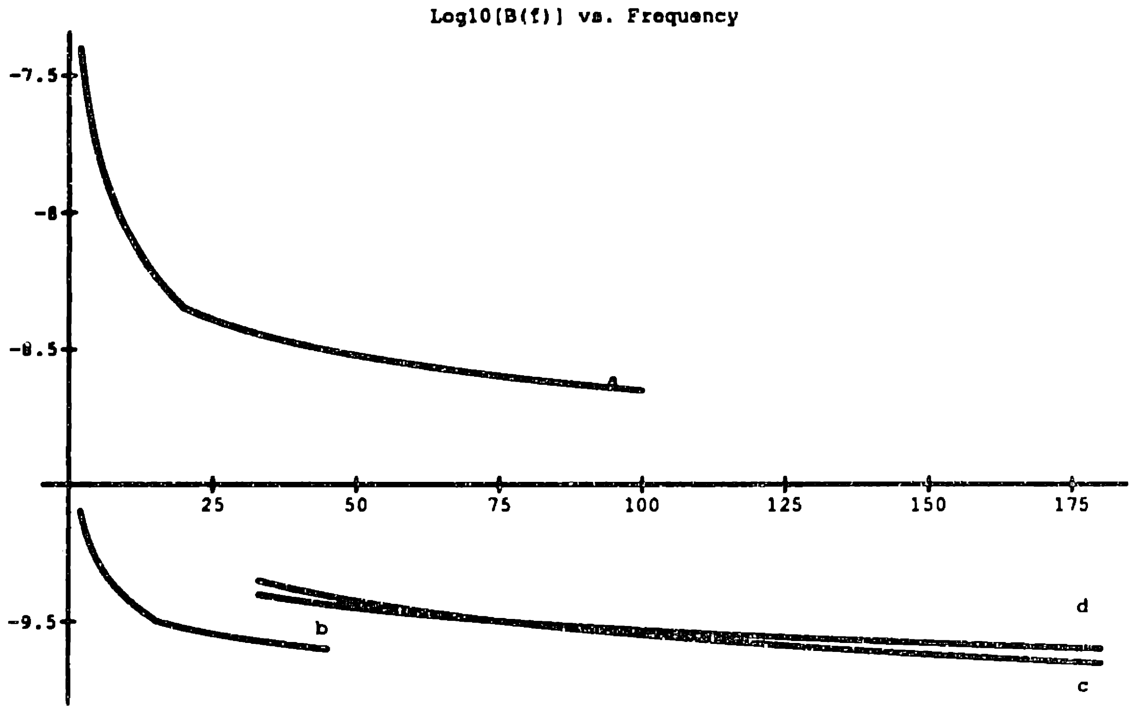

Figure 7.7 Plot of Log$_{10}$[B(f)] versus frequency (in Hz) for various measurements : Saipan during an active thunderstorm period (a), Malta during a moderate period (b), Malta over the entire fall (fall is the most active season) in 1969 (c), and Guam over the entire fall (fall is the most active season there too) in 1969 (d).

highest values for B(f). Curve d is the measured value in Guam during the fall of 1969. Guam's field fluctuations were also the largest during this season.

Figure 7.8 displays a rough approximation of the measured values for B(f) at much lower frequencies. This study was carried out by Heirtzler, De Mendonca, and Montes (1966) in Brazil. The two curves display two different batches of hour long data. The straight line has $B(f) \propto 1/f^{1.45}$ between 1.4×10^{-3} and $6.6 \times 10^{-2} Hz$. The other curve has $B(f) \propto 1/f^{.47}$ from 1.4×10^{-3} to $2 \times 10^{-2} Hz$, and $B(f) \propto 1/f^{2.66}$ between 2×10^{-2} and $6.6 \times 10^{-2} Hz$.

From Figure 7.7 one can see that $B(f) \sim 4 \times 10^{-10} gauss/\sqrt{Hz}$ at 100 Hz for both of the measurements at Malta and Guam. These values were calculated from all the observations in the fall of 1969, which had the largest magnetic field fluctuation activity over the ten months of observation. If one imparts this spectral density onto the LIGO full length-half length system, and also uses the same values for the parameters defined above, then the best limit that one could

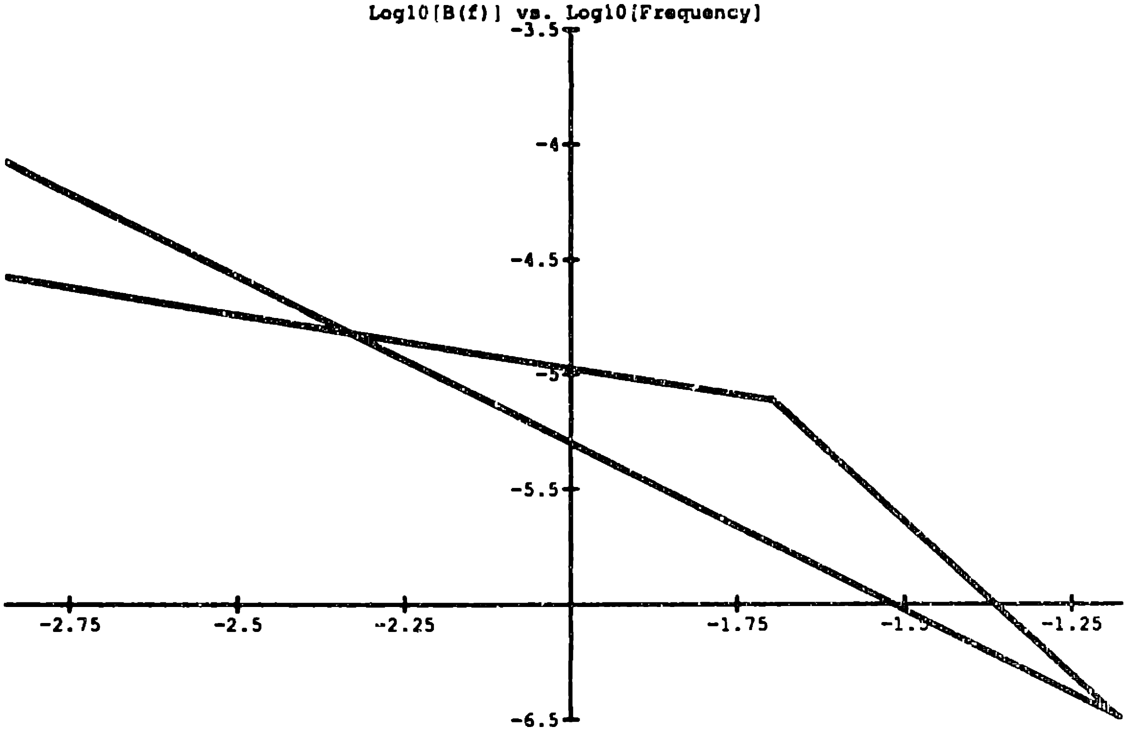

Figure 7.8 Plot of $\text{Log}_{10}[B(f)]$ versus Log_{10}[frequency] for two different measurements made in Brazil.

achieve is

$$\Omega_{gw}(f = 100Hz) \sim 2 \times 10^{-10} \quad .$$

This is a reasonable number. If the magnetic field spectral density is as good as was measured in Guam or Malta during their noisiest season, then the correlation between the outputs of the full and the half length systems at a single site will not be severely hampered by this effect.

As was mentioned before, the probability distribution for the magnetic field in the frequency regime from the tens of hertz to a few kilohertz is non-Gaussian (Ginsberg, 1974) due to numerous bursts that are primarily caused by lightning and thunderstorm activity. The current in a lightning event can be as large as 10^5 amps, with the burst lasting from about 50 to 200 μs (Volland, 1984). At a distance of 10 km the magnetic field from a typical lightning event will be about $2.5 \times 10^{-3} gauss$, while at 200 km it will be about $1.25 \times 10^{-4} gauss$. This corresponds to a current of about $1.25 \times 10^4 amps$. The field will typically rise to the maximum value in a few μs, and will drop back down to zero after another 50 μs. Then there will be a few lower amplitude wiggles over the next 150 μs. The field strength drops as 1/r away from the lightning. The field can be approximated by

$$B(r,t) \sim B_0 \frac{t}{t_0} \quad , \; for \;\; t < t_0 \;\; ,$$

$$B(r,t) \sim B_0 e^{-t/T} \cos\left[\omega(t - t_0)\right] \quad , for \;\; t < t_0 \;\; , and,$$

$$B_0 \sim \frac{I(in\ amps)}{5r(in\ cm)} \quad .$$

Volland (1984) gives the typical lightning parameters: $I \sim 1.25 \times 10^4 amps$, $t_0 \sim 10\mu s$, $T \sim 100\mu s$, and $\omega \sim 2\pi/(40\mu s)$.

There have been a few studies from satellites and U-2 aircraft on the number of lightning events that happen on the earth as a function of time (Orville, 1982). The event rate for lightning is about 100 per second, all over the earth, or about $2 \times 10^{-7} s^{-1} km^{-2}$. This value can range from about 50 to 150 depending on the weather patterns. It was also discovered that the event rate over land is about 10 times greater than that over water. Also, more lightning events occurred in the tropics than at the mid or high latitudes, although no specific latitudinal dependence is given in Orville (1982). However. the bursts in the temperate latitudes may produce more magnetic field fluctuations on the earth's surface because there 50% of the lightning busts are from clouds to earth (as opposed to cloud to cloud), while in the tropics only 10% hit the earth (Pierce, 1963).

As was mentioned above, a good correlation measurement number for Ω_{gw} may be achieved by two interferometers at a single site in spite of the magnetic field fluctuations. Therefore, a correlation between two interferometers on opposite sides of the continent will surely not be restricted. The common magnetic field noise will be insignificant. However, coincident burst events may be registered. Remember, the noise in an interferometer of length L in a strain measurement due to the magnetic field fluctuation is going to be

$$h(f) \approx \frac{\mu B(f)}{2Lm(\pi f)^2 l} \quad .$$

When one considers the magnetic field from a lightning bolt in the 100 Hz to 10000 Hz band, a number can be made for the amplitude of the response in the interferometer. A bolt with a peak current of 10^5 amps, and at a distance of 2000 km (roughly halfway between interferometers in Maine and Southern California) will produce a noise burst of strain amplitude $h \sim 10^{-22}$, which is very near to the expected sensitivity of the proposed early LIGO detectors. At a distance of 2000 km the field strength will not be severely affected by attenuation (other than the 1/r dependence). The attenuation of ELF signals has been measured at about 1 dB per 1000 km (Ginsberg, 1974b). If one uses the measured event rate for lightning of $2 \times 10^{-7}/(s - km^2)$, assumes a 500 km by 500 km area in between Maine and Southern California, and the fact that about 2% of the lightning events have a current as large as 10^5 amps (Orville, 1982), then, on average, there will be a $h \sim 10^{-22}$ burst measured simultaneously in both systems every 17 minutes. These burst will have a total magnetic field strength of $10^{-4} gauss$ at a distance of 2000 km. There is much uncertainty associated with this number. Also, it is likely that the bursts will be concentrated in time around periods of active thunderstorm activity.

It is not unreasonable to expect common events in two interferometers on the opposite sides of the country. This is why the high and low frequency magnetic field fluctuations will be monitored near each mirror mass (LIGO Proposal: Vogt, 1989) of the LIGO system. Common magnetic signals over thousands of kilometers have been measured by many investigators. Gordon (1973) measured simultaneous magnetic field bursts with frequencies greater than a kilohertz and amplitudes greater than a few tenths of a milligauss ($B \sim 10^{-4} gauss$) between Boston and Chicago at a rate of about .14 to .18 events per day. This measurement was made with 520 hours of data during the spring of 1973. The event rate could be expected to be larger during the summer and fall when thunderstorm activity is more common.

The common magnetic field fluctuations between two different locations increases as the frequency of the fluctuation decreases. A study in Brazil (Heirtzler, De Mendonca, and Montes, 1966) saw common fluctuations between two points separated by 3000 km. One point at 51°W, 2°N, the other at 44°W, 21°S. Common fluctuations with amplitudes of about $3.5 \times 10^{-4} gauss$ and periods of days were observed. In fact, the coherence of the cross spectrum of the two signals was greater than .8 for frequencies below $2.5 \times 10^{-2} Hz$. The spectral density of these measurements is displayed in Figure 7.8.

Lokken, Shand, and Wright (1962, and 1963) studied field fluctuations at frequencies around 1 Hz at Great Whale River Quebec (55°N, 78°W); Churchill, Manitoba (59°N, 94°W); Victoria, British Columbia (48°N, 124°W); and Byrd Station in Antarctica (80°S, 120°W). Simultaneous events with amplitudes of about 10^{-7} gauss were seen at all four locations, with very little time displacement. These were both impulsive and oscillatory events. No event rate for mutual detection was given. It is not surprising that events would be seen at both auroral regions, Byrd station and its conjugate point in the opposite auroral zone, Great Whale. This could be due to bunched particles oscillating between the two hemispheres along the earth's magnetic field lines, or ionospheric cavity effects. What is surprising is that it was also seen in Victoria, with a latitude of 48°N, and that sometimes the amplitude of the signal was largest at Victoria. In general, the signal is largest in the auroral zones. These researchers theorize that if an event is large enough to be observed in the mid-latitudes and the auroral zones, then it may be worldwide in extent, and is probably caused by the sudden precipitation of particles from a disturbance on the sun. Common signals at frequencies of about 8, 14, 20, and 28 Hz, which correspond with the Schumann resonances, where frequently seen at Byrd and Great Whale. These common signals occasionally were as large as a few times $10^{-5} gauss$.

Yanagihara (1963) had similar results for his study which was conducted at the same four stations, and also Ottawa, Canada (46°N, 76°W). He occasionally observed burst like micropulsations at frequencies between 2 and 30 Hz and amplitudes as big as $1 \times 10^{-7} gauss$ at all locations. These V-bursts, as they were called, are not thought to be caused by whistlers, or lightning, but by small bunches of high-energy electrons trapped in the earth's magnetic field which interact with the solar wind and the magnetosphere.

Lokken, Shand, Wright, Martin, Brice, and Helliwell (1961) measured the coherence of 48 hours of ELF signals at Byrd Station, Antarctica, and Knob Lake, Canada, which is about 400 miles south-east of Byrd's auroral conjugate point, Great Whale. The coherence was .46 at 200 Hz, .52 at 1000 Hz, .14 at 2000 Hz, .26 at 4500 Hz, .3 at 7000 Hz, and .17 at 10000 Hz.

Tepley (1964) measured the magnetic field fluctuations between .02 Hz and 7 Hz at Palo Alto, California (37°N, 122°W); Canton Island of the Phoenix group (3°S, 172°W); Kauai, Hawaii (22°N, 159°W); Tongatapu, Tonga (21°S, 175°W). He observed simultaneous events, and attributed them to particle bunches traveling along the earth's magnetic field lines.

Before concluding this section on magnetic fields there is another source that should be addressed, power lines. The power lines leading to an interferometer site will be responsible for providing the necessary megawatt of average power, or 2000 kilowatts of peak power. It is likely that the predominant source of magnetic field fluctuations will be caused by all the currents in a LIGO facility. The influence on a correlation between a full and a half length system at one site will be through the two central masses driven by

the same field fluctuation. The preliminary design for the LIGO system has the two central masses separated by about 15 meters. The tolerable current noise for all the wiring can be found from Figure 7.6 by replacing the spectral density of the field, B(f) (in $gauss/\sqrt{Hz}$), by $I(f)\left(amps/\sqrt{Hz}\right) = 5B(f)\ r(cm)$, where r should be taken to be about half the distance between the masses, or about 750 cm. $I(f)$ can then be considered to be the noise from the sum of all the currents in the near vicinity ($\sim 15m$) in between the two central masses which carry the pusher magnets. At 100 Hz one could limit Ω_{gw} to be less than 10^{-8} if $I(f) < 12\mu\, amp/\sqrt{Hz}$, $\Omega_{gw} < 10^{-9}$ if $I(f) < 3.8\mu\, amp/\sqrt{Hz}$, or $\Omega_{gw} < 10^{-10}$ if $I(f) < 1.2\mu\, amp/\sqrt{Hz}$. This may prove to be difficult. However, the whole question of magnetically shielding the masses has been omitted. This will undoubtedly improve the situation.

Section 5 Acoustic Noise

Acoustic noise is another factor that will degrade the performance of a interferometric gravity wave antenna. The acoustic disturbance can propagate through the isolation system and move the test masses. The transfer function for an acoustic disturbance will probably be similar to the seismic wave transfer function.

The acoustic noise must be common in two interferometers to affect the limit that one is trying to place on Ω_{gw}. This will only be a problem for the full length-half length system at one site. This is because the speed of sound in air is so low, $v_s \sim 331m/s$. The analysis for this problem is identical to that for the seismic waves. If the acoustic wave is defined in terms of $s_a(\vec{x}, t)$, a spectral density

$$\langle s_a^2(x,t)\rangle_{av} = \int_0^\infty S_a(f)df \quad ,$$

and transfer function $T_a(f)$, then the limit that one can place on Ω_{gw} with the full length-half length system is

$$\Omega_{gw}(f) = \frac{5\pi c^2 f^3}{2G\rho_c L^2} S_a(f)|T_a(f)|^2 \left(\left[J_0\left(\frac{2\pi f L}{v_a}\sqrt{\frac{5}{4}} \right) - J_0\left(\frac{\pi f L}{v_a} \right) - 2J_0\left(\frac{2\pi f L}{v_a} \right) + 2 \right]^2 + \left[J_0\left(\frac{\pi f L}{v_a} \right) + J_0\left(\frac{2\pi f L}{v_a}\sqrt{\frac{5}{4}} \right) \right]^2 \right)^{1/2} .$$

This limit is independent of the length of integration time and the type of interferometer used. Unfortunately, the transfer function is not known and will have to be measured on the actual constructed system. Pressure fluctuations due to acoustic events will be monitored near each test mass chamber (LIGO Proposal: Vogt, 1989). This will enable one to remove interferometer events that also are registered as acoustic disturbances. It should also be noted that 1 km is about the largest distance for coherent acoustic noise. This is from common thunderstorm acoustic noise (Posmentier, 1974).

Section 6 Cosmic Ray Showers

High-energy particles that strike a test mass will cause it to move. This will be another noise term for the interferometers. The largest source of high-energy particles will be muons with energies greater than .1GeV. Weiss (1972) estimated that the position uncertainty of a given test mass will be about

$$x(f) \sim 10^{-20}/f^2 \quad cm/\sqrt{Hz} \quad .$$

For a correlation experiment that is intended to limit Ω_{gw}, this noise source will be unimportant because it is too small. However, it could influence a gravity wave burst search, and that is why detectors will be located at every LIGO building where there are test masses (LIGO Proposal: Vogt, 1989). In this way events registered in the interferometer that are in coincidence with events seen in the particle detectors can be discounted. The range of an air shower on the surface of the earth is about 1 km for muons of energy greater than 1 GeV. This would yield one particle per m^2 (Galbraith, 1958).

Section 7 Conclusion on Correlated Noise

This chapter addresses the noise terms that may influence a correlation measurement. In order for a particular noise to hinder the correlation it must enter and influence the two interferometers that are being used. For obvious reasons, this will be a larger problem for the full length-half length pair at one site and in the same vacuum system. However, the situation for this same site pair may not be hopeless.

Seismic noise will definitely be a problem. It will influence both systems at the same time. However, if the suspension and isolation system can perform as well as has been proposed (LIGO Proposal: Vogt, 1989), then this will not hamper a correlation.

An acoustic noise problem is somewhat of an unknown. At this point in time there is no way to predict what the transfer function between an acoustic wave and the mass displacement will be. One hopes that the locations of the interferometers will be far enough away from man made noise, and that the natural noise will be minimal. Still, the acoustic wave will have to couple to a given mass by traveling through the vacuum system, and through the isolation-suspension system. This is a very formidable task, but definitely not impossible. Further research on acoustic noise seems warranted.

Gas bursts from the wall of the vacuum system will influence both of the interferometers inside. The unknown here is the event rate and size of the bursts. The situation does not appear to be hopeless. However, only the actual observation of the characteristics of the system will settle this problem. The baking out of the vacuum system and the continual pumping may allow the influence of this effect to decrease with time. This is another area where further research seems warranted.

The biggest potential problem appears to be due to magnetic field fluctuations. The spectrum of the natural magnetic field fluctuations is estimated to be small enough so it will not severely restrict the experiment. However, fields from the power lines leading to the interferometer site, and the wiring inside the site could easily restrict the correlation limit. Care will have to be taken when the actual wiring is made.

The effect of all of these problems will be decreased by the extensive monitoring systems that will be employed at the interferometer sites (LIGO Proposal: Vogt, 1989). Events registered in the interferometer output that are found to be in coincidence with events registered in the monitoring systems can be removed.

There does not appear to be any problem with regard to common noise for the correlation between two systems on opposite sides of the continent. Aside from the reduced sensitivity to the SGWB, the only potential problem is due to common magnetic field fluctuations caused by lightning or by ionospheric phenomena. However, the spectral density of the field compiled over many months of observations in Malta and Guam is not too limiting even for two systems at a single location. Magnetic field events will definitely have to be considered in a gravitational wave burst search.

Chapter 8 Experimental Projects

Section 1 Introduction

This chapter contains a description of some of the experimental projects that I have undertaken in connection with the development of laser interferometric gravity wave detectors. There are countless laboratory tasks that must be done in order to produce the quality type of apparatus that we are striving to build. Almost every job is done with other members of the scientific team. Every task ties into the large scale plan for the construction of these interferometers. I have only addressed the projects that were primarily my personal responsibility. A comprehensive description of the laboratory work done recently by the M.I.T. gravity wave group can be found in Shoemaker, Fritschel, Giaime, Christensen, and Weiss (1990), Stephens, Saulson and Kovalik (1990), Kovalik and Saulson (1990).

Section 2 Fiber Optics

Optical fibers play an important role in the operation of a laser interferometric gravity wave antenna. When a fiber is placed between the laser and the input to the interferometer it has the effect of eliminating beam jitter, which otherwise would contribute noise to the system. A step index single mode fiber also acts as a mode cleaner by eliminating wavefront distortion. A single mode fiber prepares the beam into the fiber's HE_{11} mode, which is nearly the same as the TEM_{00} Gaussian beam mode. See Marcuse (1974, 1981, or 1982) for details on fiber modes. The optical fiber is also a useful way to bring the beam from a laser into and out of the vacuum system occupied by the interferometer. This eliminates the need of having to pass the beam through a window, or leaving photodetectors with their electronics in the vacuum system. The nonlinear optical properties of a fiber induced by stresses on it can be used to mimic the effect of $\lambda/2$ or $\lambda/4$ plates, thereby reducing the number of optical components that the beam must pass through, and hence reducing the number of potential spurious interferometers caused by multiple reflections. This section discusses the experimental work that I have done with optical fibers.

Single Mode Tests

The interferometers developed at the M.I.T. lab use argon ion lasers, with the wavelength of the light being $\lambda = .5145\,\mu$. Unfortunately, fiber optics manufactures tend not to produce single mode fibers for this specific wavelength. For fibers made for other wavelengths it is imperative that they be tested to see if they are actually single mode at $\lambda = .5145\,\mu$. This practice is still a good idea even when one uses fibers designed for the wavelength of choice, such as with $\lambda = 1.06\,\mu$ light from Nd:YAG lasers, where optical fibers are produced in abundance.

The fibers used for the $\lambda = .5145\,\mu$ light tend to be about 120μ in diameter, with about a 4μ core. The refractive index of the core is slightly higher than that of the cladding. The modes of a fiber are described in detail in Marcuse (1974, 1981) and Snyder (1969), but they are basically Bessel functions in the core and Hankel functions in the cladding, with the appropriate boundary conditions relating the two. Each mode is described by two eigenvalues: U is the eigenvalue used for the core solution, and W is the eigenvalue used for the cladding. The V-parameter of the fiber is defined to be

$$V = \sqrt{U^2 + W^2} = \frac{2\pi}{\lambda}\sqrt{n_1^2 - n_2^2} \quad ,$$

where n_1 is the core index and n_2 is for the cladding. The fiber is single mode, with only the HE_{11} mode propagating, if $V < 2.405$.

The single mode test I used consisted of scanning the output beam of the fiber with a slit-photodetector mounted on a computer driven translation stage. The measured intensity of the beam was plotted against the displacement of the translation stage, and a least squares fit to the data was made.

The function to which the beam intensity was fit was found via a method similar to the one developed by Gambling, Payne, and Matsumura (1976). They propagated the HE_{11} to the far field via Fraunhofer diffraction. The intensity distribution is then given by

$$I = A_1\left[\frac{U^2W^2}{(U^2-\alpha^2)(W^2+\alpha^2)}\left\{J_0(\alpha) - \alpha J_1(\alpha)\frac{J_0(U)}{U J_1(U)}\right\}\right]^2 \quad ,$$

where A_1 is the amplitude, U and W are the eigenvalues, and $\alpha = \frac{2\pi a}{\lambda}\sin\theta$. The fiber's core radius is a, and $\theta =$ the angle from the axis defined by the fiber.

One can express the angle θ as $\sin\theta = (x - x_c)/\sqrt{d^2 + (x - x_c)^2}$, where d is the distance between the fiber end and the slit, x is the distance variable along the direction that the slit travels, and x_c is the central point where the intensity is maximized.

My fitting routine also considered the next higher mode, namely, the HE_{21} mode. When this fiber mode is propagated to the far field via Fraunhofer diffraction its intensity distribution is

$$I = A_2\left[\frac{U_2^2 W_2^2}{(U_2^2 - \alpha^2)(W_2^2 + \alpha^2)}\left\{J_1(\alpha) - \alpha J_0(\alpha)\frac{J_1(U_2)}{U_2 J_0(U_2)}\right\}\right]^2 ,$$

where A_2 is the amplitude of this mode, U_2 and W_2 are its eigenvalues. These eigenvalues are still related to the V-parameter through $V = \sqrt{U_2^2 + W_2^2}$. When one has $V < 2.405$ this mode is cut off.

Figure 8.1 displays the intensity profile of the two modes. Note that the HE_{11} is very similar to a Gaussian.

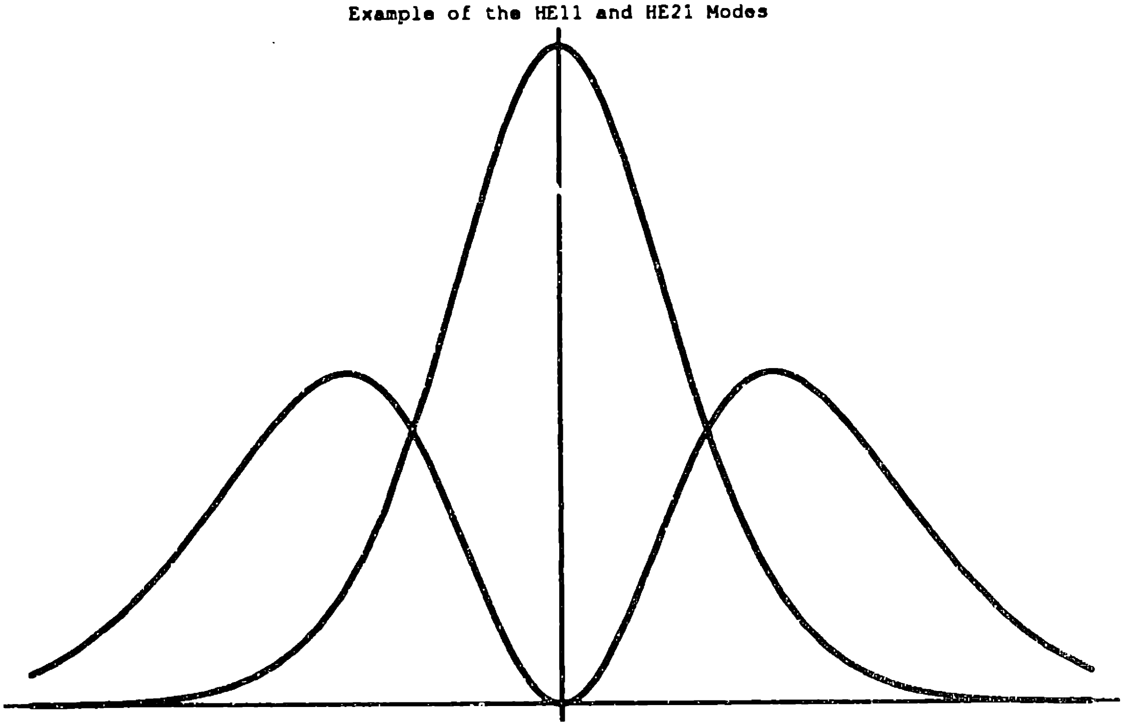

Figure 8.1 An example showing the intensity distribution for the HE_{11} mode, and the HE_{21} (with null in the middle).

A general least squares fit program developed by Jeff Livas (1987) was adapted to fit the beamscan to the far field HE_{11} mode. Once one knows the distance from the fiber to the scanning slit, a fit is made with the adjustable parameters A_1, x_c, U, W, and a. From this one can compute the V-parameter from the best fit eigenvalues, $V = \sqrt{U^2 + W^2}$. If $V < 2.405$ then the fiber is single mode. After this fit is accomplished it is compared with a fit to the far field distribution of both the HE_{11} and the HE_{21} modes. For this fit the adjustable parameters are A_1, A_2, x_c, U, W, U_2, and a. If a better fit can be achieved with the second mode present it would indicate that the fiber is not truly single mode. This is a second test.

A fiber manufactured by Lightwave Technology was tested using fitting method described above. The results from the a series of measurements are presented in Figure 8.2. The wavelength of the light was $\lambda = .5145\,\mu$. For the four scans presented in the table, no better fit was achieved when the second mode was included. The V-parameter for this fiber is below the cutoff of 2.405. A fit done to a Gaussian TEM_{00} mode was a factor of six worse in the relative χ^2. If one uses the values of $V = 1.9$, and $a = 1.7\mu$, then the index difference between the core and the cladding is $\Delta n = 4.7 \times 10^{-3}$.

Distance From Fiber To Slit (cm)	Fiber Core Radius (microns)	V-Parameter
1.3	1.6	1.8
2.0	1.7	1.9
3.2	1.8	2.0
8.8	1.8	1.8

Figure 8.2 Characteristics of the fiber derived from the best fit parameters.

Figure 8.3 shows the data and the best fit for the case where the fiber is 8.8 cm from the slit. The match is quite good.

High Power Fiber Test With Nd:YAG Laser

The use of high power lasers in a gravity wave interferometer will likely require the use of optical fibers that can handle the power. Brillouin scattering will ultimately limit the transmission of a fiber at high power. A test was made

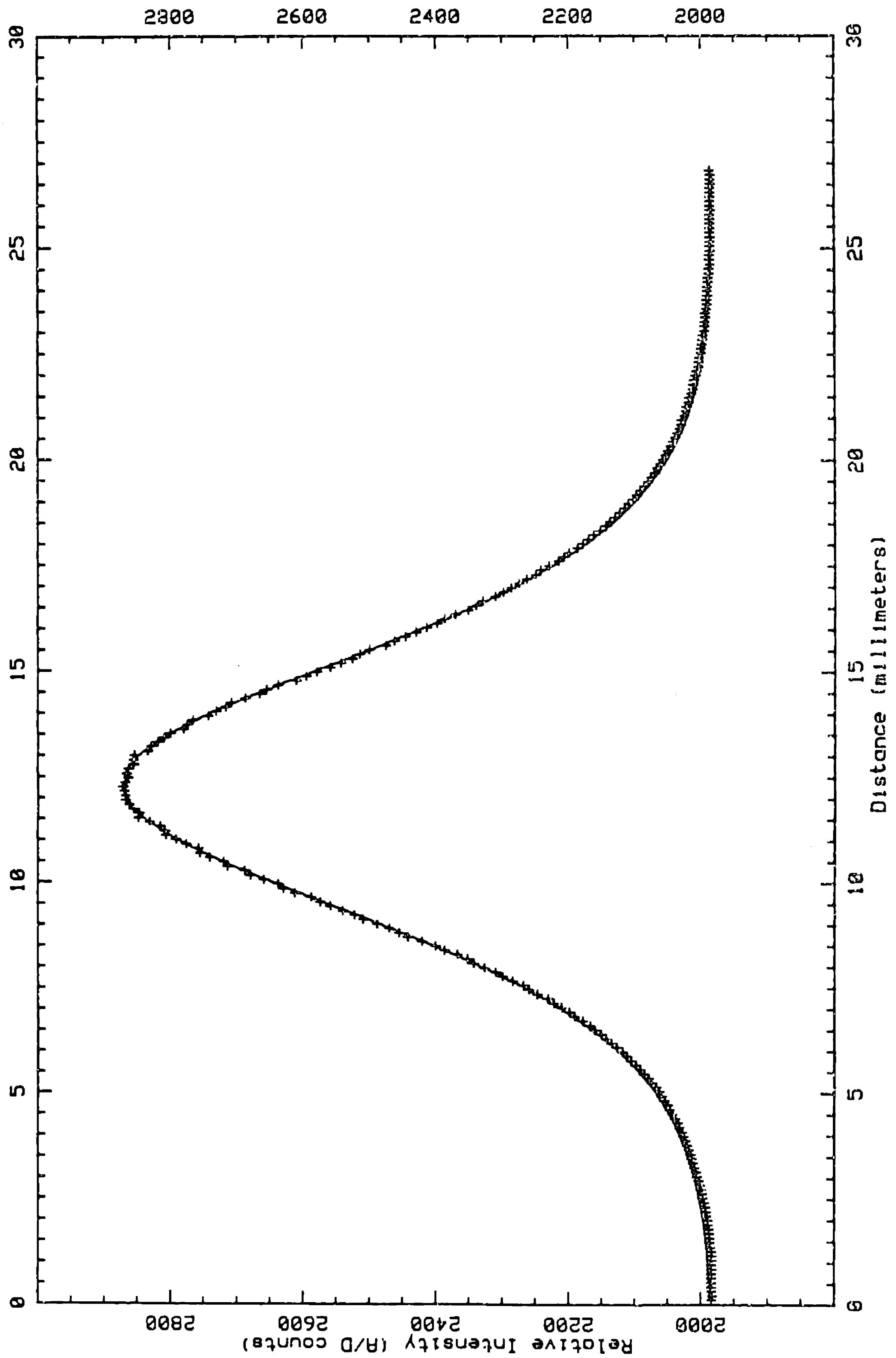
Distance (millimeters)
0
5
10
15
20
25
30
Relative Intensity (A/D counts)
2000
2200
2400
2600
2800

Figure 8.3

on a fiber made by Corning glass for use at 1.06μ. This fiber was tested and found to be single mode with a core radius of 4μ. The cladding radius was 120μ. A high power Nd:YAG slab laser was used to test the fiber. Coupling between the laser and the fiber was achieved with a microscope objective lens. The focal length of the lens was not of the ideal size for the beam and fiber parameters, but it was the closest one available at the time.

With 5.2 watts of input light I was able to get 2.4 watts through the fiber. This gives a 46% transmission for the lens-fiber system. As mentioned above, the coupling lens was less than ideal and it is likely that an even better transmission could be achieved.

There was one particularly annoying problem that arose during this test. When the input light power was greater than about 7 watts, the plastic jacket covering the fiber caught on fire. When the jacket was removed at the input end of the fiber the fire promptly started where the jacket began. The reason for the fire is that there is too much power in the cladding modes. These modes tend to decay away with the power going into the material at the boundary of the cladding. To kill cladding modes it is standard practice to strip the jacket and put black paint on the fiber. This will probably not be enough for high power situations. One will have to pass the section of fiber with its jacket stripped off through a large pool of index matching fluid. The pool of fluid will have to be big enough to absorb up to 50% of the incident light power.

Fiber Polishing

Because of the problems associated with surfaces in optical beams creating parasitic interferometers it has become standard practice to polish the ends of the optical fibers at an angle. In contrast to the trivial procedure of cleaving the fiber, polishing can be quite time consuming. The success rate for quality polishes can be quite low.

The problems associated with an optical fiber with flat, cleaved ends are real and dramatic. One can consider the fiber as a Fabry-Perot cavity. The intensity of light I_t, of wavelength λ, that is transmitted through a fiber of length h and core index n, in terms of the incident intensity, I_0, is given by

$$I_t = I_0 \frac{T^2}{(1 + R^2 - 2R\cos\delta)} \quad , \; where,$$

$$T = \frac{4n}{(n+1)^2} \quad , \quad R = \frac{(1-n)^2}{(1+n)^2} \quad , \ and,$$

$$\delta = \frac{4\pi}{\lambda} nh \quad .$$

For an index of $n \approx 1.5$ the minimum transmitted intensity, I_t^{min} is 15% less than the maximum transmitted intensity, I_t^{max}, or $I_t^{min} = .85 I_t^{max}$. This could potentially cause a great deal of amplitude noise in the system.

This effect was observed by wrapping a single mode fiber that was cleaved on both ends around a two inch diameter piezoelectric (PZT) cylinder. Three revolutions around the PZT were made. When the PZT was driven a 14.7% intensity fluctuation was observed, in excellent agreement with the Fabry-Perot effect. A fiber with one end polished at ~7° was also tested. No fluctuation was seen. The Fabry-Perot effect was eliminated. It should be noted that a temperature fluctuation of only 7×10^{-2}°C will produce a length change in a 3 meter fiber that is large enough to change the intensity of the transmitted light by that 15%.

In order for the Fabry-Perot effect to be eliminated the fiber should be polished with an angle greater than its numerical aperture (N.A.). The N.A. for a fiber is $N.A. = V\lambda/(2\pi a)$. For $V \sim 2.4$, $\lambda = .5145\mu$, and $a \sim 2\mu$, one has $N.A. \sim 6°$. When the angle on the end of the fiber exceeds the N.A. the reflected beam in the fiber will not be accepted back into the mode, and it will decay.

My method for polishing fibers is as follows. Strip the fiber of about 4 cm of its jacket. Paint the exposed cladding black to kill the cladding modes. I used quartz ferrules manufactured by A.T.&T. to hold the fiber. The ferrule should be quartz so that ultraviolet light can pass through. A hole that is $\sim 130\mu$ in diameter runs through the ferrule. The hole is filled with UV curing epoxy, and the fiber is slid through. Exposure to a UV lamp then cures the epoxy.

A jig was constructed to hold the ferrule as it was polished. A piece of aluminum with a surface area of about $5cm^2$ with a hole for the ferrule was the base for the jig. The smaller the surface area the better, as this surface gets polished along with the fiber ferrule. The hole in the aluminum should be drilled at an angle larger than the N.A. of the fiber. I usually had an angle of 7° to 8°. The hole should be snug for the ferrule. A clamping mechanism was attached to the top of the aluminum to hold the ferrule.

The polishing was done on a clean glass plate. The plate was cleaned with soap, water, and cotton balls. Polishing papers from 3M were used. The grit of the papers were 30μ, 12μ, 3μ, 1μ, and $.3\mu$. The 30μ paper was rinsed with running water and placed on the clean glass plate. The 30μ paper is used until the ferrule has been ground down so that it is flush with the aluminum holder. At this point the aluminum jig and ferrule are rinsed with running water (normal, unfiltered tap water was used without any problems), and with isopropyl alcohol. Do not remove the ferrule from the jig until the entire process to be described here is complete. The face of the fiber was then examined under a microscope. I made sure there were no major gouges in the fiber. If there were, the 30μ grind would have to continue to remove them. Also, the other end of the fiber was illuminated with a bright halogen lamp. One can see the white light coming out of the core at the other end when a microscope is used. A bright point of light, that is circularly symmetric, should be visible. This tells you two things: the fiber has not broken in the ferrule, and that the surface of the fiber at the core is not too rough. If all is well, the glass plate is recleaned and a rinsed piece of 12μ grit paper is placed on it. About ten figure eight strokes of a total length of about 10 cm should be done. Rotate the fiber jig by 90°, and do ten more strokes. Rinse the fiber ferrule and the jig with water and isopropyl alcohol, and examine it again under the microscope. Repeat this process with the 3μ grit paper. For the 1μ and $.3\mu$ grit papers reduce the number of figure eight strokes in each direction from ten to five.

After the $.3\mu$ polish has been completed, and the ferrule and jig are cleaned and examined under a microscope, a beamscan should be done. The fiber with its ferrule and jig assembly should tested with a laser. Light is coupled into the fiber on the end opposite the jig. A beamscan is done on the light exiting the polished end. The mode shape should be clean and without irregularities. If that is so, the process is complete and the ferrule can be removed from the jig. If defects in the beamscan are observed, the polishing should resume again, starting with the 3μ grit paper.

Constructing an Effective $\lambda/2$ and $\lambda/4$ Plate with an Optical Fiber

Optical fibers are highly birefringent when they are stressed. This can be a problem in that any movement of the fiber will induce polarization changes in the light. However, this birefringence can be put to constructive use. It is possible to mimic the effect of a $\lambda/2$ or $\lambda/4$ plate by stressing the fiber the right way (Lefevre, 1980).

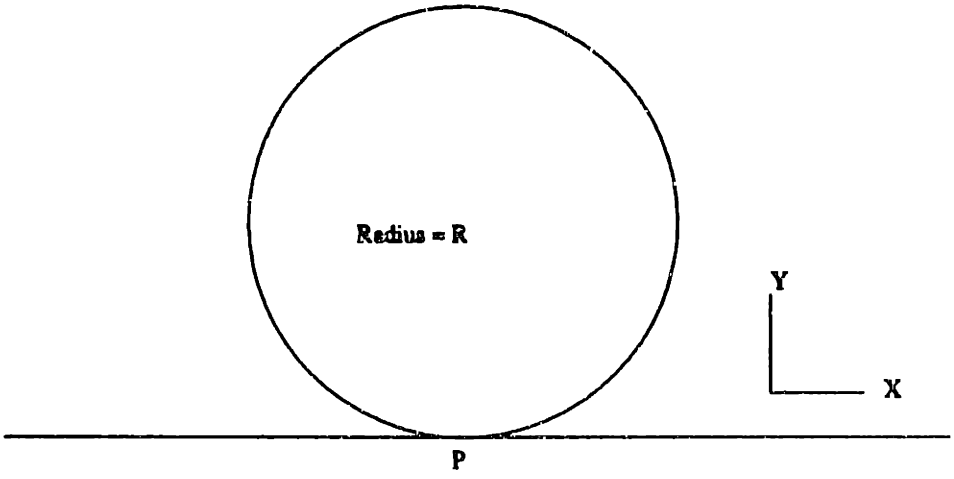

Figure 8.4 Circle of fiber of radius R.

A length of fiber is strung around a cylinder. Figure 8.4 shows an example of this. The cylinder has radius R. The circle of fiber is free to pivot about the pivot point P. This pivoting is about the X axis, which is labeled in the figure. This pivoting rotates the polarization. A rotation about the pivot point by an angle α will rotate the light's polarization by an angle β, given by $\beta = \alpha t$, where the value of t for $\lambda = .633\mu$ light in silica fibers is $t \sim .08$. The effect of stringing the fiber of radius r around the cylinder is to change the index difference between the two transverse axes of the fiber by $\delta n = a(r/R)^2$, where $a \sim .133$ for $\lambda = .633\mu$ light in silica fibers.

A fractional wave plate (a λ/m plate) can be mimicked by wrapping the fiber N times around a cylinder of radius R, given by

$$R = 2\pi a r^2 N m / \lambda \quad .$$

A device that has three pivoting cylinders was constructed for use. The cylinders were designed so that one revolution of the fiber would be the same as a $\lambda/4$ plate, and two revolutions would be the same as a $\lambda/2$ plate. In operation, the first and third cylinders have $N = 1$, and the central one has $N = 2$. With this arrangement the two $\lambda/4$ cylinders can control the ellipticity of the beam, and the one $\lambda/2$ cylinder can be used to adjust the polarization. The device with its fiber was tested against normal $\lambda/4$ and $\lambda/2$ plates. The device performed as well as the plates. This type of polarization adjuster is currently being used in the M.I.T. prototype interferometer.

Permanent Fiber Coupler and Vacuum Feedthrough

The usefulness of optical fibers in gravity wave interferometers comes with a price. The optical efficiency of fibers can be quite low if extreme care is not taken. The core diameter of a fiber that is single mode for .5145 micron light is only 4 microns. One must focus the laser light onto the core in such a way as to have a significant portion of this light transmitted through the fiber. This is where the difficulty lies. In order to maximize transmission one must bring the fiber end into the location of a 4 micron waist Gaussian beam. This means that one must be able to move the fiber end by increments of order one micron. When the proper alignment is achieved one counts on the fiber holder to be stable over reasonable periods of time.

The fiber difficulties described above can be addressed with the use of a permanently aligned fiber-lens system. This system was designed for use in the stationary interferometer at M.I.T., and will be used in the 5 meter hanging interferometer when it is constructed. Both the stationary interferometer, and the 5 meter hanging interferometer, are eventually to be operated in a vacuum system. At least four optical beams will have to be brought out of the vacuum to photodetectors and their associated electronics outside. Fibers will be used to bring the main beam to the interferometer inside the vacuum, and fibers will bring the multiple beams out of the vacuum. One will not have the liberty to manually align the fibers in the vacuum. A stable, aligned system is necessary. The vacuum feedthrough for the optical fibers is part of this system.

The most important ingredient of this system is a graded index (GRIN) lens. These lenses are small cylinders of length around 4 mm, and diameter of 2 mm. The lens has a quadratic index distribution, given by

$$n = n_0\left(1 - \frac{A}{2}r^2\right) \quad ,$$

where n_0 is the index at the center, r is the distance from the central axis of the cylindrical lens, and A is the quadratic index constant. See Nishizawa and Nishi (1984) for more GRIN details. A GRIN of length l will have a ray matrix, $\widetilde{M}$, of

$$\widetilde{M} = \begin{pmatrix} \cos\left(l\sqrt{A}\right) & \frac{\sin\left(l\sqrt{A}\right)}{n_0\sqrt{A}} \\ -n_0\sqrt{A}\sin\left(l\sqrt{A}\right) & \cos\left(l\sqrt{A}\right) \end{pmatrix} \quad .$$

A standard commercial lens (.23 pitch for .633 μ light from NSG America) with parameters $n_0 = 1.608$, $\sqrt{A} = 3.31/cm$, and $l = .43cm$ yielded good results. The ray matrix is

$$\widetilde{M} = \begin{pmatrix} .1129 & .18228cm \\ -5.416/cm & .1129 \end{pmatrix} .$$

This matrix displays the usefulness of the GRIN lens. If the incoming beam is displaced by 10μ, the exiting beam will move only 1.1μ. This provides a factor of about 10 in the resolution of movement. If the GRIN is attached to the optical fiber the alignment process will be simplified. The GRIN lens also provides a way of translating an angle change in the incoming beam to displacement in the outgoing beam. The GRIN described by the parameters above will give a 31μ displacement for a 1° change in the initial beam. This effect will be used for the fiber coupling system to be described below.

The GRIN fiber coupling scheme is illustrated in Figure 8.5. The fiber is in a quartz ferrule, with its end polished at an angle of about 6 degrees. The ferrule must be held at an appropriate angle, determined by Snell's law, for the maximum fiber transmission. For a 6 degree polish on the fiber face the GRIN must be rotated by 9 degrees with respect to the ferrule face. For the GRIN used, the beam comes to a focus at a distance of .21mm from the end of the lens. Because of the angle on the fiber face, and the fact that the ferrule must be held at another angle, it is impossible to bring the fiber core to the focal point unless the ferrule has the upper point of its face polished off too. This can be seen in Figure 8.5. Also, since the GRIN is only a couple of millimeters in diameter, the incoming laser beam will have to be focused into it. A lens with a long focal length typically maximizes the coupling. The exact lens depends on the parameters of the beam. A 50 cm lens is used in the M.I.T. stationary interferometer system. If the GRIN and the fiber are attached together, a translation or rotation of the system with respect to the incoming beam can be used to move the light onto the fiber core. The next problem to address is joining the GRIN and the fiber ferrule.

The components of the permanently aligned fiber system are illustrated in Figure 8.6. A piece of aluminum, roughly 2 inches by 1 inch by .5 inch is the foundation. A hole is machined for the GRIN. It is held in place with UV curing epoxy. This epoxy is not really vacuum compatible, but only a tiny bit is needed. The fiber and ferrule are held in a cylindrical aluminum chuck. The chuck is machined so that the ferrule fits snugly in the middle of the cylinder. Torr Seal

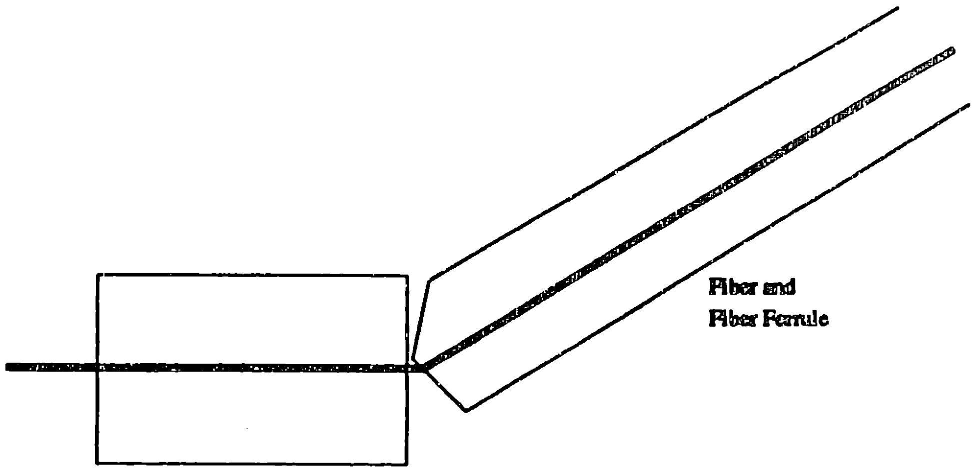

Figure 8.5 Fiber ferrule and GRIN lens system.

epoxy is used to make the snug fit permanent. Torr Seal has a low outgassing rate, so more of it may be used, but not an excessive amount. The aluminum piece holding the GRIN has been machined to accommodate the ferrule piece. When the fiber is aligned with the GRIN, the two aluminum pieces are almost touching, separated by a couple of millimeters. The GRIN piece is held in place with respect to an incoming laser beam. The fiber ferrule piece is held on an X-Y-Z translation stage, and is moved around until there is a satisfactory amount of light transmission through the fiber. A satisfactory transmission efficiency for the system is at least 50%, but typically 60%. When the proper alignment has been found the two aluminum pieces are adjoined with Torr Seal. When the system has been aligned one should note the location of the beam reflected off the surface of the GRIN with respect to the incoming beam. This will make future alignments trivial. It takes at least 24 hours for the Torr Seal to cure.

The Torr Seal does not creep while it sets. Coupling efficiencies for the GRIN-fiber system as high as 70% were achieved both before and after the Torr Seal had set. As mentioned above, one needs to note the location of the beam reflected off the front of the GRIN with respect to the incoming beam. When used as a reference, the reflected spot allows easy realignment when the fiber is moved.

After the fiber-GRIN system has had its Torr Seal set, it looks like the illustration in Figure 8.7. This system is mounted on a flex mount, which in turn is mounted on a X-Y-Z translation stage. The flex mount used was a 2 inch by 2 inch by .25 inch piece of aluminum with grooves machined in it so that it

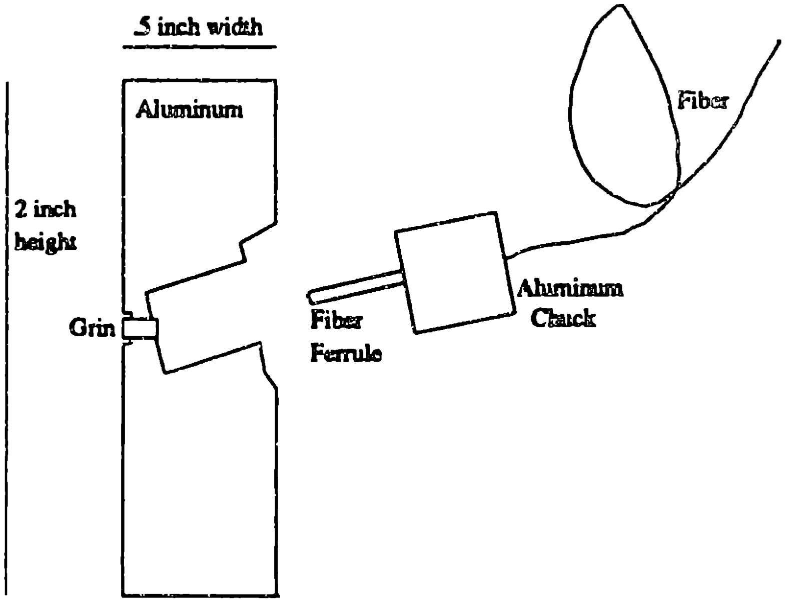

Figure 8.6 Permanent fiber-GRIN alignment system. The GRIN lens is held in the aluminum block with UV curing epoxy. The fiber ferrule is held in its aluminum chuck with Torr Seal.

would bend when it was driven by ball bearings on the end of 80 turn per inch screws. Two directions of rotations can be made. A quarter turn of an 80 turn per inch thread screw driving a one inch moment arm, which the flex mounts have, will cause the beam exiting the GRIN to move by 5 microns. Finer turns than a quarter of a revolution can be achieved, so the system has just the right range for aligning a fiber. The X-Y-Z translation stage is also driven by 80 turn per inch thread screws. A quarter turn of these screws will also move the beam exiting the GRIN by about 5 microns.

This completed system is easy to align, and stable over long periods of time. As mentioned above, this system will operate in a closed vacuum system. It may be necessary to attach the 80 turn per inch threaded screws to motors. Because of the GRIN it should be very easy to maintain alignment of the system in the vacuum.

The construction of a vacuum feedthrough system was also part of this project. By using an optical fiber to bring the beam into the vacuum it is not necessary to use windows, which can cause reflections, scatter light, and provide further losses. The feedthrough makes use of a modified Cajon vacuum fitting. The Cajon fittings are soldered into a flange. The fiber will pass through a brass plug, as illustrated in Figure 8.8. This brass plug fits into the Cajon fitting, and the

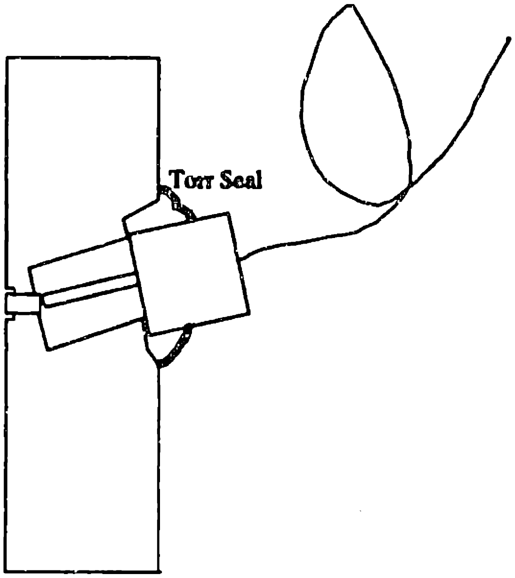

Figure 8.7 Permanent fiber-GRIN alignment system. Fiber is aligned with GRIN, and the aluminum chuck has been Torr Sealed to the aluminum block. This complete system is mounted on a flex mount for angle adjustment. and the flex mount is attached to an X-Y-Z translation stage.

vacuum seal is achieved by the compression of an O-ring around the snout of the plug. Two systems are illustrated in Figure 8.8. The top system assumes that a fiber ferrule is to be brought into the vacuum. The brass plug has a hole through it to allow the ferrule to pass. The hole is extremely small at the atmosphere end of the plug. It was made with #78 drill. The fiber has a plastic jacket. The jacket is chemically removed from a section of the fiber, and the fiber and plug are attached with Torr Seal to maintain a vacuum. If the jacket is not removed, air will leak in between the jacket and the fiber. The ferrule has to be able to fit through the hole of the Cajon fitting. This allows one to insert or remove the fiber at will. The bottom plug is slightly different. Here it is assumed that a ferrule is to be on the outside of the vacuum. The GRIN-fiber contraption on the inside of the vacuum will not fit through the Cajon fitting, and the brass plug can not be brought through the fitting into the vacuum. This makes the top system impossible for this arrangement. To fix this, one makes a larger hole in the plug. A small brass chuck is made, and the fiber is threaded through it. The fiber jacket is removed, and Torr Seal is used to attach the two. This chuck is then connected to the brass plug with Torr Seal. In order to remove the fiber it is necessary to chemically dissolve the Torr Seal between the chuck and the plug with Oak Strip. This takes a bit of patience, but the fiber can be saved.

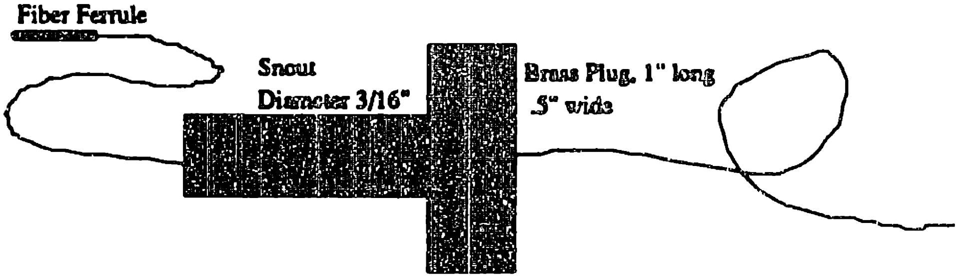

Case A: Vacuum to the Left, Ferrule to the Left

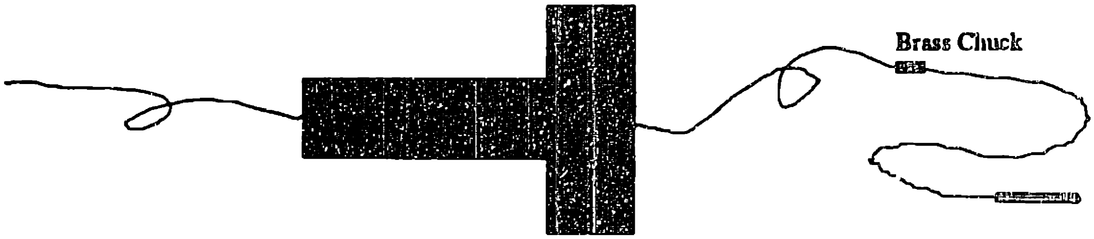

Case B: Vacuum to the Left, Ferrule to the Right.

Figure 8.8 The vacuum feedthrough plugs for the optical fibers.

The vacuum feedthrough has been tested. It works as expected. The fiber jacket tends to outgas a bit of water in the vacuum, but this can be eliminated by baking the fiber for a few hours at a reasonable temperature, say 50 C°. One must also remember to thread the fiber through the chuck and plug before ferrules are placed on both ends of the fiber. This system is currently being used in the stationary test interferometer at M.I.T. See Shoemaker, Fritschel, Giaime, Christensen, and Weiss (1990) for a detailed description of the rest of this experiment.

Section 3 Low Noise High Voltage Amplifier for the Mass Suspension System

It will be extremely important to isolate the test mass mirrors of a laser interferometric gravity wave antenna from ground motion. Therefore, much work has gone into the development of isolation and suspension systems. Because many of the expected sources of gravitational radiation will occur at low frequencies it is necessary to try and construct an interferometer that is shot noise limited below

100 Hz. The best sensitivity for a system of interferometers trying to measure the energy density of a stochastic gravity wave background, $\Omega_{gw}(f)$, will occur at the lowest frequency that the interferometers are shot noise limited.

The motion of the test masses of the interferometer will be partially controlled by electrostatic plates, and or magnets that are part of the damping servo system. A high voltage, low noise amplifier was constructed for use in the electrostatic loop of the isolation system developed at the M.I.T. lab. See Stephens and Saulson (1990) for a description of this double pendulum system. The amplifier must be low noise so it will not contribute to the mass motion. It must operate at a high voltage to allow it to have a large dynamic range. And, it must have a large bandwidth to allow it to operate over a useful range of frequencies. The displacement noise, $x(f)$ (in $cm/\sqrt{Hz}$), of a mass, m (in grams), produced by a voltage fluctuation, $V(f)$ (in $Volts/\sqrt{Hz}$), on top of the bias voltage V_b (in $Volts$), is

$$x(f) = \frac{AV_bV(f)}{16\pi^3 x_0^2 m(300)^2} \quad ,$$

where x_0 is the distance between the mass and its electrostatic pushing plate, and A (in cm^2) is the area of the plate.

Figure 8.9 displays the circuit diagram of the amplifier that was developed. The gain is 50, with the signal being added onto the bias voltage, which is normally 400 Volts. The output can range from 0 to 800 Volts, and the bandwidth of this version is 100 KHz. The noise of the present design should be dominated Johnson noise of the resistor labeled RS, which has a value of 150Ω. This yields a noise of $1.6nV/\sqrt{Hz}$ at the input of the op-amp labeled V1. This op-amp is a LT-1028 from Linear Technology, which has an input noise voltage of $1.0nV/\sqrt{Hz}$. With a gain of 50, the output voltage noise due to RS should be $80nV/\sqrt{Hz}$. Since this is a high voltage device, many of the components must have appropriate tolerances. The resistors R72, R69, R1, R41, Ry, R40, and RZ are all wire wound resistors from Dale and are rated for 30 watts. The capacitors CW, CX, CY, and CZ must be able to tolerate 400 Volts, and should be made from metalized mylar. The amplification of the signal voltage, VIN, to a high voltage is accomplished with the three MOSFETs, F1, F2, and F3. The MOSFET used was a MTM1N100 by Motorola. It is rated for 1 KV DC and 1 amp DC. The applied power supply voltage, labeled HV, was 800 Volts.

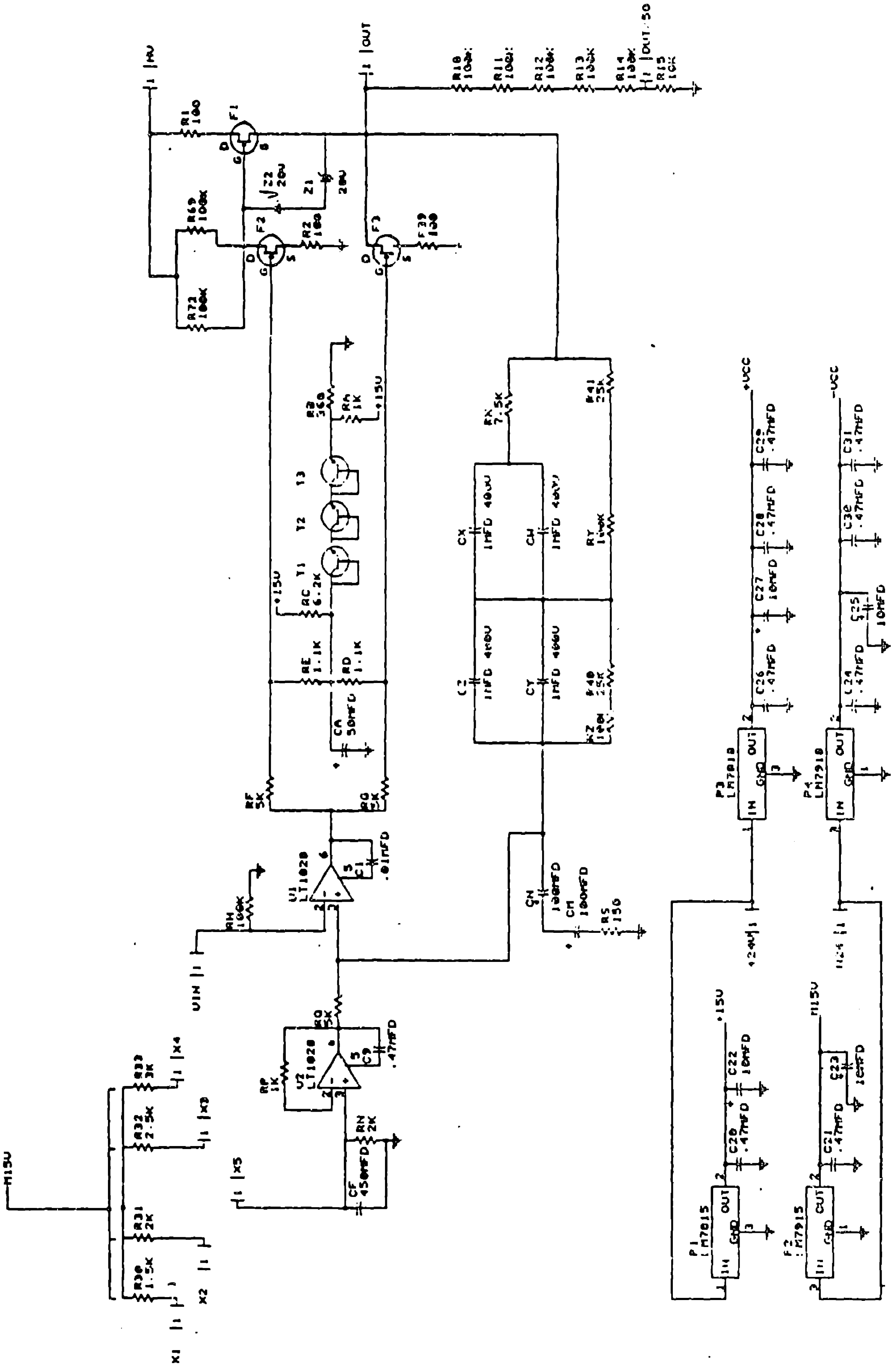
HV
OUT
R1 100
F1
Z2 20V
Z1 20V
R69 100K
R72 100K
F2
R2 100
F3
F39 100
R10 100K
R11 100K
R12 100K
R13 100K
R14 100K
OUT 50
R15 10K
RB 360
RA 1K
+15V
T1
T2
T3
RC 6.2K
RE 1.1K
RD 1.1K
CA 50MFD
RF 5K
RG 5K
U1 LT1028
C1 .01MFD
RM 100K
VIN
RO 5K
U2 LT1028
RP 1K
C9 .47MFD
RN 2K
CF 450MFD
X5
X4
X3
X2
X1
R33 3K
R32 2.5K
R31 2K
R30 1.5K
M15V
RX 7.5K
R41 25K
CX 1MFD 400V
CW 1MFD 400V
RY 100K
CZ 1MFD 400V
CY 1MFD 400V
R40 25K
RZ 100
CM 100MFD
RS 150
+VCC
C29 .47MFD
C28 .47MFD
C27 10MFD
C26 .47MFD
P3 LM7818
-VCC
C31 .47MFD
C30 .47MFD
C25 10MFD
C24 .47MFD
P4 LM7918
+24V
-24V
+15V
C22 10MFD
C20 .47MFD
P1 LM7815
M15V
C23 10MFD
C21 .47MFD
P2 LM7915
IN
GND
OUT

Figure 8.9

One of the unique features of this amplifier is its temperature compensation system. Under normal operation, with no input voltage, the MOSFETs will have 400 Volts across them with a drain-source current of about 20 mA, which will result in 8 watts of power that needs to be dissipated. They will heat up. The MOSFETs gate-source voltage versus temperature relationship was measured to be $dV_{gs}/dT \sim -6mV/°\mathrm{C}$ from 20°C to 100°C. The network of the three npn transistors, labeled T1, T2, and T3 compensates for the voltage change of the MOSFETs. The MOSFETs and the transistors are all mounted together on the same heat sink plate. This way they will have the same temperature. The npn transistors used were MJE521, and they had a collector-emitter voltage versus temperature relationship that was measured to be $dV_{ce}/dT \sim 2mV/°\mathrm{C}$ from 20°C to 100°C. The three transistors in series will virtually cancel a voltage change on the gate of MOSFETs F2 or F3, that is caused by a temperature drift.

Figure 8.10 displays the transfer function and frequency response of the amplifier displayed in Figure 8.9. Note that the 3dB point is above 100 KHz. The transfer function had the gain of 50 divided out by a voltage divider in order to spare the spectrum analyzer. The output noise is displayed in Figure 8.11. It has been passed through a $\div\frac{3}{2}$ voltage divider, so the true output noise is $135nV/\sqrt{Hz}$, yielding an input noise of $2.7nV/\sqrt{Hz}$. The dynamic range of the amplifier was about 700 Volts, peak to peak (p-p), up to 2.5 KHz.

One can make a trade-off between noise, and bandwidth and dynamic range with this amplifier. If one changes the capacitors CW, CX, CY, and CZ from 1 μF to 3 μF, and capacitors CM and CN from 100 μF to 300 μF, then the resistor RS can be reduced to 50Ω from 150Ω. This will reduce the predicted input noise by $\sqrt{3}$ to a value of $0.9nV/\sqrt{Hz}$. However, the bandwidth drops to 7 KHz. Figure 8.12 shows the transfer function, with the gain of 50 divided out. For this configuration the 3dB point occurs at 7 KHz. Figure 8.13 shows the noise, which has been passed through a $\div\frac{3}{2}$ voltage divider, so the true output noise is $98nV/\sqrt{Hz}$, yielding an input noise of $2.0nV/\sqrt{Hz}$. This noise plot exhibits many spikes at particular frequencies. These were due to the high voltage power supply. It was later discovered that these could be reduced by inserting an appropriate capacitor between the high voltage input and ground. The dynamic range for this set-up is about 650 Volts p–p up to 1 KHz, 400 Volts p-p at 2.5 KHz, and 300 Volts p-p at 5 KHz.

When a value of .33 μF was used for capacitors CW, CX, CY, and CZ, a value of 33 μF for CM and CN, and 500Ω for RS, the bandwidth was found

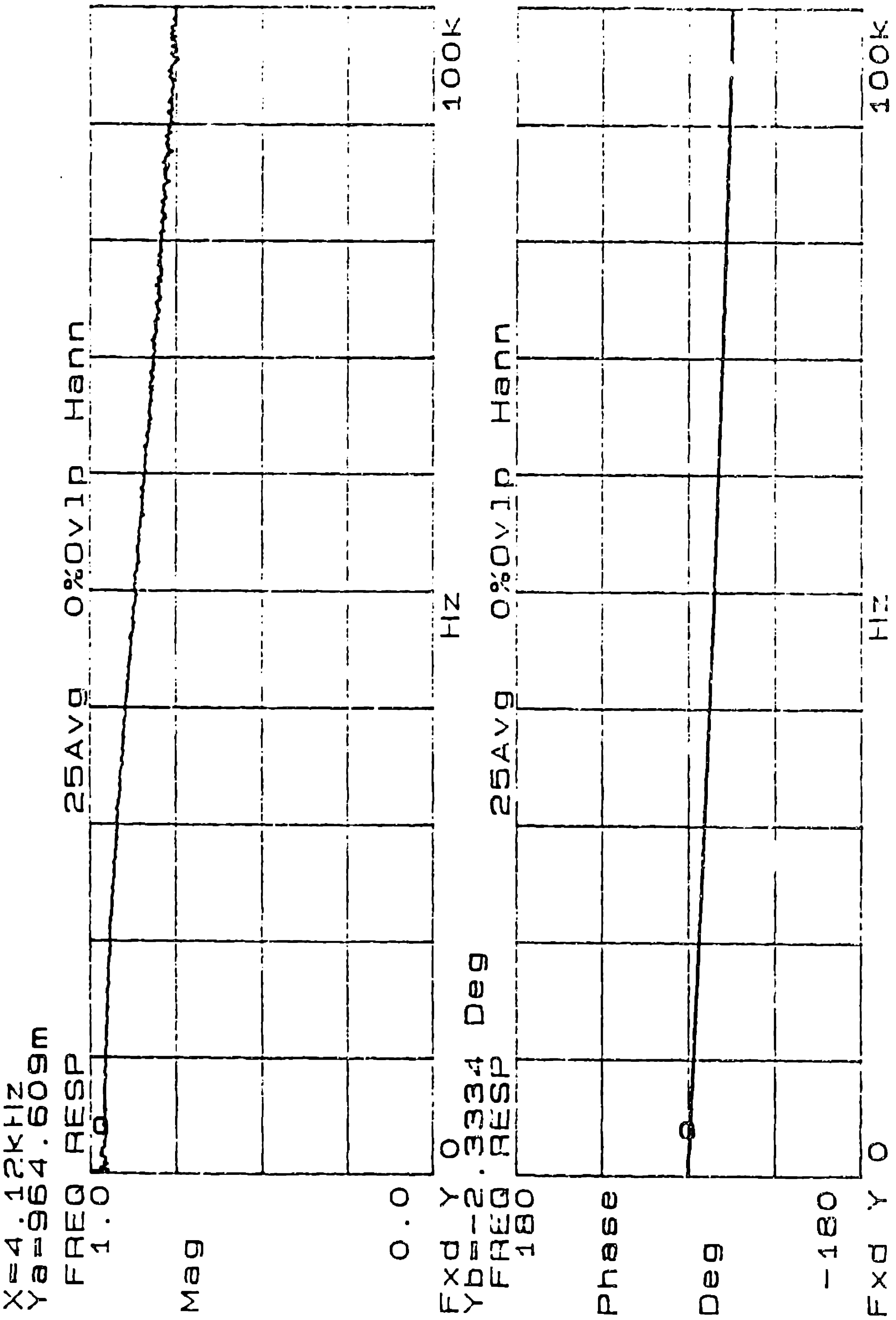
X=4.12kHz
Ya=964.609m
FREQ RESP
25Avg 0%Ovlp Hann
1.0
Mag
0.0
Fxd Y 0
Hz
100K
Yb=-2.3334 Deg
FREQ RESP
25Avg 0%Ovlp Hann
180
Phase
Deg
-180
Fxd Y 0
Hz
100K

Figure 8.10

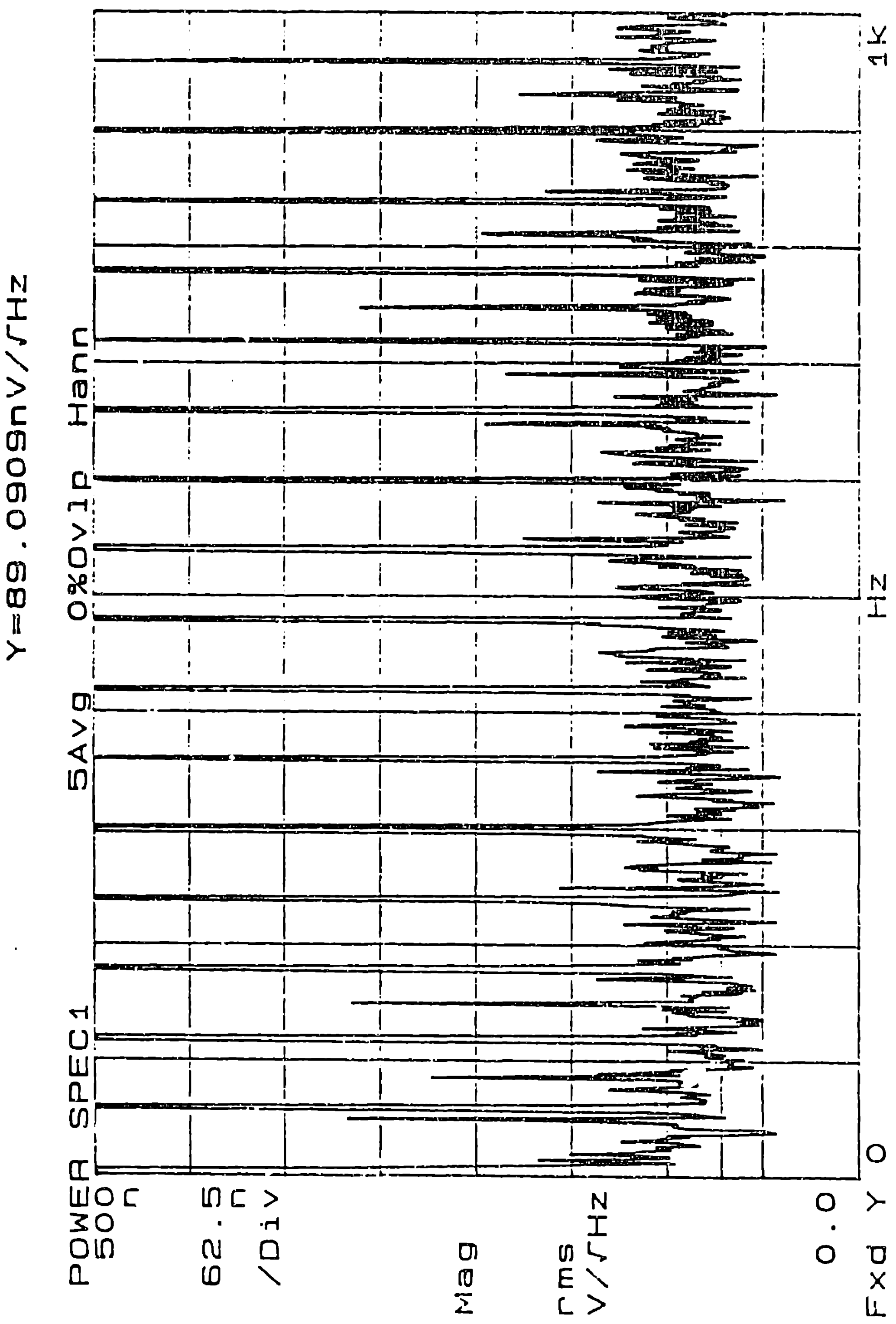

POWER SPEC1 5Avg 0%0vlp Hann
Y=89.0909nV/√Hz
500 n
62.5 n
/Div
Mag
rms
V/√Hz
0.0
Fxd Y
0
Hz
1k

Figure 8.11

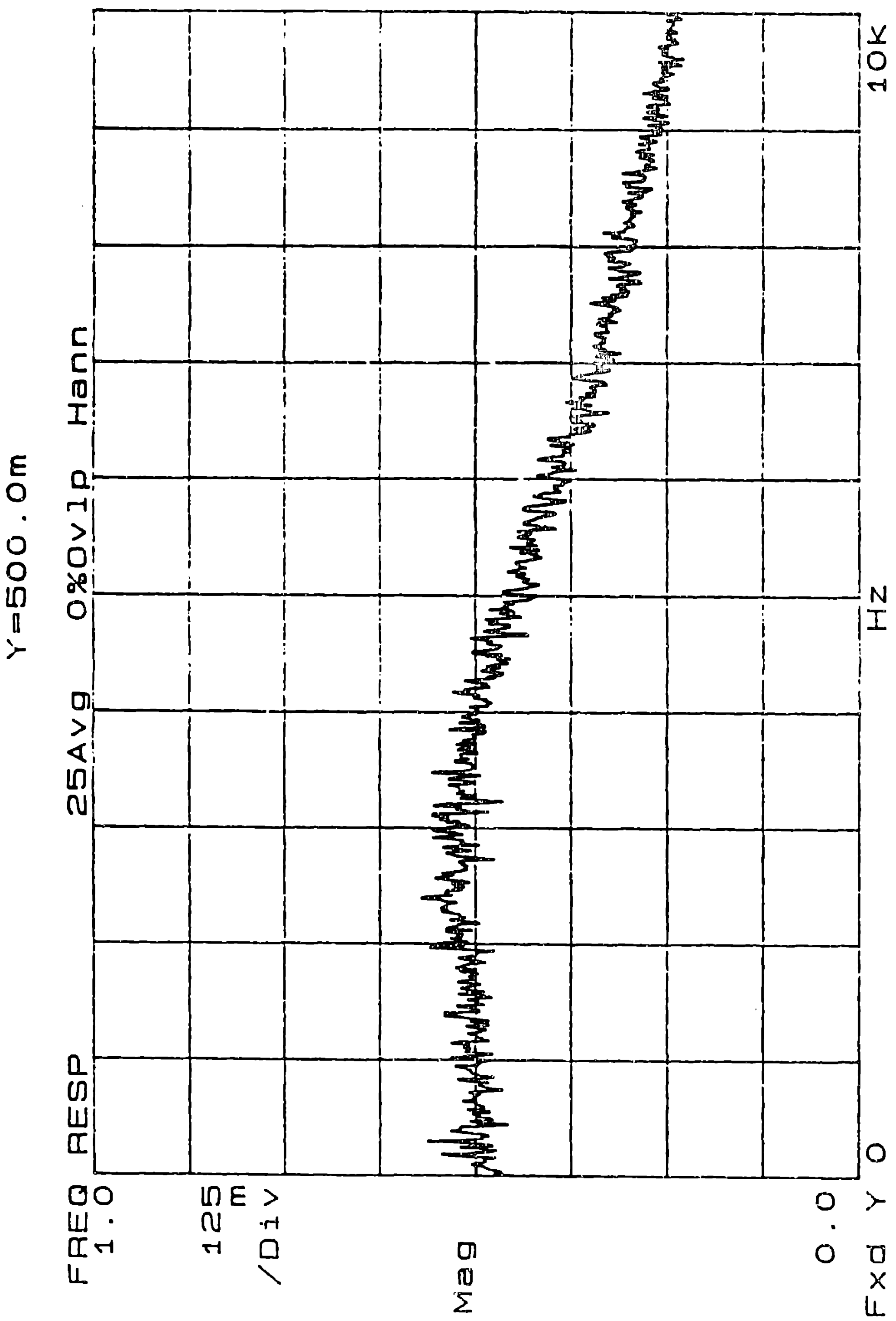
Y=500.0m
FREQ RESP 25Avg 0%0vlp Hann
FREQ 1.0
125 m /Div
Mag
0.0
Fxd Y
0
Hz
10K

Figure 8.12

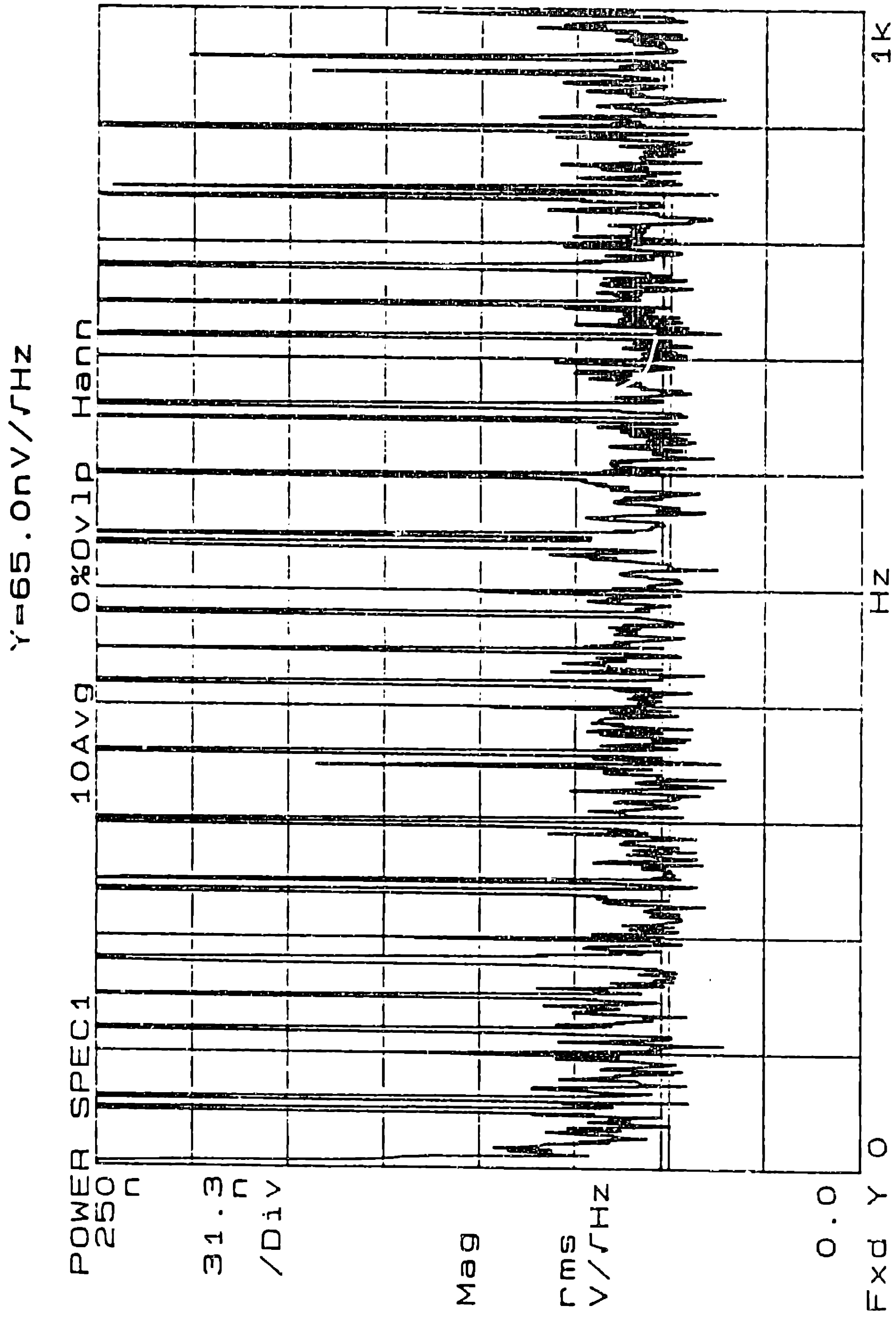
POWER SPEC1 10Avg 0%Ovlp Hann
Y=65.0nV/√Hz
250
n
31.3
n
/Div
Mag
rms
V/√Hz
0.0
Fxd Y
0
Hz
1k

Figure 8.13

to be much larger than 100 KHz (out of range of the spectrum analyzer used). The output noise was measured to be $150nV/\sqrt{Hz}$, which gives an input noise of $3.0nV/\sqrt{Hz}$.

It should be noted that the input noise value of $2.0nV/\sqrt{Hz}$ will translate into a distance displacement noise of $2.0 \times 10^{-17} cm/\sqrt{Hz}$ at 100 Hz for the double pendulum isolation system developed by Stephens and Saulson (1990).

Chapter 9 Conclusion

In this thesis I have addressed the issue of detecting the stochastic gravitational wave background (SGWB) with laser interferometric detectors. The Laser Interferometer Gravitational wave Observatory (LIGO) will be trying to detect the cosmologically produced SGWB. The analysis of this problem is presented in the thesis.

Chapter 2 contains a review of the expected sources of the SGWB. These spectra range from $10^{-18}Hz$ to $10^{14}Hz$. A summary of the experimental and observational constraints on the SGWB is also located in chapter 2. There are many predicted spectra that fall within the LIGO's range of detectability. Cosmic strings will produce an abundance of gravitational radiation through vibrations on these extremely taut objects. The constraints that the LIGO system will be able to place on cosmic strings will be more stringent than the pulsar timing limits. Successful observations by LIGO will be able to confirm or deny the existence of cosmic strings. A background fuzz of gravitational radiation will also be produced by the coalescence of neutron star binary systems in other galaxies. The predicted intensity of this source is just within the level of detectability of the planned advanced LIGO interferometers. Certain equations of state in the early universe will result in a gravity wave background that can be detected. For instance, if the equation of state is $p = -\rho/3$ from the Planck time to $10^{-27}s$ then the gravity waves produced by the acoustic waves during this primordial time will be seen by LIGO. Certain phase transitions in the early universe may result in observable gravity waves. There are many sources of gravitational radiation that LIGO may see. However, there is much uncertainty as to what exactly took place early in the history of our cosmos. Who knows what may have happened. The LIGO must look, for no other reason than to just look, regardless of the predictions. Only observation of the universe will give evidence to its correct history.

In chapter 3 I have presented my results for the general transfer functions for the interferometers that will likely be used by LIGO, and other kilometer length interferometric antennas around the world. These general transfer functions give the response of the interferometer to a gravity wave coming from any direction, with any polarization, and with any frequency. The transfer functions are necessary for a general analysis of SGWB detection because this radiation background is an ergodic stochastic ensemble of waves that impinge on the interferometer from all directions, with random polarization, and with a broad range of frequencies. The interferometers considered are the standard delay line and Fabry-Perot systems, along with the recycled light adaptations to these designs.

Chapter 4 contains my analysis of how one should optimally align two interferometers that are located anywhere on the earth. This analysis is done so that the probability for detecting the SGWB is maximized. However, this analysis is equivalent to optimizing the prospect for the joint detection of a randomly polarized burst event with two detectors. My solution is equivalent to the earlier solution by Schutz and Tinto (1987). The solution given in chapter 4 is much simpler than theirs. One need not depend on a long computer calculation, instead a proper choice of the coordinate system leads to a one line answer. The ambiguity in the published (and unpublished) results of Schutz and Tinto (1987), and Gürsel and Tinto (1989), is also addressed.

Chapter 5 contains an in-depth examination of the correlation experiment involving two, or more, interferometric detectors. The dependence of the correlation function on the interferometer design is investigated. The trade-off between strain sensitivity (in $strain/\sqrt{Hz}$, $h(f)$) and bandwidth for the dual recycling interferometer is explored, with the result that the best sensitivity does not give the best limit on the SGWB. The influence of detector orientation and separation on the correlation function is investigated. Optimum filtering is also addressed. Finally, the sensitivity of this correlation experiment is calculated. The advanced LIGO system of a full length and a half length interferometer at one site will be able to limit the energy density of the SGWB to $\Omega_{gw}(f) < 2\times 10^{-10}$ at 100 Hz with $10^7 s$ of integration time. Two interferometers, one in California and one in Maine, will be able to attain a limit of $\Omega_{gw}(f) < 6 \times 10^{-9}$ at 126 Hz. The ultimate LIGO configuration of three full length and three half length interferometers at one site, and three full length interferometers at the other site will be able to constrain the energy density to $\Omega_{gw}(f) < 4 \times 10^{-11}$ at 100 Hz.

In chapter 6 the statistical analysis of the correlation experiment is presented. The limits that can be achieved are calculated via the Neyman-Pearson criteria. The analysis is extended to the case where more than two detectors are used. The analysis also considers the gain in information by using a full length and a half length interferometer at the same site. Other coherence statistics are investigated, with the result that the direct correlation experiment provides the best means of measuring the SGWB. The effect of non-Gausian noise is considered, with the conclusion that it will not adversely affect the experiment if the LIGO interferometers perform as well as the current prototypes. The data analysis task is addressed, with the conclusion that the experiment can be done with current technology.

The question of correlated noise in two interferometers is investigated in chapter 7. This problem will be most significant for the case where there is a full length, and a half length interferometer at the same site and in the same vacuum system. Seismic noise will not be a problem if the proposed mass isolation system performs as well as predicted. The effect of acoustic noise is somewhat uncertain, but it should be less of a problem than seismic noise. Cosmic rays should not be a problem. Column density fluctuations in the vacuum will, however, be a problem. It will be important to reduce this effect by baking the walls of the vacuum system, and by using proper materials. In order for one to constrain the SGWB energy density to $\Omega_{gw}(f) < 10^{-10}$ at 100 Hz in a $10^7 s$ correlation between the full length, half length system, the column density fluctuations must be, $\delta\sigma(f) < 200 \ \ molecules/cm^2/\sqrt{Hz}$. Magnetic field fluctuations will also be a problem. The natural magnetic field fluctuations will not be at a level that will severely restrict the correlation, however power lines in the vicinity of the site, and wiring inside the site, will probably pose a problem. A limit of $\Omega_{gw}(f) < 10^{-9}$ at 100 Hz can be achieved if the magnetic field fluctuation is $B(f) < 10^{-9} gauss/\sqrt{Hz}$. Common noise in systems separated by a continental distance will not be a problem for a correlation experiment. However, common burst events due to lightning will be a problem, and extensive magnetic field monitoring at the sites must be done.

Some of my experimental work on the development of laser interferometric gravity wave antennas is presented in Chapter 8. This includes my work on fiber optics, and the development of a low noise, high voltage, high bandwidth amplifier for the mass suspension system.

In summary, the prospects for making interesting limits on the SGWB are good. The LIGO system will be able to see certain sources if they exist. Interesting astrophysical and cosmological measurements will be done. Gravitational radiation could be the unique cosmological fossil needed to help unravel the history of our universe.

Appendix A: Gravity Wave Fourier Transform

In this the appendix the gravity wave will be expressed as a four dimensional Fourier transform. One starts by expressing the gravity wave , h , as a function of four variables, three spatial and time, the proper Fourier representation is:

$$h(\vec{\mathbf{x}},t) = \int d^4k\tilde{h}\left(\vec{\mathbf{k}},\omega\right)e^{i\left(\vec{\mathbf{k}}\cdot\vec{\mathbf{x}}-\omega t\right)}$$

$$= \int d^4k\tilde{h}\left(\vec{\mathbf{k}},\omega\right)e^{i\left(\vec{\mathbf{k}}\cdot\vec{\mathbf{x}}-\omega t\right)}\delta\left(\vec{\mathbf{k}}^2-\omega^2\right)$$

The delta function in the last equation is due to the fact that h must satisfy :

$$\left(\vec{\nabla}^2-\frac{\partial^2}{\partial t^2}\right)h(\vec{\mathbf{x}},t) = 0$$

Now comes the expansion of the delta function. The claim is that :

$$\delta\left(\vec{\mathbf{k}}^2-\omega^2\right) = \frac{1}{2\left|\vec{\mathbf{k}}\right|}\left(\delta\left(\left|\vec{\mathbf{k}}\right|+\omega\right)+\delta\left(\left|\vec{\mathbf{k}}\right|-\omega\right)\right)$$

One gets this from the following :

$$\int f(x,y)\delta\left(q(x,y)\right)dx = \int f(x,y)\delta(\,q(x,y))\left(\frac{\partial x}{\partial q}\right)_y dq$$

$$= \left(\frac{f(x,y)}{\left(\frac{\partial q}{\partial x}\right)_y}\right)_{q=0}$$

For the delta function above, $q\left(\vec{\mathbf{k}},\omega\right) = \vec{\mathbf{k}}^2-\omega^2$, which implies $\left(\frac{\partial q}{\partial\omega}\right) = -2\omega$, and hence, the 2ω in the denominator. After a little algebra, and demanding that $h_{ij}(\vec{\mathbf{x}},t)$ be real the final result is:

$$h_{ij}(\vec{\mathbf{x}},\mathrm{t}) = \int\frac{d^3\vec{\mathbf{k}}}{2\omega}\left[e^{i\left(\vec{\mathbf{k}}\cdot\vec{\mathbf{x}}-\omega t\right)}\left\{\widetilde{h_+}\left(\hat{\mathbf{k}},\omega\right)\mathrm{e}^{+}_{\mathrm{ij}}\left(\hat{\mathbf{k}},\omega\right)+\right.\right.$$

$$\left.\left.\widetilde{h_\times}\left(\hat{\mathbf{k}},\omega\right)\mathrm{e}^{\times}_{\mathrm{ij}}\left(\hat{\mathbf{k}},\omega\right)\right\}+\ C.C.\right]$$

Figure B. 1 Michelson delay line interferometer.

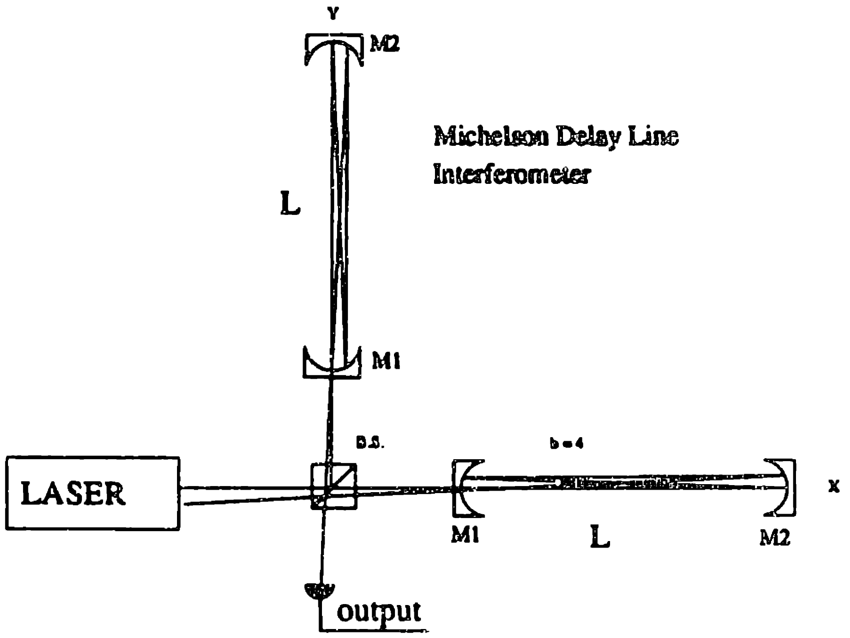

Appendix B: Shot Noise Limit for an Interferometer

The laser light entering an interferometer has a power P, with its corresponding electric field E_0. Consider an interferometer with its arms along the $\hat{x}$ and $\hat{y}$ directions. The dark fringe condition means that the phase shift acquired by the light in each arm of the interferometer is such that there will be no light exiting the antisymmetric output. Figure B.1 shows a delay line interferometer. The antisymmetric port of the beamsplitter is the one with the output photodetector. When an ideal interferometer is operated on a dark fringe the only light exiting the system at the antisymmetric output is that produced by a gravitational wave. A real interferometer will have noise sources that mask the affect of a gravity wave. One such source of noise is the light's shot affect.

The light exiting an interferometer due to a gravity wave will be

$$E_{out} = t_b r_b E_0 e^{i\alpha}\left(e^{i\delta\phi_x} - e^{i\delta\phi_y}\right) \quad .$$

The terms t_b and r_b are the electric field's transmission and reflection coefficients for the beamsplitter. The phase shift acquired by the light traveling along the

$\hat{x}$ arm due to the gravity wave is $\delta\phi_x$, the $\hat{y}$ arm's gravity wave phase shift is $\delta\phi_y$,and α is an overall phase shift. Neglecting the overall phase shift, and assuming a 50–50 beam splitter the electric field can be approximated as

$$E_{out} = \frac{E_0}{2}(\delta\phi_y - \delta\phi_x) \quad .$$

The electric field that would be produced due a normally incident gravity wave of optimum polarization would be

$$E_{out} = h_+ S_+ E_0 \quad ,$$

where S_+ is the transfer function defined in chapter 3. Also, note that for a gravity wave of normal incidence and optimum polarization one has $S_+ = 2B$, where B is also defined in chapter 3. The uncertainty in a phase measurement is given by the Heisenberg relation

$$\Delta\phi \, \Delta N = 1 \quad ,$$

where ΔN is the uncertainty in the number of photons. The photon number is governed by Poisson statistics and one has $\Delta N = \sqrt{N}$. The phase noise of the light is then

$$\delta\phi(f) = \frac{1}{\sqrt{N}} = \sqrt{\frac{\hbar\omega}{P}} \quad ,$$

with units of $radians/\sqrt{Hz.}$, where the angular frequency of the light is ω, and the total power is P. Equating the signal due to the light's phase uncertainty with the signal one hopes to detect, one has

$$\frac{E_0}{2}\delta\phi(f) = 2Bh(f)E_0 \quad , or, \quad h(f) = \frac{1}{4B}\sqrt{\frac{\hbar\omega}{P}} \quad ,$$

where h(f) has units of $1/\sqrt{Hz}$. This noise value is the same as that derived by Caves (1980).

Appendix C: Some Exact Solutions

This appendix gives the exact solutions for various functions described in chapters 4, and 5.

In chapter 4 the quantities F_+ and $F_\times$ were defined. When six Euler angle rotations are made between the gravity wave frame, $\vec{X}_{gw}$, and the detectors frame, $\vec{x}_d$, given by

$$\vec{X}_{gw} = R_z(-\psi)R_x(\theta)R_z(-\phi)R_z^T(a)R_x^T(b)R_z^T(a)\vec{x}_d \quad ,$$

then one has

$$F_+(\theta,\phi,\psi,a,b,g) = alf2\cos 2\psi - bet2\sin 2\psi$$
$$F_\times(\theta,\phi,\psi,a,b,g) = alf2\sin 2\psi + bet2\cos 2\psi \quad ,$$

where alf2 and bet2 are given with the list of functions at the end of this appendix.

A gravity wave interferometer has its location on the surface of the earth specified by two angles, a_1 and b_1, which are related to the east longitude γ_E, and the north latitude, β_N by

$$a_1 = \gamma_E - \frac{3\pi}{2} \qquad , and, \qquad b_1 = \frac{\pi}{2} - \beta_N \quad .$$

The variable g_1 represents the angle between the local meridian line and the interferometer arm that defines its $\hat{x}$ axis. The other interferometer is defined by its three angles a_2, b_2, and g_2. These six Euler rotations can be reduced to three. If the first detector is considered the origin of the coordinate system, and hence $a_1=b_1=g_1=0$, then the three rotation angles are found from the following functions listed at the end of the appendix; b = bgen; Cos(a) = cagen; Sin(a) = sagen; Cos(g) = cggen; Sin(g) = sggen.

The solution to equation (A) of chapter 4 is needed to find the optimum alignment of the two interferometers. For the case where all six Euler angles are used, one has

$$\int_0^{2\pi} d\phi \int_0^{\pi} \sin\theta d\theta \Big[F_{1+}(\theta,\phi,\psi=0,a_1,b_1,g_1)F_{2+}(\theta,\phi,\psi=0,a_2,b_2,g_2) +$$
$$F_{1\times}(\theta,\phi,\psi=0,a_1,b_1,g_1)F_{2\times}(\theta,\phi,\psi=0,a_2,b_2,g_2)\Big]$$
$$= linans2 \quad ,$$

where linans2 (for linear answer 2) is listed at the end of the appendix. For the three Euler angle case, one has

$$\int_0^{2\pi} d\phi \int_0^{\pi} \sin\theta d\theta \Big[F_{1+}(\theta,\phi,\psi = 0,0,0,0) F_{2+}(\theta,\phi,\psi = 0,a,b,g) + F_{1\times}(\theta,\phi,\psi = 0,0,0,0) F_{2\times}(\theta,\phi,\psi = 0,a,b,g) \Big] = \frac{8\pi}{5} S_A \quad ,$$

where S_A is given by

$$S_A = \frac{1}{2}(1+\cos^2 b)\cos 2a \cos 2g - \cos b \sin 2a \sin 2g \quad .$$

The more complicated, but equivalent method for finding the orientation, is found from equation (B) of chapter 4. For this one has

$$\int_0^{2\pi} d\phi \int_0^{\pi} \sin\theta d\theta \int_0^{2\pi} d\psi F_{1+}^2(\theta,\phi,\psi,0,0,0) F_{2+}^2(\theta,\phi,\psi,a,b,g) = \left(\frac{96\pi}{35}\right)\frac{1}{3}\left[1+2S_A^2\right] \quad ,$$

where S_A is defined above.

In chapter 5 the frequency dependent, orientation dependent correlation term

$$\gamma(\vec{x}_1,\vec{x}_2,\Omega) = \int_0^{2\pi} d\phi \int_0^{\pi} \sin\theta d\theta \Big[(F_{1+}F_{2+} + F_{1\times}F_{2\times}) \times \cos\Big[\Big(\vec{k}\cdot(\vec{x}_1 - \vec{x}_2)\Big)\Big],$$

was considered. For the case when the two detectors are on exactly the opposite sides of the earth from one another, but one of the detector has been rotated about its $\hat{z}$ axis by g, then γ(fr,g), where fr is the gravity wave frequency, is given at the end of the appendix as gamop.

```
bgen/: bgen[a1_, b1_, a2_, b2_] :=
   ArcCos[Cos[b1]*Cos[b2] + Sin[b1]*Sin[b2]*Cos[a1 - a2]]

cagen/: cagen[a1_, b1_, g1_, a2_, b2_] :=
   -((1*((Cos[b2]*Cos[g1]*Sin[b1] - Cos[a2]*Cos[a1]*Cos[b1]*Sin[b2]*Cos[g1] +
             Sin[a1]*Sin[g1]*Sin[b2]*Cos[a2]) -
           Cos[b1]*Cos[g1]*Sin[a1]*Sin[a2]*Sin[b2] -
          Cos[a1]*Sin[g1]*Sin[a2]*Sin[b2]))/Sin[bgen[a1, b1, a2, b2]])

sagen/: sagen[a1_, b1_, g1_, a2_, b2_] :=
   (1*((-(Cos[a2]*Cos[g1]*Sin[a1]*Sin[b2]) -
            Cos[a2]*Cos[a1]*Cos[b1]*Sin[g1]*Sin[b2] +
           Cos[a1]*Cos[g1]*Sin[a2]*Sin[b2]) -
         Cos[b1]*Sin[a1]*Sin[g1]*Sin[a2]*Sin[b2] + Cos[b2]*Sin[b1]*Sin[g1]))/
    Sin[bgen[a1, b1, a2, b2]]

cggen/: cggen[a1_, b1_, a2_, b2_, g2_] :=
   (1*((-(Cos[a1]*Cos[a2]*Cos[b2]*Cos[g2]*Sin[b1]) +
            Sin[a2]*Sin[g2]*Sin[b1]*Cos[a1]) -
          Cos[b2]*Cos[g2]*Sin[a2]*Sin[a1]*Sin[b1] -
         Cos[a2]*Sin[g2]*Sin[a1]*Sin[b1] + Cos[b1]*Cos[g2]*Sin[b2]))/
    Sin[bgen[a1, b1, a2, b2]]

sggen/: sggen[a1_, b1_, a2_, b2_, g2_] :=
   (1*((-(Cos[a1]*Cos[g2]*Sin[a2]*Sin[b1]) -
            Cos[a1]*Cos[a2]*Cos[b2]*Sin[g2]*Sin[b1] +
           Cos[a2]*Cos[g2]*Sin[a1]*Sin[b1]) -
         Cos[b2]*Sin[a2]*Sin[g2]*Sin[a1]*Sin[b1] + Cos[b1]*Sin[b2]*Sin[g2]))/
    Sin[bgen[a1, b1, a2, b2]]

alf2 = 0.5*Cos[a]^2*Cos[g]^2*Cos[phi]^2 +
   0.5*Cos[a]^2*Cos[b]^2*Cos[g]^2*Cos[phi]^2*Cos[the]^2 -
   0.5*Cos[b]^2*Cos[g]^2*Cos[phi]^2*Sin[a]^2 -
   0.5*Cos[g]^2*Cos[phi]^2*Cos[the]^2*Sin[a]^2 -
   2.*Cos[a]*Cos[b]*Cos[g]*Cos[phi]^2*Sin[a]*Sin[g] -
   2.*Cos[a]*Cos[b]*Cos[g]*Cos[phi]^2*Cos[the]^2*Sin[a]*Sin[g] -
   0.5*Cos[a]^2*Cos[phi]^2*Sin[g]^2 -
   0.5*Cos[a]^2*Cos[b]^2*Cos[phi]^2*Cos[the]^2*Sin[g]^2 +
   0.5*Cos[b]^2*Cos[phi]^2*Sin[a]^2*Sin[g]^2 +
   0.5*Cos[phi]^2*Cos[the]^2*Sin[a]^2*Sin[g]^2 -
   1.*Cos[a]*Cos[g]^2*Cos[phi]*Sin[a]*Sin[phi] -
   1.*Cos[a]*Cos[b]^2*Cos[g]^2*Cos[phi]*Sin[a]*Sin[phi] -
   1.*Cos[a]*Cos[g]^2*Cos[phi]*Cos[the]^2*Sin[a]*Sin[phi] -
   1.*Cos[a]*Cos[b]^2*Cos[g]^2*Cos[phi]*Cos[the]^2*Sin[a]*Sin[phi] -
   2.*Cos[a]^2*Cos[b]*Cos[g]*Cos[phi]*Sin[g]*Sin[phi] -
   2.*Cos[a]^2*Cos[b]*Cos[g]*Cos[phi]*Cos[the]^2*Sin[g]*Sin[phi] +
   2.*Cos[b]*Cos[g]*Cos[phi]*Sin[a]^2*Sin[g]*Sin[phi] +
   2.*Cos[b]*Cos[g]*Cos[phi]*Cos[the]^2*Sin[a]^2*Sin[g]*Sin[phi] +
   1.*Cos[a]*Cos[phi]*Sin[a]*Sin[g]^2*Sin[phi] +
   1.*Cos[a]*Cos[b]^2*Cos[phi]*Sin[a]*Sin[g]^2*Sin[phi] +
   1.*Cos[a]*Cos[phi]*Cos[the]^2*Sin[a]*Sin[g]^2*Sin[phi] +
   1.*Cos[a]*Cos[b]^2*Cos[phi]*Cos[the]^2*Sin[a]*Sin[g]^2*Sin[phi] -
   0.5*Cos[a]^2*Cos[b]^2*Cos[g]^2*Sin[phi]^2 -
   0.5*Cos[a]^2*Cos[g]^2*Cos[the]^2*Sin[phi]^2 +
   0.5*Cos[g]^2*Sin[a]^2*Sin[phi]^2 +
   0.5*Cos[b]^2*Cos[g]^2*Cos[the]^2*Sin[a]^2*Sin[phi]^2 +
   2.*Cos[a]*Cos[b]*Cos[g]*Sin[a]*Sin[g]*Sin[phi]^2 +
   2.*Cos[a]*Cos[b]*Cos[g]*Cos[the]^2*Sin[a]*Sin[g]*Sin[phi]^2 +
   0.5*Cos[a]^2*Cos[b]^2*Sin[g]^2*Sin[phi]^2 +
   0.5*Cos[a]^2*Cos[the]^2*Sin[g]^2*Sin[phi]^2 -
   0.5*Sin[a]^2*Sin[g]^2*Sin[phi]^2 -
   0.5*Cos[b]^2*Cos[the]^2*Sin[a]^2*Sin[g]^2*Sin[phi]^2 +
   1.*Cos[a]*Cos[b]*Cos[g]^2*Cos[phi]*Cos[the]*Sin[b]*Sin[the] -
   2.*Cos[g]*Cos[phi]*Cos[the]*Sin[a]*Sin[b]*Sin[g]*Sin[the] -
   1.*Cos[a]*Cos[b]*Cos[phi]*Cos[the]*Sin[b]*Sin[g]^2*Sin[the] -
   1.*Cos[b]*Cos[g]^2*Cos[the]*Sin[a]*Sin[b]*Sin[phi]*Sin[the] -
```

```
    2.*Cos[a]*Cos[g]*Cos[the]*Sin[b]*Sin[g]*Sin[phi]*Sin[the] +
    1.*Cos[b]*Cos[the]*Sin[a]*Sin[b]*Sin[g]^2*Sin[phi]*Sin[the] +
    0.5*Cos[g]^2*Sin[b]^2*Sin[the]^2 - 0.5*Sin[b]^2*Sin[g]^2*Sin[the]^2


bet2 = Cos[a]*Cos[g]^2*Cos[phi]^2*Cos[the]*Sin[a] +
    Cos[a]*Cos[b]^2*Cos[g]^2*Cos[phi]^2*Cos[the]*Sin[a] +
    2*Cos[a]^2*Cos[b]*Cos[g]*Cos[phi]^2*Cos[the]*Sin[g] -
    2*Cos[b]*Cos[g]*Cos[phi]^2*Cos[the]*Sin[a]^2*Sin[g] -
    Cos[a]*Cos[phi]^2*Cos[the]*Sin[a]*Sin[g]^2 -
    Cos[a]*Cos[b]^2*Cos[phi]^2*Cos[the]*Sin[a]*Sin[g]^2 +
    Cos[a]^2*Cos[g]^2*Cos[phi]*Cos[the]*Sin[phi] +
    Cos[a]^2*Cos[b]^2*Cos[g]^2*Cos[phi]*Cos[the]*Sin[phi] -
    Cos[g]^2*Cos[phi]*Cos[the]*Sin[a]^2*Sin[phi] -
    Cos[b]^2*Cos[g]^2*Cos[phi]*Cos[the]*Sin[a]^2*Sin[phi] -
    8*Cos[a]*Cos[b]*Cos[g]*Cos[phi]*Cos[the]*Sin[a]*Sin[g]*Sin[phi] -
    Cos[a]^2*Cos[phi]*Cos[the]*Sin[g]^2*Sin[phi] -
    Cos[a]^2*Cos[b]^2*Cos[phi]*Cos[the]*Sin[g]^2*Sin[phi] +
    Cos[phi]*Cos[the]*Sin[a]^2*Sin[g]^2*Sin[phi] +
    Cos[b]^2*Cos[phi]*Cos[the]*Sin[a]^2*Sin[g]^2*Sin[phi] -
    Cos[a]*Cos[g]^2*Cos[the]*Sin[a]*Sin[phi]^2 -
    Cos[a]*Cos[b]^2*Cos[g]^2*Cos[the]*Sin[a]*Sin[phi]^2 -
    2*Cos[a]^2*Cos[b]*Cos[g]*Cos[the]*Sin[g]*Sin[phi]^2 +
    2*Cos[b]*Cos[g]*Cos[the]*Sin[a]^2*Sin[g]*Sin[phi]^2 +
    Cos[a]*Cos[the]*Sin[a]*Sin[g]^2*Sin[phi]^2 +
    Cos[a]*Cos[b]^2*Cos[the]*Sin[a]*Sin[g]^2*Sin[phi]^2 +
    Cos[b]*Cos[g]^2*Cos[phi]*Sin[a]*Sin[b]*Sin[the] +
    2*Cos[a]*Cos[g]*Cos[phi]*Sin[b]*Sin[g]*Sin[the] -
    Cos[b]*Cos[phi]*Sin[a]*Sin[b]*Sin[g]^2*Sin[the] +
    Cos[a]*Cos[b]*Cos[g]^2*Sin[b]*Sin[phi]*Sin[the] -
    2*Cos[g]*Sin[a]*Sin[b]*Sin[g]*Sin[phi]*Sin[the] -
    Cos[a]*Cos[b]*Sin[b]*Sin[g]^2*Sin[phi]*Sin[the]
gamop = -(c*Cos[g]^2*Sin[(-4*Pi*fr*rad)/c])/(16*fr*rad) +
    (c*Sin[g]^2*Sin[(-4*Pi*fr*rad)/c])/(16*fr*rad) +
    (3*Pi*Cos[g]^2*((c^2*Cos[(-4*Pi*fr*rad)/c])/(8*Pi^2*fr^2*rad^2) +
         (c^3*Sin[(-4*Pi*fr*rad)/c])/(32*Pi^3*fr^3*rad^3) -
         (c*Sin[(-4*Pi*fr*rad)/c])/(4*Pi*fr*rad)))/2 -
    (3*Pi*Sin[g]^2*((c^2*Cos[(-4*Pi*fr*rad)/c])/(8*Pi^2*fr^2*rad^2) +
         (c^3*Sin[(-4*Pi*fr*rad)/c])/(32*Pi^3*fr^3*rad^3) -
         (c*Sin[(-4*Pi*fr*rad)/c])/(4*Pi*fr*rad)))/2 +
    (Pi*Cos[g]^2*((-3*c^4*Cos[(-4*Pi*fr*rad)/c])/(32*Pi^4*fr^4*rad^4) +
         (c^2*Cos[(-4*Pi*fr*rad)/c])/(4*Pi^2*fr^2*rad^2) -
         (3*c^5*Sin[(-4*Pi*fr*rad)/c])/(128*Pi^5*fr^5*rad^5) +
         (3*c^3*Sin[(-4*Pi*fr*rad)/c])/(16*Pi^3*fr^3*rad^3) -
         (c*Sin[(-4*Pi*fr*rad)/c])/(4*Pi*fr*rad)))/4 -
    (Pi*Sin[g]^2*((-3*c^4*Cos[(-4*Pi*fr*rad)/c])/(32*Pi^4*fr^4*rad^4) +
         (c^2*Cos[(-4*Pi*fr*rad)/c])/(4*Pi^2*fr^2*rad^2) -
         (3*c^5*Sin[(-4*Pi*fr*rad)/c])/(128*Pi^5*fr^5*rad^5) +
         (3*c^3*Sin[(-4*Pi*fr*rad)/c])/(16*Pi^3*fr^3*rad^3) -
         (c*Sin[(-4*Pi*fr*rad)/c])/(4*Pi*fr*rad)))/4 +
    (c*Cos[g]^2*Sin[(4*Pi*fr*rad)/c])/(16*fr*rad) -
    (c*Sin[g]^2*Sin[(4*Pi*fr*rad)/c])/(16*fr*rad) -
    (3*Pi*Cos[g]^2*(-(c^2*Cos[(4*Pi*fr*rad)/c])/(8*Pi^2*fr^2*rad^2) +
         (c^3*Sin[(4*Pi*fr*rad)/c])/(32*Pi^3*fr^3*rad^3) -
         (c*Sin[(4*Pi*fr*rad)/c])/(4*Pi*fr*rad)))/2 +
    (3*Pi*Sin[g]^2*(-(c^2*Cos[(4*Pi*fr*rad)/c])/(8*Pi^2*fr^2*rad^2) +
         (c^3*Sin[(4*Pi*fr*rad)/c])/(32*Pi^3*fr^3*rad^3) -
         (c*Sin[(4*Pi*fr*rad)/c])/(4*Pi*fr*rad)))/2 -
    (Pi*Cos[g]^2*((3*c^4*Cos[(4*Pi*fr*rad)/c])/(32*Pi^4*fr^4*rad^4) -
         (c^2*Cos[(4*Pi*fr*rad)/c])/(4*Pi^2*fr^2*rad^2) -
         (3*c^5*Sin[(4*Pi*fr*rad)/c])/(128*Pi^5*fr^5*rad^5) +
         (3*c^3*Sin[(4*Pi*fr*rad)/c])/(16*Pi^3*fr^3*rad^3) -
         (c*Sin[(4*Pi*fr*rad)/c])/(4*Pi*fr*rad)))/4 +
    (Pi*Sin[g]^2*((3*c^4*Cos[(4*Pi*fr*rad)/c])/(32*Pi^4*fr^4*rad^4) -
         (c^2*Cos[(4*Pi*fr*rad)/c])/(4*Pi^2*fr^2*rad^2) -
         (3*c^5*Sin[(4*Pi*fr*rad)/c])/(128*Pi^5*fr^5*rad^5) +
```

```
        (3*c^3*Sin[(4*Pi*fr*rad)/c])/(16*Pi^3*fr^3*rad^3) -
        (c*Sin[(4*Pi*fr*rad)/c])/(4*Pi*fr*rad)))/4


linans2 = (Pi*Cos[A]^2*Cos[G]^2*Cos[a]^2*Cos[g]^2)/6 +
   (Pi*Cos[A]^2*Cos[B]^2*Cos[G]^2*Cos[a]^2*Cos[g]^2)/6 +
   (Pi*Cos[A]^2*Cos[G]^2*Cos[a]^2*Cos[b]^2*Cos[g]^2)/6 +
   (Pi*Cos[A]^2*Cos[B]^2*Cos[G]^2*Cos[a]^2*Cos[b]^2*Cos[g]^2)/6 -
   (Pi*Cos[G]^2*Cos[a]^2*Cos[g]^2*Sin[A]^2)/6 -
   (Pi*Cos[B]^2*Cos[G]^2*Cos[a]^2*Cos[g]^2*Sin[A]^2)/6 -
   (Pi*Cos[G]^2*Cos[a]^2*Cos[b]^2*Cos[g]^2*Sin[A]^2)/6 -
   (Pi*Cos[B]^2*Cos[G]^2*Cos[a]^2*Cos[b]^2*Cos[g]^2*Sin[A]^2)/6 -
   (4*Pi*Cos[A]*Cos[B]*Cos[G]*Cos[a]^2*Cos[g]^2*Sin[A]*Sin[G])/3 -
   (4*Pi*Cos[A]*Cos[B]*Cos[G]*Cos[a]^2*Cos[b]^2*Cos[g]^2*Sin[A]*Sin[G])/3 -
   (Pi*Cos[A]^2*Cos[a]^2*Cos[g]^2*Sin[G]^2)/6 -
   (Pi*Cos[A]^2*Cos[B]^2*Cos[a]^2*Cos[g]^2*Sin[G]^2)/6 -
   (Pi*Cos[A]^2*Cos[a]^2*Cos[b]^2*Cos[g]^2*Sin[G]^2)/6 -
   (Pi*Cos[A]^2*Cos[B]^2*Cos[a]^2*Cos[b]^2*Cos[g]^2*Sin[G]^2)/6 +
   (Pi*Cos[a]^2*Cos[g]^2*Sin[A]^2*Sin[G]^2)/6 +
   (Pi*Cos[B]^2*Cos[a]^2*Cos[g]^2*Sin[A]^2*Sin[G]^2)/6 +
   (Pi*Cos[a]^2*Cos[b]^2*Cos[g]^2*Sin[A]^2*Sin[G]^2)/6 +
   (Pi*Cos[B]^2*Cos[a]^2*Cos[b]^2*Cos[g]^2*Sin[A]^2*Sin[G]^2)/6 +
   (2*Pi*Cos[A]*Cos[G]^2*Cos[a]*Cos[g]^2*Sin[A]*Sin[a])/3 +
   (2*Pi*Cos[A]*Cos[B]^2*Cos[G]^2*Cos[a]*Cos[g]^2*Sin[A]*Sin[a])/3 +
   (2*Pi*Cos[A]*Cos[G]^2*Cos[a]*Cos[b]^2*Cos[g]^2*Sin[A]*Sin[a])/3 +
   (2*Pi*Cos[A]*Cos[B]^2*Cos[G]^2*Cos[a]*Cos[b]^2*Cos[g]^2*Sin[A]*Sin[a])/3 +
   (4*Pi*Cos[A]^2*Cos[B]*Cos[G]*Cos[a]*Cos[g]^2*Sin[G]*Sin[a])/3 +
   (4*Pi*Cos[A]^2*Cos[B]*Cos[G]*Cos[a]*Cos[b]^2*Cos[g]^2*Sin[G]*Sin[a])/3 -
   (4*Pi*Cos[B]*Cos[G]*Cos[a]*Cos[g]^2*Sin[A]^2*Sin[G]*Sin[a])/3 -
   (4*Pi*Cos[B]*Cos[G]*Cos[a]*Cos[b]^2*Cos[g]^2*Sin[A]^2*Sin[G]*Sin[a])/3 -
   (2*Pi*Cos[A]*Cos[a]*Cos[g]^2*Sin[A]*Sin[G]^2*Sin[a])/3 -
   (2*Pi*Cos[A]*Cos[B]^2*Cos[a]*Cos[g]^2*Sin[A]*Sin[G]^2*Sin[a])/3 -
   (2*Pi*Cos[A]*Cos[a]*Cos[b]^2*Cos[g]^2*Sin[A]*Sin[G]^2*Sin[a])/3 -
   (2*Pi*Cos[A]*Cos[B]^2*Cos[a]*Cos[b]^2*Cos[g]^2*Sin[A]*Sin[G]^2*Sin[a])/3 -
   (Pi*Cos[A]^2*Cos[G]^2*Cos[g]^2*Sin[a]^2)/6 -
   (Pi*Cos[A]^2*Cos[B]^2*Cos[G]^2*Cos[g]^2*Sin[a]^2)/6 -
   (Pi*Cos[A]^2*Cos[G]^2*Cos[b]^2*Cos[g]^2*Sin[a]^2)/6 -
   (Pi*Cos[A]^2*Cos[B]^2*Cos[G]^2*Cos[b]^2*Cos[g]^2*Sin[a]^2)/6 +
   (Pi*Cos[G]^2*Cos[g]^2*Sin[A]^2*Sin[a]^2)/6 +
   (Pi*Cos[B]^2*Cos[G]^2*Cos[g]^2*Sin[A]^2*Sin[a]^2)/6 +
   (Pi*Cos[G]^2*Cos[b]^2*Cos[g]^2*Sin[A]^2*Sin[a]^2)/6 +
   (Pi*Cos[B]^2*Cos[G]^2*Cos[b]^2*Cos[g]^2*Sin[A]^2*Sin[a]^2)/6 +
   (4*Pi*Cos[A]*Cos[B]*Cos[G]*Cos[g]^2*Sin[A]*Sin[G]*Sin[a]^2)/3 +
   (4*Pi*Cos[A]*Cos[B]*Cos[G]*Cos[b]^2*Cos[g]^2*Sin[A]*Sin[G]*Sin[a]^2)/3 +
   (Pi*Cos[A]^2*Cos[g]^2*Sin[G]^2*Sin[a]^2)/6 +
   (Pi*Cos[A]^2*Cos[B]^2*Cos[g]^2*Sin[G]^2*Sin[a]^2)/6 +
   (Pi*Cos[A]^2*Cos[b]^2*Cos[g]^2*Sin[G]^2*Sin[a]^2)/6 +
   (Pi*Cos[A]^2*Cos[B]^2*Cos[b]^2*Cos[g]^2*Sin[G]^2*Sin[a]^2)/6 -
   (Pi*Cos[g]^2*Sin[A]^2*Sin[G]^2*Sin[a]^2)/6 -
   (Pi*Cos[B]^2*Cos[g]^2*Sin[A]^2*Sin[G]^2*Sin[a]^2)/6 -
   (Pi*Cos[b]^2*Cos[g]^2*Sin[A]^2*Sin[G]^2*Sin[a]^2)/6 -
   (Pi*Cos[B]^2*Cos[b]^2*Cos[g]^2*Sin[A]^2*Sin[G]^2*Sin[a]^2)/6 +
   (4*Pi*Cos[A]*Cos[B]*Cos[G]^2*Cos[a]*Cos[b]*Cos[g]^2*Sin[B]*Sin[b])/3 -
   (8*Pi*Cos[G]*Cos[a]*Cos[b]*Cos[g]^2*Sin[A]*Sin[B]*Sin[G]*Sin[b])/3 -
   (4*Pi*Cos[A]*Cos[B]*Cos[a]*Cos[b]*Cos[g]^2*Sin[B]*Sin[G]^2*Sin[b])/3 +
   (4*Pi*Cos[B]*Cos[G]^2*Cos[b]*Cos[g]^2*Sin[A]*Sin[B]*Sin[a]*Sin[b])/3 +
   (8*Pi*Cos[A]*Cos[G]*Cos[b]*Cos[g]^2*Sin[B]*Sin[G]*Sin[a]*Sin[b])/3 -
   (4*Pi*Cos[B]*Cos[b]*Cos[g]^2*Sin[A]*Sin[B]*Sin[G]^2*Sin[a]*Sin[b])/3 +
   (4*Pi*Cos[A]*Cos[G]^2*Cos[a]^2*Cos[b]*Cos[g]*Sin[A]*Sin[g])/3 +
   (4*Pi*Cos[A]*Cos[B]^2*Cos[G]^2*Cos[a]^2*Cos[b]*Cos[g]*Sin[A]*Sin[g])/3 +
   (8*Pi*Cos[A]^2*Cos[B]*Cos[G]*Cos[a]^2*Cos[b]*Cos[g]*Sin[G]*Sin[g])/3 -
   (8*Pi*Cos[B]*Cos[G]*Cos[a]^2*Cos[b]*Cos[g]*Sin[A]^2*Sin[G]*Sin[g])/3 -
   (4*Pi*Cos[A]*Cos[a]^2*Cos[b]*Cos[g]*Sin[A]*Sin[G]^2*Sin[g])/3 -
   (4*Pi*Cos[A]*Cos[B]^2*Cos[a]^2*Cos[b]*Cos[g]*Sin[A]*Sin[G]^2*Sin[g])/3 -
   (4*Pi*Cos[A]^2*Cos[G]^2*Cos[a]*Cos[b]*Cos[g]*Sin[a]*Sin[g])/3 -
   (4*Pi*Cos[A]^2*Cos[B]^2*Cos[G]^2*Cos[a]*Cos[b]*Cos[g]*Sin[a]*Sin[g])/3 +
```

```
(4*Pi*Cos[G]^2*Cos[a]*Cos[b]*Cos[g]*Sin[A]^2*Sin[a]*Sin[g])/3 +
(4*Pi*Cos[B]^2*Cos[G]^2*Cos[a]*Cos[b]*Cos[g]*Sin[A]^2*Sin[a]*Sin[g])/3 +
(32*Pi*Cos[A]*Cos[B]*Cos[G]*Cos[a]*Cos[b]*Cos[g]*Sin[A]*Sin[G]*Sin[a]*
   Sin[g])/3 + (4*Pi*Cos[A]^2*Cos[a]*Cos[b]*Cos[g]*Sin[G]^2*Sin[a]*Sin[g])/
 3 + (4*Pi*Cos[A]^2*Cos[B]^2*Cos[a]*Cos[b]*Cos[g]*Sin[G]^2*Sin[a]*Sin[g])/
 3 - (4*Pi*Cos[a]*Cos[b]*Cos[g]*Sin[A]^2*Sin[G]^2*Sin[a]*Sin[g])/3 -
(4*Pi*Cos[B]^2*Cos[a]*Cos[b]*Cos[g]*Sin[A]^2*Sin[G]^2*Sin[a]*Sin[g])/3 -
(4*Pi*Cos[A]*Cos[G]^2*Cos[b]*Cos[g]*Sin[A]*Sin[a]^2*Sin[g])/3 -
(4*Pi*Cos[A]*Cos[B]^2*Cos[G]^2*Cos[b]*Cos[g]*Sin[A]*Sin[a]^2*Sin[g])/3 -
(8*Pi*Cos[A]^2*Cos[B]*Cos[G]*Cos[b]*Cos[g]*Sin[G]*Sin[a]^2*Sin[g])/3 +
(8*Pi*Cos[B]*Cos[G]*Cos[b]*Cos[g]*Sin[A]^2*Sin[G]*Sin[a]^2*Sin[g])/3 +
(4*Pi*Cos[A]*Cos[b]*Cos[g]*Sin[A]*Sin[G]^2*Sin[a]^2*Sin[g])/3 +
(4*Pi*Cos[A]*Cos[B]^2*Cos[b]*Cos[g]*Sin[A]*Sin[G]^2*Sin[a]^2*Sin[g])/3 +
(8*Pi*Cos[B]*Cos[G]^2*Cos[a]*Cos[g]*Sin[A]*Sin[B]*Sin[b]*Sin[g])/3 +
(16*Pi*Cos[A]*Cos[G]*Cos[a]*Cos[g]*Sin[B]*Sin[G]*Sin[b]*Sin[g])/3 -
(8*Pi*Cos[B]*Cos[a]*Cos[g]*Sin[A]*Sin[B]*Sin[G]^2*Sin[b]*Sin[g])/3 -
(8*Pi*Cos[A]*Cos[B]*Cos[G]^2*Cos[g]*Sin[B]*Sin[a]*Sin[b]*Sin[g])/3 +
(16*Pi*Cos[G]*Cos[g]*Sin[A]*Sin[B]*Sin[G]*Sin[a]*Sin[b]*Sin[g])/3 +
(8*Pi*Cos[A]*Cos[B]*Cos[g]*Sin[B]*Sin[G]^2*Sin[a]*Sin[b]*Sin[g])/3 -
(Pi*Cos[A]^2*Cos[G]^2*Cos[a]^2*Sin[g]^2)/6 -
(Pi*Cos[A]^2*Cos[B]^2*Cos[G]^2*Cos[a]^2*Sin[g]^2)/6 -
(Pi*Cos[A]^2*Cos[G]^2*Cos[a]^2*Cos[b]^2*Sin[g]^2)/6 -
(Pi*Cos[A]^2*Cos[B]^2*Cos[G]^2*Cos[a]^2*Cos[b]^2*Sin[g]^2)/6 +
(Pi*Cos[G]^2*Cos[a]^2*Sin[A]^2*Sin[g]^2)/6 +
(Pi*Cos[B]^2*Cos[G]^2*Cos[a]^2*Sin[A]^2*Sin[g]^2)/6 +
(Pi*Cos[G]^2*Cos[a]^2*Cos[b]^2*Sin[A]^2*Sin[g]^2)/6 +
(Pi*Cos[B]^2*Cos[G]^2*Cos[a]^2*Cos[b]^2*Sin[A]^2*Sin[g]^2)/6 +
(4*Pi*Cos[A]*Cos[B]*Cos[G]*Cos[a]^2*Sin[A]*Sin[G]*Sin[g]^2)/3 +
(4*Pi*Cos[A]*Cos[B]*Cos[G]*Cos[a]^2*Cos[b]^2*Sin[A]*Sin[G]*Sin[g]^2)/3 +
(Pi*Cos[A]^2*Cos[a]^2*Sin[G]^2*Sin[g]^2)/6 +
(Pi*Cos[A]^2*Cos[B]^2*Cos[a]^2*Sin[G]^2*Sin[g]^2)/6 +
(Pi*Cos[A]^2*Cos[a]^2*Cos[b]^2*Sin[G]^2*Sin[g]^2)/6 +
(Pi*Cos[A]^2*Cos[B]^2*Cos[a]^2*Cos[b]^2*Sin[G]^2*Sin[g]^2)/6 -
(Pi*Cos[a]^2*Sin[A]^2*Sin[G]^2*Sin[g]^2)/6 -
(Pi*Cos[B]^2*Cos[a]^2*Sin[A]^2*Sin[G]^2*Sin[g]^2)/6 -
(Pi*Cos[a]^2*Cos[b]^2*Sin[A]^2*Sin[G]^2*Sin[g]^2)/6 -
(Pi*Cos[B]^2*Cos[a]^2*Cos[b]^2*Sin[A]^2*Sin[G]^2*Sin[g]^2)/6 -
(2*Pi*Cos[A]*Cos[G]^2*Cos[a]*Sin[A]*Sin[a]*Sin[g]^2)/3 -
(2*Pi*Cos[A]*Cos[B]^2*Cos[G]^2*Cos[a]*Sin[A]*Sin[a]*Sin[g]^2)/3 -
(2*Pi*Cos[A]*Cos[G]^2*Cos[a]*Cos[b]^2*Sin[A]*Sin[a]*Sin[g]^2)/3 -
(2*Pi*Cos[A]*Cos[B]^2*Cos[G]^2*Cos[a]*Cos[b]^2*Sin[A]*Sin[a]*Sin[g]^2)/3 -
(4*Pi*Cos[A]^2*Cos[B]*Cos[G]*Cos[a]*Sin[G]*Sin[a]*Sin[g]^2)/3 -
(4*Pi*Cos[A]^2*Cos[B]*Cos[G]*Cos[a]*Cos[b]^2*Sin[G]*Sin[a]*Sin[g]^2)/3 +
(4*Pi*Cos[B]*Cos[G]*Cos[a]*Sin[A]^2*Sin[G]*Sin[a]*Sin[g]^2)/3 +
(4*Pi*Cos[B]*Cos[G]*Cos[a]*Cos[b]^2*Sin[A]^2*Sin[G]*Sin[a]*Sin[g]^2)/3 +
(2*Pi*Cos[A]*Cos[a]*Sin[A]*Sin[G]^2*Sin[a]*Sin[g]^2)/3 +
(2*Pi*Cos[A]*Cos[B]^2*Cos[a]*Sin[A]*Sin[G]^2*Sin[a]*Sin[g]^2)/3 +
(2*Pi*Cos[A]*Cos[a]*Cos[b]^2*Sin[A]*Sin[G]^2*Sin[a]*Sin[g]^2)/3 +
(2*Pi*Cos[A]*Cos[B]^2*Cos[a]*Cos[b]^2*Sin[A]*Sin[G]^2*Sin[a]*Sin[g]^2)/3 +
(Pi*Cos[A]^2*Cos[G]^2*Sin[a]^2*Sin[g]^2)/6 +
(Pi*Cos[A]^2*Cos[B]^2*Cos[G]^2*Sin[a]^2*Sin[g]^2)/6 +
(Pi*Cos[A]^2*Cos[G]^2*Cos[b]^2*Sin[a]^2*Sin[g]^2)/6 +
(Pi*Cos[A]^2*Cos[B]^2*Cos[G]^2*Cos[b]^2*Sin[a]^2*Sin[g]^2)/6 -
(Pi*Cos[G]^2*Sin[A]^2*Sin[a]^2*Sin[g]^2)/6 -
(Pi*Cos[B]^2*Cos[G]^2*Sin[A]^2*Sin[a]^2*Sin[g]^2)/6 -
(Pi*Cos[G]^2*Cos[b]^2*Sin[A]^2*Sin[a]^2*Sin[g]^2)/6 -
(Pi*Cos[B]^2*Cos[G]^2*Cos[b]^2*Sin[A]^2*Sin[a]^2*Sin[g]^2)/6 -
(4*Pi*Cos[A]*Cos[B]*Cos[G]*Sin[A]*Sin[G]*Sin[a]^2*Sin[g]^2)/3 -
(4*Pi*Cos[A]*Cos[B]*Cos[G]*Cos[b]^2*Sin[A]*Sin[G]*Sin[a]^2*Sin[g]^2)/3 -
(Pi*Cos[A]^2*Sin[G]^2*Sin[a]^2*Sin[g]^2)/6 -
(Pi*Cos[A]^2*Cos[B]^2*Sin[G]^2*Sin[a]^2*Sin[g]^2)/6 -
(Pi*Cos[A]^2*Cos[b]^2*Sin[G]^2*Sin[a]^2*Sin[g]^2)/6 -
(Pi*Cos[A]^2*Cos[B]^2*Cos[b]^2*Sin[G]^2*Sin[a]^2*Sin[g]^2)/6 +
(Pi*Sin[A]^2*Sin[G]^2*Sin[a]^2*Sin[g]^2)/6 +
(Pi*Cos[B]^2*Sin[A]^2*Sin[G]^2*Sin[a]^2*Sin[g]^2)/6 +
(Pi*Cos[b]^2*Sin[A]^2*Sin[G]^2*Sin[a]^2*Sin[g]^2)/6 +
```

```
(Pi*Cos[B]^2*Cos[b]^2*Sin[A]^2*Sin[G]^2*Sin[a]^2*Sin[g]^2)/6 -
(4*Pi*Cos[A]*Cos[B]*Cos[G]^2*Cos[a]*Cos[b]*Sin[B]*Sin[b]*Sin[g]^2)/3 +
(8*Pi*Cos[G]*Cos[a]*Cos[b]*Sin[A]*Sin[B]*Sin[G]*Sin[b]*Sin[g]^2)/3 +
(4*Pi*Cos[A]*Cos[B]*Cos[a]*Cos[b]*Sin[B]*Sin[G]^2*Sin[b]*Sin[g]^2)/3 -
(4*Pi*Cos[B]*Cos[G]^2*Cos[b]*Sin[A]*Sin[B]*Sin[a]*Sin[b]*Sin[g]^2)/3 -
(8*Pi*Cos[A]*Cos[G]*Cos[b]*Sin[B]*Sin[G]*Sin[a]*Sin[b]*Sin[g]^2)/3 +
(4*Pi*Cos[B]*Cos[b]*Sin[A]*Sin[B]*Sin[G]^2*Sin[a]*Sin[b]*Sin[g]^2)/3 +
(Pi*(11*Cos[A]^2*Cos[G]^2*Cos[a]^2*Cos[g]^2 +
     3*Cos[A]^2*Cos[B]^2*Cos[G]^2*Cos[a]^2*Cos[g]^2 +
     3*Cos[A]^2*Cos[G]^2*Cos[a]^2*Cos[b]^2*Cos[g]^2 +
     11*Cos[A]^2*Cos[B]^2*Cos[G]^2*Cos[a]^2*Cos[b]^2*Cos[g]^2 -
     3*Cos[G]^2*Cos[a]^2*Cos[g]^2*Sin[A]^2 -
     11*Cos[B]^2*Cos[G]^2*Cos[a]^2*Cos[g]^2*Sin[A]^2 -
     11*Cos[G]^2*Cos[a]^2*Cos[b]^2*Cos[g]^2*Sin[A]^2 -
     3*Cos[B]^2*Cos[G]^2*Cos[a]^2*Cos[b]^2*Cos[g]^2*Sin[A]^2 +
     8*Cos[G]^2*Cos[a]^2*Cos[g]^2*Sin[B]^2 -
     8*Cos[G]^2*Cos[a]^2*Cos[b]^2*Cos[g]^2*Sin[B]^2 -
     56*Cos[A]*Cos[B]*Cos[G]*Cos[a]^2*Cos[g]^2*Sin[A]*Sin[G] -
     56*Cos[A]*Cos[B]*Cos[G]*Cos[a]^2*Cos[b]^2*Cos[g]^2*Sin[A]*Sin[G] -
     11*Cos[A]^2*Cos[a]^2*Cos[g]^2*Sin[G]^2 -
     3*Cos[A]^2*Cos[B]^2*Cos[a]^2*Cos[g]^2*Sin[G]^2 -
     3*Cos[A]^2*Cos[a]^2*Cos[b]^2*Cos[g]^2*Sin[G]^2 -
     11*Cos[A]^2*Cos[B]^2*Cos[a]^2*Cos[b]^2*Cos[g]^2*Sin[G]^2 +
     3*Cos[a]^2*Cos[g]^2*Sin[A]^2*Sin[G]^2 +
     11*Cos[B]^2*Cos[a]^2*Cos[g]^2*Sin[A]^2*Sin[G]^2 +
     11*Cos[a]^2*Cos[b]^2*Cos[g]^2*Sin[A]^2*Sin[G]^2 +
     3*Cos[B]^2*Cos[a]^2*Cos[b]^2*Cos[g]^2*Sin[A]^2*Sin[G]^2 -
     8*Cos[a]^2*Cos[g]^2*Sin[B]^2*Sin[G]^2 +
     8*Cos[a]^2*Cos[b]^2*Cos[g]^2*Sin[B]^2*Sin[G]^2 +
     28*Cos[A]*Cos[G]^2*Cos[a]*Cos[g]^2*Sin[A]*Sin[a] +
     28*Cos[A]*Cos[B]^2*Cos[G]^2*Cos[a]*Cos[g]^2*Sin[A]*Sin[a] +
     28*Cos[A]*Cos[G]^2*Cos[a]*Cos[b]^2*Cos[g]^2*Sin[A]*Sin[a] +
     28*Cos[A]*Cos[B]^2*Cos[G]^2*Cos[a]*Cos[b]^2*Cos[g]^2*Sin[A]*Sin[a] +
     56*Cos[A]^2*Cos[B]*Cos[G]*Cos[a]*Cos[g]^2*Sin[G]*Sin[a] +
     56*Cos[A]^2*Cos[B]*Cos[G]*Cos[a]*Cos[b]^2*Cos[g]^2*Sin[G]*Sin[a] -
     56*Cos[B]*Cos[G]*Cos[a]*Cos[g]^2*Sin[A]^2*Sin[G]*Sin[a] -
     56*Cos[B]*Cos[G]*Cos[a]*Cos[b]^2*Cos[g]^2*Sin[A]^2*Sin[G]*Sin[a] -
     28*Cos[A]*Cos[a]*Cos[g]^2*Sin[A]*Sin[G]^2*Sin[a] -
     28*Cos[A]*Cos[B]^2*Cos[a]*Cos[g]^2*Sin[A]*Sin[G]^2*Sin[a] -
     28*Cos[A]*Cos[a]*Cos[b]^2*Cos[g]^2*Sin[A]*Sin[G]^2*Sin[a] -
     28*Cos[A]*Cos[B]^2*Cos[a]*Cos[b]^2*Cos[g]^2*Sin[A]*Sin[G]^2*Sin[a] -
     3*Cos[A]^2*Cos[G]^2*Cos[g]^2*Sin[a]^2 -
     11*Cos[A]^2*Cos[B]^2*Cos[G]^2*Cos[g]^2*Sin[a]^2 -
     11*Cos[A]^2*Cos[G]^2*Cos[b]^2*Cos[g]^2*Sin[a]^2 -
     3*Cos[A]^2*Cos[B]^2*Cos[G]^2*Cos[b]^2*Cos[g]^2*Sin[a]^2 +
     11*Cos[G]^2*Cos[g]^2*Sin[A]^2*Sin[a]^2 +
     3*Cos[B]^2*Cos[G]^2*Cos[g]^2*Sin[A]^2*Sin[a]^2 +
     3*Cos[G]^2*Cos[b]^2*Cos[g]^2*Sin[A]^2*Sin[a]^2 +
     11*Cos[B]^2*Cos[G]^2*Cos[b]^2*Cos[g]^2*Sin[A]^2*Sin[a]^2 +
     8*Cos[G]^2*Cos[g]^2*Sin[B]^2*Sin[a]^2 -
     8*Cos[G]^2*Cos[b]^2*Cos[g]^2*Sin[B]^2*Sin[a]^2 +
     56*Cos[A]*Cos[B]*Cos[G]*Cos[g]^2*Sin[A]*Sin[G]*Sin[a]^2 +
     56*Cos[A]*Cos[B]*Cos[G]*Cos[b]^2*Cos[g]^2*Sin[A]*Sin[G]*Sin[a]^2 +
     3*Cos[A]^2*Cos[g]^2*Sin[G]^2*Sin[a]^2 +
     11*Cos[A]^2*Cos[B]^2*Cos[g]^2*Sin[G]^2*Sin[a]^2 +
     11*Cos[A]^2*Cos[b]^2*Cos[g]^2*Sin[G]^2*Sin[a]^2 +
     3*Cos[A]^2*Cos[B]^2*Cos[b]^2*Cos[g]^2*Sin[G]^2*Sin[a]^2 -
     11*Cos[g]^2*Sin[A]^2*Sin[G]^2*Sin[a]^2 -
     3*Cos[B]^2*Cos[g]^2*Sin[A]^2*Sin[G]^2*Sin[a]^2 -
     3*Cos[b]^2*Cos[g]^2*Sin[A]^2*Sin[G]^2*Sin[a]^2 -
     11*Cos[B]^2*Cos[b]^2*Cos[g]^2*Sin[A]^2*Sin[G]^2*Sin[a]^2 -
     8*Cos[g]^2*Sin[B]^2*Sin[G]^2*Sin[a]^2 +
     8*Cos[b]^2*Cos[g]^2*Sin[B]^2*Sin[G]^2*Sin[a]^2 +
     8*Cos[A]*Cos[B]*Cos[G]^2*Cos[a]*Cos[b]*Cos[g]^2*Sin[B]*Sin[b] -
     16*Cos[G]*Cos[a]*Cos[b]*Cos[g]^2*Sin[A]*Sin[B]*Sin[G]*Sin[b] -
     8*Cos[A]*Cos[B]*Cos[a]*Cos[b]*Cos[g]^2*Sin[B]*Sin[G]^2*Sin[b] +
```

```
8*Cos[B]*Cos[G]^2*Cos[b]*Cos[g]^2*Sin[A]*Sin[B]*Sin[a]*Sin[b] +
16*Cos[A]*Cos[G]*Cos[b]*Cos[g]^2*Sin[B]*Sin[G]*Sin[a]*Sin[b] -
8*Cos[B]*Cos[b]*Cos[g]^2*Sin[A]*Sin[B]*Sin[G]^2*Sin[a]*Sin[b] +
8*Cos[A]^2*Cos[G]^2*Cos[g]^2*Sin[b]^2 -
8*Cos[A]^2*Cos[B]^2*Cos[G]^2*Cos[g]^2*Sin[b]^2 +
8*Cos[G]^2*Cos[g]^2*Sin[A]^2*Sin[b]^2 -
8*Cos[B]^2*Cos[G]^2*Cos[g]^2*Sin[A]^2*Sin[b]^2 +
16*Cos[G]^2*Cos[g]^2*Sin[B]^2*Sin[b]^2 -
8*Cos[A]^2*Cos[g]^2*Sin[G]^2*Sin[b]^2 +
8*Cos[A]^2*Cos[B]^2*Cos[g]^2*Sin[G]^2*Sin[b]^2 -
8*Cos[g]^2*Sin[A]^2*Sin[G]^2*Sin[b]^2 +
8*Cos[B]^2*Cos[g]^2*Sin[A]^2*Sin[G]^2*Sin[b]^2 -
16*Cos[g]^2*Sin[B]^2*Sin[G]^2*Sin[b]^2 +
56*Cos[A]*Cos[G]^2*Cos[a]^2*Cos[b]*Cos[g]*Sin[A]*Sin[g] +
56*Cos[A]*Cos[B]^2*Cos[G]^2*Cos[a]^2*Cos[b]*Cos[g]*Sin[A]*Sin[g] +
112*Cos[A]^2*Cos[B]*Cos[G]*Cos[a]^2*Cos[b]*Cos[g]*Sin[G]*Sin[g] -
112*Cos[B]*Cos[G]*Cos[a]^2*Cos[b]*Cos[g]*Sin[A]^2*Sin[G]*Sin[g] -
56*Cos[A]*Cos[a]^2*Cos[b]*Cos[g]*Sin[A]*Sin[G]^2*Sin[g] -
56*Cos[A]*Cos[B]^2*Cos[a]^2*Cos[b]*Cos[g]*Sin[A]*Sin[G]^2*Sin[g] -
56*Cos[A]^2*Cos[G]^2*Cos[a]*Cos[b]*Cos[g]*Sin[a]*Sin[g] -
56*Cos[A]^2*Cos[B]^2*Cos[G]^2*Cos[a]*Cos[b]*Cos[g]*Sin[a]*Sin[g] +
56*Cos[G]^2*Cos[a]*Cos[b]*Cos[g]*Sin[A]^2*Sin[a]*Sin[g] +
56*Cos[B]^2*Cos[G]^2*Cos[a]*Cos[b]*Cos[g]*Sin[A]^2*Sin[a]*Sin[g] +
448*Cos[A]*Cos[B]*Cos[G]*Cos[a]*Cos[b]*Cos[g]*Sin[A]*Sin[G]*Sin[a]*
 Sin[g] + 56*Cos[A]^2*Cos[a]*Cos[b]*Cos[g]*Sin[G]^2*Sin[a]*Sin[g] +
56*Cos[A]^2*Cos[B]^2*Cos[a]*Cos[b]*Cos[g]*Sin[G]^2*Sin[a]*Sin[g] -
56*Cos[a]*Cos[b]*Cos[g]*Sin[A]^2*Sin[G]^2*Sin[a]*Sin[g] -
56*Cos[B]^2*Cos[a]*Cos[b]*Cos[g]*Sin[A]^2*Sin[G]^2*Sin[a]*Sin[g] -
56*Cos[A]*Cos[G]^2*Cos[b]*Cos[g]*Sin[A]*Sin[a]^2*Sin[g] -
56*Cos[A]*Cos[B]^2*Cos[G]^2*Cos[b]*Cos[g]*Sin[A]*Sin[a]^2*Sin[g] -
112*Cos[A]^2*Cos[B]*Cos[G]*Cos[b]*Cos[g]*Sin[G]*Sin[a]^2*Sin[g] +
112*Cos[B]*Cos[G]*Cos[b]*Cos[g]*Sin[A]^2*Sin[G]*Sin[a]^2*Sin[g] +
56*Cos[A]*Cos[b]*Cos[g]*Sin[A]*Sin[G]^2*Sin[a]^2*Sin[g] +
56*Cos[A]*Cos[B]^2*Cos[b]*Cos[g]*Sin[A]*Sin[G]^2*Sin[a]^2*Sin[g] +
16*Cos[B]*Cos[G]^2*Cos[a]*Cos[g]*Sin[A]*Sin[B]*Sin[b]*Sin[g] +
32*Cos[A]*Cos[G]*Cos[a]*Cos[g]*Sin[B]*Sin[G]*Sin[b]*Sin[g] -
16*Cos[B]*Cos[a]*Cos[g]*Sin[A]*Sin[B]*Sin[G]^2*Sin[b]*Sin[g] -
16*Cos[A]*Cos[B]*Cos[G]^2*Cos[g]*Sin[B]*Sin[a]*Sin[b]*Sin[g] +
32*Cos[G]*Cos[g]*Sin[A]*Sin[B]*Sin[G]*Sin[a]*Sin[b]*Sin[g] +
16*Cos[A]*Cos[B]*Cos[g]*Sin[B]*Sin[G]^2*Sin[a]*Sin[b]*Sin[g] -
11*Cos[A]^2*Cos[G]^2*Cos[a]^2*Sin[g]^2 -
3*Cos[A]^2*Cos[B]^2*Cos[G]^2*Cos[a]^2*Sin[g]^2 -
3*Cos[A]^2*Cos[G]^2*Cos[a]^2*Cos[b]^2*Sin[g]^2 -
11*Cos[A]^2*Cos[B]^2*Cos[G]^2*Cos[a]^2*Cos[b]^2*Sin[g]^2 +
3*Cos[G]^2*Cos[a]^2*Sin[A]^2*Sin[g]^2 +
11*Cos[B]^2*Cos[G]^2*Cos[a]^2*Sin[A]^2*Sin[g]^2 +
11*Cos[G]^2*Cos[a]^2*Cos[b]^2*Sin[A]^2*Sin[g]^2 +
3*Cos[B]^2*Cos[G]^2*Cos[a]^2*Cos[b]^2*Sin[A]^2*Sin[g]^2 -
8*Cos[G]^2*Cos[a]^2*Sin[B]^2*Sin[g]^2 +
8*Cos[G]^2*Cos[a]^2*Cos[b]^2*Sin[B]^2*Sin[g]^2 +
56*Cos[A]*Cos[B]*Cos[G]*Cos[a]^2*Sin[A]*Sin[G]*Sin[g]^2 +
56*Cos[A]*Cos[B]*Cos[G]*Cos[a]^2*Cos[b]^2*Sin[A]*Sin[G]*Sin[g]^2 +
11*Cos[A]^2*Cos[a]^2*Sin[G]^2*Sin[g]^2 +
3*Cos[A]^2*Cos[B]^2*Cos[a]^2*Sin[G]^2*Sin[g]^2 +
3*Cos[A]^2*Cos[a]^2*Cos[b]^2*Sin[G]^2*Sin[g]^2 +
11*Cos[A]^2*Cos[B]^2*Cos[a]^2*Cos[b]^2*Sin[G]^2*Sin[g]^2 -
3*Cos[a]^2*Sin[A]^2*Sin[G]^2*Sin[g]^2 -
11*Cos[B]^2*Cos[a]^2*Sin[A]^2*Sin[G]^2*Sin[g]^2 -
11*Cos[a]^2*Cos[b]^2*Sin[A]^2*Sin[G]^2*Sin[g]^2 -
3*Cos[B]^2*Cos[a]^2*Cos[b]^2*Sin[A]^2*Sin[G]^2*Sin[g]^2 +
8*Cos[a]^2*Sin[B]^2*Sin[G]^2*Sin[g]^2 -
8*Cos[a]^2*Cos[b]^2*Sin[B]^2*Sin[G]^2*Sin[g]^2 -
28*Cos[A]*Cos[G]^2*Cos[a]*Sin[A]*Sin[a]*Sin[g]^2 -
28*Cos[A]*Cos[B]^2*Cos[G]^2*Cos[a]*Sin[A]*Sin[a]*Sin[g]^2 -
28*Cos[A]*Cos[G]^2*Cos[a]*Cos[b]^2*Sin[A]*Sin[a]*Sin[g]^2 -
28*Cos[A]*Cos[B]^2*Cos[G]^2*Cos[a]*Cos[b]^2*Sin[A]*Sin[a]*Sin[g]^2 -
```

```
56*Cos[A]^2*Cos[B]*Cos[G]*Cos[a]*Sin[G]*Sin[a]*Sin[g]^2 -
56*Cos[A]^2*Cos[B]*Cos[G]*Cos[a]*Cos[b]^2*Sin[G]*Sin[a]*Sin[g]^2 +
56*Cos[B]*Cos[G]*Cos[a]*Sin[A]^2*Sin[G]*Sin[a]*Sin[g]^2 +
56*Cos[B]*Cos[G]*Cos[a]*Cos[b]^2*Sin[A]^2*Sin[G]*Sin[a]*Sin[g]^2 +
28*Cos[A]*Cos[a]*Sin[A]*Sin[G]^2*Sin[a]*Sin[g]^2 +
28*Cos[A]*Cos[B]^2*Cos[a]*Sin[A]*Sin[G]^2*Sin[a]*Sin[g]^2 +
28*Cos[A]*Cos[a]*Cos[b]^2*Sin[A]*Sin[G]^2*Sin[a]*Sin[g]^2 +
28*Cos[A]*Cos[B]^2*Cos[a]*Cos[b]^2*Sin[A]*Sin[G]^2*Sin[a]*Sin[g]^2 +
3*Cos[A]^2*Cos[G]^2*Sin[a]^2*Sin[g]^2 +
11*Cos[A]^2*Cos[B]^2*Cos[G]^2*Sin[a]^2*Sin[g]^2 +
11*Cos[A]^2*Cos[G]^2*Cos[b]^2*Sin[a]^2*Sin[g]^2 +
3*Cos[A]^2*Cos[B]^2*Cos[G]^2*Cos[b]^2*Sin[a]^2*Sin[g]^2 -
11*Cos[G]^2*Sin[A]^2*Sin[a]^2*Sin[g]^2 -
3*Cos[B]^2*Cos[G]^2*Sin[A]^2*Sin[a]^2*Sin[g]^2 -
3*Cos[G]^2*Cos[b]^2*Sin[A]^2*Sin[a]^2*Sin[g]^2 -
11*Cos[B]^2*Cos[G]^2*Cos[b]^2*Sin[A]^2*Sin[a]^2*Sin[g]^2 -
8*Cos[G]^2*Sin[B]^2*Sin[a]^2*Sin[g]^2 +
8*Cos[G]^2*Cos[b]^2*Sin[B]^2*Sin[a]^2*Sin[g]^2 -
56*Cos[A]*Cos[B]*Cos[G]*Sin[A]*Sin[G]*Sin[a]^2*Sin[g]^2 -
56*Cos[A]*Cos[B]*Cos[G]*Cos[b]^2*Sin[A]*Sin[G]*Sin[a]^2*Sin[g]^2 -
3*Cos[A]^2*Sin[G]^2*Sin[a]^2*Sin[g]^2 -
11*Cos[A]^2*Cos[B]^2*Sin[G]^2*Sin[a]^2*Sin[g]^2 -
11*Cos[A]^2*Cos[b]^2*Sin[G]^2*Sin[a]^2*Sin[g]^2 -
3*Cos[A]^2*Cos[B]^2*Cos[b]^2*Sin[G]^2*Sin[a]^2*Sin[g]^2 +
11*Sin[A]^2*Sin[G]^2*Sin[a]^2*Sin[g]^2 +
3*Cos[B]^2*Sin[A]^2*Sin[G]^2*Sin[a]^2*Sin[g]^2 +
3*Cos[b]^2*Sin[A]^2*Sin[G]^2*Sin[a]^2*Sin[g]^2 +
11*Cos[B]^2*Cos[b]^2*Sin[A]^2*Sin[G]^2*Sin[a]^2*Sin[g]^2 +
8*Sin[B]^2*Sin[G]^2*Sin[a]^2*Sin[g]^2 -
8*Cos[b]^2*Sin[B]^2*Sin[G]^2*Sin[a]^2*Sin[g]^2 -
8*Cos[A]*Cos[B]*Cos[G]^2*Cos[a]*Cos[b]*Sin[B]*Sin[b]*Sin[g]^2 +
16*Cos[G]*Cos[a]*Cos[b]*Sin[A]*Sin[B]*Sin[G]*Sin[b]*Sin[g]^2 +
8*Cos[A]*Cos[B]*Cos[a]*Cos[b]*Sin[B]*Sin[G]^2*Sin[b]*Sin[g]^2 -
8*Cos[B]*Cos[G]^2*Cos[b]*Sin[A]*Sin[B]*Sin[a]*Sin[b]*Sin[g]^2 -
16*Cos[A]*Cos[G]*Cos[b]*Sin[B]*Sin[G]*Sin[a]*Sin[b]*Sin[g]^2 +
8*Cos[B]*Cos[b]*Sin[A]*Sin[B]*Sin[G]^2*Sin[a]*Sin[b]*Sin[g]^2 -
8*Cos[A]^2*Cos[G]^2*Sin[b]^2*Sin[g]^2 +
8*Cos[A]^2*Cos[B]^2*Cos[G]^2*Sin[b]^2*Sin[g]^2 -
8*Cos[G]^2*Sin[A]^2*Sin[b]^2*Sin[g]^2 +
8*Cos[B]^2*Cos[G]^2*Sin[A]^2*Sin[b]^2*Sin[g]^2 -
16*Cos[G]^2*Sin[B]^2*Sin[b]^2*Sin[g]^2 +
8*Cos[A]^2*Sin[G]^2*Sin[b]^2*Sin[g]^2 -
8*Cos[A]^2*Cos[B]^2*Sin[G]^2*Sin[b]^2*Sin[g]^2 +
8*Sin[A]^2*Sin[G]^2*Sin[b]^2*Sin[g]^2 -
8*Cos[B]^2*Sin[A]^2*Sin[G]^2*Sin[b]^2*Sin[g]^2 +
16*Sin[B]^2*Sin[G]^2*Sin[b]^2*Sin[g]^2))/30
```

References

Abbott, L. and Wise, M. (1984), Nucl. Phys. **B244**, 541.

Abbott, L. and Wise, M. (1984b), Ap.J. Letters **282**, L47.

Abramowitz, M. and Stegun, I.E. (1972), *Handbook of Mathematical Functions*, U.S. National Bureau of Standards, Washington, D.C.

Accetta, F.S. and Krauss, L.M. (1989), Nuc. Phys. B **319**, 747.

Albrecht, A. and Turok, N. (1989), Phys. Rev. D **40**, 973.

Allen, B. (1988), Phys. Rev. D **37**, 2078.

Allen, B. (1989), Phys. Rev. Letters **63**, 2017.

Anderson, J.D., Armstrong, J.W., Estabrook, F.B., Hellings, R.W., Law, E.K. and Wahlquist, H.D. (1984), Nature **308**, 158.

Armstrong, J.W., Estabrook, F.B. and Wahlquist, H.D. (1987), Ap.J. **318**, 536.

Armstrong, J.W., Woo, R. and Estabrook, F.B. (1979), Ap.J. **230**, 570.

Bardeen, J. (1980), Phys. Rev. D. **22**, 1982.

Bendat, J.S. (1958), *Principles and Applications of Random Noise Theory*, John Wiley and Sons, New York.

Bennett, D.P. (1988a), Phys. Rev. D **33**, 872.

Bennett, D.P. (1988b), Phys. Rev. D **34**, 3592.

Bertotti, B., Carr, B.J. and Rees, M.J. (1983), M.N.R.A.S. **203**, 945.

Blandford, R., Narayan, R. and Romani, R.W. (1984), J. Astrophys. Astr. **5**, 369.

Blandford, R.R. (1974), Geophysics **39**, 633.

Bouchet, F.R. and Bennett, D.B. (1990), Phys. Rev. D **41**, 720.

Boughn, S.P., Cheng, E.S. and Wilkinson, D.T. (1981), Ap.J. Letters**243**, L113.

Boughn, S.P. and Kuhn, J.R. (1984), Ap.J. **286**, 387.

Carr, B.J. (1980), Astron. Astrophys. **89**, 6.

Caves, C.M. (1980), Phys. Rev. Letters **45**, 75.

Caves, C.M. (1981), Phys. Rev. D **23**, 1693.

Corning (1989), *Corning Glass Works Document on Premium-Quality Fused Silica*, Corning, N.Y.

Cottingham, D. (1990), private communication.

DeGroot, M.H. (1986), *Probablity and Statistics*, Addison-Wesley, Reading, Ma.

Deryagin, D.V., Grigoriev, D.Yu., Rubakov, V.A. and Sazhin, M.V. (1987), M.N.R.A.S. **229**, 357.

Detweiler, S. (1979), Ap.J. **234**, 1100.

Dewey, D. (1986), *A Search for Astronomical Gravitational Radiation With an Interferometric Broad Band Antenna*, PhD Thesis, M.I.T. Cambridge, Mass.

Douze, E.J. and Laster, S.J. (1979), Geophysics **44**, 1999.

Drever, R.W.P. (1982), in *Gravitational Radiation*, eds. N. Deruelle and T. Piran, North-Holland, Amsterdam, 321.

Einstein, A. (1916), *Preuss. Akad. Wiss. Berlin, Sitzungberichte der Physikalisch-mathematischen Klasse*, 688.

Estabrook, F.B. and Wahlquist, H.D. (1975), Gen. Rel. Grav. **6**, 439.

Evans, J.E. and Griffiths, A.S. (1974), IEEE Trans. Comm. **COM-22**, 528.

Fairbank, W.M., Bassan, M., Mapoles, E.R., McAshan, M.S., Michelson, P.F. and Moskowitz, B.E. (1986), in *Proceedings of the Fourth Marcel Grossmann Meeting on General Relativity*, ed. R. Ruffini, North-Holland, Amsterdam, 543.

Faller, J.E., Bender, P.L., Hall, J.L., Hils, D. and Vincent, M.A. (1984), in *Proceedings, Colloquium on Kilometric Optical Arrays in Space*, Cargese, Corsica, France, 157.

Fante, R.L. (1988), *Signal Analysis and Estimation: An Introduction*, John Wiley and Sons, New York.

Fixen, D., Cheng, E.S. and Wilkonson, D.T. (1983), Phys. Rev. Letters **50**, 620.

Forward, R.L. (1978), Phys. Rev. D **17**, 379.

Frantti, G.E. (1963), Geophysics **28**, 547.

Frieman, J.A., Gelmini, G.B., Gleiser, M.and Kolb, E.W. (1988), Phys. Rev. Letters **60**, 2101.

Galbraith, W. (1958), *Extensive Air Showers*, Academic Press, N.Y.

Gambling, W.A., Payne, D.N. and Matsumura, H. (1976), Elect. Lett. **Vol. 12, No. 21**, 546.

Gibbons, G.W. and Hawking, S.W. (1977), Phys. Rev. D **15**, 2738.

Ginsberg, L.E. (1974), IEEE Trans. Comm. **COM-22**, 555.

Ginsberg, L.E. (1974b), IEEE Trans. Comm. **COM-22**, 452.

Gleiser, M. (1989), Phys. Rev. Letters **63**, 1199.

Gleiser, M. (1990), private communication.

Gordon. M. (1973), *Detection of Rapid Fluctuations in the Earth's Magnetic Field*, B.S. Thesis, M.I.T. Cambridge, Mass.

Grishchuk, L.P. (1988), Sov. Sci. Rev. E. Astrophys. Space Phys. 7, 267.

Grishchuk, L.P. and Polnarev, A.G. (1980), in *General Relativity and Gravitation*, ed. A. Held, Plenum Press, New York, Vol. 2, 393

Gürsel, Y. and Tinto, M. (1989), Phys. Rev. D **40**, 3884.

Gürsel, Y. and Tinto, M. (1990), private communication.

Hellings, R.W., Callahan, P.S., Anderson, J.D. and Moffett, A.T. (1981), Phys. Rev. D **23**, 844.

Hellings, R.W. and Downs, G.S. (1983), Ap.J. Letters **265**, L39.

Heirtzler, J.R., De Mendonca, F. and Montes, H. (1966), Annales de Géophysique, **22**, 502.

Hill, C.T., Schramm, D.N. and Fry, J.N. (1989), Comments Nucl. Part. Phys. **19**, 25.

Hils, D., Bender, P.L. and Webbink, R.F. (1990), *Gravitational Radiation from the Galaxy*, preprint.

Hogan, C.J. (1983), Phys. Lett. **133B**, 172.

Hogan, C.J. (1986), M.N.R.A.S. **218**, 629.

Hough, J., Pugh, J.R., Bland, R. and Drever, R.W.P. (1975), Nature **254**, 498.

Hough, J. et al. (1989), *Proposal for a Joint German-British Interferometeric Gravitational Wave Detector*, Max-Planck Institute für Quantenoptik, Garching, F.R.G.

Joo, T.H. (1989), *Detection Statistics for Multichannel Data*, PhD Thesis, M.I.T. Cambridge, Mass.

Kimball, C.V. and Marzetta, T.L. (1984), Geophysics **49**, 274.

Kolb, E.W. and Turner, M.S. (1990), *The Early Universe*, Addison-Wesley, Redwood City, Ca.

Kovalik, J. (1990), *Measurements of Internal Friction in Various Materials*, preprint.

Kovalik, J. and Saulson, P. (1990), *Quad-Cell Reflective Position Sensor*, preprint.

Lange, K.L., Little, R.J.A. and Taylor, J.M.G. (1989), Journ. Am. Stat. Ass. **84**, 881.

Lefevre, H.C. (1980), Elect. Lett. **Vol. 16, No. 20**, 778.

Linder, E.V. (1988a), Ap.J. **326**, 517.

Linder, E.V. (1988b), Ap.J. **328**, 77.

Lipunov, V.M. and Postnov, K.A. (1987), Sov. Astron. **31**, 228.

Lipunov, V.M., Postnov, K.A. and Prokhorov, M.E. (1987), Astron. Astrophys. **176**, L1.

Livas, J.C. (1987), *Upper Limits for Gravitational Radiation from Some Astrophysical Sources*, PhD Thesis, M.I.T. Cambridge, Mass.

Lokken, J.E., Shand, J.A. and Wright, C.S. (1962), Can. Journ. Phys. **40**, 1000.

Lokken, J.E., Shand, J.A. and Wright, C.S. (1963), Journ. Geophys. Res. **68**, 789.

Lokken, J.E., Shand, J.A., Wright, C.S., Martin, L.H., Brice, N.M. and Helliwell, R.A. (1961), Nature **192**, 319.

Man, Shoemaker, Pham Tu, and Dewey (1990), preprint.

Marcuse, D. (1974), *Theory of Dielectric Optical Waveguides*, Academic Press, N.Y.

Marcuse, D. (1981), *Principles of Optical Fiber Measurements*, Academic Press, N.Y.

Marcuse, D. (1982), *Light Transmission Optics*, Van Nostrand Reinhold, N.Y.

Mashhoon, B. (1982), M.N.R.A.S. **199**, 659.

Mashhoon, B., Carr, B.J. and Hu, B.L. (1981), Ap.J. **246**, 569.

Meers, B.J., (1988), Phys. Rev. D **38**, 2317.

Michelson, P.F. (1986), Phys. Rev. D **34**, 2966.

Michelson, P.F. (1987), M.N.R.A.S. **227**, 933.

Michelson, P.F., Price, J.C. and Taber, R.C. (1987), Science **237**, 150.

Michelson, P.F. and Taber, R.C. (1984), Phys. Rev. D **29**, 2149.

Misner,W., Thorne, K.S. and Wheeler, J.A. (1973), *Gravitation*, W.H. Freeman and Company, San Francisco.

Morrison, D.F. (1976), *Multivariate Statistical Methods*, McGraw-Hill, New York.

Moss, G.E., Miller, L.R., and Forward, R.L. (1971), Appl. Optics **10**,, 2495.

Neidell, N.S. and Taner, M.T. (1971), Geophysics **36**, 482.

Nishizawa, K. and Nishi, H. (1984), App. Optics **23**, 1711.

Ohanian, H.C. (1976), *Gravitation and Spacetime*, W.W. Norton and Company, New York.

Orville, R.E. (1982), in *CRC Handbook on Atmospherics: Vol. 2*, ed. H. Volland, CRC Press, Boca Raton, Fl. 79.

Peccei, R.D. and Quinn, H. (1977), Phys. Rev. Letters **38**, 1440.

Pierce, E.T. (1963), Jour. Geophys. Res. **68**, 4125.

Polk, C. (1982), in *CRC Handbook on Atmospherics: Vol. 1*, ed. H. Volland, CRC Press, Boca Raton, Fl. 111.

Posmentier, E.S. (1974), Journ. Geophys. Res. **79**, 1755.

Rawley, L.A., Taylor, J.H., Davis, M.M. and Allan, D.W. (1987), Science **238**, 761.

Rees, M.J. (1983), in *Gravitational Radiation*, ed. N. Deruelle and T. Piran, North-Holland, Amsterdam, 297.

Rice, S.O. (1954), in *Selected Papers on Noise and Stochastic Processes*, ed. N. Wax, Dover Publications, New York, 133.

Robertson, H.P. (1938), Ann. of Math. **39**, 101.

Romani, R.W. (1988), Phys. Lett. B **215**, 477.

Rosi, L.A. and Zimmerman, R.L. (1976), Astrophys. Space Sci. **45**, 447.

Rubakov, V., Sazhin, M. and Veryaskin, A. (1982), Phys. Lett. **115B**, 189.

Sachs, R. and Wolfe, A. (1967), Ap.J. **147**, 73.

Sazhin, M.V. (1978), Sov. Astron. **22**, 36.

Sciama, D.W., Candelas, P. and Deutsch, D. (1981), Adv. Phys. **30**, 327.

Segal, M. (1990), private communication.

Shapiro, S.L and Teukolsky, S.A. (1983), *Black Holes, White Dwarfs, and Neutron Stars: The Physics of Compact Objects*, John Wiley and Sons, New York.

Schutz, B.F. and Tinto, M. (1987), M.N.R.A.S. **224** , 131.

Shoemaker, D., Fritschel, P., Giaime, J., Christensen, N. and Weiss, R. (1990), *A Prototype Michelson Interferometer with Fabry-Perot Cavities*, preprint.

Smith, S. (1988), *Search for Coalescing Binary Chirps*, PhD Thesis, Caltech, Pasadena, Ca.

Snyder, A.W. (1969), IEEE Trans. Microwave Theory and Techniques MIT-17, 1130.

Stecker, F.W. and Shafi, Q. (1983), Phys. Rev. Letters **50**, 928.

Stephens, M., Saulson, P. and Kovalik, J. (1990), *A Double Pendulum Vibration Isolation System for a Laser Interferometric Gravitational Wave Antenna*, preprint.

Stinebring, D.R., Ryba, M.F., Taylor, J.H. and Romani, R.W. (1990), Phys. Rev. Letters **65**, 285.

Taylor, J.H. and Weisberg, J.M. (1982), Ap. J. **253**, 908.

Taylor, J.H. (1987), in *Proceedings of the 11th International Conference on General Relativity and Gravitation*, ed.M. MacCallum, Cambridge University Press, Cambridge, 209.

Tepley, L. (1964), Journ. Geophys. Res. **69**, 2273.

Thompson, A.R., Moran, J.M. and Swenson, G.W. (1986), *Interferometry and Synthesis in Radio Astronomy*, John Wiley and Sons, New York.

Thorne, K.S. (1987), in *300 Years of Gravitation*, eds. S.W. Hawking and W. Israel, Cambridge University Press, Cambridge, 330.

Tinto, M. (1987), *Theoretical Aspects of Gravitational Wave Detection*, PhD Thesis, University College, Cardiff, Wales.

Traschen, J., Turok, N. and Brandenberger, R. (1986), Phys. Rev. D **34**, 919.

Vachaspati, T. and Vilenkin, A. (1985), Phys. Rev. D. **31**, 3052.

Vanderriest, C., Schneider, J., Herpe, G., Chevreton, M., Moles, M. and Wlerick, G. (1989), Astron. Astrophys. **215**, 1.

Vilenkin, A. (1981), Phys. Lett. **107B**, 47.

Vilenkin, A. (1981b), Phys. Rev. Letters **46**, 1169.

Vinet, J.Y. (1986), J. Physique **47**, 639.

Vinet, J.Y., Meers, B.J., Man, C.N. and Brillet, A. (1988), Phys. Rev. D **38**, 433.

Vogt, R.E. (1989), *A Laser Interferometer Gravitational-Wave Observatory (LIGO): Proposal to the National Science Foundation*, California Institute of Technology.

Volland, H. (1984), *Atmospheric Electrodynamics*, Springer-Verlag, Berlin, F.R.G.

Weber, J. (1969), Phys. Rev. Letters, **22**, 1302.

Weinberg, S. (1972), *Gravitation and Cosmology: Principles and Applications of the General Theory of Relativity*, John Wiley and Sons, New York.

Weisberg, J.M. and Taylor, J.H. (1984), Phys. Rev. Letters, **52**, 1348.

Weiss, R. (1972), *Electromagnetically Coupled Broadband Gravitational Antenna, Quarterly Progress Report*, Res. Lab. Electron. M.I.T. **105**, 54.

Weiss, R. (1979), in *Sources of Gravitational Radiation*, ed. L. Smarr, Cambridge Press, Cambridge, 7.

Weiss, R. (1989), *Vacuum Monitor for Interferometer Phase Fluctuations*, unpublished.

Weiss, R. (1990), unpublished.

Weiss, R., Saulson, P., Linsay, P. and Whitcomb, S. (1983), *A Study of a Long Baseline Gravitational Wave Antenna System.* A report prepared for the National Science Foundation, M.I.T.

Whitcomb, S., Gürsel, Y., Linsay, P., Saulson, P., Spero, R. and Weiss, R. (1983), *The Response of a Free Mass Gravitational Wave Antenna*, unpublished.

Wilkinson, D.T. (1987), in *Proceedings of the Thirteenth Texas Symposium on Relativistic Astrophysics*, ed. M. Ulmer, World Scientific, Singapore, 209.

Witten, E. (1984), Phys. Rev. D. **30**, 272.

Yanagihara, K. (1963), Journ. Geophys. Res. **68**, 3383.

Yokoyama, J. (1989), Phys. Rev. Letters **63**, 712.

Zel'dovich, Ya. B. and Novikov, I.D. (1983), *Relativistic Astrophysics, Volume 2, The Structure and Evolution of the Universe*, University of Chicago Press, Chicago.

Epilog

It is no secret that I did not enjoy my time at M.I.T. Never before have I experienced such a drain on my feelings and emotions. For whatever reason, the M.I.T. environment suppresses the ability and desire to laugh, cry, love, and enjoy the company of fellow humans. The concepts of basic human politeness and civility are absent. All interactions are strictly technical, the garnish to a meal being a spectral density, or some such thing. This environment is not normal, and I will not allow myself to be subjected to similar circumstances again.

The situation at M.I T. is not hopeless. I have developed many friendships while I have been here. It has been a pleasure to spend some time and share a laugh with these friends. Rainer Weiss has been a unique advisor. His unpretentious and straightforward style are refreshing. There are a number of malicious, cruel, and even sinister professors at M.I.T., and I was fortunate to work for someone who was on the level.

The attitude that I have towards science, especially experimental physics, may have been a source of controversy. Experimental physicists must be prepared to do every task by themselves. That is a given, and must be accepted by everyone who chooses this field. I have no argument here. However, one must not divorce him/herself from the goal of the experiment. You are no more than a drone if you have no care in the outcome, or the implications. Big science today does not allow the grunts a chance to worry about the final outcome. I was not deceived on what I was going to do when I entered grad school. I was aware that the experiment would still be in its development when I finished. However, I hoped that along the way I would be encouraged to understand *why* we were building the experiment. It is not good enough for me to build an experiment because someone has studied the problem and *told* us to do it. No, I have to understand why. I don't think I should have to apologize for this attitude. Ultimately, this thesis allowed me to think about why the experiment was being done. The thesis came at the end though, and I was a little annoyed that I was discouraged from thinking about gravity waves and general relativity in the beginning.

I now leave M.I.T. and gravity wave astronomy. Science is interesting, and sometimes it can even be useful. However, it is not the Holy Grail. We are still humans that have to live. I intend to start living again.